UC Irvine
UC Irvine Electronic Theses and Dissertations

Title
Investigation of new silver alloys and invention of Ag foil bonding and Ag-Ag direct bonding through in-situ reduction of surface oxides for high power and high temperature electronics

Permalink
https://escholarship.org/uc/item/6595h5br

Author
Wu, Jiaqi

Publication Date
2018

Peer reviewed|Thesis/dissertation

eScholarship.org Powered by the California Digital Library
University of California

UNIVERSITY OF CALIFORNIA,
IRVINE

Investigation of new silver alloys and invention of Ag foil bonding and Ag-Ag direct bonding through in-situ reduction of surface oxides for high power and high temperature electronics

DISSERTATION

submitted in partial satisfaction of the requirements
for the degree of

DOCTOR OF PHILOSOPHY

in Engineering

by

Jiaqi Wu

Dissertation Committee:
Professor Chin C. Lee, Chair
Professor Daniel Mumm
Professor Lizhi Sun

2018

© 2018 Jiaqi Wu

DEDICATION

To

my dear family and friends
whose unconditional love, support and encouragement
make it possible for me complete the degree work

I love you

TABLE OF CONTENTS

Page

LIST OF FIGURES vii
LIST OF TABLES xiv
ACKNOWLEDGMENTS xv
CURRICULUM VITAE xvii
ABSTRACT OF THE DISSERTATION xix
Chapter 1. Introduction 1
1.1 Electronic Packaging and Metals 1
1.2 Silver in Electronics Industry 2
1.3 Wire Bonding Technology 3
1.4 Die attachment for high temperature electronics 7
1.5 Direct bonding technology 10
1.6 Research aims and objectives 12
1.7 Dissertation outline 13
1.8 Reference 14
Chapter 2. Materials and Methods 19
2.1 Materials preparation and bonding 19
2.1.1 Growth of metallic ingots 19
2.1.2 Preparation of metallic foils 20
2.1.3 Thin film deposition 20
2.1.4 Thermal compression bonding 22
2.2 Sample preparation 23
2.2.1 Grinding and Polishing 23
2.2.2 Ion milling (Ar ion milling and FIB) 24
2.2.3 TEM sample preparation 26
2.3.4 Sample preparation for tensile test 30
2.3 Characterization techniques 30
2.3.1 Scanning electron microscopy 30
2.3.2 Energy dispersive spectroscopy 32
2.3.3 Transmission electron microscopy 33
2.3.4 X-ray diffraction 38

2.3.5 X-ray photoelectron spectroscopy 40
2.3.6 Tensile/shear test 41
2.3.7 Surface profilometer 42
2.4 Reference: 43
Chapter 3. Preparation and evaluation of mechanical properties and tarnish resistance of Ag solid solution phase with zinc 44
3.1 Introduction 44
3.2 Materials and Characterization 46
3.3 Tensile test 51
3.4 Failure analysis 56
3.5 Evaluation of tarnishing resistance 61
3.5.1 Test design and setup 61
3.5.2 Characterization and measurement 64
3.6 Conclusions 67
3.7 Reference 67
Chapter 4. Complete elimination of Ag3Al in Ag wire bonds onto Al pad through alloying In into Ag 71
4.1 Reliability issue of Ag wire bonding on Al pad 71
4.2 The motivation of alloying In into Ag 72
4.2.1 Cross-sectional examination of as-bonded samples 73
4.2.2 Cross-sectional images after FIB cutting 75
4.2.3 TEM analysis of the bonding interface 77
4.2.4 Drawbacks of the preliminary study 80
4.3 Test vehicle and results 81
4.3.1 Morphology of as prepared sample and Ag-Al intermetallics after HTS test 82
4.3.1.1 Microstructure of as-prepared films 82
4.3.1.2 Interfacial IMCs evolution of Al/(Ag)-5In samples 83
4.3.1.3 Interfacial IMC evolution of Al/(Ag)-12In samples 84
4.3.2 The sequence of intermetallic phase transformations 88
4.3.2.1 Al/(Ag)-5In samples 88
4.3.2.2 Al/(Ag)-12In samples 92
4.3.3 Behavior of oxides and voids 96
4.3.3.1 Oxides and voids in Al/(Ag)-5In 96

4.3.3.2 Oxides and voids in Al/(Ag)-12In 97
4.4 Discussions 98
4.4.1 Microstructural evolution and phase transformations 98
4.4.2 The impacts of In on thermodynamics and kinetics 102
4.4.2.1 Thermodynamics of nucleation and growth of IMCs 102
4.4.2.2 Kinetics and local structure 109
4.4.3 Growth mechanism of voids and aluminum oxide 111
4.4.4 Properties of ternary phase 114
4.5 Conclusions 118
4.6 Reference 119
Chapter 5. Low pressure solid-state bonding technology using fine-grained silver foils for high temperature electronics 125
5.1 Reliability issues of joint produced by sintering Ag nanoparticles 125
5.2 Solid-state bonding technology 129
5.3 Experimental procedures 132
5.3.1 Preparation and characterization of Ag foils with recrystallized microstructure 132
5.3.2 Solid-state bonding process 133
5.4 Results and discussions 134
5.4.1 XRD and PF measurement 134
5.4.2 Cross-section examinations of as-bonded Si/Ag/Cu structures 137
5.4.3 HTS test results 138
5.4.4 Shear test results, fractography and discussion 141
5.5 Conclusion 150
5.6 Reference 151
Chapter 6. Direct Ag-Ag bonding by in-situ reduction of pre-oxidized surface for high performance interconnects 154
6.1 Recent accomplishments in direct bonding technology 154
6.2 Materials selection and motivation 158
6.3 Results and discussion 160
6.3.1 Characterization of as-deposited Ag film 160
6.3.2 Optimization of oxidation condition 162
6.3.3 Cross-sectional study (SEM/FIB) 169

6.3.4 TEM analysis of the joint ... 175
6.4 Conclusions ... 179
6.5 Reference ... 180
Chapter 7. Summary ... 182
7.1 Main conclusions ... 182
7.2 Recommendations to future work ... 184

LIST OF FIGURES

Page

Fig. 1.1 Illustration of wedge bonding 4

Fig. 1.2 Illustration of ball bonding 5

Fig. 1.3 Development of international bonding wire market........ 6

Fig. 1.4 Sketch of die-substrate bonding through die-attachment process........ 7

Fig. 1.5 Copper pillar joint in commercialized chip 10

Fig. 1.6 Cu-Cu direct bonded joint 11

Fig. 1.7 Cu-Cu joint with post-annealing process 12

Fig. 1.8 Outline of the dissertation. 13

Fig. 2.1 Procedure of ingot growth........ 19

Fig. 2.2 Angstrom Engineering EvoVac Glovebox Evaporator in IMRI........ 21

Fig. 2.3 Schematic of the vacuum furnace showing the key components: (a) quartz cylinder, (b) upper stainless plate, (c) base plate, (d) graphite platform, (e) heating wire, (f) electrical feedthroughs, (g) platform thermocouple, and (h) sample thermocouple. 22

Fig. 2.4 Vacuum bonder details: (a) Graphite stage with sample fixed; (b) Chamber ready for bonding........ 23

Fig. 2.5 Comparison between mechanical polishing and FIB cutting: (a) cross-sectional image after mechanical polishing; (b) FIB cutting into the joint at the same position. 25

Fig. 2.6 Configurations of Ar ion milling system (a) and dual beam system (b). 26

Fig. 2.7 TEM sample preparation through in-situ lift-out process........ 29

Fig. 2.8 The geometry of tensile specimen, in accordance with ASTM E8/E8M-08........ 30

Fig. 2.9 Interactions between electron beam and bulk materials 31

Fig. 2.10 SEMs in IMRI: (a) XL30 FEG SEM; (B) TESCAN GAIA3 SEM/FIB. 32

Fig. 2.11 Interactions between electron beam and TEM sample. 34
Fig. 2.12 Signals generated under STEM optics. 37
Fig. 2.13 Schematic illustration of Bragg's law. 38
Fig. 2.14 Rigaku Smartlab in IMRI with BB optics. 39
Fig. 2.15 Optics of pole figure measurement. 40
Fig. 2.16 Setup of shear test 42
Fig. 3.1 Silver-zinc binary phase diagram. 46
Fig. 3.2 XRD pattern of Pure silver (blue), (Ag)-5Zn (red) and (Ag)-15Zn (black). 47
Fig. 3.3 Illustration of data collection in EDX. 50
Fig. 3.4 Engineering stress vs. strain curve of pure silver (blue), (Ag)-5Zn (black) and (Ag)-15Zn (red) 52
Fig. 3.5 True stress vs. strain curve of pure silver (blue), (Ag)-5Zn (black) and (Ag)-15Zn (red) 53
Fig. 3.6 SEM Image of fracture surface of (Ag)-5Zn at different magnifications. 58
Fig. 3.7 SEM Image of fracture surface of (Ag)-15Zn at different magnifications. 59
Fig. 3.8 Illustration of tensile instability and rupture. 60
Fig. 3.9 Internal voids in the sample after tensile test. 61
Fig. 3.10 Equilibrium vapor pressure of sulfur, $\sum_i$ is the total pressure, $2 \leq n \leq 8$, is the partial pressures of S_n. 62
Fig. 3.11 Process flow of evaluation of anti-tarnishing properties. 63
Fig. 3.12 Sulfurization test setup. 63
Fig. 3.13 Phase identification of silver sulfide. 64
Fig. 3.14 Optical images of boundaries between protected and unprotected region. 65
Fig. 3.15 The thickness of Ag_2S as a function of reaction time for tested samples. 66
Fig. 4.1 Failure mechanism of traditional Ag-Al bonds during HAST. 72

Fig. 4.2 Illustration of pre-bonding structure. 73

Fig. 4.3 Optical images of as-bonded samples (a) pure Ag/Al; (b) (Ag)-10In/Al. 74

Fig. 4.4 SEM images of as-bonded samples (a) pure Ag/Al; (b) (Ag)-10In/Al. 75

Fig. 4.5 SEM images of cross-sections created by FIB cutting (a) (Ag)-10In side; (b) Al side. 76

Fig. 4.6 HRTEM images of original bonding interface between (Ag)-10In and Al. 78

Fig. 4.7 SAED result of IMCs near the original interface 79

Fig. 4.8 HAADF image and SAED analysis of the joint (a) STEM image of the sample; (b) SAED from point 3; (c) SAED from point 5. 79

Fig. 4.9 Structure of test vehicle: (a) overview of multi-layer structure; (b) microstructure of a thin (Ag)-xIn cross section layer prepared by FIB. A platinum (Pt) layer was deposited before FIB cutting to get a clean cross-section. 83

Fig. 4.10 Microstructure of (Ag)-5In after 1000 h aging at 150 °C: a. overview; b. magnified image of an area indicated in a. 83

Fig. 4.11 Cross-sectional images of Al/(Ag)-5In sample aging at 175 °C for different durations: 72 h (a and a'); 144 h (b and b'); 192 h (c and c'); 264 h (d and d'). (a', b' c' and d' are magnified images of typical features in a, b, c and d, respectively). 85

Fig. 4.12 Cross-sectional images of Al/(Ag)-5In sample aging at 250 °C for different durations: 1 h (a and a'); 2 h (b and b'). 86

Fig. 4.13 Cross-sectional images of Al/(Ag)-12In sample aging at 175 °C for different durations: (a) 300 h; (b) 500 h. 86

Fig. 4.14 Cross-sectional images of Al/(Ag)-12In sample aging at 250 °C for different duration: 2.5 h (a and a'); 3 h (b and b'); 3.5 h (c and c'); 4.5 h (d and d'). 87

Fig. 4.15 (a) HAADF image of Al/(Ag)-5In interface after 72 h aging at 175 °C; (b) STEM-EDX results collected from circled region in (a); (c) and (d) are lattice imaging and SAED from region A-1 in (a), respectively. 88

Fig. 4.16 (a) HAADF image of Al/(Ag)-5In interface after 144 h aging at 175 °C; (b) STEM-EDX results collected from circled region in (a); (c) and (d) are lattice imaging and SAED from region A-1 in (a), respectively. 89

Fig. 4.17 (a) HAADF image of Al/(Ag)-5In interface after 192 h aging at 175 °C; (b) STEM-EDX results collected from circled region in (a); (c) and (d) are SAED collected from region 2 and 3 in (a), respectively. 90

Fig. 4.18 (a) HAADF image of Al/(Ag)-5In interface after 264 h aging at 175 °C; (b) STEM-EDX results collected from circled region in (a); (c) lattice imaging and corresponding FFT result from region 3 in a; (d) lattice imaging from region A-1, FFT are from marked region in d. 91

Fig. 4.19 (a) HAADF image of Al/(Ag)-5In interface after 2 h aging at 250 °C; (b) STEM-EDX results collected from circled region in (a). 92

Fig. 4.20 (a) HAADF image of Al/(Ag)-12In interface after 2.5 h aging at 250 °C; (b) STEM-EDX results collected from circled region in (a); (c) lattice image captured in region 3 in (a). 93

Fig. 4.21 (a) and (d) BF images of Al/(Ag)-12In interface after 3 h aging at 250 °C; (b) and (e) SAED captured from region 2 in (a) and region 1 in (d), respectively; (c) and (f) STEM-EDX results collected from circled regions in (a) and (d), respectively. 94

Fig. 4.22 (a) BF image of Al/(Ag)-12In after 4.5 h aging at 250 °C; (b) STEM-EDX results collected from circled region in (a); (c) and (d) are SAED collected from region 1 and 3 in (a), respectively. 95

Fig. 4.23 HRTEM images of the original interface of Al/(Ag)-5In samples and void issue after aging at 175 °C: (a) and (c) 144h; (b) and (d) 264 h. 96

Fig. 4.24 HRTEM images of the interface of Al/(Ag)-12In samples and void issue after aging at 250 °C: (a) 2.5 h; and (c) 3 h; (b) and (d) 4.5 h. 97

Fig. 4.25 Illustration of phase transformation in Al/(Ag)-5In during thermal aging. 99

Fig. 4.26 Ag-Al binary phase diagram (Recolored by ASM international). 100

Fig. 4.27 Illustration of phase transformation in Al/(Ag)-12In during thermal aging. 102

Fig. 4.28 Thermodynamic calculation result: (a) Molar Gibbs free energy (G_m) of (Ag)-xIn vs. In concentration; (b) dG_m/dx vs. In concentration. 108

Fig. 4.29 Sketch of interfacial atoms and vacancies (the quantity of vacancies is exaggerated). 111

Fig. 4.30 XRD result of the ingot consisting of the ternary phase. 114

Fig. 4.31 EDX result of the ingot. 115

Fig. 4.32 Hardness test results: (a), (b) and (c) are Vickers indentation under different load; (d) is Knoop indentation........116

Fig. 4.33 HAST test setup, following JEDEC JESD22-A110C. 117

Fig. 4.34 The measurement of the corroded layer on the surface of ternary phase. 118

Fig. 5.1 Strength degradation of joints produced by sintering Ag on Cu substrate during HTS test in air [3]. 126

Fig. 5.2 Cross-sectional study of joints produced by sintering Ag process: (a) low magnification image; (b) high magnification image 126

Fig. 5.3 Sketch of the penetration of oxygen and formation of copper oxides 127

Fig. 5.4 Ag-coated Cu substrate still get oxidized during aging process 127

Fig. 5.5 Sintering Ag process using Cu substrate with ENIG surface finish. The strength corresponding to these four images: (a) 15MPa, (b) 17MPa, (c) 12 MPa, (d) 10 MPa 128

Fig. 5.6 Illustration of the behaviors of materials near the interface during bonding assisted by pressure and heat........130

Fig. 5.7 Ag-Cu binary phase diagram (Recolored by ASM international)........131

Fig. 5.8 Illustration of bonding structure (dimensions of small features are exaggerated). 133

Fig. 5.9 XRD pattern of a typical annealed Ag foil, where the Cu peaks were caused by X-ray incident on the Cu sheet on which the Ag foil was adhered to. 135

Fig. 5.10 PF measurement results: (a) (111) poles of as-rolled sample, (b) (220) poles of as-rolled sample, (c) (111) poles of annealed sample, (d) (220) poles of annealed sample........136

Fig. 5.11 Optical microscopy image of an as bonded Si/Ag/Cu structure. 138

Fig. 5.12 SEM images of interface region of a sample prepared by FIB cutting: (a) Cu/Ag bonding interface, (b) orientation contrast image on Ag region. 138

Fig. 5.13 Cross section OM images of samples after aging at 300°C in air: (a) sample after 72 hours, (b) sample after 200 hours. 139

Fig. 5.14 SEM images of cross sections produced by FIB cutting on samples after aging at 300°C in air : (a) interfacial region after 72-hour aging), (b) orientation contrast

image of Ag region after 72-hour aging, (c) interfacial region after 200-hour aging, (d) orientation contrast image on Ag region after 200-hour aging. 140

Fig. 5.15 Configuration of shear test and illustration of fracture surface examination. 142

Fig. 5.16 Fracture surfaces of an as-bonded sample: (a) overview of broken end of Ag foil and Ag traces on Cu substrate, (b) one type of morphology of Ag traces on Cu substrate, (c) another type of Ag traces, (d) high magnification image of circled region in (c). 143

Fig. 5.17 Fracture surfaces of a sample after 72-hour aging at 300°C: (a) overview of broken end of Ag foil, (b) overview of Ag traces on Cu substrate, (c) and (d) are high magnification images of circled regions in (b). 144

Fig. 5.18 Fracture surfaces of a sample after 200-hour aging: (a) overview of broken end of Ag foil, (b) overview of Ag traces on Cu substrate, (c) and (d) are high magnification images of circled regions in (b). 145

Fig. 5.19 TEM analysis of Ag-Cu bonding interfaces after 200 hours aging: (a) bright field imaging, (b) EDX line scan along the red arrow in (a). 147

Fig. 5.20 HRTEM image of the Ag-Cu bonding interface after 200 h aging at 300 °C. (111) Cu and (200) Ag are aligned. 149

Fig. 6.1 Evolution of interfacial structure during bonding that only involving solid state materials. 155

Fig. 6.2 Joints produced by sintering Cu particles: (a) shear strength; (b) sintering pure Cu particles under reducing atmosphere; (c) sintering pre-oxidized Cu particles without reducing atmosphere; (d) sintering pre-oxidized Cu particles under reducing atmosphere. 157

Fig. 6.3 Ag-O binary phase diagram (Recolored by ASM International) 159

Fig. 6.4 Pre-bonding Structure of joint formed by in-site reducing silver oxides. 160

Fig. 6.5 Surface morphology of as-deposited film. 161

Fig. 6.6 Cross-sectional view of the as-deposited film. 161

Fig. 6.7 Surface morphologies of samples with difference plasma treatment time: (a) 3s; (b) 5s; (c) 10s. 163

Fig. 6.8 Cross-sectional view of surface oxides after 3s plasma treatment. 164

Fig. 6.9 XPS survey scan of the oxidized surface. 165

Fig. 6.10 XPS regional scan results: (a) Ag 3d; (b) O 1s. 166

Fig. 6.11 Surface morphologies after decomposition of surface oxides at 210 °C: (a), (b) and (c) are corresponding to the conditions specified in (a), (b) and (c) of Fig. 6.7. 167

Fig. 6.12 AFM results of the film of different conditions. 169

Fig. 6.13 Cross-sectional images of joint bonded by pure Ag film and Ag film with surface oxides produced by oxygen plasma treatment for 3 s. 170

Fig. 6.14 Cross-sectional study after FIB cutting (Site 1): (a) Overview of the clean cross-section; (b) and (c): High magnification images of highlighted regions in (a). 171

Fig. 6.15 Cross-sectional study after FIB cutting (Site 2): (a) Overview of the clean cross-section; (b) and (c): High magnification images of highlighted regions in (a). 172

Fig. 6.16 TKD result of the bonded joint. 174

Fig. 6.17 Cross-sectional images of joint bonded by pure Ag film and Ag film with surface oxides produced by oxygen plasma treatment for 5 s. 175

Fig. 6.18 BF image of the joint. 176

Fig. 6.19 Details of the bonding interface between two grains: (a) low magnification; (b) HRTEM with FFT results of the highlighted regions. 177

Fig. 6.20 STEM/EDX mapping of the joint. 178

Fig. 6.21 EDX line scan result of the center region of the joint. 178

LIST OF TABLES

Page

Table 2.1 The dimensions of tensile specimen, in accordance with ASTM E8/E8M-08. 30

Table 2.2 Detailed measurement condition of XRD under BB mode. 40

Table 3.1 Peak list and analysis results of pure silver 47

Table 3.2 Peak list and analysis results of (Ag)-5Zn 48

Table 3.3 Peak list and analysis results of (Ag)-15Zn 48

Table 3.4 EDX (point and shoot mode) results for (Ag)-5Zn and (Ag)-15Zn 50

Table 3.5 Summary of tensile test results with pure silver as comparison................................ 54

Table 3.6 Step height after reaction 65

Table 4.1 EDX results, collection sequence can be found in Fig. 4.4. 74

Table 4.2 STEM-EDX results, positions of points are shown in Fig. 10a 80

Table 4.3 Crystallographic information molar volume of phases involved in this paper. The molar volume is calculated by V_C*N_A/Z where V_C is the volume of the unit cell, N_A is the Avogadro constant and Z is the number of formula weights per unit cell. 101

Table 4.4 Atomic size and electronegativity of selected elements. 103

Table 4.5 Calculated molar free energy values involved in equation (7)................................ 107

Table 4.6 Possible inter-metallic reactions and corresponding volumetric changes............ 112

Table 4.7 Comparison of mechanical properties of Ag_2Al, Ag_3Al and ternary phase. 116

Table 5.1 XRD peaks and analysis results. 134

Table 5.2 Shear test results. 142

Table 6.1 Specifications of Gatan® plasma system. 162

ACKNOWLEDGMENTS

I would like to express the appreciation to my supervisor and committee chair, Professor Chin C. Lee, for his support, patient guidance and valuable suggestions not only in the project as well as in the altitude towards research and life. His commitment to hard work and discipline greatly inspired me through the whole life of Ph.D. study. I also would like to thank him for several nomination of fellowships and TA ships and financial support from his research funding.

I would like to thank my committee members, Professor Daniel Mumm and Professor Lizhi Sun, for their guidance, encouragement and insightful comments on my work. I also would like to express my gratitude towards the director and scientists in Irvine Materials Research Institute (IMRI), Dr. Jian-Guo Zheng, Dr. Qiyin Lin, Dr. Toshihiro Aoki, Dr. Li Xing and Dr. Ich Tran, for their training and guidance in operating these state-of-art facilities. In addition, a thank you to Dr. Wei Zeng from Shanghai Jiaotong University, for his valuable suggestions and help in my TEM study.

I also would like to express my gratitude towards my colleagues and friends, Dr. Yongjun Huo, Dr. Shao-Wei Fu, Dr. Yi-Ling Chen, Dr. Chun-An Yang, Ms. Yipin Wu, Mr. Roozbeh Sheikhishooshtari and Mr. Hsiang-Yu Chan for their help, support, suggestions and love. I also would like to thank Richard Chang in INRF for his training of cleanroom operations.

I would like thank everyone who helped me during my PhD study but not mentioned above due to the limitation of content.

Last but not least, I would like to express my deepest appreciation to my family members. Without their unconditional love, spiritual encouragement and materials support, I can't complete the degree work. My parents' altitude towards work and life greatly inspired me to keep moving in my career. I also would like to thank my fiancée, Wenjun Zhu, for her dedication to our relationship, support and companion during my hardest time, and happiness time we shared. In addition, I would like express the appreciation to my old friends, those connected by the internet, for their support and love.

CURRICULUM VITAE

Jiaqi Wu

2014	B.E. in Electronic Packaging Technology, School of Materials Science and Engineering Beijing Institute of Technology
2016	M.S. in Engineering in Materials and Manufacturing Technology, University of California, Irvine
2016-2017	Teaching Assistant, Department of Electrical Engineering and Computer Science, University of California, Irvine
2016-2018	Lab Assistant, Irvine Materials Research Institute (IMRI), University of California, Irvine
2018	Ph.D. in Engineering in Materials and Manufacturing Technology, University of California, Irvine

PUBLICATIONS

1. J. Wu, Y. Huo, C.C. Lee, Complete elimination of Ag3Al in Ag wire bonds on Al by alloying In into Ag, Materialia (2018).
2. J. Wu, C.C. Lee, Low-pressure solid-state bonding technology using fine-grained silver foils for high-temperature electronics, J Mater Sci 53(4) (2018) 2618-2630.
3. J. Wu, C.C. Lee, The growth and tensile deformation behavior of the silver solid solution phase with zinc, Materials Science and Engineering: A 668 (2016) 160-165.
4. C.A. Yang, J. Wu, C.C. Lee, C.R. Kao, Analyses and design for electrochemical migration suppression by alloying indium into silver, Journal of Materials Science: Materials in Electronics 29(16) (2018) 13878-13888.
5. Y. Huo, J. Wu, C.C. Lee, Solid solution softening and enhanced ductility in concentrated FCC silver solid solution alloys, Materials Science and Engineering: A 729 (2018) 208-218.
6. Y.-L. Chen, J. Wu, C.C. Lee, Solid-state bonding of silicon chips to copper substrates with graded circular micro-trenches, Journal of Materials Science: Materials in Electronics 29(12) (2018) 10037-10043.
7. Y. Huo, J. Wu, C.C. Lee, Study of Anti-Tarnishing Mechanism in Ag-In Binary System by Using Semi-Quantum-Mechanical Approach, J Electrochem Soc 164(7) (2017) C418-C427.
8. J. Wu, C.C. Lee, Low Pressure Solid-State Bonding Using Silver Preforms for High Power Device Packaging, 2017 IEEE 67th Electronic Components and Technology Conference (ECTC), 2017, pp. 2002-2007.

ABSTRACT OF THE DISSERTATION

Investigation of new silver alloys and invention of Ag foil bonding and Ag-Ag direct bonding through in-situ reduction of surface oxides for high power and high temperature electronics

By

Jiaqi Wu

Doctor of Philosophy in Engineering

University of California, Irvine, 2018

Professor Chin C. Lee, Chair

Despite the superior physical properties of silver (Ag) and its alloys such as high electrical and thermal conductivities and high ductility, their applications in electronics have been quite limited due to corrosion and tarnishing concerns. To expand their applications in electronic packaging, developing new materials and processes and investigating new materials properties are essential. This PhD research aims to design and grow novel Ag alloys and address the intermetallic compound (IMC) issues associated with Ag wire bonds, followed by producing Ag and alloys in various forms for solid state bonding processes valuable for high temperature electronics.

Firstly, the growth of homogeneous Ag solid solution phase with zinc (Zn) is conducted at two different compositions and their mechanical properties are evaluated by tensile test. According to the experimental results, Ag solid solution phase with Zn at either composition show tempered yield strength, high tensile strength and large uniform strain compared to those of Ag. Moreover, the tarnish resistance is improved with the alloying of zinc. Secondly, Ag_3Al has been reported to be the weakest part in the Ag-Al wire bonds due

to its low toughness and low corrosion resistance. A method to suppress Ag_3Al through alloying indium (In) into Ag is devised. The working mechanism is studied through transmission electron microscopy (TEM) and thermodynamic modeling. Reaction kinetics and evolution of defects are further discussed.

A new approach for die attachment through solid-state bonding using fine-grained Ag foils is developed. The bonding is conducted at 300 °C, assisted by low pressure. The strength of the joints far exceeds the requirement specified in military standards. No degradation can be observed after aging test. This approach avoids the oxidation issue on bonding interfaces in present sintered-silver technique.

Lastly, an Ag-Ag direct bonding process is invented using in-situ decomposition of silver oxide. The bonding is performed at 210 °C under 0.1 torr vacuum and assisted by only 1.4 MPa pressure. Encouragingly, the resulting Ag-Ag joints are strong with only sparse voids in nano-scale. Cross-sectional study shows that the bonding is formed by grain growth across the original interface. No residual oxygen is trapped. This new process is a breakthrough in Ag-Ag bonding at low temperature and low pressure that produce pure Ag joints. Its applications are wide open.

The Ag solid solution phases investigated here show great potential not only in wire bonding and other mechanical component in electronic devices but also photonic applications. The novel bonding processes achieved in this study should be highly valuable for applications in advanced electronic and photonic packages where performance and reliability are highly preferred.

Chapter 1. Introduction

1.1 Electronic Packaging and Metals

It has been more than seventy years since the invention of the semiconductor devices. There has been tremendous development in the related areas such as integrated circuit (IC), power electronics, micro-electro-mechanical system (MEMS) and photonics. Nowadays, from mobile phones to aerospace exploration, these semiconductor technologies influence the civilization of humanity in various aspects. The design and manufacturing of electronic devices with more function, high performance, reliability and low cost are hot topics in industry and research. In general, the manufacture process of semiconductor chips are divided into two stages. The products of the front end of line (FEOL) of semiconductor industry are called wafers. A wafer consists of lots of repeated units which are named as die. The die is the core of the electronic device since most of the functional units are built within the die. However, the die must enter into back end of line (BEOL) and get properly packaged before realizing its function. The packaging process provides physical protection, mechanical support, electrical interconnection between the die and external circuit, and the heat dissipation path. Based on the requirement of different applications, the materials and manufacturing process must be justified. For example, the mobile phones are getting thinner and thinner, which requires the packaging size (especially the height) of the microprocessor to be reduced accordingly. On the other hand, the length of the signal transmission line must be reduced to ensure the signal integrity since the frequency of the signals are getting higher. Instead of using traditional packaging architecture, the fan-out wafer level packaging (FOWLP) technology is successfully utilized and eliminates the substrate in package and reduces the packaging

height and the length of transmission line. Meanwhile, the cost of the packaging process is decreased due to the high throughput. In contrast, the packaging size is less of an issue in aerospace applications where the capability of sustaining the extreme environment becomes critical. Instead of using epoxy molding compounds (EMCs) and organic substrate, hermetical packaging method and multi-layer ceramic substrates are preferred. In every case, the selection of materials and appropriate process is critical.

Among all the materials can be found in electronic products, metals form the most important branch since metals are usually mechanically strong, malleable, and electrically and thermally conductive. For example, tin (Sn) can be found in virtually every electronic product since the assembly of electronic devices on printed circuit board (PCB) requires soldering. Recently, the development of advanced device technologies (i.e. high speed device and high power device) have raised a few challenges for the packaging industry. For example, in order to enhance the signal integrity in high frequency devices, the RC delay of the transmission line must be reduced. Also, the increase of power density in high power devices requires the thermal resistance between the active chip and heat sink to be as small as possible while the stability of the bonding medium must be high. Unfortunately, many traditionally used materials cannot meet those requirements, which motivates the researchers in related fields to look for new candidates.

1.2 Silver in Electronics Industry

Since metals are mostly used as conductors (either heat or current) in electronic devices, silver (Ag) looms large due to its best electrical and thermal conductivities among metals. In 2016, nearly 242.9 million ounces of silver were consumed in electronic products, which takes up about 25% of the overall supply of Ag [1]. In televisions,

telephones and microwave ovens, silver membrane switches can be easily found and they are reliable for millions of on/off cycles. For printed circuit boards (PCBs), silver based inks and films are applied to the composite boards to create electrical pathways. In the field of electronic packaging, Ag is also widely applied. For example, Ag is alloyed into the Sn matrix and the Sn-Ag-Cu (SAC) solder has been demonstrated and standardized as the substitution of tin-lead (Sn-Pb) solder [2]. Moreover, Ag particles are added into epoxy adhesives to increase the thermal conductivity and the adhesive is widely used in die-attachment for consumable electronic devices [3]. In addition, Ag can be found in low temperature co-fired ceramic (LTCC) substrate as conductor and electrode material [4]. Recently, numerous new applications of Ag are rising on the horizon in the packaging industry such as bonding wire materials [5], die-attachment for high power devices and direct bonding technology [6]. However, improvements are essential either in materials aspect or process to realize wide acceptance and applications. To have a comprehensive view of the aims of my research, those three process/technology are briefly reviewed in the following three sections.

1.3 Wire Bonding Technology

Among all the interconnection technologies utilized between chips and external circuits, wire bonding is dominant and over 90% of chips including IC chips, LEDs and MEMS are wire bonded [7]. Particularly, for applications where low cost, high yield, flexibility and reliability are highly concerned, wire bonding is the best approach. Nowadays, the infrastructure of wire bonding has been worldwide established and the development of wire bonding is so extensive that no other chip-interconnection technologies can substitute it in near future. Even in the packages (i.e. package on package

(PoP)) of most advanced cellphone, wire bonding is still used for the communication between chips. On the other hand, the advancement of wire bonding technology is continued and multiple goals including finer pitch (down to 20 μm), higher yield and lower cost will be achieved in the future.

There are two typical geometries of the wire bonding: wedge bonding (Fig. 1.1) and ball bonding (Fig. 1.2) [8]. Wedge bond occurs in both geometry is formed by pressing the wire against the bond pad. The bonding is implemented at room temperature with low pressure and ultrasonic energy which can clean the surface and disrupt the oxide. The wedge bonding was the dominant method in large pitch application until the application of ball bonding. One of the major challenge of wedge bonding is that the bonding must be prefect directional, which limits the flexibility of the layout. Secondly, the risk of first bonds short circuit is high in wedge bonding especially the second bond is lower than the first bond. Nowadays, the wedge bonding is mostly used power electronic devices or discrete devices.

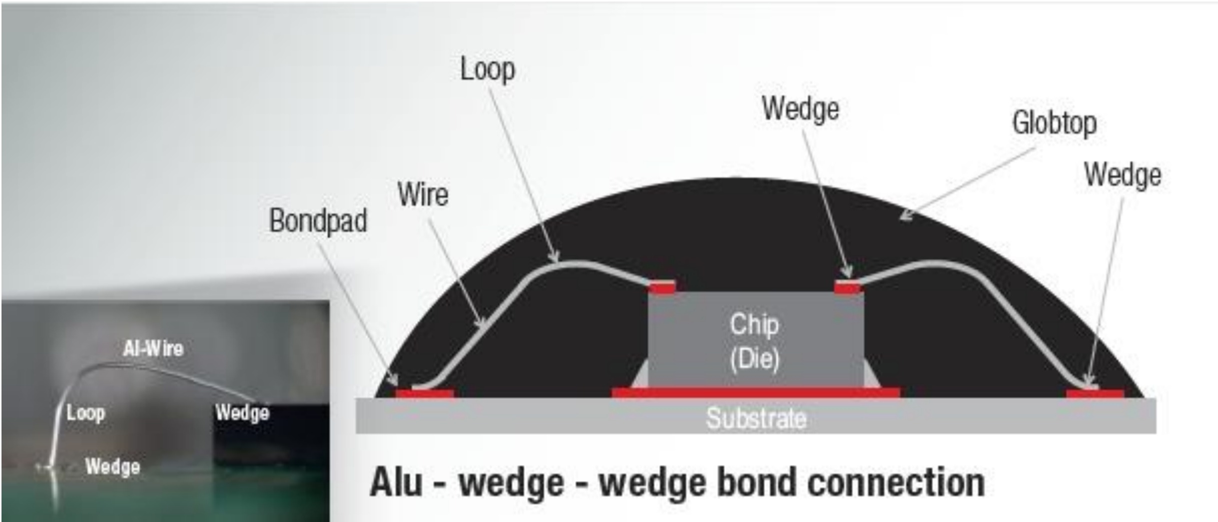

Fig. 1.1 Illustration of wedge bonding [8]

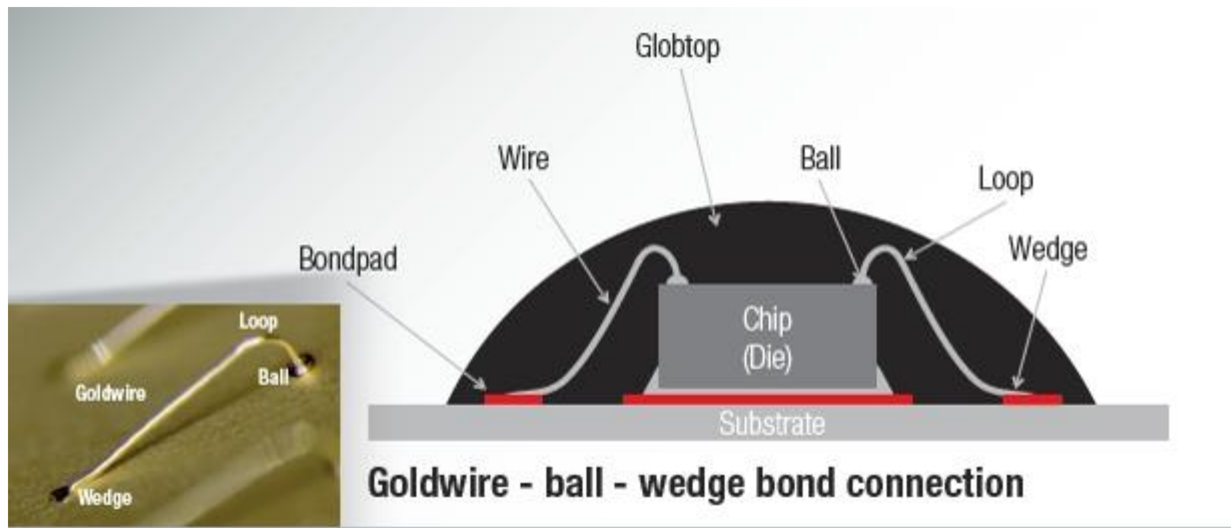

Fig. 1.2 Illustration of ball bonding [8]

For ball bond, a free-air-ball (FAB) is firstly formed through electrical discharge and the FAB is bonded to the pad on the chips through either thermal compression bonding (TCB) or thermosonic bonding (TSB). In TCB, high pressure and high temperature (300-400 °C) are needed to flatten the surface asperities to form metallurgic joint while the requirement of pressure and temperature are much lower in TSB (only 125-240 °C) with the assistance from ultrasonic energy. In addition, the throughput of TSB is also higher than that of TCB. Therefore, TSB is the dominant process, occupying over 90% of the wire bonding domain [7].

The evolution of bonding materials is shown in Fig. 1.3 [9]. In the early days, gold (Au) was firstly proposed as the bonding wire material because of its high ductility, low hardness, corrosion resistance and high electrical conductivity. The bonding is formed between Au and Al pad on the active chip. The diameter of the Au wire has been scaled down to 15 μm in order to meet the requirement of fine pitch interconnection. However, the Au/Al binary system readily leads to the excessive growth of the intermetallic

compounds (IMCs), voids and oxides, which significantly affects the lifetime of the electronic products [10]. In addition, the high cost of the raw materials motivated the industry to look for alternative bonding wire materials.

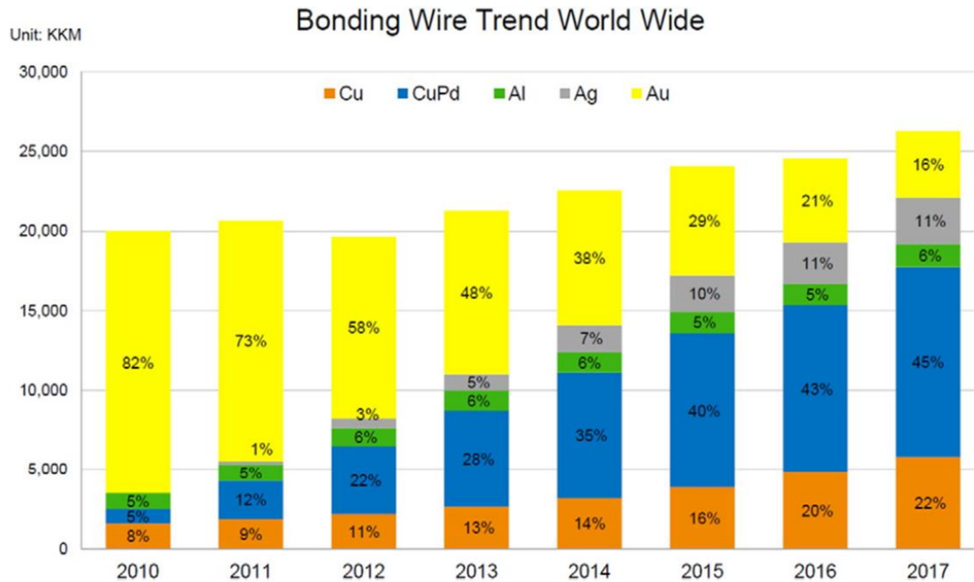

Fig. 1.3 Development of international bonding wire market [9].

In the past decade, copper (Cu) wire bonding technologies have been developed and the relevant reliability studies have been performed. Compare to Au/Al systems, Cu/Al bonding exhibits much lower growth rate of IMCs and voids [11, 12]. Since Cu get oxidized easily during the electronic flame-off (EFO) process, palladium (Pd) is employed to passivate the surface, which largely increases the cost of the materials. On the other hand, the hardness of Cu is higher than that of Au, which dramatically increases the possibility of damages of pads and chips, especially in products sensitive to the bonding force such as memory devices [13].

Recently, Ag and its alloys have been introduced as wire materials due to its ease of manufacturability, moderate hardness, high electrical and thermal conductivities, and

acceptable cost. The market is in continuous growth and a few vendors are focusing on the development of novel Ag and its alloys bonding materials. However, systematic studies regarding to the process parameters, IMC growth and other reliability issues are required to be done to realize the wide application of Ag in wire bonding technology.

1.4 Die attachment for high temperature electronics

In electronic packaging, die attachment (shown in Fig. 1.4) is a crucial step that provides the active chips with mechanical support and heat dissipation path. In consumable electronics that function at room or slightly elevated temperature, epoxy with silver fillers is employed as bonding medium. However, the epoxy cannot meet the requirements when the devices are operated at high temperature (100 °C or higher) in terms of mechanical strength and thermal conductivity.

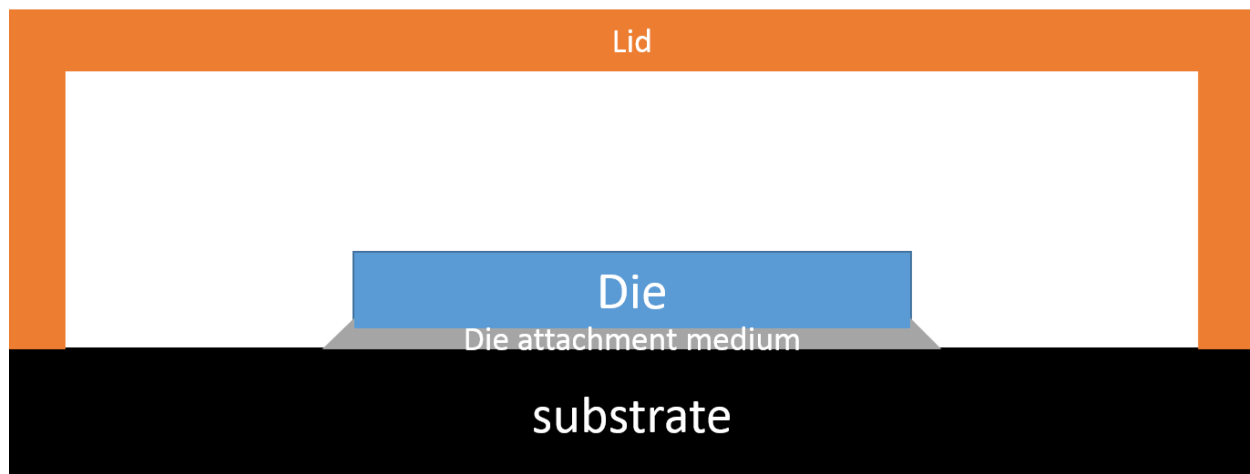

Fig. 1.4 Sketch of die-substrate bonding through die-attachment process.

Nowadays, advanced development in aircraft, automotive, aerospace, and deep oil and gas drilling requires electronic devices to operate at high temperature. For example, the operating temperature of devices in deep oil exploration has increased to 300 °C [14]. The harsh environment brings much more challenges to the fabrication of devices and

packaging process. Recently, the successful demonstration and application of power devices (IGBT, power BJT) fabricated by wide band-gap semiconductor materials (i.e. GaN and SiC) enable the device to function at elevated temperature. However, in the aspect of packaging, especially the die attachment, the challenges brought by high temperature are not well addressed. Firstly, traditional high temperature die-attach materials such as gold-germanium (AuGe) eutectic alloy and high-Pb solder cannot sustain this temperature because their melting temperatures are not high enough. On the other hand, the melting temperature cannot be regarded as the highest temperature that the joint can sustain since all the metals would be seriously softened or deformed by creep when the temperature is elevated. In the present study, 0.8 T_h (80% of the homologous temperature) is defined as the highest tolerable temperature of the die-attach material. If the working temperature of the electronic device is 350 °C, the lowest homologous temperature required is 506 °C. If soldering is employed for die attachment, the process temperature will be at least 520 °C. Unfortunately, the device may not be able to sustain at this temperature. Therefore, conventional soldering process can't address the issues in die attachment for high temperature electronics.

One method to circumvent this constraint is the solid liquid inter-diffusion (SLID) bonding that employs a structure consisting of a low melting point component and a high melting point component [15]. During bonding, the low melting point component melts and is consumed by reacting with the high melting component to form a new phase that has high melting temperature. Thus, high temperature joints can be made during a low temperature process. SLID processes based on Ag/Sn [16], Cu/Sn [17, 18], and Au/Sn [19] had been developed. A concern on SLID joints is the IMCs region formed when the molten

phase is consumed during bonding. IMCs are usually hard, brittle, and thermally resistive [20]. Although the mechanical properties of IMC joints can be improved through post heat treatments [21, 22], the formation of pores is an issue. Ga and In had also been used in SLID designs due to its low melting temperature. SLID joints made with Ag/In [23, 24] and Cu/Ga [25, 26] systems had been reported, where the IMC formation issue persists. A technique to eliminate the IMC region is to convert it into a solid solution phase by post annealing, as demonstrated using the Ag/In system [27]. The resulting joints between Si chips and Cu substrates survive 5,000 thermal cycles between - 40 and +200 °C. SLID method has already been employed for wafer bonding and high power photonic die attachment by a few foundries. However, converting the IMCs into solid solution phase is time-consuming, which may limit the wide acceptance of SLID in the industry.

A recent approach to produce high temperature joints is to sinter nano-silver paste where Ag nanoparticles dispersed in binder agglomerate during sintering. For low temperature application of power devices, this technology works well. Theoretically, the joints produced by sintering Ag nano-particles can reach 715 °C which is 0.8 T_m of Ag. However, serious reliability issues arises when the temperature is elevated over 150 °C, which is due to the porous nature of the joints produced through sintering process. Regardless of pores in sintered Ag, Ag is still an attractive bonding medium because of its superior physical properties: highest electrical conductivity (63×10^6S/m) and highest thermal conductivity (429 W/m-K) among metals, high melting temperature, and high ductility. To improve the reliability of the joint produced by Ag, the porous issue must be addressed and thus the development of new process is essential.

1.5 Direct bonding technology

Nowadays, with the increase of the integration density on the IC chips, the I/O density needed to be addressed during packaging process increases drastically. In advanced flip chip process, copper pillar technology is utilized instead of traditional C4 process (controlled collapse chip connection). A typical Cu pillar joint on chip produced by Intel 22 nm node is shown in Fig. 1.5 [28]. In the joint, there is a solder cap. During reflow and usage, the IMCs grow at the interface between Cu and solder and voids appears as a result of kirkendall effect and volumetric reduction of phase transformation. However, as the size of pillar continues to scale down, the growth rate of IMCs will increase drastically [29]. Since the surface to volume ratio increases as the size scales down, the surface diffusion plays more important role in the inter-diffusion between Cu and Sn, resulting in higher growth rate of IMCs and voids.

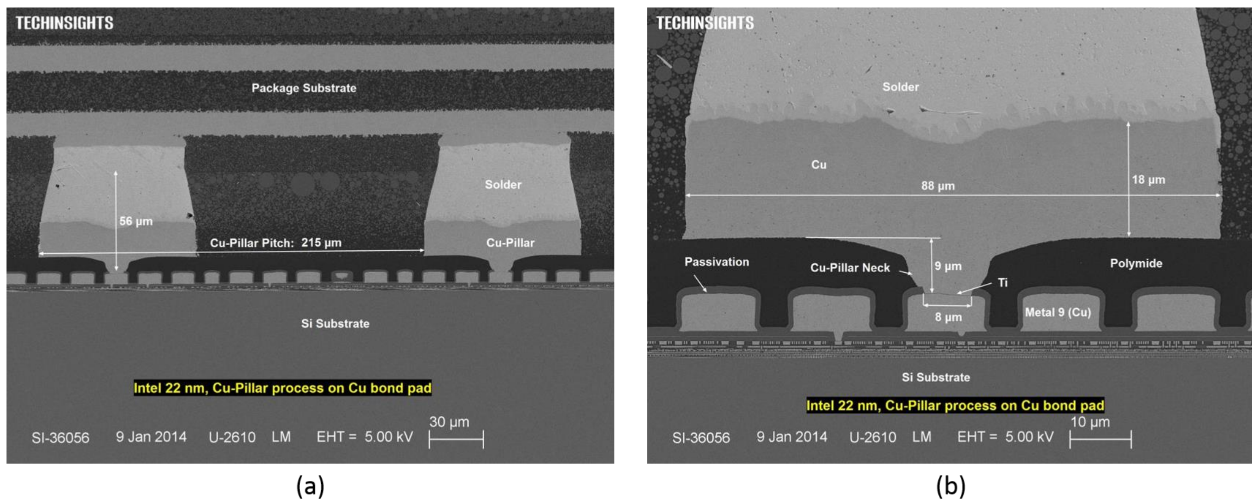

Fig. 1.5 Copper pillar joint in commercialized chip [28].

Another issue of the Cu pillar joint is associated with the resistance. Although Cu is highly conductive, the electrical conductivity of IMCs and Sn are much lower. As the

diameter of joint scales down, the IMCs are thicker and thus the resistance is higher, which may raise signal integrity problems in high speed device due to high RC delay.

In order to avoid IMCs, researchers investigate the direct bonding technology where the materials from both sides are same such as Cu-Cu and Au-Au. The Au-Au direct bonding technology is not widely accepted since it requires high temperature (more than 350 °C) [30] and the materials are highly costive. Cu-Cu direct bonding have attracted lots of research interests in the past few years. However, the hardness of Cu is higher than Au and thus requires higher bonding pressure. Another thing is that the requirement of surface roughness of forming high quality joint is high. Fig. 1.6 shows the Cu-Cu joint bonded at 350 °C for 1 h assisted by 20 MPa pressure [31, 32]. There are lots of voids and cracks along the interface. It is also worth mentioning that the grains from both side are not merged. Given that the orientation of grains are quite random, the lattices near the bonding interface is highly distorted or even amorphous. To facilitate the merging of grains from two sides, reducing the grain size and post-annealing are proposed. Fig. 1.7 shows the joint with 1 h post-annealing process [33]. It can be clearly seen that the original boundary vanish, and grains merge and recrystallize.

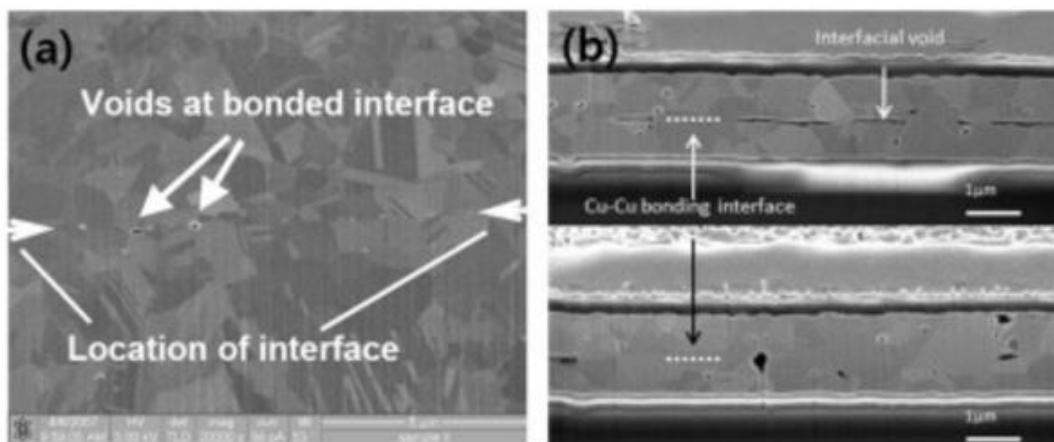

Fig. 1.6 Cu-Cu direct bonded joint [31, 32].

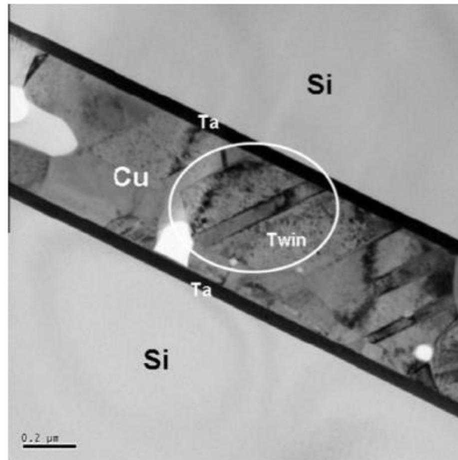

Fig. 1.7 Cu-Cu joint with post-annealing process [33].

Another issue of Cu-Cu bonding is associated with the oxidation. Cu get oxidized easily and the bonding may need to be performed under reducing ambient. Therefore, efforts in process development or materials selection are still essential to produce high quality direct bonded joint for high performance electronic devices.

1.6 Research aims and objectives

This dissertation addresses existing issues raised by introducing Ag and its alloys into electronic packaging. The objectives are formulated below:

a. To develop new compositions of Ag alloys to meet the higher requirement in mechanical properties and corrosion resistance.

b. To explore the intermetallic reaction between Ag and Al and the effects of dopants in IMCs growth, defects evolution, and underlying mechanism.

c. To develop new process for die attachment by utilizing Ag as bonding medium and demonstrate joints can sustain at elevated temperature.

d. To develop new process for direct bonding and investigate the bonding mechanism, interfacial structure, and reliability.

*1.*7 Dissertation outline

This dissertation contains four sections (Fig. 1.8) : (1) materials and method; (2) Ag alloys in wire bonding; (3) Ag in die attachment for high temperature electronics; (4) Ag in direct bonding; and (5) summary.

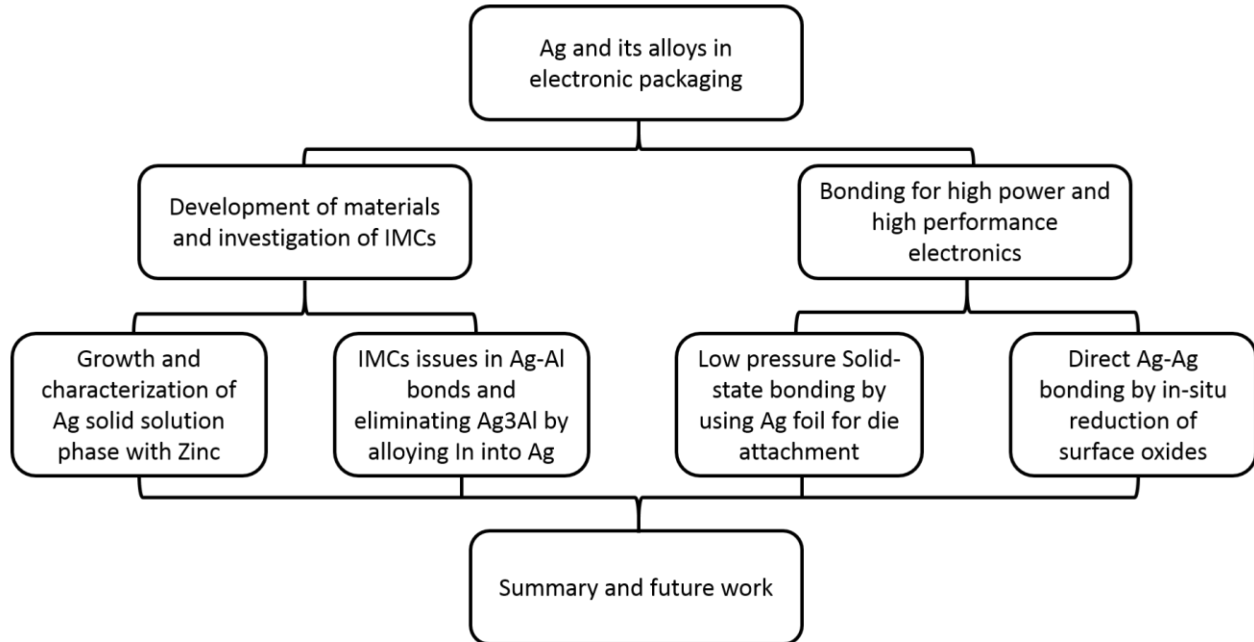

Fig. 1.8 Outline of the dissertation.

The first section (Chapter 2) provides a detailed description of the methods and processes of materials preparation, experimental setups, sample preparation procedures, and characterization techniques and analysis.

The second section is divided into two chapters (3 and 4). In Chapter 3, the preparation and characterization of Ag solid solution phase with zinc at two compositions are described and the mechanical properties are studied through static tensile tests. Fractography is also conducted and the failure mechanism is discussed. The tarnish resistance of the materials is evaluated through sulfurization test.

In Chapter 4, the IMCs growth between Ag and Al, evolution of defects, effects of Indium alloying and underlying mechanism are systematically studied through high resolution characterization techniques and thermodynamic modeling. The failure mechanism of Ag-Al bonds is proposed. The method of completely eliminating Ag_3Al is reported and it could be an effective solution to current Ag-Al wire bonding reliability issue.

In the third section (Chapter 5), a solid-state bonding technique using fine-grained silver (Ag) foils for die attachment of high temperature electronics is presented. The preparation and characterization of fine-grained Ag foils are firstly introduced. The quality of the joints is carefully examined by cross-sectional study and mechanical test. The high temperature reliability test is performed and the results show that our process can effectively address the reliability issues faced by sintering Ag approach.

In the fourth section (Chapter 6), a novel Ag-Ag direct bonding process utilizing in-situ reduction of pre-oxidized Ag surface is proposed.

In the last section (Chapter 7), the important findings are summarized and potential future work is outlined.

1.8 Reference

[1] The Silver Institute, Silver in electronics, https://www.silverinstitute.org/silver-in-electronics/, last accessed July 20th, 2018.

[2] H. Ma, J.C. Suhling, A review of mechanical properties of lead-free solders for electronic packaging, J Mater Sci 44(5) (2009) 1141-1158.

[3] A.J. Lovinger, Development of Electrical Conduction in Silver-filled Epoxy Adhesives, J Adhes 10(1) (1979) 1-15.

[4] Y. Wang, G. Zhang, J. Ma, Research of LTCC/Cu, Ag multilayer substrate in microelectronic packaging, Mater Sci Eng, B 94(1) (2002) 48-53.

[5] L.J. Kai, L.Y. Hung, L.W. Wu, M.Y. Chiang, D.S. Jiang, C.M. Huang, Y.P. Wang, Silver alloy wire bonding, 2012 IEEE 62nd Electronic Components and Technology Conference, 2012, pp. 1163-1168.

[6] R. Kisiel, Z. Szczepański, Die-attachment solutions for SiC power devices, Microelectron Reliab 49(6) (2009) 627-629.

[7] G. G. Harman, Wire Bonding in Microelectronics. Third Edition. New York, London: McGraw-Hill, 2010.

[8] Gold and aluminum wire bonding, Wurth electronics. https://www.we-online.com/web/en/leiterplatten/produkte_/bonden/verfahren/Verfahren.php, last accessed July 20th, 2018.

[9] M. Schneider-Ramelow, C. Ehrhardt, The reliability of wire bonding using Ag and Al, Microelectron Reliab 63 (2016) 336-341.

[10] H. Xu, C. Liu, V.V. Silberschmidt, S.S. Pramana, T.J. White, Z. Chen, V.L. Acoff, Intermetallic phase transformations in Au–Al wire bonds, Intermetallics 19(12) (2011) 1808-1816.

[11] H.G. Kim, S.M. Kim, J.Y. Lee, M.R. Choi, S.H. Choe, K.H. Kim, J.S. Ryu, S. Kim, S.Z. Han, W.Y. Kim, S.H. Lim, Microstructural evaluation of interfacial intermetallic compounds in Cu wire bonding with Al and Au pads, Acta Mater 64 (2014) 356-366.

[12] H. Xu, C. Liu, V.V. Silberschmidt, S.S. Pramana, T.J. White, Z. Chen, V.L. Acoff, Behavior of aluminum oxide, intermetallics and voids in Cu–Al wire bonds, Acta Mater 59(14) (2011) 5661-5673.

[13] G. Liqun, C. Qiang, L. Juanjuan, C. Zhengrong, Z. Jianwei, D. Maohua, M. Chung, Comparison of Ag Wire and Cu Wire in Memory Package, ECS Trans 52(1) (2013) 747-751.

[14] Beckwith R, Downhole Electronic Components: Achieving Performance Reliability, J. Petroleum Technol., 65 (2013) 42-57.

[15] L. Bernstein, Semiconductor Joining by the Solid-Liquid-Interdiffusion (SLID) Process I. The Systems Ag-In, Au-In, and Cu-In, J Electrochem Soc 113(12) (1966) 1282-1288.

[16] X. Li, J. Cai, Y. Sohn, Q. Wang, W. Kim, S. Wang, Microstructure of Ag-Sn Bonding for MEMS Packaging, 2007 8th International Conference on Electronic Packaging Technology, 2007, pp. 1-5.

[17] J.F. Li, P.A. Agyakwa, C.M. Johnson, Interfacial reaction in Cu/Sn/Cu system during the transient liquid phase soldering process, Acta Mater 59(3) (2011) 1198-1211.

[18] N.S. Bosco, F.W. Zok, Critical interlayer thickness for transient liquid phase bonding in the Cu–Sn system, Acta Mater 52(10) (2004) 2965-2972.

[19] Z.X. Zhu, C.C. Li, L.L. Liao, C.K. Liu, C.R. Kao, Au–Sn bonding material for the assembly of power integrated circuit module, J Alloy Compd 671 (2016) 340-345.

[20] C.C. Lee, P.J. Wang, J.S. Kim, Are Intermetallics in Solder Joints Really Brittle?, 2007 Proceedings 57th Electronic Components and Technology Conference, 2007, pp. 648-652.

[21] J.F. Li, P.A. Agyakwa, C.M. Johnson, Suitable Thicknesses of Base Metal and Interlayer, and Evolution of Phases for Ag/Sn/Ag Transient liquid-phase Joints Used for Power Die Attachment, J Electron Mater 43(4) (2014) 983-995.

[22] N.S. Bosco, F.W. Zok, Strength of joints produced by transient liquid phase bonding in the Cu–Sn system, Acta Mater 53(7) (2005) 2019-2027.

[23] R.W. Chuang, C.C. Lee, Silver-indium joints produced at low temperature for high temperature devices, Ieee T Compon Pack T 25(3) (2002) 453-458.

[24] Y.Y. Wu, C.C. Lee, High temperature Ag-In joints between Si chips and aluminum, 2013 IEEE 63rd Electronic Components and Technology Conference, 2013, pp. 1617-1620.

[25] J. Froemel, M. Baum, M. Wiemer, T. Gessner, Low-Temperature Wafer Bonding Using Solid-Liquid Inter-Diffusion Mechanism, J Microelectromech Syst 24(6) (2015) 1973-1980.

[26] S.K. Lin, M.J. Wang, C.Y. Yeh, H.M. Chang, Y.C. Liu, High-strength and thermal stable Cu-to-Cu joint fabricated with transient molten Ga and Ni under-bump-metallurgy, J Alloy Compd 702 (2017) 561-567.

[27] Y.-Y. Wu, D. Nwoke, F.D. Barlow, C.C. Lee, Thermal cycling reliability study of Ag–In joints between Si chips and Cu substrates made by fluxless processes, IEEE Trans. Compon. Packag. Manuf. Technol. 4(9) (2014) 1420-1426.

[28] Arabinda DAS, Cu-Pillar in Advanced Logic Devices, Semiwiki.com, https://www.semiwiki.com/forum/content/4518-cu-pillar-advanced-logic-devices.html, last accessed July 20th, 2018.

[29] Y. Liu, Y.-C. Chu, K.N. Tu, Scaling effect of interfacial reaction on intermetallic compound formation in Sn/Cu pillar down to 1 μm diameter, Acta Mater 117 (2016) 146-152.

[30] H.R. Tofteberg, K. Schjølberg-Henriksen, E.J. Fasting, A.S. Moen, M.M. Taklo, E.U. Poppe, C.J. Simensen, Wafer-level Au–Au bonding in the 350–450° C temperature range, J Micromech Microeng 24(8) (2014) 084002.

[31] W. Ruythooren, A. Beltran, R. Labie, Cu-Cu Bonding Alternative to Solder based Micro-Bumping, 2007 9th Electronics Packaging Technology Conference, 2007, pp. 315-318.

[32] L. Peng, L. Zhang, H.Y. Li, C.S. Tan, Cu-Cu Bond Quality Enhancement Through the Inclusion of a Hermetic Seal for 3-D IC, Ieee T Electron Dev 60(4) (2013) 1444-1450.

[33] Y.-S. Tang, Y.-J. Chang, K.-N. Chen, Wafer-level Cu–Cu bonding technology, Microelectron Reliab 52(2) (2012) 312-320.

Chapter 2. Materials and Methods

2.1 Materials preparation and bonding

2.1.1 Growth of metallic ingots

The study of the intrinsic properties of materials starts with the preparation. In this dissertation, the bulk metallic materials are grown through vacuum casting. The raw metals in the form of shots are purchased from ESPI® metals. Prior to casting, the metals shots are cleaned by hydrochloric acid if necessary. The details of the procedure is shown in Fig. 2.1.

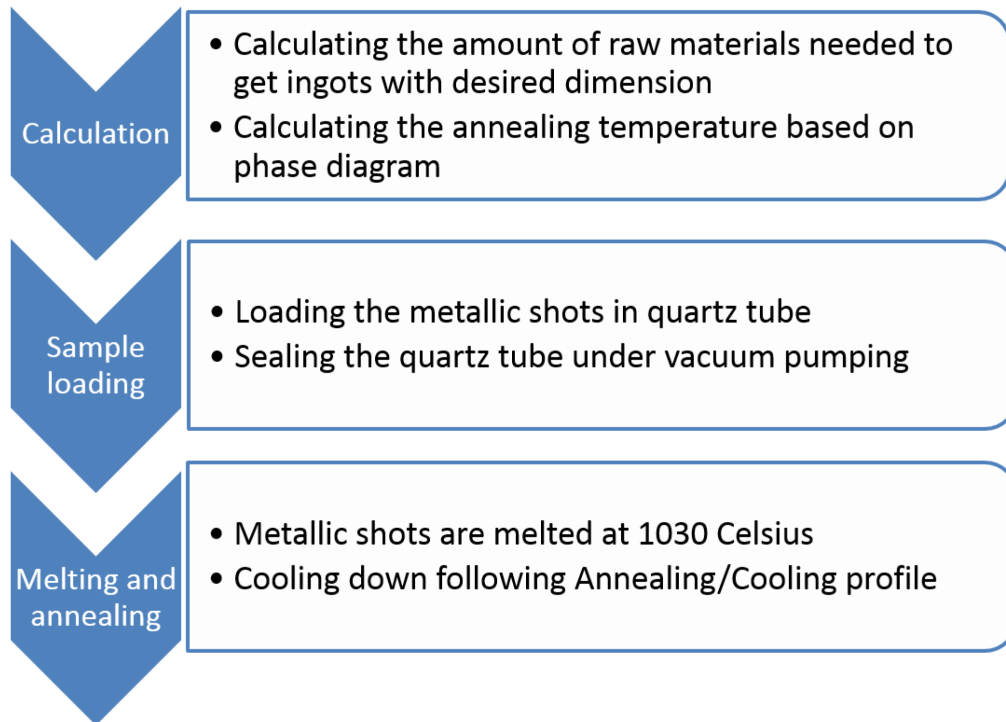

Fig. 2.1 Procedure of ingot growth.

The annealing profile is designed for the homogeneity of the ingot. A multi-stage annealing is conducted and the temperature of each stage is calculated based on the homologous temperature of the desired composition. For example, for the Ag solids solution phase with zinc, the ingots are cooled down from 0.95 T_m to 0.3 T_m (lower than

100 Celsius) in 8 days and the cooling between adjacent stages is quite fast and done within 2 hours.

2.1.2 Preparation of metallic foils

The metallic foils are prepared after the ingot is acquired. Cold rolling and annealing are chosen to fabricate foils with recrystallized microstructure. The reason why we need recrystallized microstructure is because the foils will be used in solid state bonding where low hardness is preferred. The parameters of rolling and annealing for one specific materials are chosen after several rounds of trials and adjustments. For Ag foils, in each rolling run, the thickness is reduced by 70%, and the annealing temperature is set at 300℃, corresponding to a homologous temperature of 0.46 at which recrystallization is confirmed to initiate and finish in one hour by the pole figure measurement. The final foil thickness is approximately 75 μm, suitable for bonding experiments. Prior to bonding, the foils are fine polished by using 1 μm diamond suspension and silica colloid, resulting in mirror finish. Lastly, the foils are rinsed by acetone and de-ionized (DI) water and dried by nitrogen flow.

2.1.3 Thin film deposition

All the thin film depositions in this dissertation are performed by using Angstrom E-beam evaporator in UC Irvine Materials Research Institute (IMRI). E-beam evaporation is categorized into the physical vapor deposition (PVD). During the deposition, the electron beam is focused on the raw materials and the materials are heated to be evaporated. Due to the high vacuum in the chamber, the mean free path of the vapor is larger than the distance between the source and substrate. Therefore, the gaseous metal can be directly deposited on the cold substrate and form metallic thin films. With a modern power control system, the error of the deposition rate can be limited within 0.02 Å /s.

Fig. 2.2 Angstrom Engineering EvoVac Glovebox Evaporator in IMRI.

In this dissertation, the raw materials in the form of shots are Ag, Al, In, Cr and Au, which are 4N grade and purchased from ESPI® metals. The crucibles are either made of graphite (for Ag, In, Cr and Au) or intermetallics (for Al). The deposition is conducted under 2×10^{-7} torr vacuum and the pre-soaked time is 5 minutes. The deposition rates for Ag, Al are 1 Å/s and 0.2 Å/s for Au and Cr. During the evaporation process, the deposition rate is monitored by a quartz crystal microbalance (QCM), and controlled within 5% fluctuation, using a proportional–integral–derivative (PID) controller. The substrate used is single side polished silicon (Si) with the thickness of 275 ±25 μm. Prior to deposition, the polished side is cleaned by dilute hydrofluoric acid, rinsed by DI water, and baked.

2.1.4 Thermal compression bonding

Fig. 2.3 depicts the vacuum bonder for all of the thermal compression bonding processes performed in this dissertation. The key parts are marked in the figure. With the quartz cylinder, stainless upper/base, and the O-ring seals between them, the chamber can be pumped down to 100 mTorr vacuum under which the oxidation will be reduced. The temperature of the sample can be directly measure by the thermocouple and controlled by adjusting the AC power.

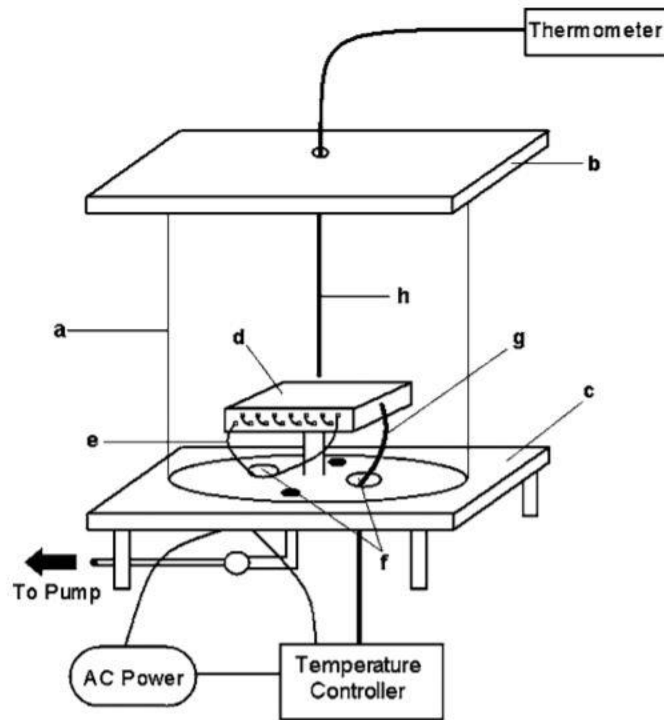

Fig. 2.3 Schematic of the vacuum furnace showing the key components: (a) quartz cylinder, (b) upper stainless plate, (c) base plate, (d) graphite platform, (e) heating wire, (f) electrical feedthroughs, (g) platform thermocouple, and (h) sample thermocouple.

A photo of a sample ready for bonding is shown in Fig. 2.4. The sample is fixed between the graphite stage and a short stainless steel plate by using screws and springs. The pressure is applied by adjusting the amount of compression of the springs. The fixture

is symmetric and two springs are installed to balance the force applied on the sample. After the sample is installed, the chamber is pumped down to 100 mTorr and the temperature can be ramped up to the target temperature within 10 min. After staying at target temperature for desire time, the AC power will be turned off and the stage will cool down to room temperature naturally (usually takes about 30 min to 100 °C and another 1 h to room temperature).

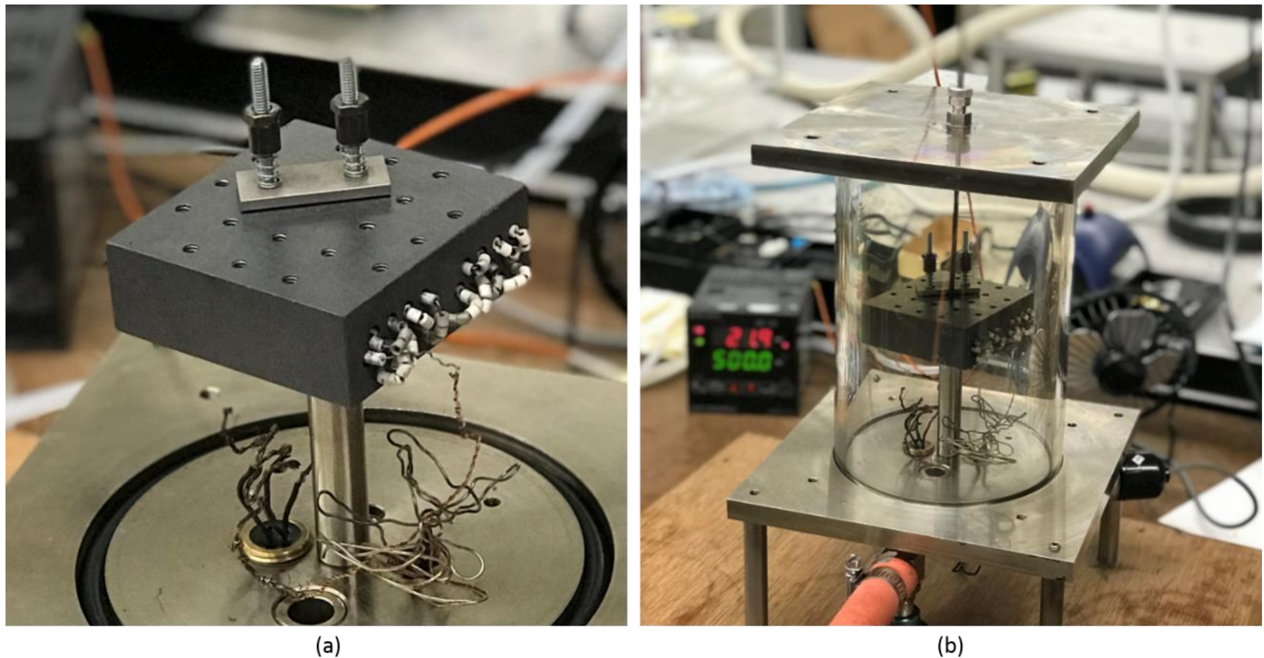

Fig. 2.4 Vacuum bonder details: (a) Graphite stage with sample fixed; (b) Chamber ready for bonding.

2.2 Sample preparation

2.2.1 Grinding and Polishing

After acquiring synthesized materials or bonded joints, sample preparation is performed for the subsequent characterization and the examination of other properties. For different types of samples, the method of sample preparation may be different. Only the right method chosen, the characterization results can be trusted.

For materials in the form of ingot, a disk (2 mm in thickness and 10 mm is diameter) is cut from the ingot by slow speed diamond saw. Then, the disk is ground by using diamond paper from LECO® in the sequence of 240, 600, 800 and 1200 (in terms of grit size). After grinding, the disk is polished by using diamond suspension from Buehler® in the sequence of 6 μm, 3 μm and 1 μm (in terms of particle size). The final polishing is performed by using silica colloid from Buehler®. Prior to characterization, the sample is cleaned by using DI water.

For bonded joints, it's essential to perform the cross-sectional study. Due to the small size of the joint, the sample is firstly mounted into epoxy resin and cut into halve by using slow speed diamond saw. Since the joints contain materials with a wide range in hardness (from Ag to Si), the ground process starts with a finer grit size (i.e. 800). After grinding, a fine polishing process same as the disk sample is conducted. For joints contain materials with different hardness, the polishing direction should be from the soft side to hard side to reduce the smearing the interface. However, it's nearly impossible to avoid the smearing of the interface when you work with soft materials such as Ag and Cu. The smearing issue will be addressed in next section.

2.2.2 Ion milling (Ar ion milling and FIB)

Generally, the mechanical polishing methods inevitably induce surface damages or smearing of the interface due to the large strain rate during grinding/polishing process. For example, the surface damage can degrade the contrast of channeling effects under scanning electron microscopy (SEM). In the case of interfacial smearing, the characterization result may be misleading since all the joints were seemed to be well bonded. An example is given to illustrate these two cases and shown in Fig. 2.5.

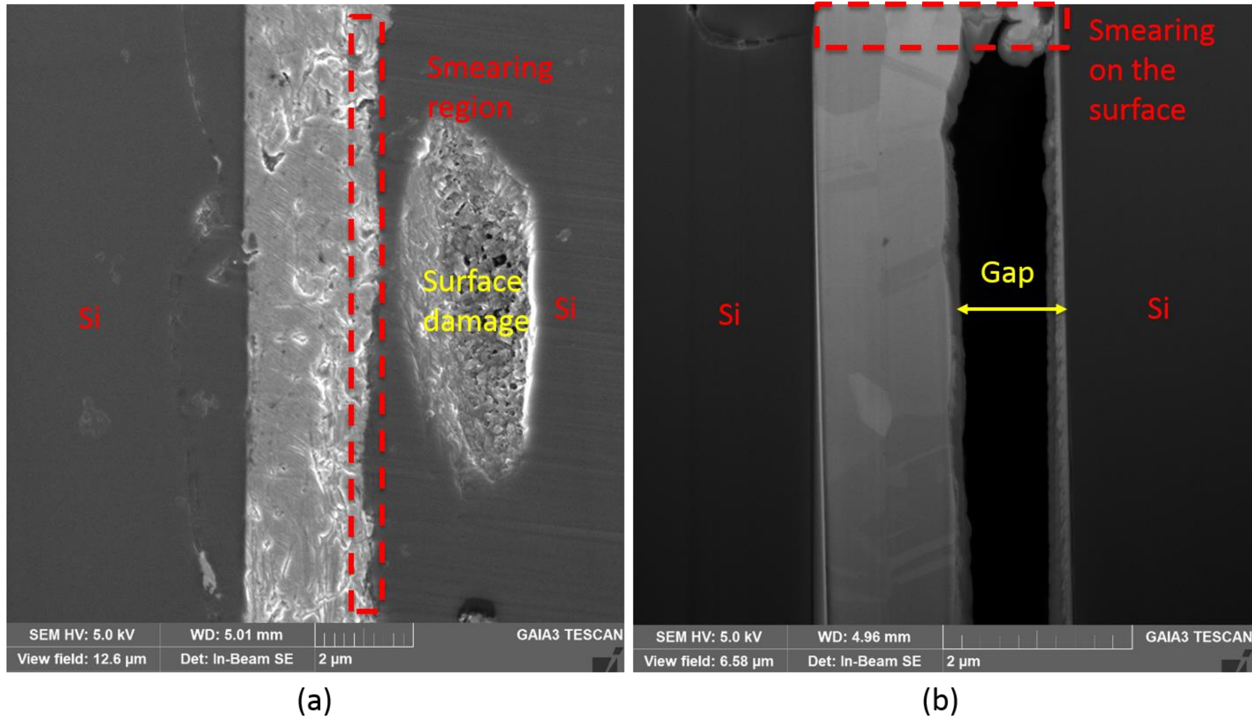

Fig. 2.5 Comparison between mechanical polishing and FIB cutting: (a) cross-sectional image after mechanical polishing; (b) FIB cutting into the joint at the same position.

From Fig. 2.5(a), it can be seen that there is no voids or gap on the bonding interface between Si and bonding medium. However, after cutting into the joint by using FIB, it can be seen from Fig. 2.5(b) that there is a gap between Si and bonding medium and the gap is filled near the surface during the grinding and polishing process. On the other hand, there is no grain contrast in Fig. 2.5(a) while this contrast appears in Fig. 2.5(b) since the surface damage induced by ion milling is much smaller than that induced by mechanical polishing.

In this dissertation, two types of ion milling approaches are used, those are, Ar ion milling and FIB. The configuration of those two methods are shown in Fig. 2.6. The Ar ion milling is performed on Hitachi® IM4000 Ion Milling system, which employs an Ar ion gun with relatively lower acceleration voltage (1-4 kV). According to Fig. 2.6(a), the Ar ion beam (the diameter is hundreds of micron) is focused on the edge of the sample and the

region not protected by the mask will be milled by the ion, creating a clean area on the top surface. This method can create a relatively larger area but with low spatial resolution.

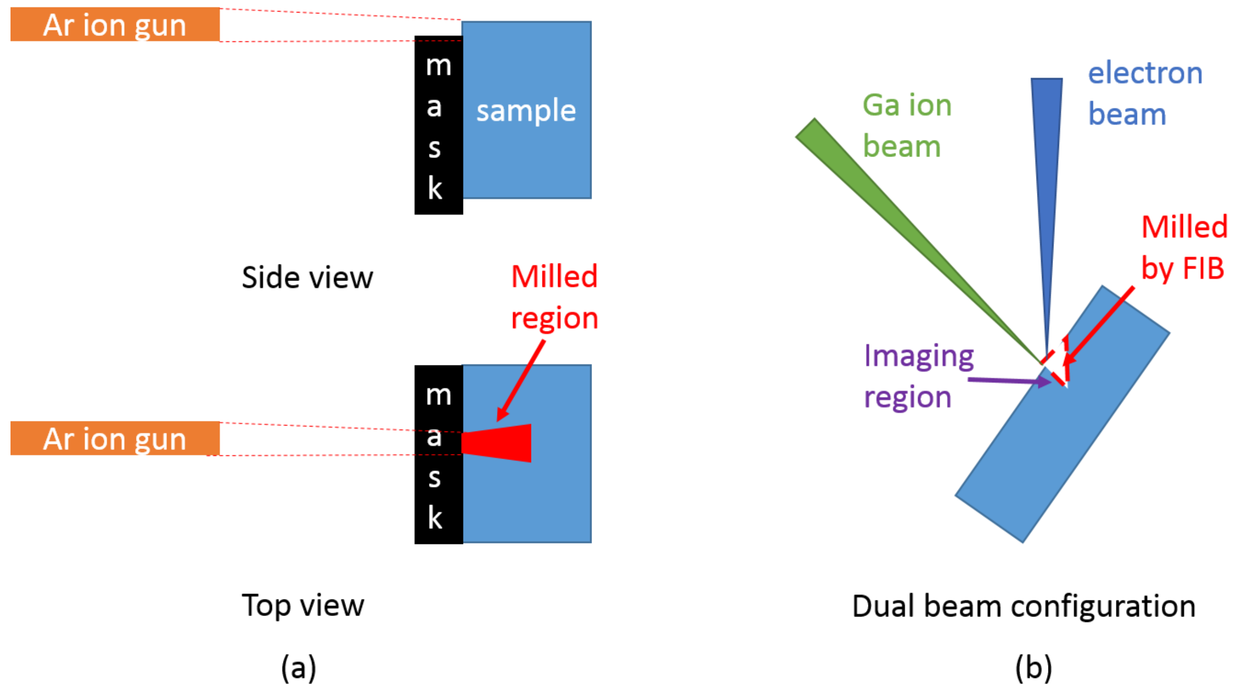

Fig. 2.6 Configurations of Ar ion milling system (a) and dual beam system (b).

The FIB cutting is performed by using TESCAN GAIA3 SEM/FIB dual beam system in IMRI. The system employs Ga liquid metal ion source (LMIS) and the acceleration voltage can be as high as 30 kV. The beam can be focused within tens of nanometers and thus high spatial resolution cutting can be performed. According to Fig. 2.6 (b), In-situ high resolution imaging can be conducted by SEM and the area of interests can be easily located.

2.2.3 TEM sample preparation

In order to perform high resolution characterization (from tens of nanometers down to atomic resolution), transmission electron microscopy (TEM) needs to be conducted. Sample preparation is the most time-consuming part of TEM analysis since the sample needs to maintain its original structure while being electron transparent. Typically,

the thickness of the sample should be within 100 nm (depending the atomic weight of the element). In this dissertation, the TEM sample preparation is performed through in-situ lift-out process since our sampling needs to be site specific. The process is operated on TESCAN GAIA3 SEM/FIB dual beam system and major steps are illustrated in Fig. 2.7.

Firstly, the area of interested is located by SEM and a thin strip of platinum (Pt) (length: 20 μm, width: 2 μm) is deposited in-situ by e-beam assisted deposition. Then, the sample is tilted to 55 degree and a thicker strip (2 μm in thickness) of Pt is deposited on top of previous thin Pt by FIB assisted deposition (shown in Fig. 2.7a). The Pt strip functions as a protection of the lamella underneath and reduce the amount of defects (i.e. curtain effects) induced by the surface roughness. After building up protection layer, two trenches are cut in front and rear of the protection layer by using large ion beam current (30 kV, 18 nA) and the sidewalls of underneath the protection layer are cleaned by using small current (30 kV, 2 nA) (shown in Fig. 2.7b). "J" cut is performed when stage is back to 0 degree and after which only the upper right corner of the lamella is attached the bulk sample (Fig. 2.7c). Then the stage is tilted to 55 degree again and the lift-out process is conducted by using Omniprobe micro-manipulator (Oxyford®). The tip of the probe is driven to the left edge of the lamella and attached onto the lamella by FIB assisted deposition. The lamella is lifted out after the right edge is released by FIB cutting and attached to the edge of the post on Omnigrid (Ted Pella®) by Pt (Fig. 2.7d). The thinning process is conducted by using small current to mill the front and rear sides with a small milling angle (2-4 degree). A rough thinning is performed firstly to reduce the thickness of the lamella to 500 nm (30kV, 600 pA). Then, the final thinning is performed by using low voltage and low current (15kV, 150 pA) to reduce the thickness to achieve electron

transparent (Fig. 2.7e and 2.7f). Since the final thinning process will induce a thin ion-damaged layer on the surface, two sides of the sample are cleaned by using a very low voltage and current (3kV, 60 pA). The site-specific TEM sample of stress-free and contamination-free is now produced, and readily for HRTEM observation.

In some cases, the surface damages cannot fully removed by the cleaning process performed by FIB. An ex-situ cleaning is conducted by using Fischione® Nanomill system, which employs an Ar ion gun and the beam can be focused within 1 μm in diameter. The acceleration voltage is ranged from 0.3 kV to 1 kV and the current is 100 pA. In general, the sample can meet the requirements of atomic resolution imaging after performing a two-step cleaning with a higher voltage (0.7 kV) and lower voltage (0.3 kV) for a few minutes.

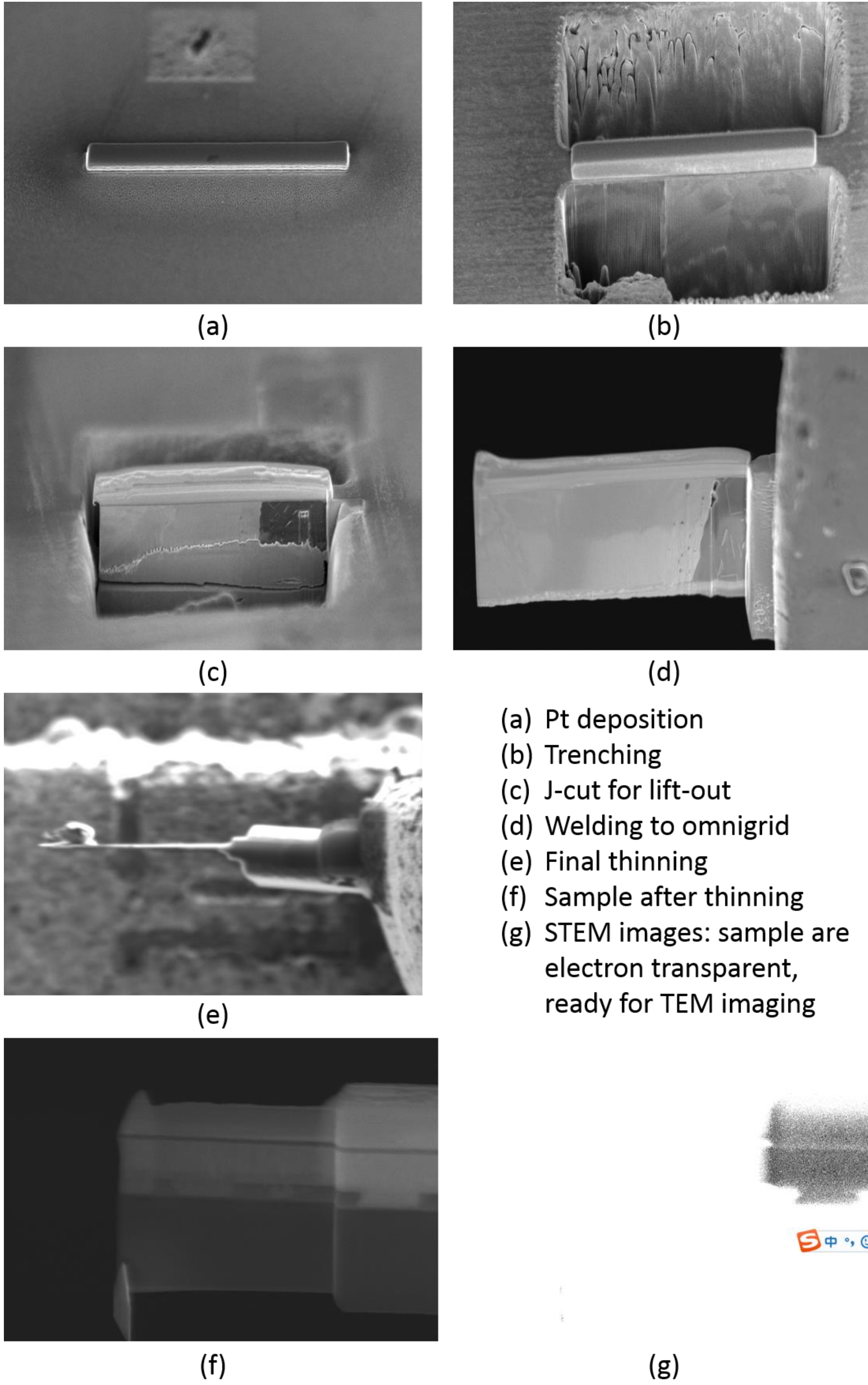

Fig. 2.7 TEM sample preparation through in-situ lift-out process.

2.3.4 Sample preparation for tensile test

The tensile specimens from each ingots were machined by electrical discharge machining (EDM) in accordance with ASTM E8/E8M-08 specification [1]. In Fig. 2.8 and Table. 2.1, the geometry and dimension are shown respectively. These samples were carefully polished in order to remove surface damage caused by EDM and then annealed at 200 Celsius for 1h to release residue stress induced by polishing.

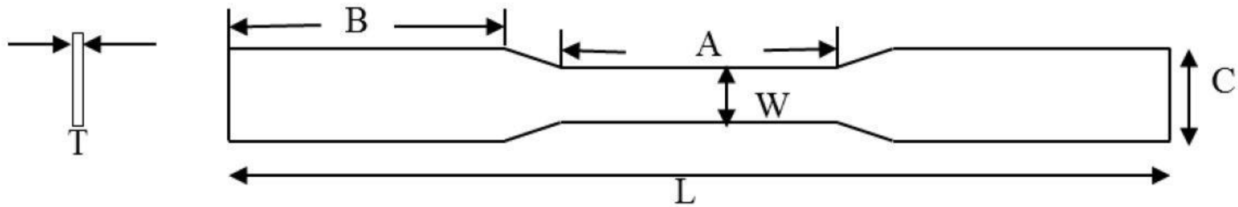

Fig. 2.8 The geometry of tensile specimen, in accordance with ASTM E8/E8M-08

Table 2.1 The dimensions of tensile specimen, in accordance with ASTM E8/E8M-08.

	W	T	L	A	B	C
mm	2	1.1	33.33	10.67	10	3.33
inch	0.0787	0.0433	1.3120	0.4200	0.3937	0.1311

2.3 Characterization techniques

2.3.1 Scanning electron microscopy

Nowadays, scanning electron microscope (SEM) is commonly used in scientific research related to fine feature characterization, surface topography, compositional imaging and so on. During the imaging process, the electron beam scans on the surface while the detector collects the signal site by site, resulting an image with grey contrast.

To interpret the SEM images, the electron-materials interaction should be understood. Fig. 2.9 illustrates the process and signals generating during the electron beam-materials interaction [2]. As electrons incident on the materials, both elastic and inelastic collisions can happen. During elastic interaction, the direction of the electrons are

changed with negligible energy loss. After multiple times elastic interaction, the original electrons can escape from the surface of the materials, which are called back-scattered electrons (BSE). Since the probability of the elastic collision is a function of atomic weight, the contrast in BSE image is mainly induced by the site-specific composition.

During inelastic collision, the direction of the electron may change but the kinetic energy is reduced. These kinetic energy may be transferred to phonon or electron. The electron may be exited and leave its original orbital, which is called secondary electron (SE). However, only those SEs generated near the surface can escape the material due to their low kinetic energy. Therefore, the intensity of SE signal is a determined by surface morphology. In addition, the spatial resolution of SE is higher than BSE since the lateral diffusion of SE is smaller. The SE signal is often used to characterize the fine features on the surface.

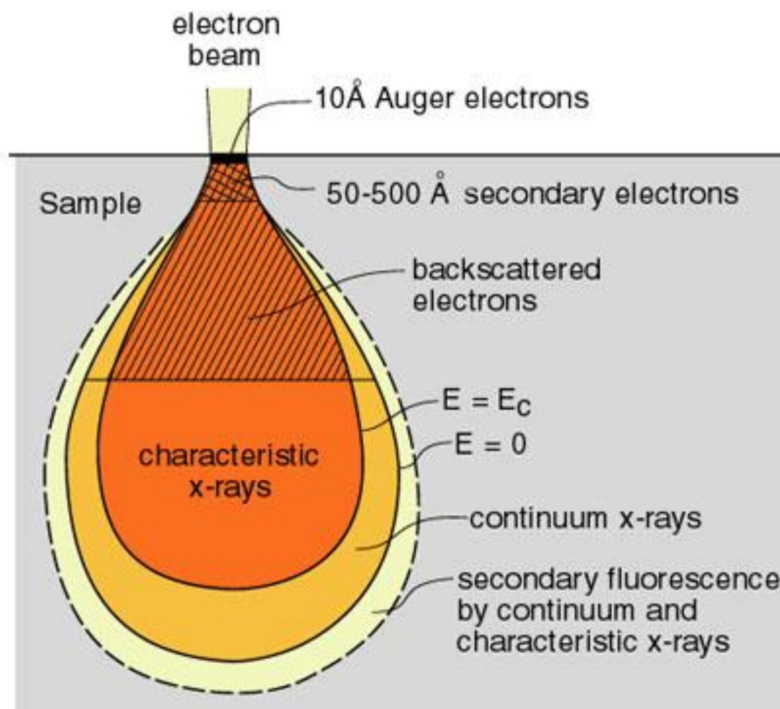

Fig. 2.9 Interactions between electron beam and bulk materials [2].

In this dissertation, two SEMs are used, those are, FEI XL30 FEG SEM and TESCAN GAIA3 SEM/FIB dual beam system (shown in Fig. 2.10). For SEM imaging, the major difference of these two microscopes lies in the detector part. XL30 employs a traditional Everhart-Thornley (ET) detector which has a larger acquisition angle, ensuring a good signal to noise ratio. TESCAN GAIA3 SEM/FIB employs in-beam detector, which is installed within the beam column. This configuration can achieve higher resolution than ET detector since it can avoid collecting SEs that generated other than the site where beam incidents on.

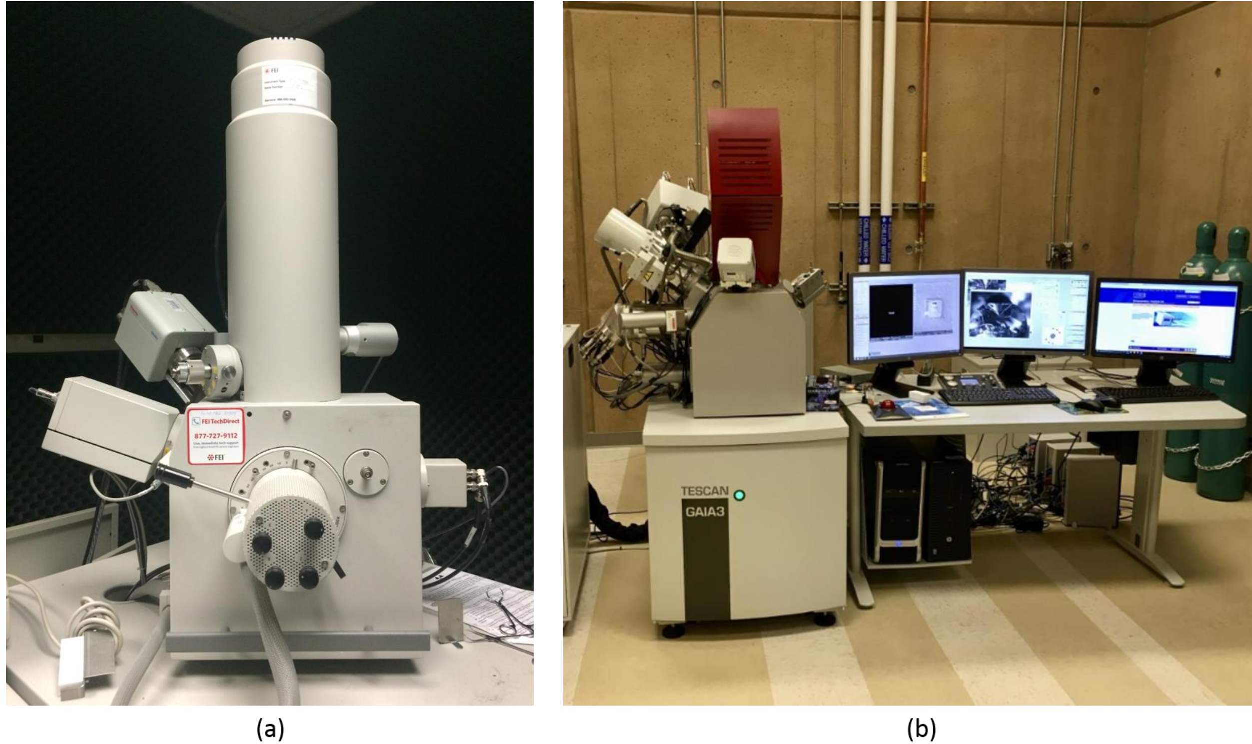

Fig. 2.10 SEMs in IMRI: (a) XL30 FEG SEM; (B) TESCAN GAIA3 SEM/FIB.

2.3.2 Energy dispersive spectroscopy

Energy dispersive spectroscopy (EDX), usually used as a supplementary of SEM or TEM, can uncover the elemental information in the tested sample and quantify the chemical composition in many cases. The fundamental mechanism of EDX is illustrated below.

When electrons interact with materials, x-rays are generated as shown in Fig. 2.8. The continuum x-ray is generated due to the deceleration of the electrons, which cannot provide any information and is background noise. However, the electron beams may excite the inner shell electron of the atom and a vacant is on the inner shell orbital. Then, the electron from outer shell can jump to the vacant on the inner shell and the energy is released in the form of radiation which is called characteristic x-ray. Since the energy difference between outer shells and inner shells is element-specific, the energy of the photon can be used to identify the element. Moreover, the energy-dispersive detector is able to separate the characteristic x-rays of different elements into an energy spectrum. The chemical composition can be quantified by the area of peaks in the spectrum after essential correction methods (i.e. ZAF correction). As the electron beam scan on the surface of the material, the mapping of the chemical composition can be acquired. The limitation of the EDX is that the light elements cannot be quantified since the signal of these light elements (i.e. C, N and O) is mixed with continuum x-rays, resulting in overestimation of the quantity.

2.3.3 Transmission electron microscopy

Transmission electron microscope (TEM) is one of the most powerful instrument that is capable of exploring the materials in atomic scale. Nowadays, TEM is widely used in materials science, chemistry, physics, biology and geology for the investigation of nanostructure, crystal structure, chemical composition, defects, strain, and so on.

The imaging mechanism of TEM is similar to optical microscope (OM). OM employs visible light whose wavelength is too large to achieve atomic resolution imaging. In TEM, electron beam of high kinetic energy (80-300 keV) with ultra-short wavelength (10^{-3} nm)

are utilized and the beam is controlled by electromagnetic lens. To interpret the TEM images, the interaction between electron beams and TEM samples should be understood. As it was mentioned in previous section, the thickness of TEM sample is within 100 nm to realize electron transparent. Therefore, the interaction between electron beams and TEM samples (Fig. 2.11) would be slightly different to that between electron beams and bulk samples (Fig. 2.9). SE, BSE, characteristic x-ray, visible light and auger electrons are generated during electrons interacting with TEM samples. However, since the sample is thin and the kinetic energy of electrons in TEM is much higher, most electrons transmit the sample and these electrons can be used to reveal lots of information about the structure of the sample.

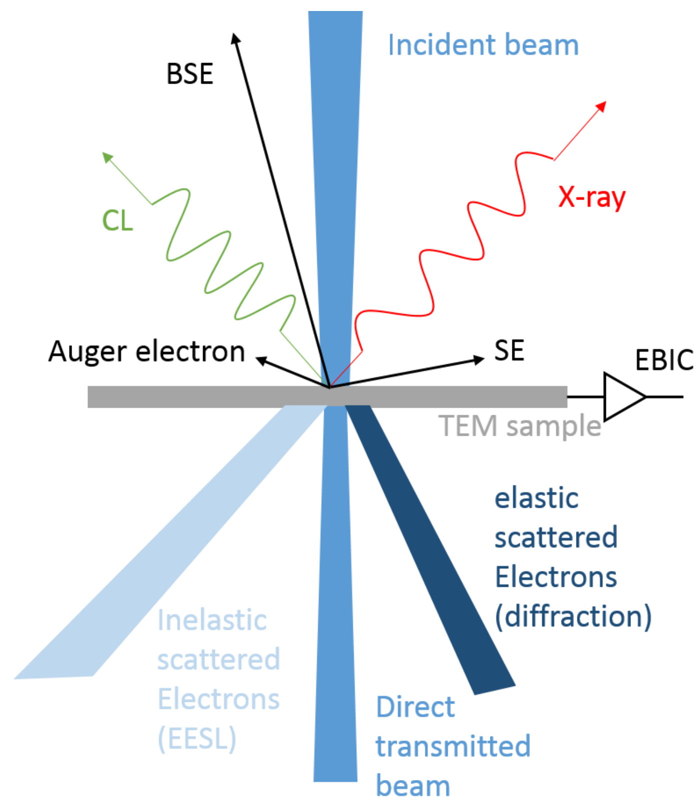

Fig. 2.11 Interactions between electron beam and TEM sample.

Electrons in transmitted beam can be categorized into three parts. Firstly, most electrons pass the sample without any interaction with sample, which is called direct transmitted beam. Secondly, a few electrons interact with the sample without any loss in kinetic energy, these are called elastic-scattered beam. Last but not least, some electrons interact with the sample and lose some kinetic energy during the interaction, which are called inelastic-scattered beam. By using one of these beam or the combination of these beams, different contrast will contribute to the imaging. A few commonly used imaging mode is illustrated in the following paragraphs.

The most straightforward imaging mode is the bright field (BF) imaging mode. In this mode, an objective aperture is inserted and only allows the direct transmitted beam to reach the detector (camera/screen). For TEM sample contains a few grains with different orientation, if a set of crystallographic planes in one grain meet the condition of Bragg' law, the elastic-scattered beam will be stronger from this grain than the grains with other orientation. As a result, the transmitted beam from this grain will be weaker. In the imaging, this grain will appear darker. Another contrast can be detected from BF mode is the mass-thickness contrast. For a region with high average atomic-weight or large thickness, more electrons will be scattered. As a result, the direct transmitted beam will be weaker.

Another very important mode is the dark field (DF) imaging mode. In dark field mode, an objective aperture is inserted and only allows one direct beam to reach the detector. In contrast to the BF mode, if a set of crystallographic planes in one grain meet the condition of Bragg' law, the elastic-scattered beam will be stronger from this grain and the grain will appear brighter than other grains. DF mode can also be used to detect the

internal stress, thickness and defects (i.e. dislocations and stacking faults) in crystalline solids by using specific diffracted beam.

For high resolution transmission electron microscopy (HRTEM) that capable of acquiring lattice fringes, both direct beams and elastic-scattered beam are used. In this case, no objective aperture is used. Since the potential within crystalline solids can be described by Bloch function. When electrons interact with crystalline solids, the phase of the electrons will be modulated by the potential described by Bloch function. As a result, phase contrast are generated and the contrast that reflects the d-spacing in lattice can be acquired.

The phase identification can also be conducted under TEM. In the experiment, the sample could be tilted so that the specific zone axis of the grain of interest can be aligned with the incident electron beam. By inserting an aperture at the imaging plane that can block the electrons interacting with other regions, the diffraction pattern can be acquired. The whole process is called selected area electron diffraction (SAED). It can used to identify the phase and calculate the lattice constant. The advantage of SAED over XRD is the spatial resolution while the accuracy of SAED is inferior to that of XRD.

In this dissertation, scanning transmission electronic microscopy (STEM) is also used. Different from the parallel illumination in TEM imaging, the electron beam are focused forming a very tiny probe whose size can be within 0.1 nm (in aberration-corrected STEM). Similar to SEM, the probe scan on the surface of the sample and the signal from each point is collected and shown in the final image with grey contrast. One of the most important imaging mode in STEM is called high angle annulus dark field (HAADF) imaging. The mechanism is shown in Fig. 2.12. Similar to the signals generated in TEM

mode, there are direct transmitted beam and scattered beam. It is known that the quantity of scattered electrons with large scattering angle is a strong function of average atomic weight (Z) in the region scanned by the beam. These scattered electrons are collected by an annulus shape detector and the resulting images have the Z contrast. It is very useful to show the geometry and thickness of IMCs in our research. It is worth mentioning that HAADF is capable of acquiring image with atomic resolution by using the ultra-fine electron probe.

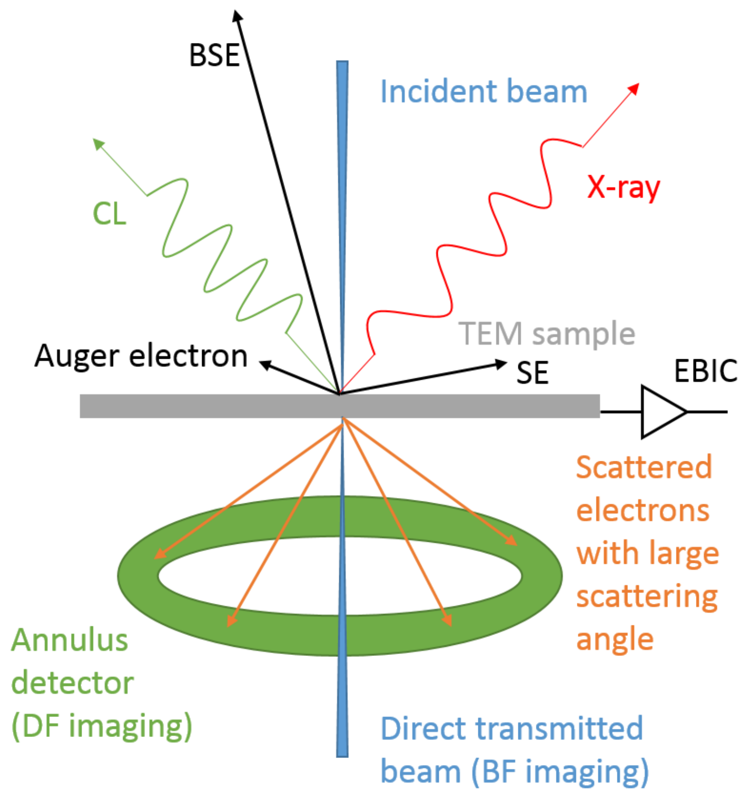

Fig. 2.12 Signals generated under STEM optics.

2.3.4 X-ray diffraction

X-ray diffraction (XRD) is a widely accepted tool for phase identification, lattice constants measurement and refinement, grain size evaluation, macroscopic strain (residue stress), microscopic strain (dislocation density), crystallinity and grain orientation. All these applications are based on one simple principle, that is, Bragg's law, shown in Fig. 2.13. Only when the product of the angle between incident wave (x-ray or electron) and a set of crystallographic planes and the d-spacing of these planes is equal to the wavelength of the incident wave, the scattered waves interfere constructively. Given that the wavelength of the incident wave is fixed (i.e. $K_{\alpha 1}$ of Cu used in this dissertation), the d-spacing can be calculated by the scattering angle. The lattice constant and other parameters can be deduced.

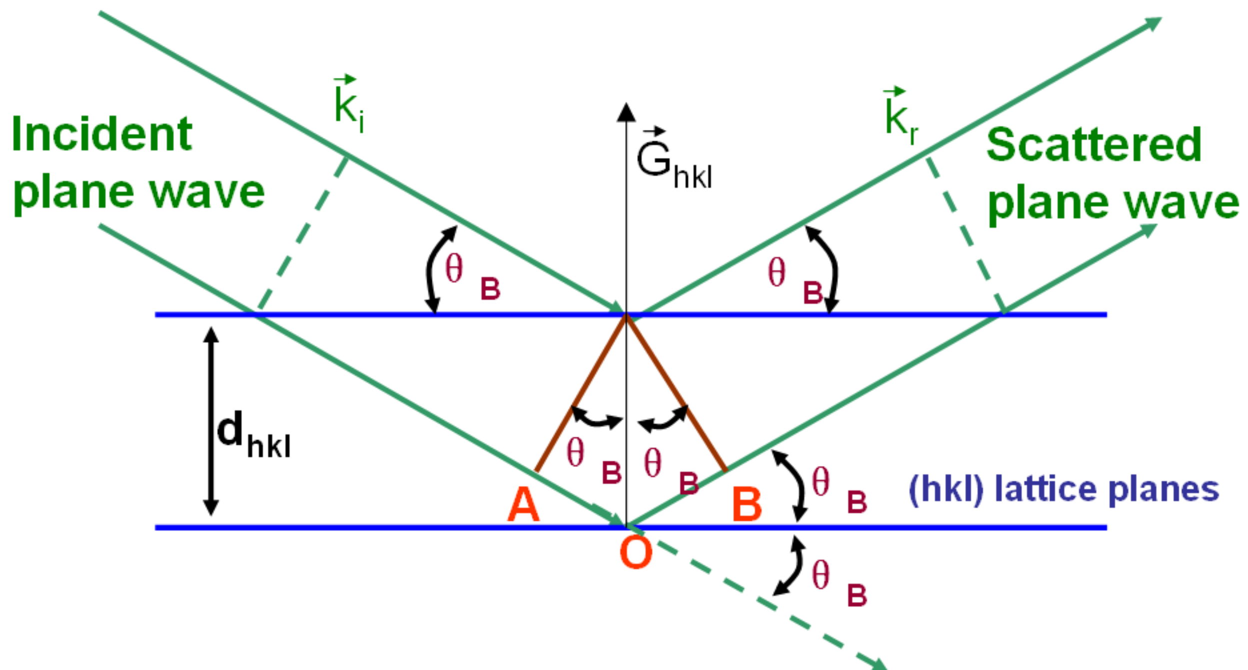

Fig. 2.13 Schematic illustration of Bragg's law.

In this dissertation, the XRD is performed on Rigaku Smartlab in IMRI (Fig. 2.14). For the phase identification of polycrystalline materials, Bragg-Brentano (BB) optics is

utilized. During the measurement, the incident arms and receiving arms rotate simultaneously with the same angular speed while the sample is still. The equipment setup of BB mode is listed in Table 2.2.

Another application of XRD is pole figure measurement. Pole figure is an orientation mapping of a specific family of crystallographic planes in polycrystalline materials. In our research, the pole figure measurement is utilized to identify textures after cold rolling and the recrystallization after annealing. The optics of in-plane parallel beam pole figure measurement is shown in Fig. 2.15.

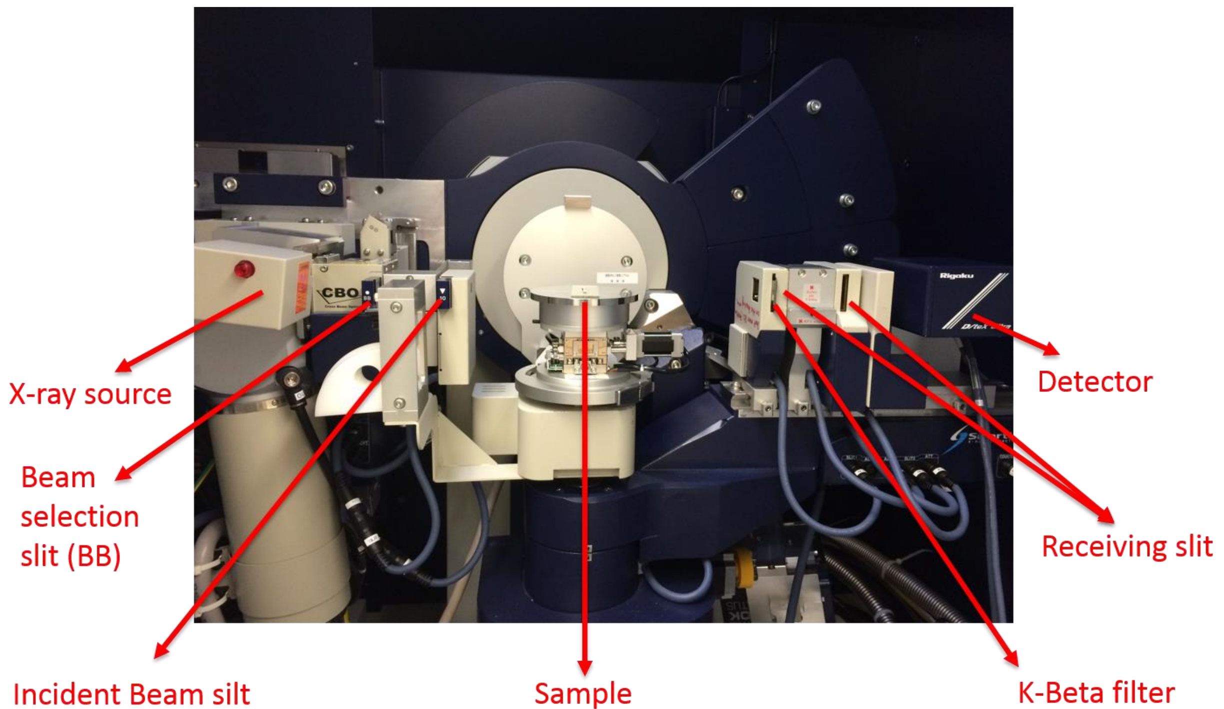

Fig. 2.14 Rigaku Smartlab in IMRI with BB optics.

Table 2.2 Detailed measurement condition of XRD under BB mode.

X-Ray	**40 kV, 44 mA**	Scan speed / Duration	**1.0000 deg/min**
Goniometer	In-plane	**Step width**	0.0500 deg
Attachment	RxRy	**Scan axis**	Theta/2-Theta
Filter	Cu_K-beta	**Scan range**	30.0000-90.0000 deg
CBO selection slit	BB	**Incident slit**	0.5 deg
Monochromator	None	**Length limiting slit**	10.0 mm
Detector	D-tex/ ultra	**Receiving slit #1**	4.000 deg
Scan mode	Continuous	**Receiving slit #2**	13.000 mm

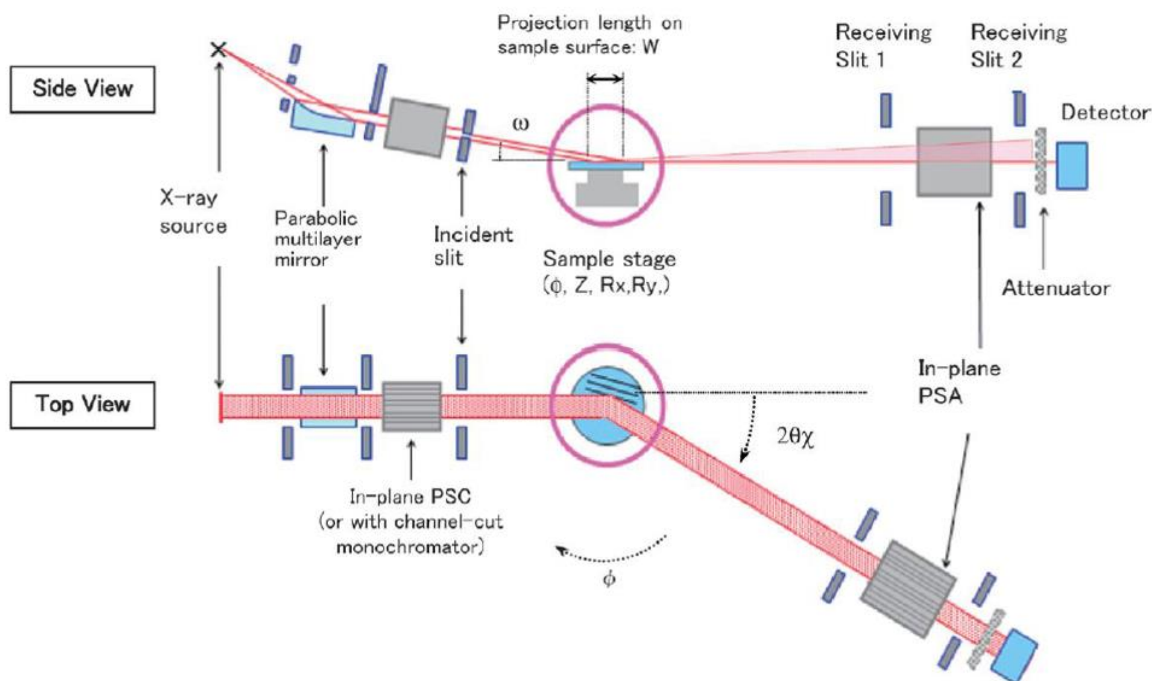

Fig. 2.15 Optics of pole figure measurement.

2.3.5 X-ray photoelectron spectroscopy

X-ray photoelectron spectroscopy (XPS) is one of the most important techniques to investigate the elemental composition and chemical state of the materials. Since only signals generated on the very top layer (within 5 nm) of the materials can escape the collected by the detector, XPS is a surface sensitive characterization technique. The fundamental principle of XPS is Einstein's photoelectric effect. When a photon is completely

absorbed by an electron in an atomic orbital, the electron is able to escape from the material if the energy of photon (hν) is larger than the binding energy of the electron (E_B). During XPS measurement, the kinetic energy (E_K) is measured and the E_B is calculated by the following equation:

$$E_B = h\nu - E_K - \phi_A$$

Where ϕ_A is the work function of the analyzer. The XPS is capable of measuring electrons from core levels and valence levels. In this dissertation, the XPS is used to perform identify surface composition and the chemical state of materials by using the electrons from core levels. Although E_B is a characteristic of the element, the change in local chemical environment can induce the shift of binding energy of core levels (0 to 10 eV). Therefore, the chemical state of the concerned materials can be acquired by measuring the chemical shift. The XPS is performed on KRATOS AXIS SUPRA in IMRI. The machine is equipped with monochromatic X-ray (K_α of Al) source and the energy resolution is 0.3 eV.

2.3.6 Tensile/shear test

In this dissertation, the uniaxial tensile tests were performed on INSTRON 5500R tensile tester at room temperature with a nominal strain rate of about 10^{-5} s^{-1}.

The setup of the shear test is schematically shown in Fig. 2.13. The test is performed on Nordson Dage 4000 tester at a shear speed of 500 μm/s. The shear height is determined by a specific sample.

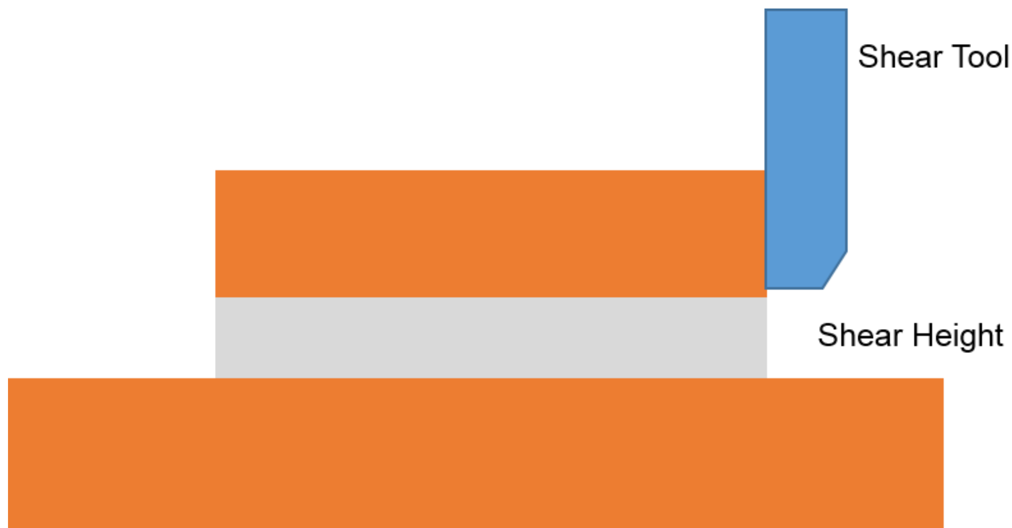

Fig. 2.16 Setup of shear test

2.3.7 Surface profilometer

The surface profilometer provides measurements of the topographic features on the surface of the sample such as step height, depth the trenches and substrate bowing.

During measurement, a diamond stylus moves vertically to contact the sample and then moves laterally across the sample surface for a designated distance with low contact force. The instrument can measure small surface variations in vertical stylus displacement as a function of position.

In this dissertation, Dektak XT Profilometer in Integrated Nanosystems Research Facility (INRF) is used (shown in Fig. 2.17). This instrument is capable of measuring vertical variation ranging from 0.6 nm to 512 microns with high repeatability. In addition, the stylus contact force is low so that the measurement can be regarded as non-destructive. In our research, this instrument is utilized to measure the step height and evaluate the surface roughness.

Fig. 2.17 Dektak XT Profilometer in INRF.

2.4 Reference:

[1] ASTM standard E8/E8M-08, Standard Test Methods for Tension Testing of Metallic Materials, ASTM International, West Conshohocken, PA, 2008, http://dx.doi.org/10.1520/E0008_E0008M-08. www.astm.org.

[2] Electron interactions, http://www.radiation-therapy-review.com/Radiation_Physics_and_Biology.html, last accessed July 20th, 2018.

Chapter 3. Preparation and evaluation of mechanical properties and tarnish resistance of Ag solid solution phase with zinc

3.1 Introduction

In electronic packaging, silver alloys have been proposed as alternative materials for the bonding wire [1-4]. In consideration of the wire bonding process, performance and reliability issues, it's necessary for the bonding wire to have not only good thermal and electrical conductivity but also sufficient tensile strength and elongation [2]. Ag-Au-Pd [2, 4] systems have been reported to have better tensile strength and elongation than pure silver. However, the addition of gold and palladium will no doubt increase the cost of bonding wire. Therefore, it's still challenging to make silver based alloy both strong and ductile while keeping its low cost.

In spite of these facts, alloying is still a strategy to achieve this goal. Recall that alpha brass, the copper solid solution phase with zinc, is stronger and more ductile than copper and thus suitable for cold working and many other applications. Moreover, silver and copper are in the same column in the periodic table and thus have similar valence electron configuration. This gives rise to an interesting question: whether alloying zinc into silver can make the alloy both strong and ductile? According to the Ag-Zn phase diagram [5], which is shown in Fig. 3.1, the solid solubility of zinc in silver is about thirty atomic percent (30 at. %) at 100 Celsius. This value will be decreased but the zinc concentration as large as 25 at. % was acquired in the literature [6]. Usually, the total dopants concentration in silver alloy is below 15. at%, such as sterling silver (Ag-12.1 at. %Cu) and Ag-Au-Pd system [2,4]. As a preliminary study of Ag-Zn system, silver solid solution phase with 5 at. % and 15 at. % zinc concentration were chosen to prepare, which are designated as (Ag)-5Zn and (Ag)-

15Zn, respectively. Meanwhile, pure silver was used as the controlled group for the following experiments [7].

Another issue associated with Ag is tarnishing. Ag is very sensitive to the presence of gaseous sulfur-containing species such as sulfur vapor, hydrogen sulfide (H_2S), sulfur dioxide (SO_2), and carbonyl sulfide, etc. Typically, the concentrations of those corrosive gases are very low, ranging from less than one parts per billion (ppb) under normal atmosphere to hundreds of ppb in heavy industrial environment [8]. However, the corrosion phenomenon can be commonly observed from silver used anywhere. For example, the Ag containing TEM sample was prepared and left in ambient overnight. Large amount of sulfide can be observed in the next day's TEM session. The corrosive reaction product is silver sulfide (Ag_2S) which can be the killer of electronic products in several aspects. First of all, the mechanical strength of Ag_2S is poor, resulting in easy detachment from its original site and contamination. Secondly, Ag_2S also poses a threat to circuits because its dendritic growth nature might result in the formation of silver sulfide whiskers [9]. Since Ag_2S is not a good insulator, these whiskers may induce short circuit in the fine pitch applications. Last but not least, the reflectance of Ag_2S is poor, which will seriously limits the application and acceptance of Ag in optoelectronic devices (LED).

In the following section, the phase identification and chemical composition analysis of materials will be described. Next, the engineering and true stress vs. strain curve which are acquired in tensile test will be discussed. Then, the fracture surface of the tensile specimen will be examined by SEM and the fracture mode and failure mechanism will be analyzed. In addition, the evaluation of the tarnish resistance is illustrated. Lastly, the potential application and scientific value of the research will be discussed.

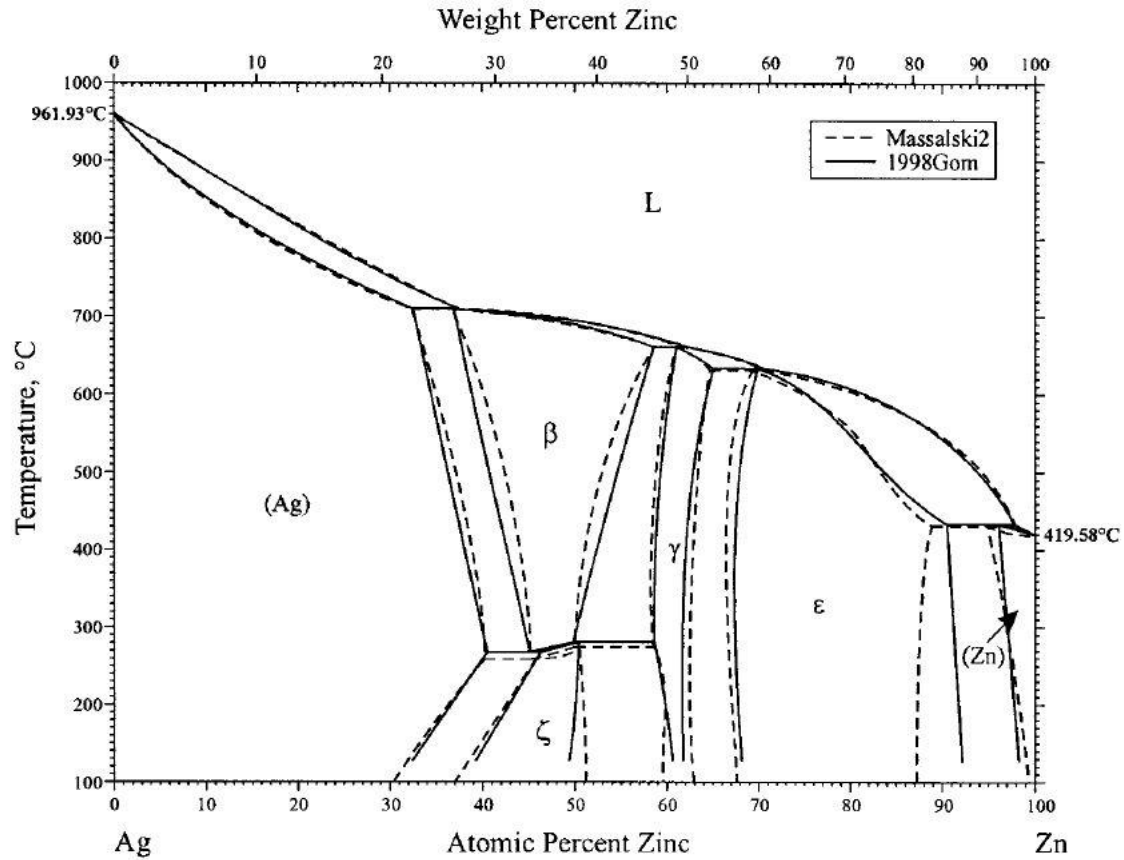

Fig. 3.1 Silver-zinc binary phase diagram.

3.2 Materials and Characterization

XRD results of pure silver, (Ag)-5Zn and (Ag)-15Zn disk samples are shown in Fig. 3.2. The data collected in the tests were processed and analyzed by PDXL, an integrated powder XRD analysis software package. The peaks in Fig. 3.2 are indexed and the crystallography information of samples are acquired and listed in Table 3.1, 3.2 and 3.3.

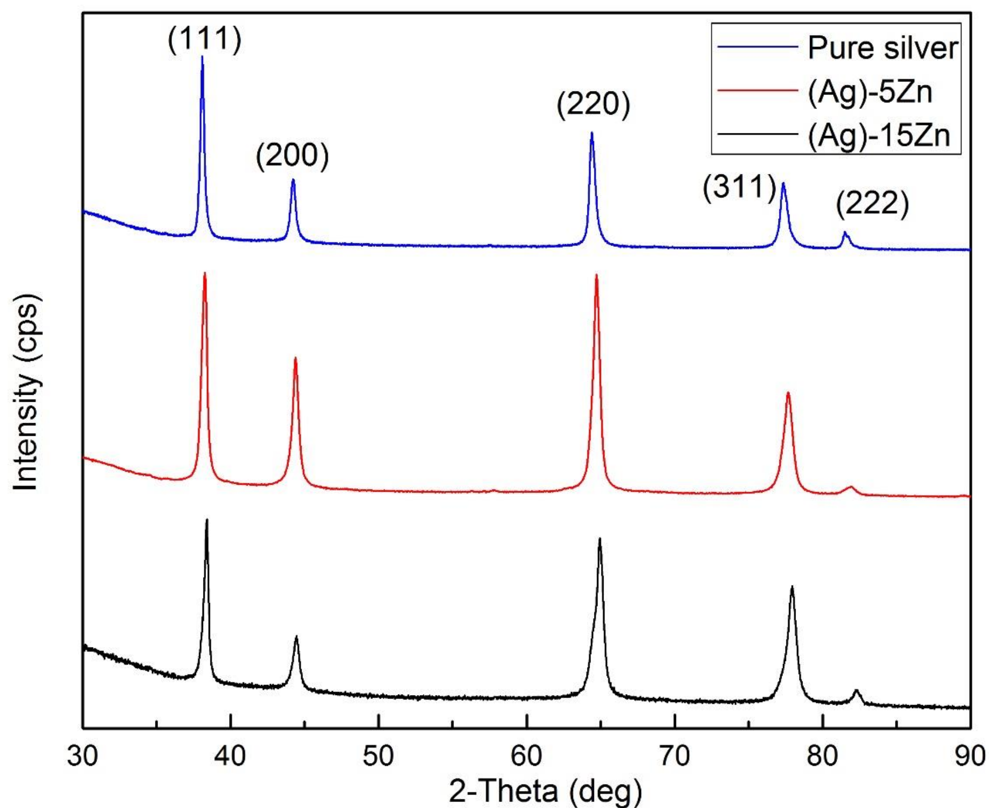

Fig. 3.2 XRD pattern of Pure silver (blue), (Ag)-5Zn (red) and (Ag)-15Zn (black).

Table 3.1 Peak list and analysis results of pure silver

Peak #	2-Theta (deg)	d (Å)	(hkl)	a (Å)
1	38.092	2.3605	(111)	4.0885
2	44.221	2.0455	(200)	4.0910
3	64.382	1.4459	(220)	4.0896
4	77.328	1.2330	(311)	4.0894
5	81.493	1.1801	(222)	4.0880

Table 3.2 Peak list and analysis results of (Ag)-5Zn

Peak #	2-Theta (deg)	d (Å)	(hkl)	a (Å)
1	38.204	2.3539	(111)	4.0771
2	44.277	2.0441	(200)	4.0882
3	64.618	1.4412	(220)	4.0763
4	77.546	1.2300	(311)	4.0794
5	81.770	1.1769	(222)	4.0769

Table 3.3 Peak list and analysis results of (Ag)-15Zn

Peak #	2-Theta (deg)	d (Å)	(hkl)	a (Å)
1	38.404	2.3421	(111)	4.0566
2	44.441	2.0369	(200)	4.0738
3	64.925	1.4351	(220)	4.0591
4	77.843	1.2261	(311)	4.0665
5	82.300	1.1707	(222)	4.0554

From Fig. 3.2, it is apparent that the crystal structure of pure silver, (Ag)-5Zn and (Ag)-15Zn are face centered cubic (FCC) in terms of diffraction patterns' systematic absence. In addition, there are no impurity peaks other than the peaks of pure silver, (Ag)-5Zn and (Ag)-15Zn in each XRD pattern. Therefore, it is conservatively concluded that the materials composing the disk samples are nearly homogeneous. In Table 3.1, 3.2 and 3.3, d is d-spacing between corresponding crystallographic plane, (hkl) is the Miller's indices with classic denotation, and a is the calculated lattice constant by using values of each d-spacing under the assumption that the geometry of lattice is perfect cubic. As results, the weighted average value for lattice constants are 4.0893 Å, 4.0796 Å and 4.0623 Å for pure silver, (Ag)-5Zn and (Ag)-15Zn respectively. The trend of decreasing values for lattice constant is consistence with the right-shifted peaks in XRD patterns, which can be

explained by reviewing the atomic radii for silver and zinc elements. The empirical atomic radii of zinc is 134 pm, which is smaller than that of silver's, 144pm. Therefore, if one silver atom is replaced by zinc in silver crystalline, it would result in dent in its crystal structure, which caused the decrease in lattice constant as the concentration of zinc increased. Besides, the lattice distortion makes the crystal not a perfect cubic any more, which induces the slight difference between calculated lattice constants in Table 3.2 and 3.3 by using different d-spacing from the same solid solution phase.

The chemical composition of (Ag)-xZn is examined by EDX. Test areas were randomly chosen from the samples and data was collected from nine points per area under 1000X magnification (shown in Fig. 3.3). EDX results of (Ag)-5Zn and (Ag)-15Zn disk samples are listed in Table 3.4. For both compositions, the measured zinc concentration are nominal concentration with small deviation. In consideration of the limitation of EDX and our group's facility condition, the errors are acceptable and the nominal composition can be regarded as real composition.

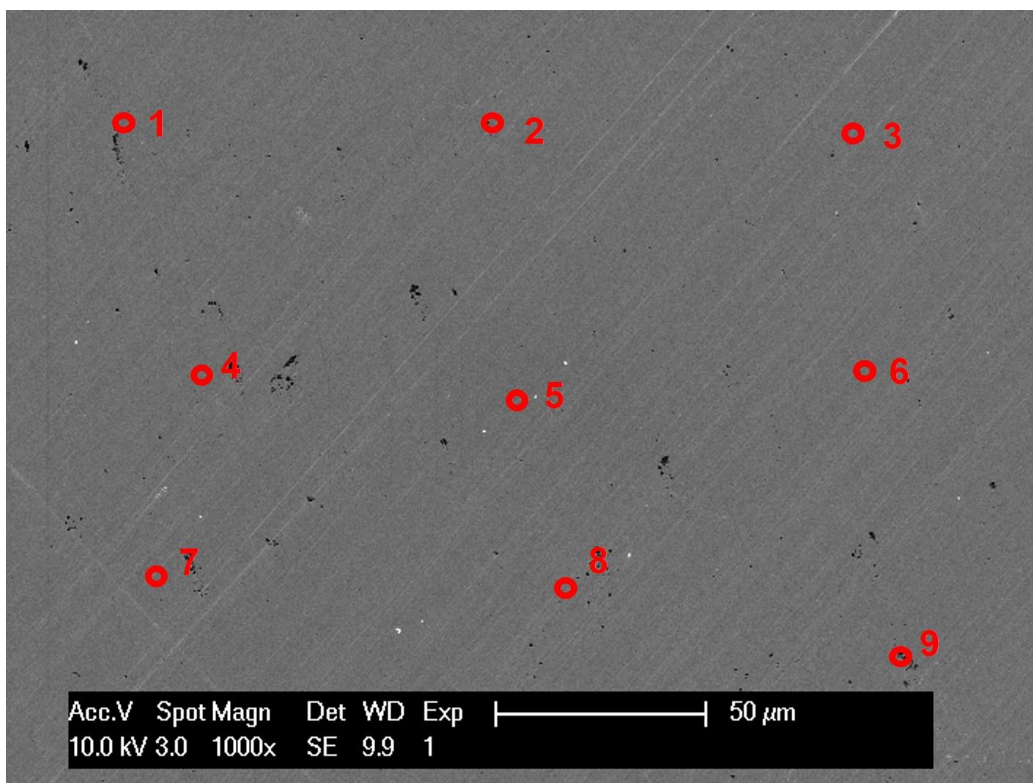

Fig. 3.3 Illustration of data collection in EDX.

Table 3.4 EDX (point and shoot mode) results for (Ag)-5Zn and (Ag)-15Zn

	(Ag)-5Zn		(Ag)-15Zn	
Data point #	Ag (at %)	Zn (at %)	Ag (at %)	Zn (at %)
1	5.34	94.66	16.22	83.78
2	6.41	93.59	13.82	86.18
3	5.76	94.24	14.37	85.63
4	4.77	95.23	15.59	84.41
5	4.99	95.01	14.51	85.49
6	5.35	94.65	16.67	83.33
7	5.53	94.47	14.10	85.90
8	6.18	93.82	16.38	83.62
9	5.25	94.75	13.23	86.77

The XRD and EDX results shown above are representative and repeatable for disk samples' crystallography and chemical composition examination. Besides, the results of

tensile samples which are from different region of the ingots show the consistency. In conclusion, nearly homogeneous polycrystalline (Ag)-5Zn and (Ag)-15Zn have been successfully prepared by vacuum casting and specific annealing process. Even so, further efforts and improvement can be made to improve the quality of the ingots (i.e. reduce porosity).

3.3 Tensile test

In consideration of the limitation of our facility and preparation process, defects such as cavities of which the size is in micron range exist in the ingots. Besides, tensile test samples are cut from different regions of the ingots. Therefore, the quality and orientation distribution of grains of these samples may vary a little from one to another. In our current research, multiple rounds of tests are conducted on each specific composition. Representative results of pure silver, (Ag)-5Zn and (Ag)-15Zn will be discussed. Fig. 3.4 exhibits the engineering stress vs. strain curve of pure silver, (Ag)-5Zn and (Ag)-15Zn. To get a true indication of the deformation characteristics of materials, true stress vs. true strain curve (known as flow curve) are also plotted and shown in Fig. 3.5. The calculation of true stress and true strain are based on equation (1) and (2), in which s is engineering stress, e is engineering strain, σ is true stress and ε is true strain.

$$\sigma = s(e+1) \tag{1}$$

$$\varepsilon = \ln(e+1) \tag{2}$$

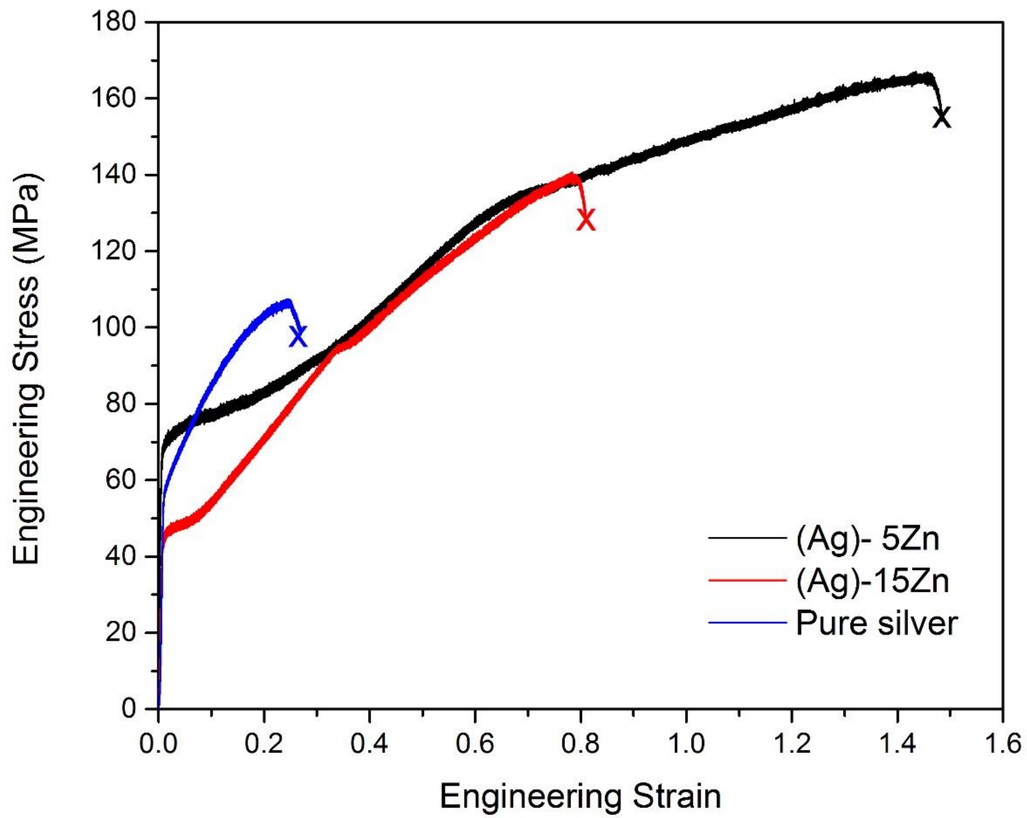

Fig. 3.4 Engineering stress vs. strain curve of pure silver (blue), (Ag)-5Zn (black) and (Ag)-15Zn (red)

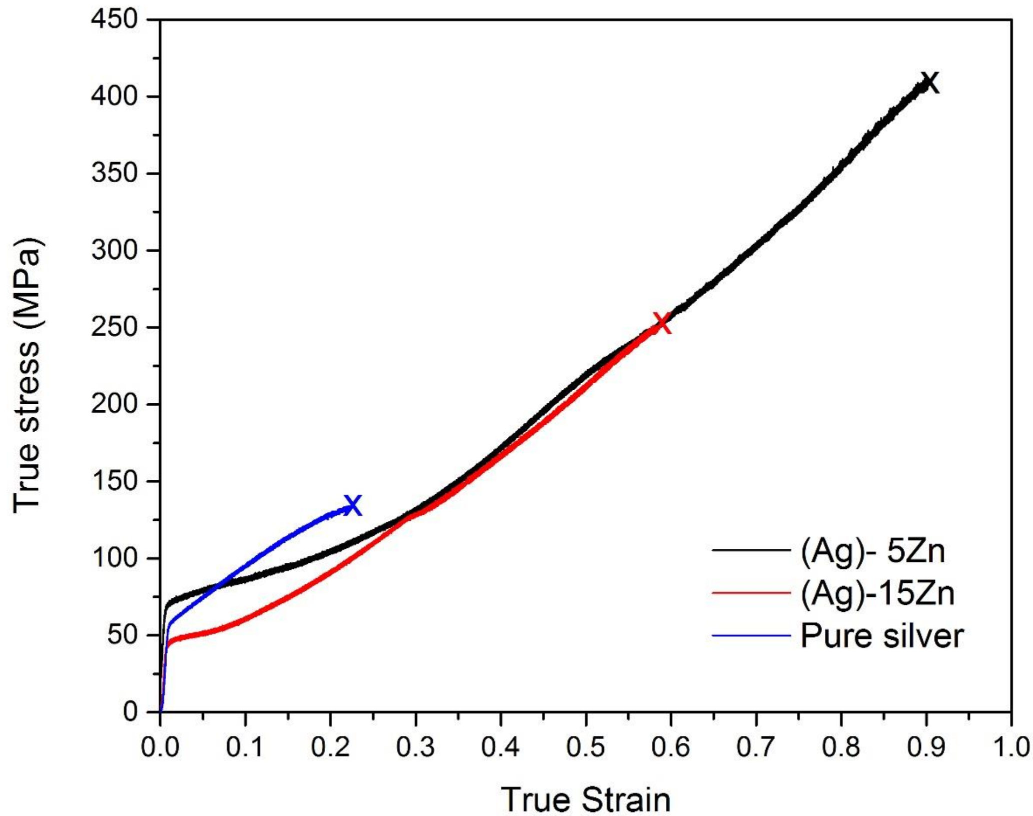

Fig. 3.5 True stress vs. strain curve of pure silver (blue), (Ag)-5Zn (black) and (Ag)-15Zn (red)

According to the flow curve, all three materials start with linear elastic deformation and then transit into plastic stage. The transition behavior of silver solid solution phase is quite different from that of pure silver's. For Pure silver, the transition is relatively smooth and followed strain hardening rate is high. However, sharp transition occurs in solid solution phase and followed with a low strain hardening region. This phenomenon can be interpreted as the interaction between dislocation and Short-Range Order (SRO) in the solid solution phase [10]. Although the solute arrangement in solid solution phase is disordered in long range in our cases, SRO may occur with the increase of the solute

concentration. The SRO can be an obstacle for the dislocation to glide in the lattice. When the leading dislocation begins to glide, the SRO is destroyed. Since the order is only of a short range, it won't be restored and the following dislocations can glide easily on this plane [11]. This phenomenon is also referred as glide plane softening. As a result, a yield point effect [12] or low strain hardening rate at low strains [13] is found in solid solution phase with FCC structure.

The yield strength, ultimate tensile strength, uniform strain, true stress at maximum load and true uniform strain are summarized and listed in Table 3.5. Here, true stress at maximum load is used instead of true fracture stress because true fracture stress should be corrected for the triaxial state of stress existing in the tensile specimen at fracture. However, the data required for this correction are often not available, true fracture values are thus frequently in error. Similarly, true uniform strain is used since it's impossible to calculate true fracture strain simply through fracture elongation for tensile specimen with rectangular cross section.

Table 3.5 Summary of tensile test results with pure silver as comparison

Composition	**Yield strength (MPa)**	**Ultimate tensile strength (MPa)**	**Uniform strain (%)**	**True stress at maximum load (MPa)**	**True uniform strain (%)**
Pure silver	56.6	106.7	25	133.8	22
(Ag)-5Zn	68.5	166.5	148	412.2	92
(Ag)-15Zn	48.2	127.4	90	250.0	65

According to Table. 3.5, the yield strength of (Ag)-5Zn is higher than that of pure silver while (Ag)-15Zn shows a decrease in yield strength. Based on classical solid solution strengthening theory for coarse-grained polycrystalline such as those from Fleischer [14]

and Labusch [15], the solid solution will be further strengthened with the increase in solute concentration. Therefore, the decrease in yield strength of (Ag)-15Zn seems abnormal in consideration of the traditional theory. However, this phenomenon can be referred as solid solution softening, which is not limited to metallic system but has also been reported in covalent and ionic systems [16]. It is possible, therefore, that a common but unknown mechanism may exist for this phenomenon. In literatures, solid solution softening in body-centered cubic (BCC) crystal structure has been most extensively studied in the past. In iron-carbon system, a mechanism has been developed by examining the motion of a screw dislocation through a combination of Peierls field and misfit strain centers [17]. In Molybdenum based solid solution, the softening additions will locally alter the chemical bonding which results in a decrease of the generalized stacking fault energy and atomic row shear resistance [18]. It is also reported that the addition of zinc will soften the secondary glide systems in magnesium based solid solution phase of which the crystal structure is hexagonal-closed packed (HCP) [19]. For silver solid solution phase with indium (FCC), solid solution strengthening occurs in dilute indium concentration [20] while a decrease in yield strength has been reported when the atomic concentration of zinc is higher than 9.5% [7]. From well-studied systems, the interaction between dislocation and localized structure that induced by solute contribute to the decrease in yield strength. In our case, in view of the localized factors that can influence the mobility of dislocation, the ease of destroying SRO for the leading dislocation in (Ag)-15Zn may partially contribute to the softening phenomenon. However, further quantitative research and modelling are needed to evaluate solid solution softening and the critical solute concentration between softening and hardening for solid solution phase with FCC structure.

It is also noticeable that the uniform strain of (Ag)-5Zn is 148% which is about 5 times larger than that of pure silver. For (Ag)-15Zn, the uniform strain is 90% which is smaller than that of (Ag)-5Zn but still shows substantial increase compared to pure silver. Even in limited report on pure silver [21], the uniform strain is smaller than 50% under room temperature. Moreover, from Table 3.5, the true stress at maximum load of (Ag)-5Zn is more than 3 times that of pure silver. Similarly, (Ag)-15Zn shows the decrease in strength compared to (Ag)-5Zn but is still superior to pure silver. Recall that any point on the flow curve can be considered as the yield strength for a metal strained in tension by the amount shown on the curve. Thus, if the load is removed at this point and then reapplied, the material will behave elastically throughout the entire range of reloading. Therefore, the huge increase in true stress at maximum load is highly remarkable since it indicates that the yield strength of silver solid solution phase can be largely increased by cold work such as forging and rolling. In total, (Ag)-5Zn and (Ag)-15Zn not only increase the true stress at maximum load but also exhibit much better ductility compared to pure silver. The materials will hopefully exhibit better mechanical properties if the quality is further improved.

3.4 Failure analysis

The fracture surface of (Ag)-5Zn and (Ag)-15Zn are examined by using SEM to analyze the failure mode. The images at different magnification for (Ag)-5Zn and (Ag)-15Zn are shown in Fig. 3.6 and Fig. 3.7, respectively.

According to Fig. 3.6(a), the necking of (Ag)-5Zn tensile samples is rather serious so that the parts above and below the neck separate along an extremely narrow plane of which the width is less than 100 micron. Compared to the original thickness of the tensile

sample, 1.1 mm, the width of cross section is reduced by a factor of 12. In addition, the surface is featureless and smooth. For (Ag)-15Zn, as shown in Fig. 3.7(a) and 3.7(b), the topography of fracture surface is similar as that of (Ag)-5Zn. The only difference is that the final width of the fracture plane is a little bit larger, which is an indication that the ductility is decreased compared to that of (Ag)-5Zn. However, the shrinkage in cross section of (Ag)-15Zn is still remarkable.

This type of fracture mode is called rupture, which is induced by localization of plastic deformation (shown in Fig. 3.8). More specifically, in tensile test, for specimen with rectangular cross section, there are two types of tensile flow instability. The first is diffuse necking, which induces the shrinkage in width. Diffuse necking may terminate in fracture but usually it's not serious and followed by second instability process called localized necking [22]. In this mode, continued thinning around one section finally leads to fracture. Orowan [23] proposed that rupture is a strong indication that the material is very ductile.

Another indication of the high ductility of (Ag)-xZn can be found in the no-breakge region on the samples after tensile test. The situation inside the tensile test samples is analyzed after polishing by ion beam polisher, which is capable of revealing the internal structure without any smearing. The structure inside the sample is shown in Fig. 3.9. It can be seen that there are a few elongated voids whose size are up to tens of microns! Recall that the size of original voids generated during the preparation process is within micron range. The elongated voids without any cracks could be another strong indication of the superior ductility of Ag-xZn. In conclusion, the results of fractography and failure analysis show the consistency with the tensile test data, confirming that the ductility of silver solid solution phase with zinc is largely enhanced compared to that of pure silver.

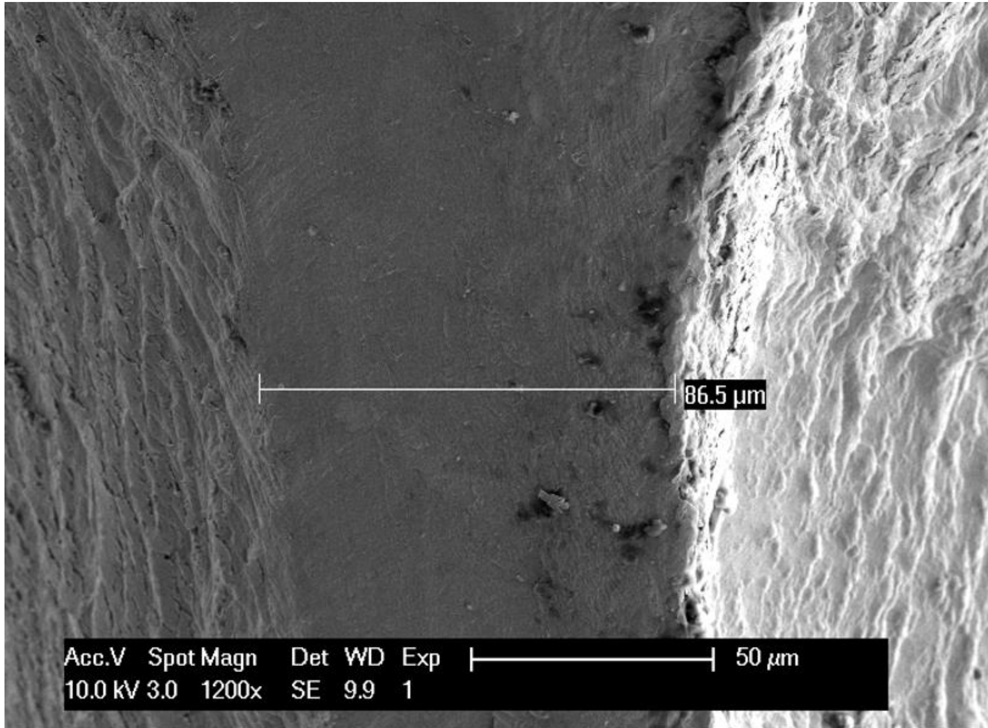

(a)

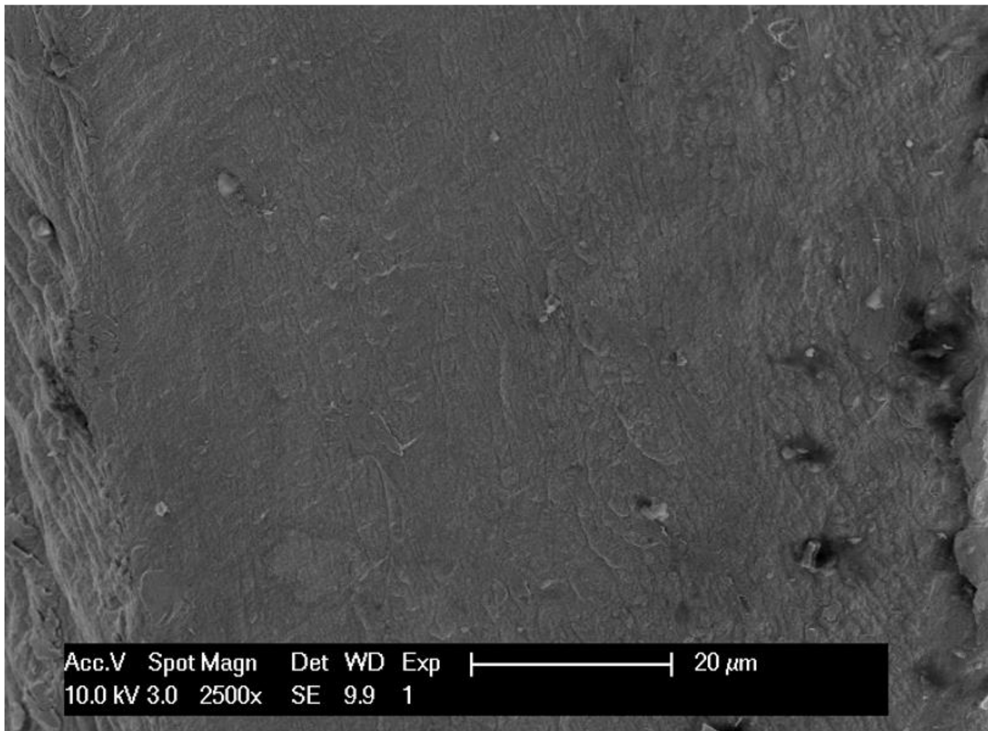

(b)

Fig. 3.6 SEM Image of fracture surface of (Ag)-5Zn at different magnifications.

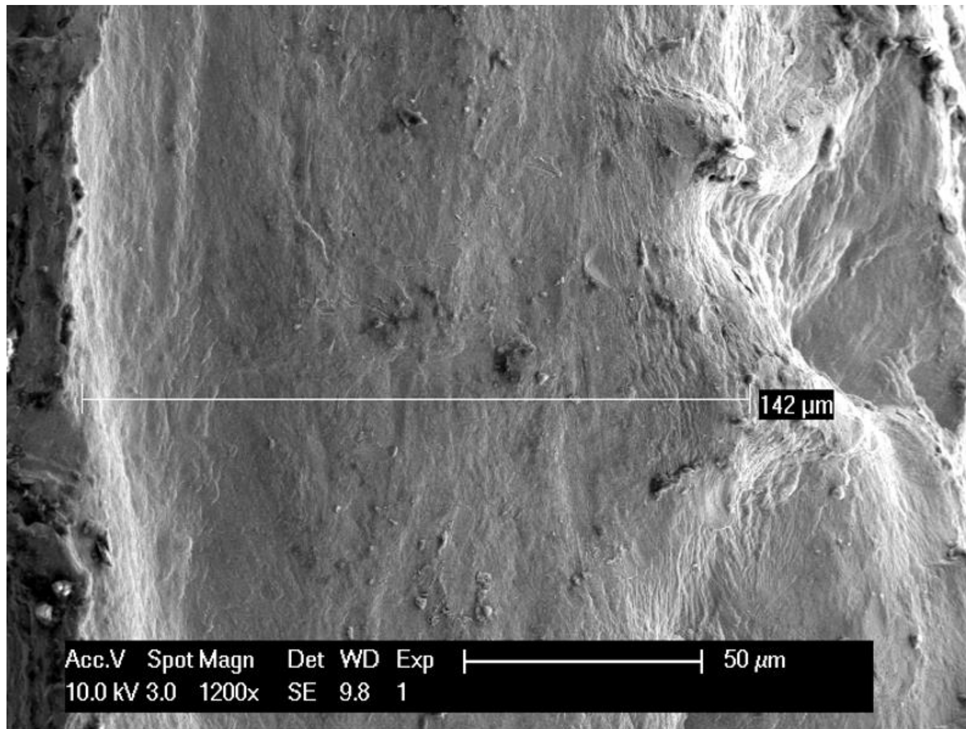

(a)

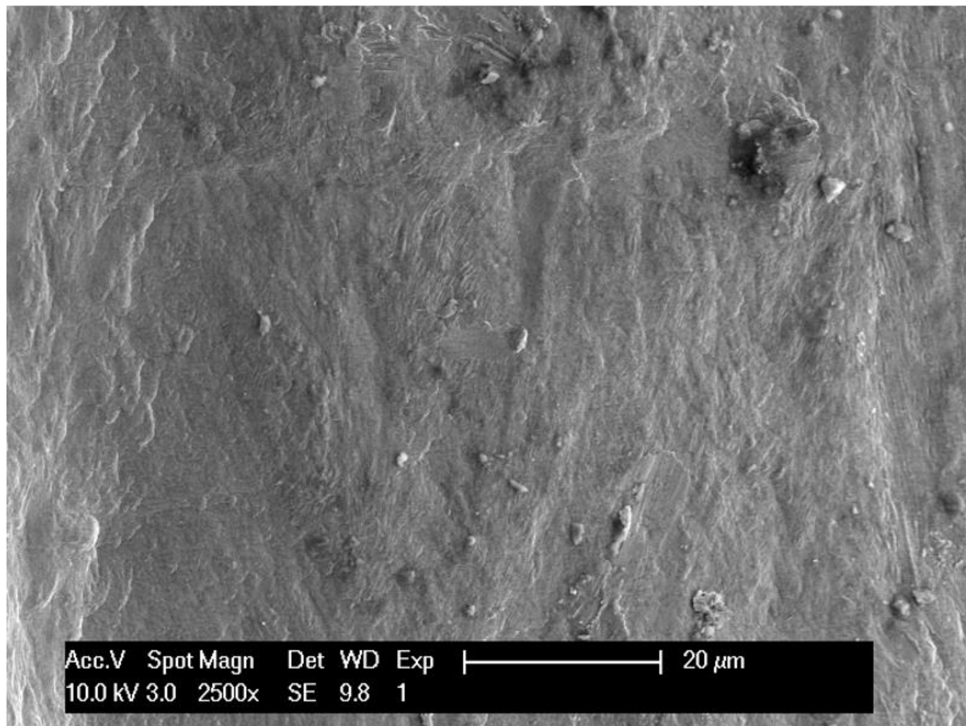

(b)

Fig. 3.7 SEM Image of fracture surface of (Ag)-15Zn at different magnifications.

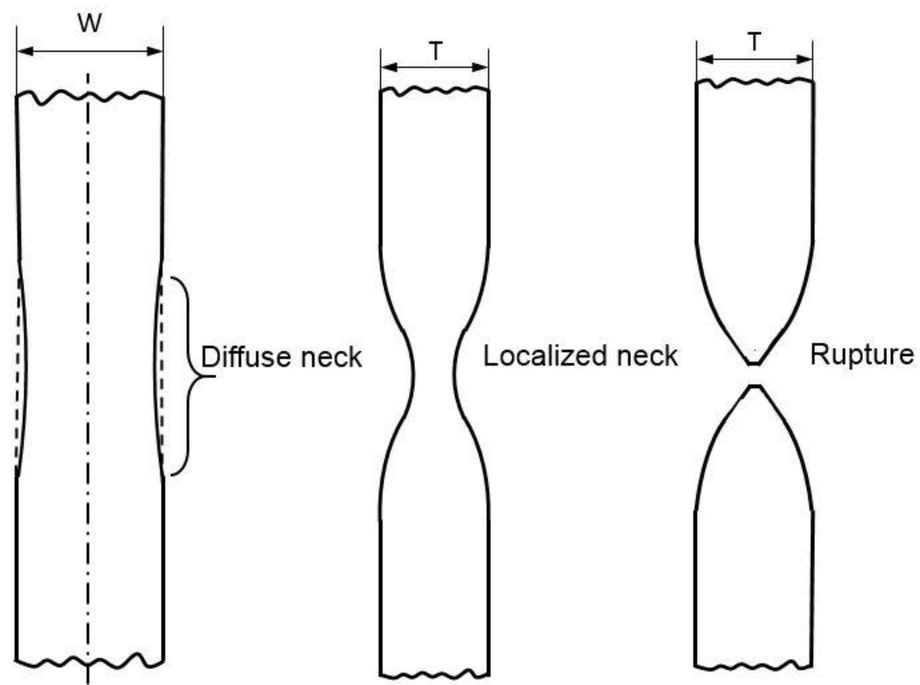

Fig. 3.8 Illustration of tensile instability and rupture.

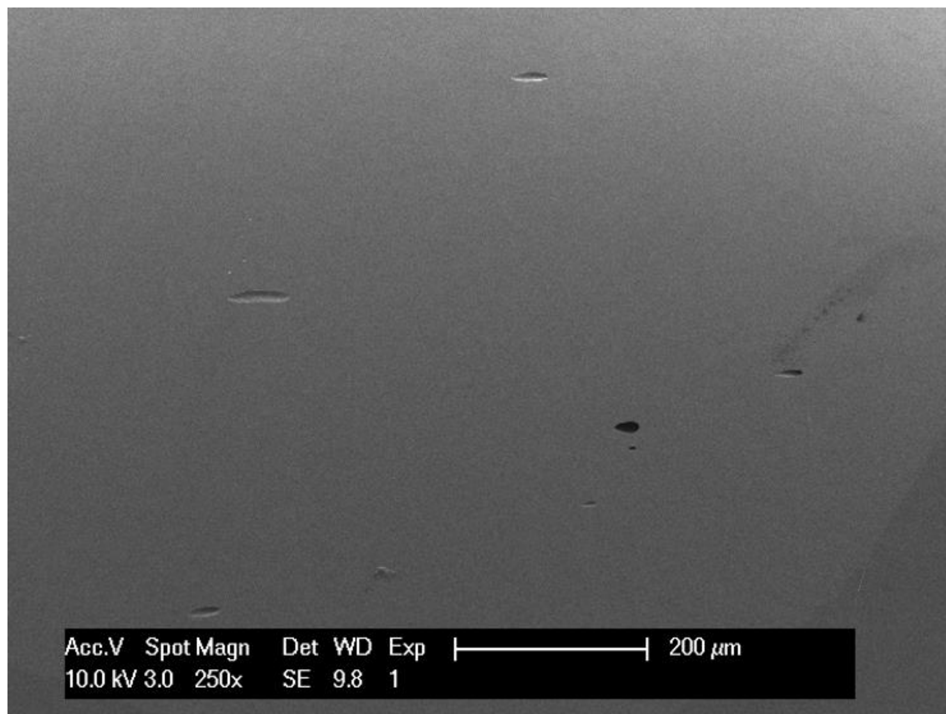

(a)

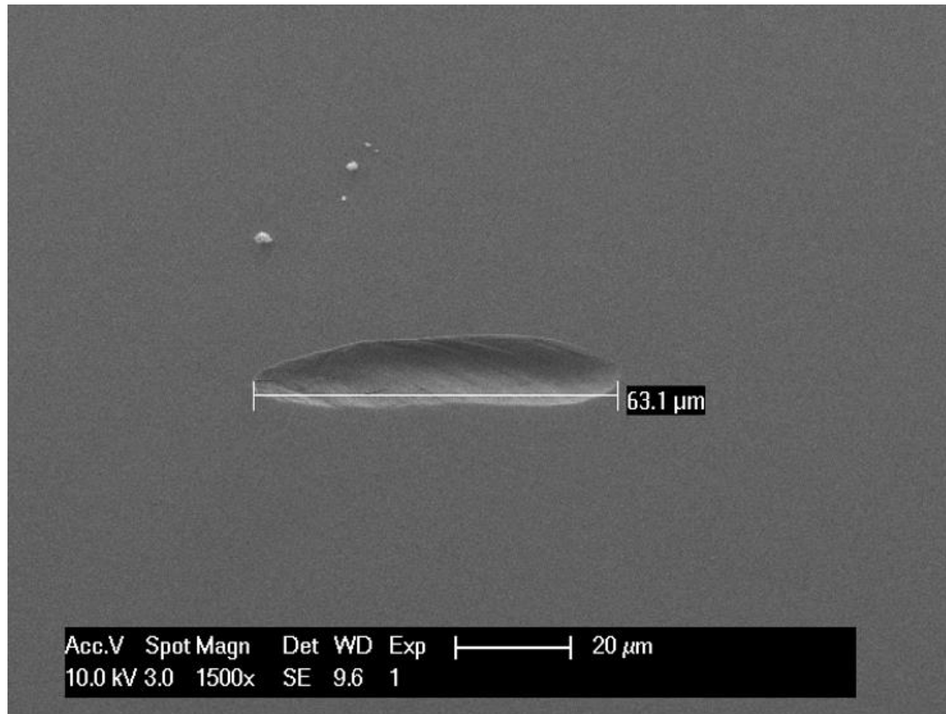

(b)

Fig. 3.9 Internal voids in the sample after tensile test.

3.5 Evaluation of tarnishing resistance

3.5.1 Test design and setup

To examine the tarnish resistance of (Ag)-xZn, we conduct environmental test where Ag is exposed to gaseous sulfur (S_8) and dry air. The reaction temperature is set at 120 °C, which is chosen due to the following reasons. Firstly, the melting temperature of precipitated sulfur (S595-500) is 115.21 °C, so 120 °C is enough to completely melt the sulfur into liquid phase, thereby generating sulfur vapor through evaporation to reach the equilibrium vapor pressure. As shown in Fig. 3.10 [24], most of sulfur vapor molecules would be in the form of S_8, so the total sulfur vapor pressure at thermal equilibrium is almost equal to partial vapor pressure of S_8. As a result, the reactants and its concentration are in good control at 120 °C.

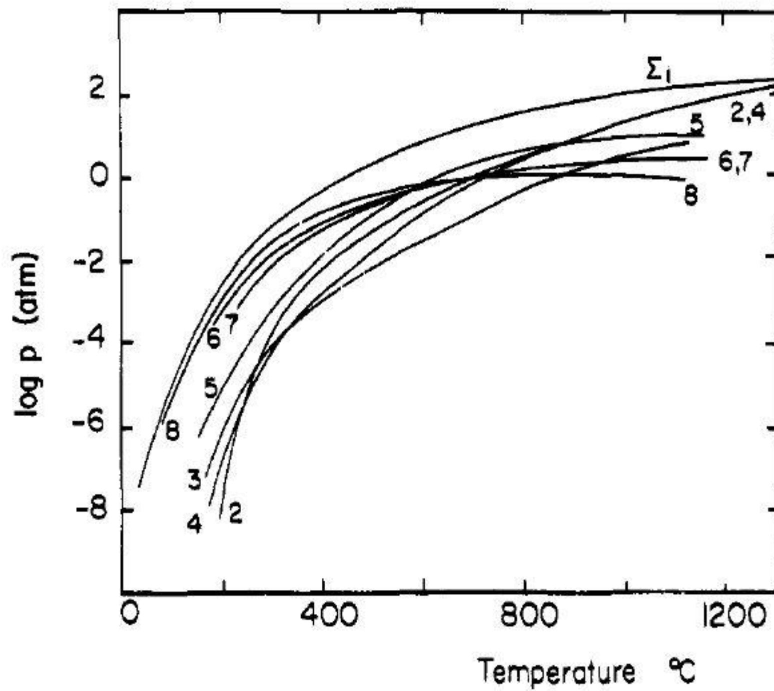

Fig. 3.10 Equilibrium vapor pressure of sulfur, $\sum_i$ is the total pressure, $2 \leq n \leq 8$, is the partial pressures of S_n.

The experimental process flow is shown in Fig. 3.11. After fine polishing, the disk sample is half coated by AZ4620 photoresist which acts as protection layer during the sulfurization test. Then disk samples is loaded into a chamber shown in Fig. 3.12. This chamber is closed and put into convection oven which is preheated to 120 °C. After reaction, the photoresist is removed by stripper and the step height is measured by using Dektak profilometer. Pure Ag disk sample is also put in the chamber as a control group.

The reaction chamber is shown in Fig. 3.12. The volume of the chamber is 1 L and the chamber is sealed by the O-ring. Four samples are placed in the corner and a beaker with sulfur in the form is power is placed at the center. The quantity of sulfur is calculated using ideal gas law. According to the calculation results, 5 mg sulfur element in weight would be enough for the sulfur vapor to reach the equilibrium vapor pressure at 120 °C.

Considering that the gas could be consumed during the reactions, oversupplying the amount of precipitated sulfur (0.15 g) is essential to ensure that sulfur vapor concentration remains as a constant during the experiment.

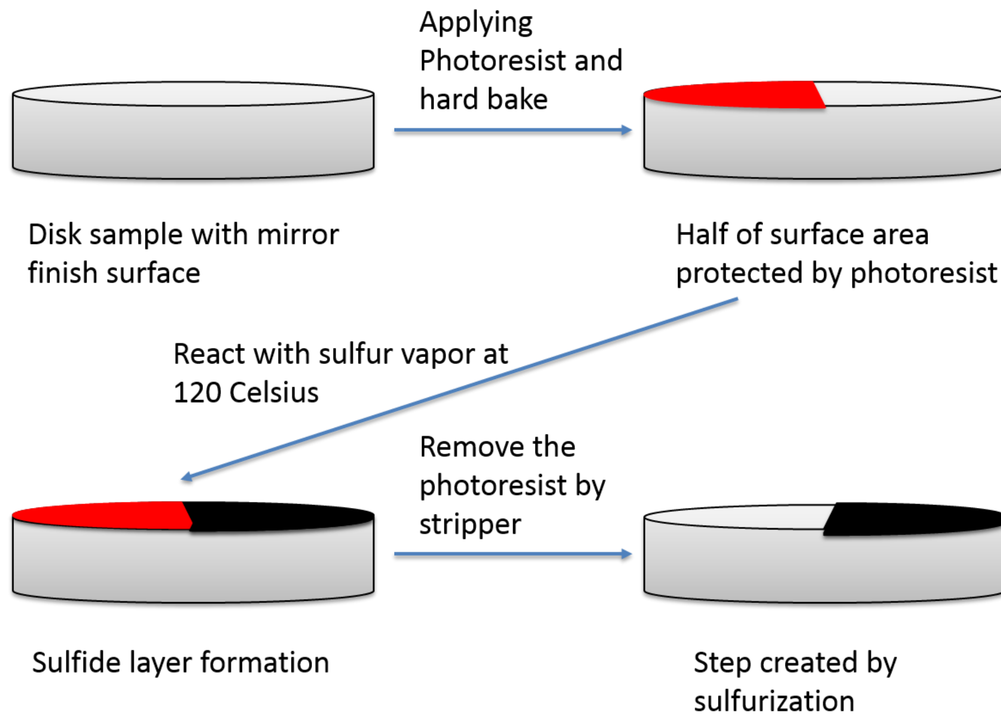

Fig. 3.11 Process flow of evaluation of anti-tarnishing properties.

Fig. 3.12 Sulfurization test setup.

3.5.2 Characterization and measurement

After reactions, XRD is performed to examine the resultant. According to Fig. 3.13, all the peaks except for three indexed (from Ag) are from Ag_2S. Peaks from Ag or Ag-xZn are acquired since the half of the surface area is protected by photoresist during the reaction.

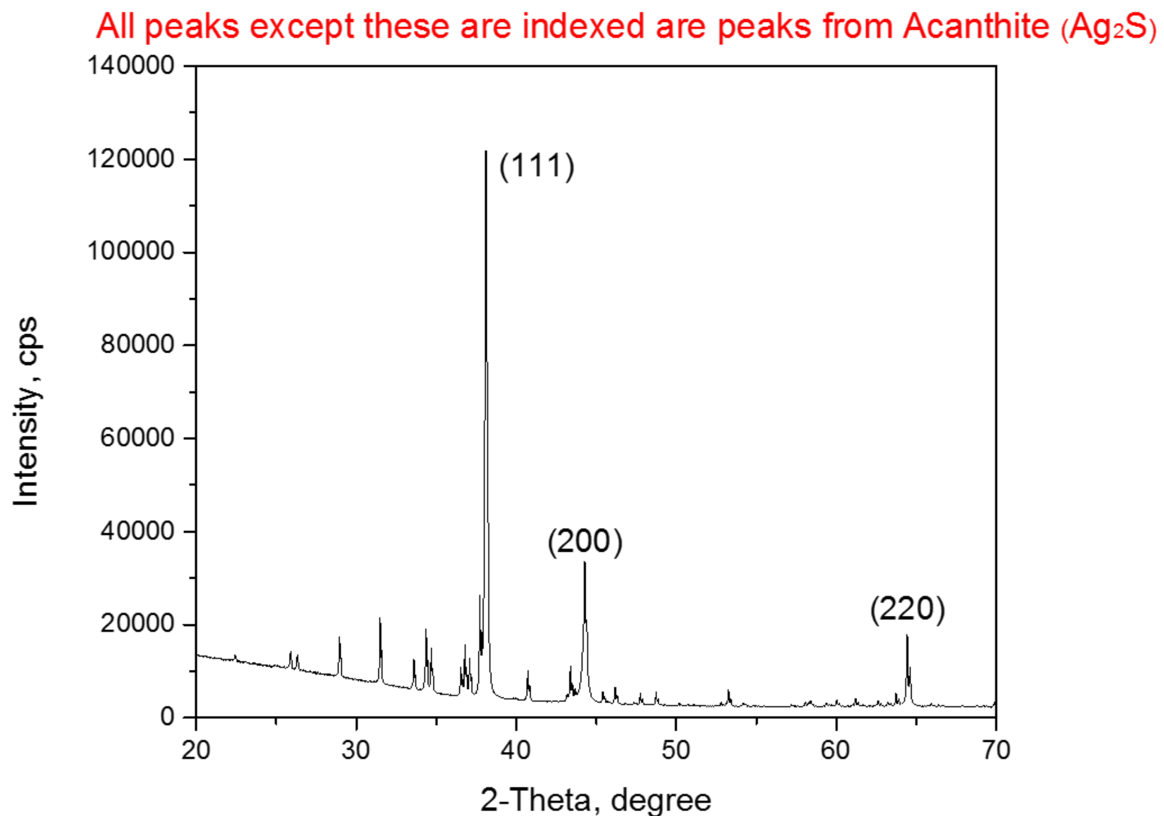

Fig. 3.13 Phase identification of silver sulfide.

The steps between reacted region and protected region are examined by optical microscope. According to Fig. 3.14, the steps are clear and the contrast between reacted region and unreacted region is sharp. Moreover, it can be easily identified that the thickness of Ag_2S on top of Ag-xZn is thinner than that on top of pure Ag where the Ag_2S is

thick so that it's hard to focus the both sides at the same time due to the limited depth of focus (DOF) of optical microscope.

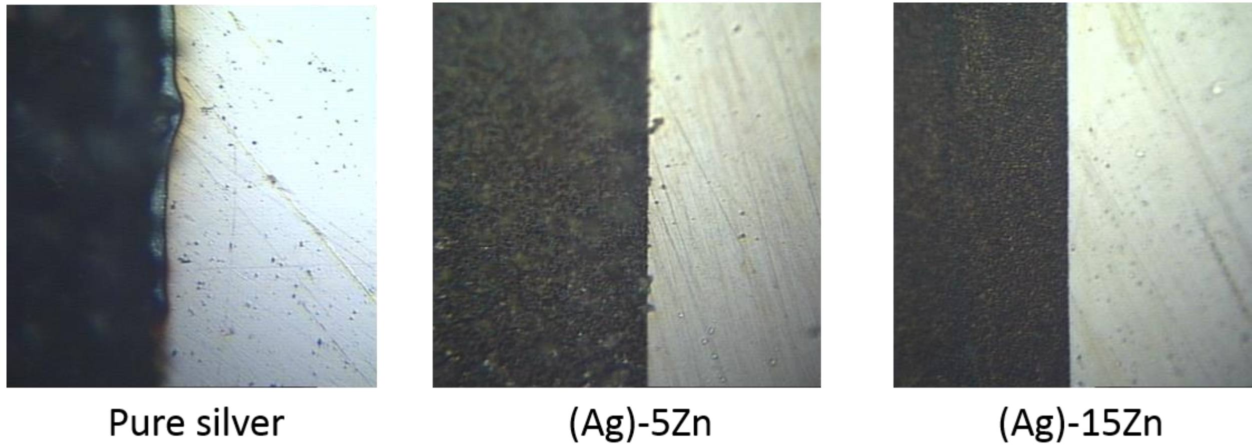

Fig. 3.14 Optical images of boundaries between protected and unprotected region.

The step height of samples of different compositions after reaction for different durations are listed in Table 3.6. The thickness vs. time is plotted in Fig. 3.15. It can be seen that the sulfurization is a reaction rate controlled process. Since Ag_2S is not dense, sulfur vapor is still capable of penetrating the Ag_2S on the surface easily. Also, the reaction rate is decreased with the increase in Zn concentration. It is surprising that the reaction rates of (Ag)-5Zn and (Ag)-15Zn are only 40% and 15% of that of pure Ag. It is worth mentioning here that our reaction condition is really harsh since there is only limited sulfur gaseous even in the air near a volcano.

Table 3.6 Step height after reaction

Unit: μm	15 min	30 min	45 min	60 min
Pure Ag	0.82	1.33	2.01	2.51
(Ag)-5Zn	0.39	0.52	0.78	1.08
(Ag)-15Zn	0.10	0.22	0.29	0.41

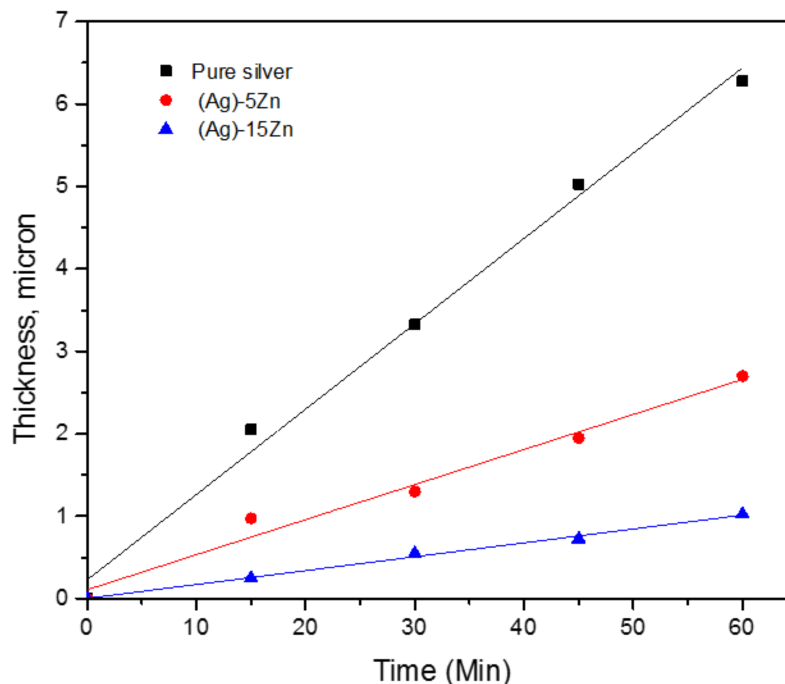

Fig. 3.15 The thickness of Ag_2S as a function of reaction time for tested samples.

The mechanism of increased tarnish resistance has been studied assisted by hard-soft-acid-base (HASB) theory [25]. In HSAB, hard acid tends to react with hard base forming stable resultant and soft acid tends to react with soft base. The reaction between soft acid (base) and hard base (acid) is slow and the resultant is not stable. For example, Ag^+ is soft base and O^{2-} is hard acid. As a result, Ag doesn't get oxidized easily and the stability of Ag_2O is poor (decompose at 180 °C). However, S^{2-} is soft acid and thus Ag get sulfurized easily and Ag_2S is stable. To illustrate the interaction, the concept of highest occupied molecular orbital (HOMO) and lowest unoccupied molecular orbital (LUMO) shall be introduced. The soft acid-soft base reaction is through transferring electrons from HOMO of the base to LUMO of acid to form covalent bonds. However, with the increase in dopant concentration in Ag, the valence band shifts towards higher binding energy. As a

result, transferring electrons at HOMO of Ag to LUMO of sulfur needs more activation energy, leading to the reduction in the reaction rate. As it was mentioned, the sulfurization is reaction rate controlled process, this mechanism is further confirmed.

3.6 Conclusions

The ingots of silver solid solution phase with zinc have been successfully prepared at two compositions. A preliminary evaluation of mechanical property has been conducted by tensile test. Solid solution strengthening phenomenon is observed in (Ag)-5Zn while solid solution softening occurs in (Ag)-15Zn. The tensile test results also indicate that the addition of certain amount of zinc into silver will not only largely increase the ductility but also the strength. Therefore, the silver solid solution phase with zinc is a promising candidate for bonding wire and interconnect medium in microelectronics industry. On the other hand, the tarnish resistance of Ag-xZn is evaluated by sulfurization test. According to the results, the tarnish resistance is large enhanced with the increase of Zn concentration. The mechanism is studied through HSAB theory and could serve as a guideline for other systems.

The silver solid solution phase with zinc is not only a promising candidate for bonding wire and interconnect medium in microelectronics industry but also promising in reflective films used in photonics and telescopes. Future efforts will be made to investigate the other properties of silver solid solution with zinc such as electrical conductivity and reflectivity.

3.7 Reference

[1] C. Lu, Review on silver wire bonding, Microsystems, Packaging, Assembly and Circuits Technology Conf.(IMPACT), 2013, pp. 226-229.

[2] T.-H. Chuang, C.-H. Tsai, H.-C. Wang, C.-C. Chang, C.-H. Chuang, J.-D. Lee, H.-H. Tsai, Effects of annealing twins on the grain growth and mechanical properties of Ag-8Au-3Pd bonding wires, J Electron Mater 41(11) (2012) 3215-3222.

[3] T.-H. Chuang, H.-J. Lin, C.-H. Chuang, Y.-Y. Shiue, F.-S. Shieu, Y.-L. Huang, P.-C. Hsu, J.-D. Lee, H.-H. Tsai, Thermal stability of grain structure and material properties in an annealing twinned Ag–4Pd alloy wire, J Alloy Compd 615 (2014) 891-898.

[4] L.J. Kai, L.Y. Hung, L.W. Wu, M.Y. Chiang, D.S. Jiang, C. Huang, Y.P. Wang, Silver alloy wire bonding, Electronic Components and Technology Conference (ECTC), 2012 IEEE 62nd, IEEE, 2012, pp. 1163-1168.

[5] B. Predel, Ag-Zn (Silver-Zinc), Ac-Au–Au-Zr, Springer1991, pp. 1-9.

[6] W.B. Pearson, A handbook of lattice spacings and structures of metals and alloys: International series of monographs on metal physics and physical metallurgy, Elsevier2013.

[7] Y. Huo, C.C. Lee, The growth and stress vs. strain characterization of the silver solid solution phase with indium, J Alloy Compd 661 (2016) 372-379.

[8] C. Hillman, J. Arnold, S. Binfield, J. Seppi, Silver and sulfur: case studies, physics and possible solutions, SMTA Inter., October (2007).

[9] D. Minzari, M.S. Jellesen, P. Møller, R. Ambat, Morphological study of silver corrosion in highly aggressive sulfur environments, Eng Fail Anal 18(8) (2011) 2126-2136.

[10] J. Fisher, On the strength of solid solution alloys, Acta Metall 2(1) (1954) 9-10.

[11] V. Gerold, H. Karnthaler, On the origin of planar slip in fcc alloys, Acta Metall 37(8) (1989) 2177-2183.

[12] T. Steffens, C. Schwink, A. Korner, H. Karnthaler, Transmission electron microscopy study of the stacking-fault energy and dislocation structure in CuMn alloys, Philos Mag A 56(2) (1987) 161-173.

[13] N. Clement, D. Caillard, J. Martin, Heterogeneous deformation of concentrated Ni� Cr FCC alloys: Macroscopic and microscopic behaviour, Acta Metall 32(6) (1984) 961-975.

[14] R. Fleischer, Substitutional solution hardening, Acta Metall 11(3) (1963) 203-209.

[15] R. Labusch, A statistical theory of solid solution hardening, Phys Status Solidi B 41(2) (1970) 659-669.

[16] A. Sato, M. Meshii, Solid solution softening and solid solution hardening, Acta Metall 21(6) (1973) 753-768.

[17] D. Quesnel, A. Sato, M. Meshii, Solution softening and hardening in the Iron-Carbon system, Mater Sci Eng 18(2) (1975) 199-208.

[18] N. Medvedeva, Y.N. Gornostyrev, A. Freeman, Solid solution softening in bcc Mo alloys: Effect of transition-metal additions on dislocation structure and mobility, Phys Rev B 72(13) (2005) 134107.

[19] A. Blake, C. Cáceres, Solid-solution hardening and softening in Mg–Zn alloys, Mater Sci Eng A 483 (2008) 161-163.

[20] H. Suga, T. Imura, Solid solution hardening of silver single crystals by indium, by tin and by antimony, Jpn J Appl Phys 14(8) (1975) 1253.

[21] J. Bailey, P. Hirsch, The dislocation distribution, flow stress, and stored energy in cold-worked polycrystalline silver, Philos Mag 5(53) (1960) 485-497.

[22] G.E. Dieter, D.J. Bacon, Mechanical metallurgy, McGraw-hill New York1986.

[23] E. Orowan, Fracture and strength of solids, Rep Prog Phys 12(1) (1949) 185.

[24] B. Meyer, Elemental sulfur, Chem Rev 76(3) (1976) 367-388.

[25] Y. Huo, J. Wu, C.C. Lee, Study of Anti-Tarnishing Mechanism in Ag-In Binary System by Using Semi-Quantum-Mechanical Approach, J Electrochem Soc 164(7) (2017) C418-C427.

Chapter 4. Complete elimination of Ag3Al in Ag wire bonds onto Al pad through alloying In into Ag

4.1 Reliability issue of Ag wire bonding on Al pad

Recently, Ag and its alloys have been introduced as wire materials. The Ag wire market is in continuing growth due to the moderate hardness, oxidation resistance, high ductility, and electrical conductivity of these materials. To further increase the strength and corrosion resistance of the wire, several alloying recipes (i.e. Ag-Pd, Ag-Au-Pd) have been demonstrated and the corresponding reliability tests have been conducted [1-6]. The most commonly used pad material is Al and the IMCs formed between Ag and Al during the reliability tests are identified as Ag_2Al and Ag_3Al [1, 7]. A recent study showed that the failure of Ag/Al bonding joints during highly accelerated stressing test (HAST) is due to the cracking in Ag_3Al layers induced by chemical corrosion, which is considered to be related to the moisture and halogen residue in epoxy molding compound (EMC) [6]. Based on these reports, the failure mechanism of Ag/Al wire bonds during HAST test is concluded and schematically shown in Fig. 4.1. During the test, the Ag_3Al will be corroded by the humid and chlorine ions which are the byproduct residue in EMC and micro cracks nucleate and propagate within Ag_3Al. However, this study cannot explain why no cracks can be observed in Ag_2Al layer since Ag_2Al can also be corroded by the same species with a slower rate (about 40% of that of Ag_3Al) [8]. Since the initiation and propagation of cracks are involved, fracture toughness is considered to be another important factor. The facture toughness (K_{IC}) of Ag_2Al and Ag_3Al have been studied though micro-indentation [9] and it shows that K_{IC} of Ag_3Al is 1.31 $MPa \bullet m^{1/2}$, which should be much smaller than that of Ag_2Al since Ag_2Al is so tough that no cracks can be observed during the indentation test when the largest load (1000 g) is applied. Then a coupling effect of chemical reaction and mechanical properties

can be used to explain the failure in Ag_3Al, that is, the corrosion will induce more defects (voids, micro-cracks) in Ag_3Al and the enlargement of these defects are easier due to the low toughness, which in turn facilitate the corrosive species invading deeper. As a result, the initiation and propagation of micro-cracks will be largely accelerated. Therefore, the suppression or even elimination of the growth of Ag_3Al becomes the key point to further improve the reliability of Ag wire bonding.

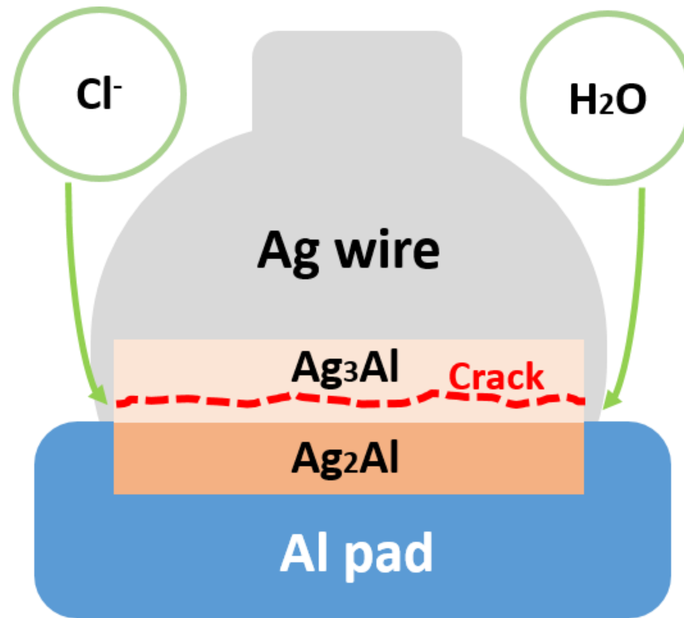

Fig. 4.1 Failure mechanism of traditional Ag-Al bonds during HAST.

4.2 The motivation of alloying In into Ag

Previously, it was demonstrated by our group that the tensile strength and ductility of Ag solid solution phase with In (designated as (Ag)-xIn, where x is the concentration of In in atomic percent) are much higher than those of pure Ag while still maintaining moderate hardness for bonding [10]. Moreover, the tarnish resistance is largely improved with the increase in In concentration, and corresponding mechanism of this resistance has been studied [11]. Therefore, (Ag)-xIn is considered to be an excellent candidate for the

bonding wire materials, and the study of the intermetallic reaction and phase evolution of Al/(Ag)-xIn system becomes essential and critical.

As a preliminary evaluation of the effects of In on the formation of IMCs, (Ag)-10In foil is bonded to Al plates at 420 °C (shown in Fig. 4.2). The cross section of the joint is studied by optical microscope, SEM/EDX, TEM/EDX and SAED. Pure Ag foil are also used as a control group.

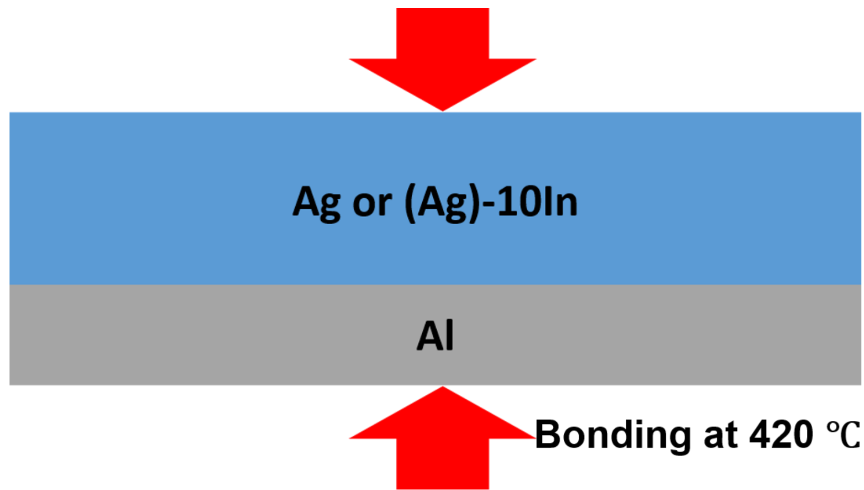

Fig. 4.2 Illustration of pre-bonding structure.

4.2.1 Cross-sectional examination of as-bonded samples

The cross sections are firstly examined by using optical microscope and the images are shown in Fig. 4.3. It can be seen that significant inter-diffusion proceeds during the bonding process and IMCs of a few microns are formed. Through comparing two images, it can be seen that the IMCs growth rate in (Ag)-10In is lower than that in pure Ag.

To examine the fine structure near the interface, SEM/EDX is conducted for both samples and the result is shown in Fig. 4.4 and Table 4.1. According to Fig. 4.4a, there are 3 layers of IMCs between the unreacted Ag and Al. From Table 4.1, we can see that the IMC layer with light grey color (point 2) is Ag_3Al while the IMCs layers which are darker (point

3 and 4) are Ag_2Al. It is worth mentioning that the Ag_2Al is divided by a dark line which is thought to be original interface. Since SEM doesn't has the capability of investigating structure in nanometer range, the black line will be discussed later.

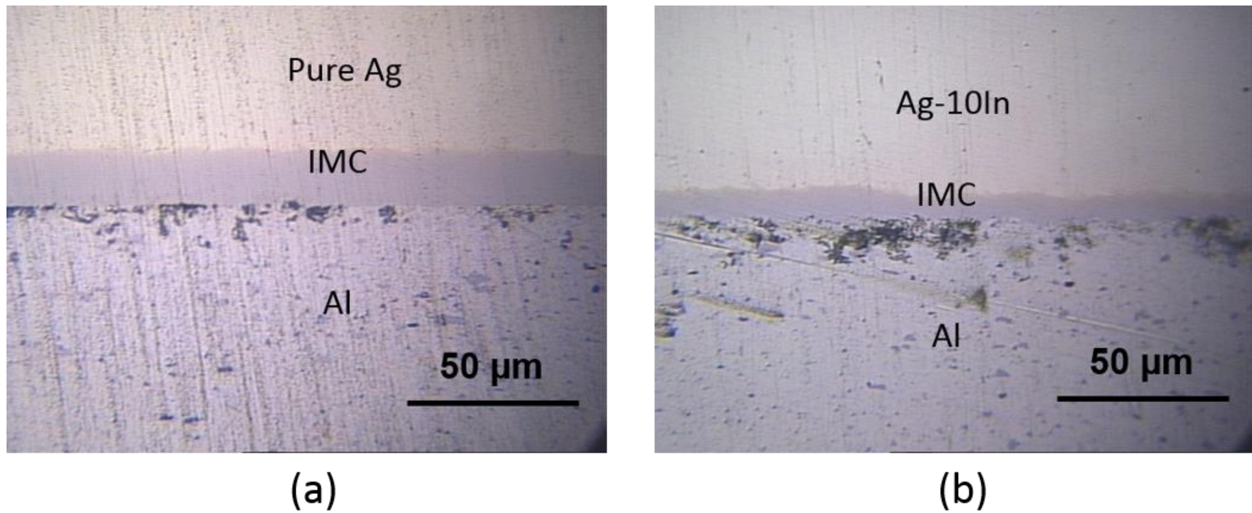

Fig. 4.3 Optical images of as-bonded samples (a) pure Ag/Al; (b) (Ag)-10In/Al.

Table 4.1 EDX results, collection sequence can be found in Fig. 4.4.

	Ag (at.%)	Al (at.%)	In (at.%)
1	99.7	0.3	0
2	74.6	25.4	0
3	66.5	33.5	0
4	66.9	33.1	0
5	0	100	0
6	90.5	0	9.5
7	69.2	15.1	15.7
8	70.0	14.8	15.2
9	71.2	14.5	14.3
10	66.4	33.4	0.2
11	66.2	33.7	0.1
12	0	100	0

The (Ag)-10In sample exhibits a different microstructure based on Fig. 4.4b and Table 4.1. Firstly, a sharp layer can't be found between Ag_2Al and (Ag)-10In, which means that the Ag_3Al layer may vanish in this case. Instead, based on EDX result, the composition of the region between Ag_2Al and (Ag)-10In is quite uniform, which means that there may be a new phase in between. Another thing which is interesting is that the no Indium can be detected in Ag_2Al region although there are 10 at.% indium there before inter-diffusion. Meanwhile, the indium concentration in the intermediate layer between Ag_2Al and (Ag)-10In is around 15% which is higher than that of original region, which indicates that In atoms are repelled out of the region where Ag_2Al occupies. However, due to the damage induced by mechanical polishing and smearing, the boundary is not sharp any more. To avoid these issues, FIB is utilized to cut an atomic-sharp interface to reveal more phase information.

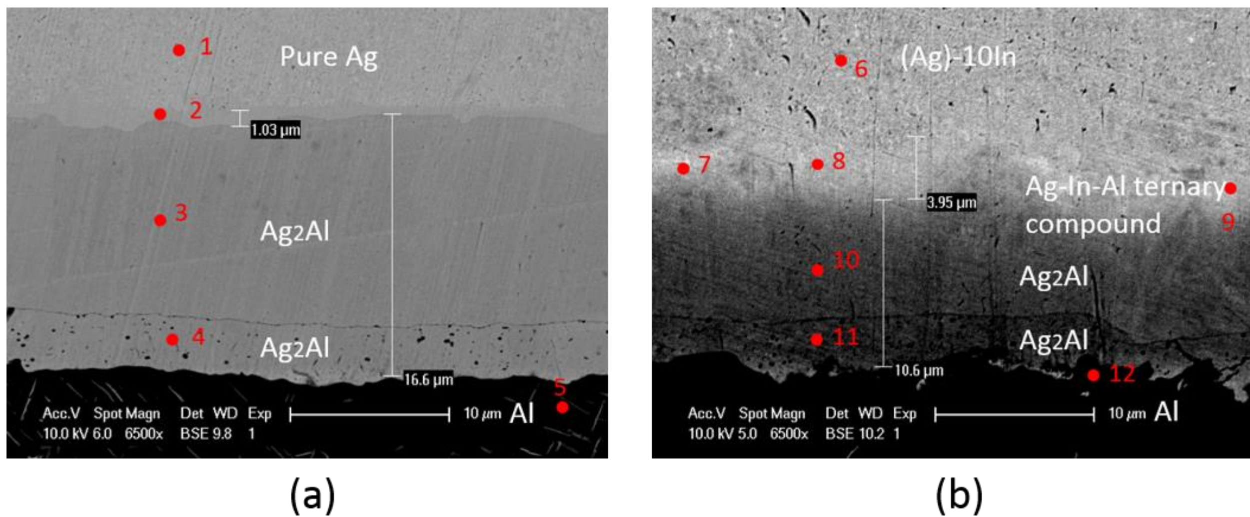

Fig. 4.4 SEM images of as-bonded samples (a) pure Ag/Al; (b) (Ag)-10In/Al.

4.2.2 Cross-sectional images after FIB cutting

The cross-sectional images of (Ag)-10In/Ag sample after FIB cutting are shown in Fig. 4.5. According to Fig. 4.5a, the intermediate phase between Ag_2Al and (Ag)-10In is

sharp. The thickness of this ternary phase is around 3-5 microns. Another information is that the grain size of Ag_2Al is pretty large, which is more than 5 microns. This is due to the high temperature at which the overcool is not high so that nucleation rate is low. The black line is still between two Ag_2Al layers and should be the original interface. The right side Ag_2Al is attributed to the diffusion of Ag into Al and the left side Ag_2Al is due to the diffusion of Al into Ag. It is worth noticing that indium doesn't diffuse into Al.

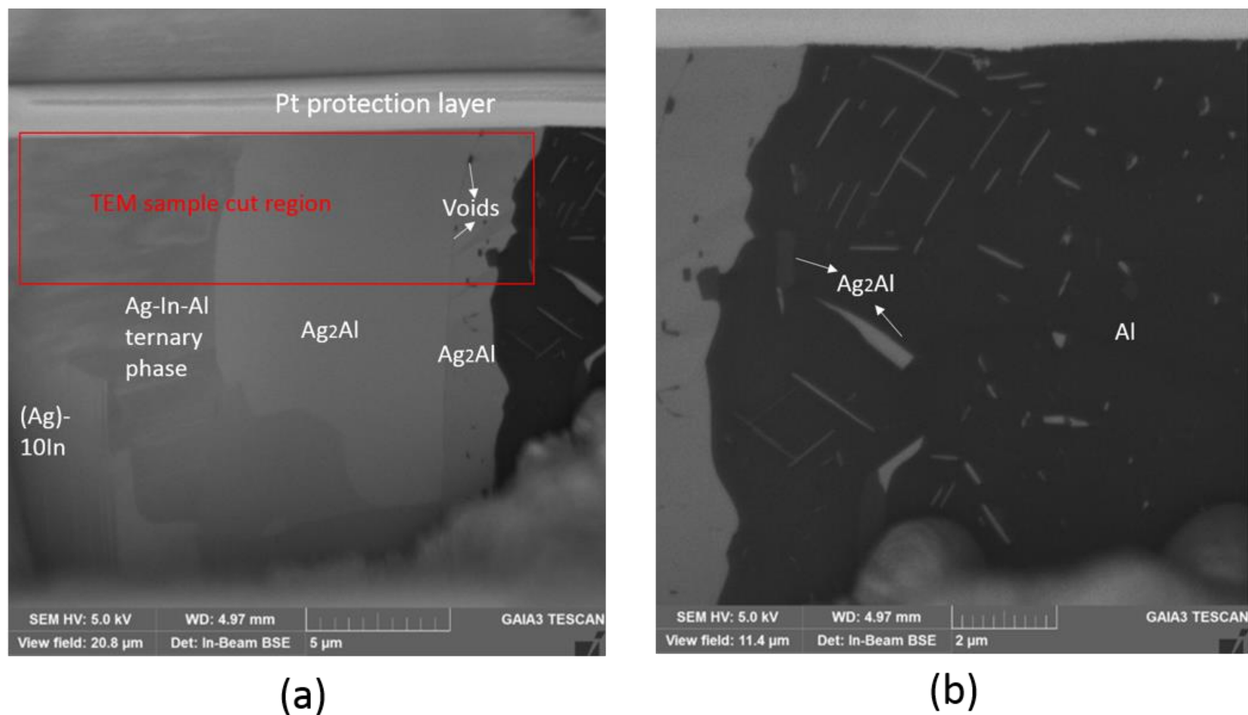

Fig. 4.5 SEM images of cross-sections created by FIB cutting (a) (Ag)-10In side; (b) Al side.

Another thing needs to be paid attention to is that a few voids of tens of nanometers can be found in the right side Ag_2Al while no voids can be found in the right side. In general, the voids that form during inter-diffusion and intermetallic reaction may arise from two reasons. One is that the diffusion rates of Ag into Al and Al into Ag are different, resulting in the vacancy accumulation in one side, which is called Kirkendall voids. Another reason

could be the volumetric changes induced by intermetallic reactions. Here, the intermetallic reaction at both sides is:

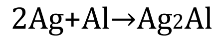

$$2Ag+Al \rightarrow Ag_2Al$$

A simple calculation can be made based on the lattice constants of these three phases and the number of atoms per unit cell, which shows that the volumetric change is -2%. When the IMCs get thicker, voids may occur due to the volume shrinkage. Based on our observation, voids can be found in the right side while no voids can be found in the left side where Ag_2Al is thicker, which means that the volume shrinkage may be compensated by the excessive diffusion of Al into (Ag) side. On the right side, the accumulation of vacancies together with volumetric shrinkage cause the voids formation and expansion.

It can also be observed from Fig. 5b that there are a few second phases are embedded into the Al matrix. These particles are identified as Ag_2Al based on EDX. Since the bonding is performed at 420 °C, the solid solubility of Ag into Al is around 6 at.%. After cooling down to room temperature, the solid solubility is down to less than 1 at.%. Based on phase diagram, the Ag is repelled out of Al lattice through the precipitation of Ag_2Al. So far, the microstructure of (Ag)-10In/Al bonding structure is clear, nanostructure and phase identification and high spatial resolution mapping will be discussed in next section.

4.2.3 TEM analysis of the bonding interface

The TEM sample is cut from the highlighted region in Fig. 4.5a, which include the Ag_2Al, Ag-Al-In ternary phase and (Ag)-10In. Recall that the Ag_2Al is separated by a black line in the SEM images, the detailed information is captured under TEM and shown in Fig. 4.6. It can be easily found that the black line is alumina on the original Al sheet. Although the surface cleaning is preformed, it's still hard to fully remove the oxides. The thickness of

alumina is not uniform. In some region it's too thin to be observed while in some region the thickness can reach around 10 nm.

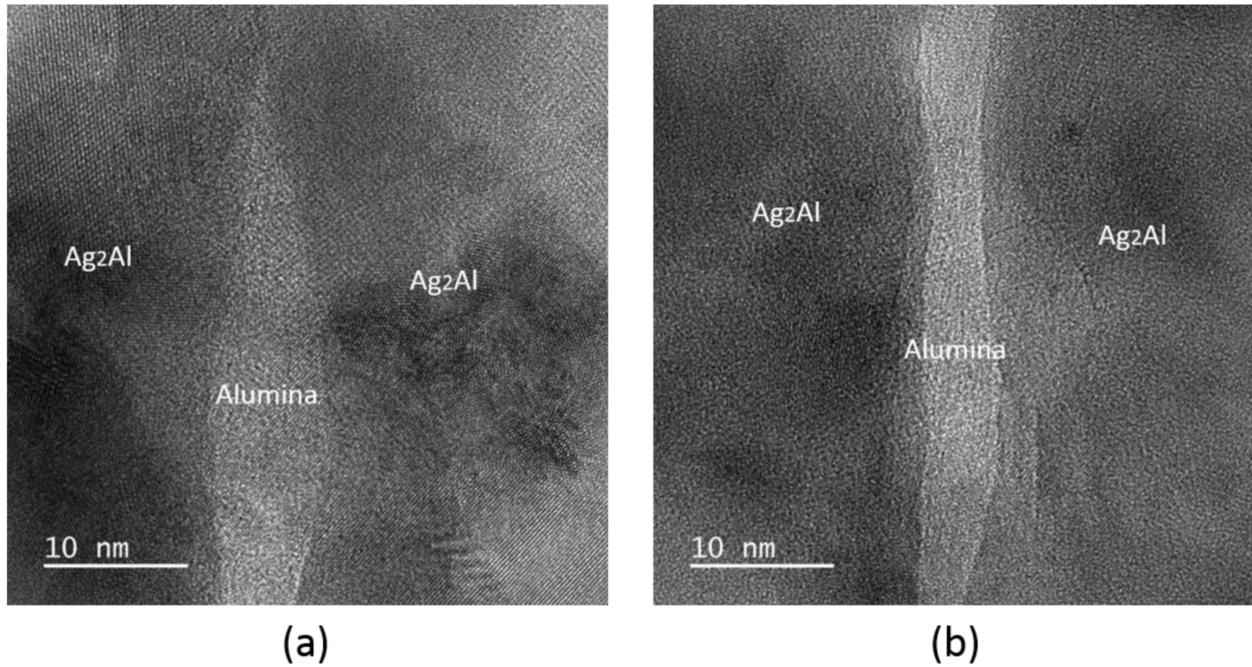

Fig. 4.6 HRTEM images of original bonding interface between (Ag)-10In and Al.

The residue alumina can be detrimental to the strength of the joint. During the real wire bonding process, the alumina will be broken into pieces since the bonding is assisted by the ultrasonic. However, these remnant alumina will retain during usage and may cause reliability issues. Further efforts are still in need to reduce the quantity of alumina in the final joint. To further confirm the crystal structure of the IMC near the original interface, SAED is conducted on the circled grain in Fig. 4.6a and the result is shown in Fig. 4.7. After compared to the standard diffraction pattern, the acquired image is consistent with HCP [01-11] the zone axis pattern, which confirms the formation of Ag_2Al during inter-diffusion.

To examine the crystal structure and chemical composition of Ag-In-Al ternary phase, SAED and STEM-EDX are conducted the results are shown in Fig. 4.8 and Table 4.2.

Firstly, the EDX results are consistent with the SEM/EDX results. There is a ternary phase between Ag_2Al and unreacted (Ag)-10In. The SAED result from this region shows that the crystal structure of this phase is HCP.

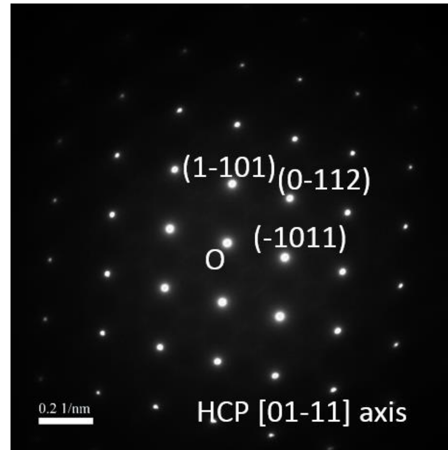

Fig. 4.7 SAED result of IMCs near the original interface

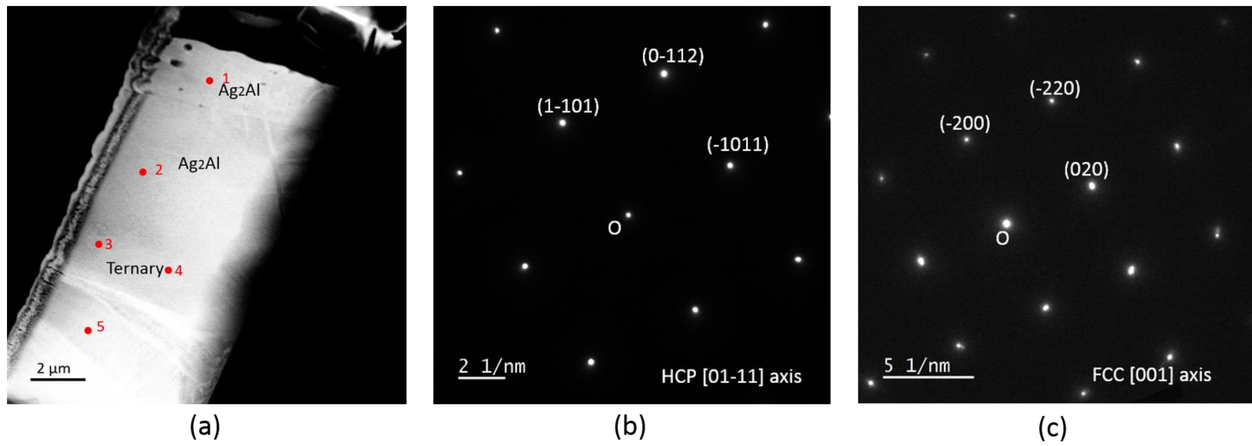

Fig. 4.8 HAADF image and SAED analysis of the joint (a) STEM image of the sample; (b) SAED from point 3; (c) SAED from point 5.

Table 4.2 STEM-EDX results, positions of points are shown in Fig. 10a

	Ag (at.%)	Al (at.%)	In (at.%)
1	42.8	56.9	0.3
2	43.6	56.3	0.1
3	69.8	13.5	16.7
4	71.2	13.6	15.2
5	88.5	1.3	10.2

The lattice constant of the ternary phase can be calculated based on the electron diffraction result, which shows that the lattice constant is almost same to that of Ag_2Al. Recall that the crystal structure of Ag_3Al is quite complex, the properties (hardness, toughness and corrosion resistance) should be similar to those of Ag_2Al.

Based on the STEM and SAED analysis, we can conclude that the existence of In can eliminate the growth of Ag_3Al and an Ag-In-Al ternary phase will form between (Ag)-10In and Ag_2Al, which may largely increase the reliability of the joints.

4.2.4 Drawbacks of the preliminary study

Although the preliminary study shows that the existence of In dopants can suppress the growth of Ag3Al, it cannot solve the following questions:

1. Since the IMCs in the thermal compression joint is already very thick (more than 10 μm), the situation may be different in the real wire bonding joint where the thickness of IMCs is within 1-2 μm. What are the early stages of the evolution of IMCs?
2. What's the evolution sequence of IMCs in Ag-Al joint? This is not conclusive based on previous study since most research are conducted by SEM/EDX which cannot reveal the details (i.e. composition and crystallography) of materials on nano-scale.

3. If Ag_3Al is also suppressed in the early stage, what's the mechanism or the driving force?
4. What's the critical concentration of In above which there is no formation of Ag_3Al?
5. How is the evolution of the defects (i.e. voids)?
6. What's the property of the ternary phase? (hardness, toughness and corrosion resistance)

To reveal those underlying mysteries, new test vehicle with similar dimension of wire bonding joint is needed. In the next few sections, the new tested structures will be firstly illustrated. The intermetallic reaction between (Ag)-xIn and Al and accompanying defects evolution are studied through HRTEM ,high angle annulus dark field (HAADF) imaging and energy dispersive spectroscopy (EDX) after high temperature storage (HTS) test. These high spatial resolution characterization techniques provide analytical results on the nano scale about the behavior of In during the formation of Ag_3Al. Based on these findings, a numerical thermodynamic model of the nucleation of Ag_3Al is constructed, and the effects of In on the phase evolution are explained quantitatively. Moreover, kinetics is discussed and the mechanism of formation of voids and alumina are thoroughly investigated. Lastly, the mechanical properties and corrosion resistance of the ternary phase are characterized.

4.3 Test vehicle and results

In the present work, (Ag)-5In and (Ag)-12In are chosen to study since the doping concentration in commercialized Ag alloys ranges from 4 at.% to 12 at.%. To emulate the bonding structure between Ag wire and Al pad, E-beam evaporation is chosen to deposit 1

μm (Ag)-xIn and 400 nm Al on silicon (Si) substrate. Ag and In are deposited simultaneously and 50 nm chromium (Cr) is pre-deposited directly on Si to increase the adhesion between Al and Si. In order to accelerate the interfacial reaction between metals, HTS test is conducted following the JEDEC standard JESD-A103E. Samples are aged at 150 °C, 175 °C and 250 °C for different duration in air.

4.3.1 Morphology of as prepared sample and Ag-Al intermetallics after HTS test

4.3.1.1 Microstructure of as-prepared films

The SEM and TEM images of as-prepared film are shown in Fig. 4.9. (Ag)-xIn grains are in columnar shape and lots of twins and stacking faults can be observed within (Ag)-xIn grains since the stacking fault energy of Ag is low compare to other metals [12]. STEM-EDX are conducted for as-prepared samples and the In concentration in both samples are 5 at. % and 12 at. %, respectively, which indicates that the designated composition are successfully achieved through E-beam deposition.

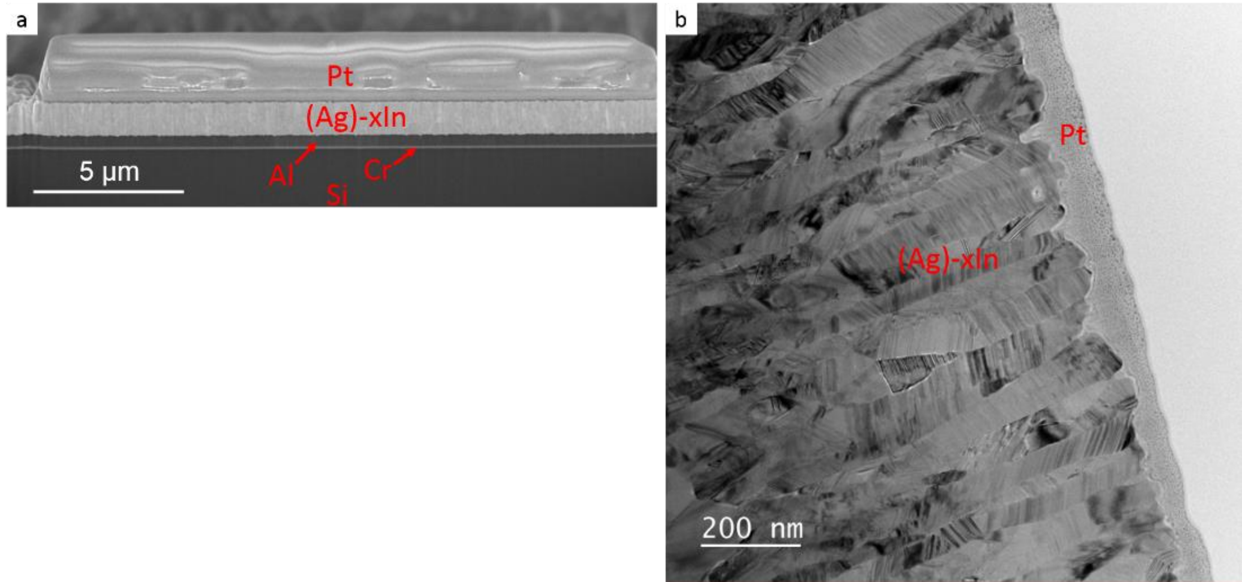

Fig. 4.9 Structure of test vehicle: (a) overview of multi-layer structure; (b) microstructure of a thin (Ag)-xIn cross section layer prepared by FIB. A platinum (Pt) layer was deposited before FIB cutting to get a clean cross-section.

4.3.1.2 Interfacial IMCs evolution of Al/(Ag)-5In samples

During HTS tests, the elevated temperature leads to the acceleration in inter-diffusion and IMC growth since both processes are thermal-activated. For (Ag)-5In sample, after 1000 h aging at 150 °C, small amount of IMCs form in the Al layer while no IMC can be observed in the Ag solid solution layer, which is shown in Fig. 4.10.

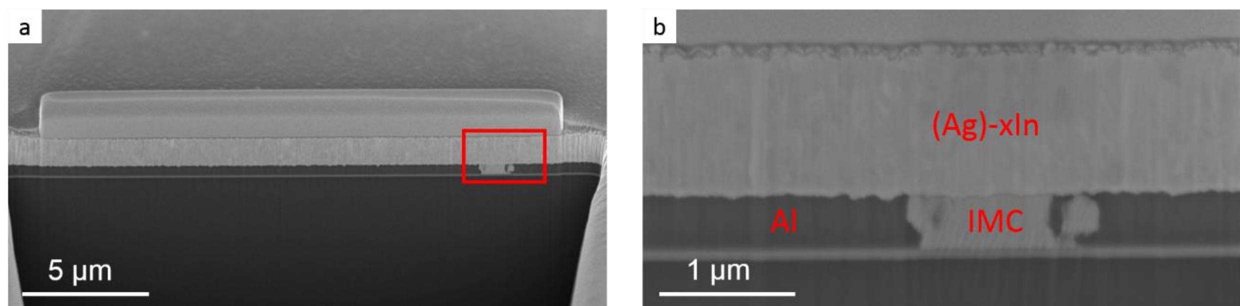

Fig. 4.10 Microstructure of (Ag)-5In after 1000 h aging at 150 °C: a. overview; b. magnified image of an area indicated in a.

When the aging temperature is elevated, the IMC growth rate increases significantly. According to Fig. 4.11, a few isolated IMC islands form in Al layer after 72 h at 175 °C and IMC starts to appear in (Ag)-5In layer after 144 h. The Al layer is completely consumed and turns into IMC phase after 264 h. Moreover, as it can be seen in Fig. 4.11d and d', the original columnar Ag solid solution grains are replaced by two different type of IMC grains.

When the sample is aged at 250 °C, the IMC growth rate is much higher than that at 175 °C. Isolated IMC islands appear after 1 h aging (Fig. 4.12a). Moreover, as it can be seen in Fig 4.12b and b', Al layer is almost depleted after 2 h and two types of IMC grains can be observed within original (Ag)-5In layer.

4.3.1.3 Interfacial IMC evolution of Al/(Ag)-12In samples

Fig. 4.13 shows that the IMC growth rate at 175 °C in Al/(Ag)-12In samples is much lower than that in Al/(Ag)-5In samples. As it can be seen in Fig. 4.13a, only a few isolated islands appear in the Al layer and no IMC grains can be observed in (Ag)-12In after 300 h. As the aging duration increases, IMC grains start to appear in the (Ag)-12In layer. However, the growth behavior is different from that of (Ag)-5In sample where the IMCs are laminar. Fig. 4.13b shows that the growth of IMCs is not uniform at the interface between Ag solid solution phase and Al. Moreover, some IMC grains nucleate in the matrix of (Ag)-12In rather than the interfacial region.

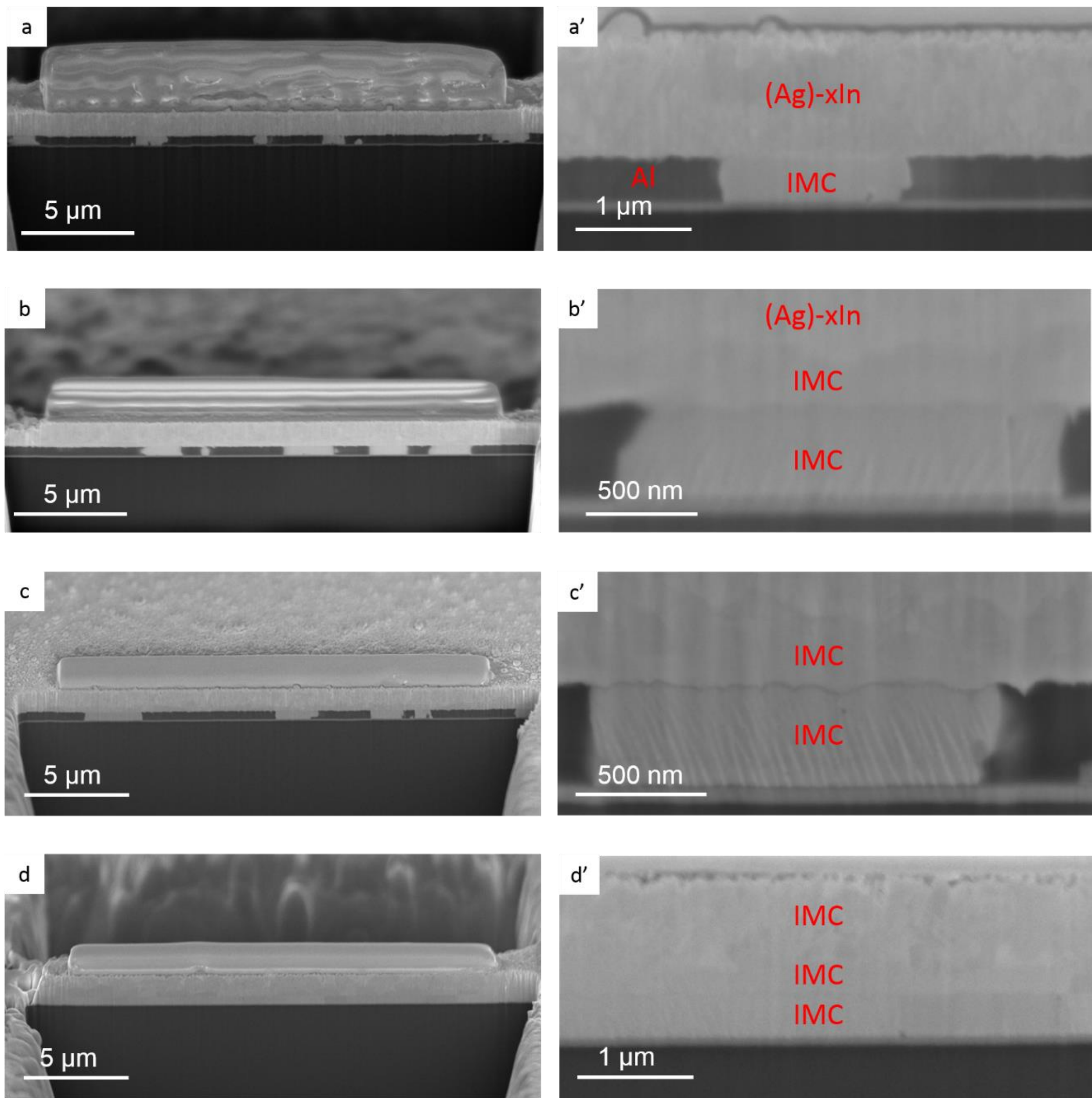

Fig. 4.11 Cross-sectional images of Al/(Ag)-5In sample aging at 175 °C for different durations: 72 h (a and a'); 144 h (b and b'); 192 h (c and c'); 264 h (d and d'). (a', b' c' and d' are magnified images of typical features in a, b, c and d, respectively).

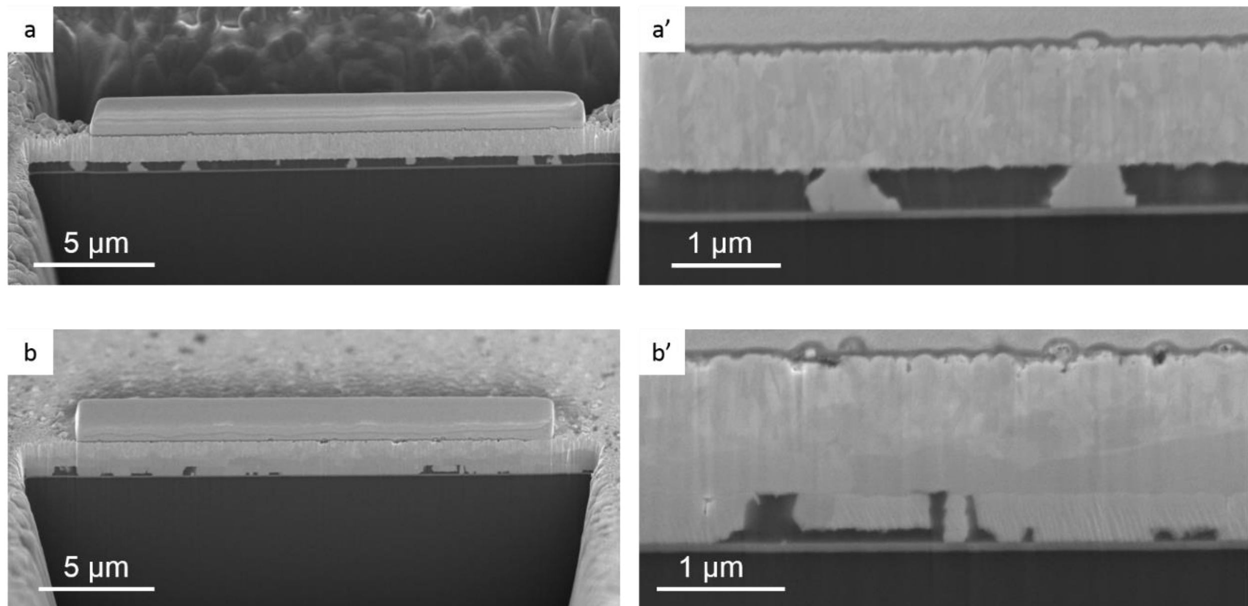

Fig. 4.12 Cross-sectional images of Al/(Ag)-5In sample aging at 250 °C for different durations: 1 h (a and a'); 2 h (b and b').

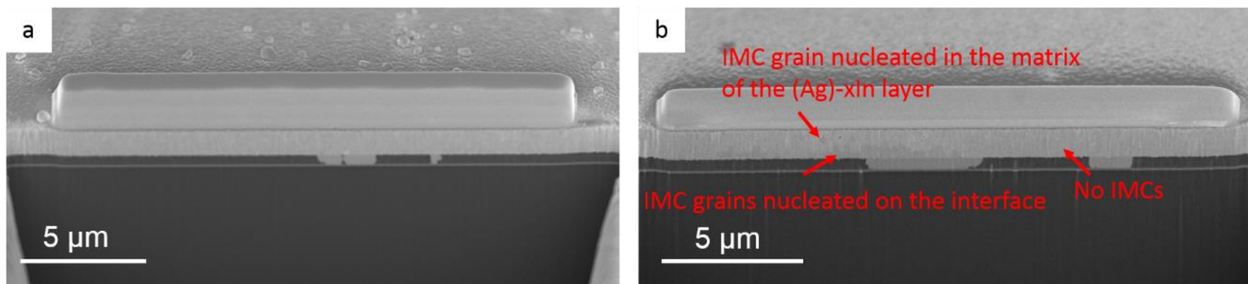

Fig. 4.13 Cross-sectional images of Al/(Ag)-12In sample aging at 175 °C for different durations: (a) 300 h; (b) 500 h.

When the aging temperature is increased to 250 °C, the IMC growth rate is largely enhanced while the growth behavior is also quite different from that of Al/(Ag)-5In samples. According to Fig. 4.14a, a few isolated IMC islands form in Al layer after 2.5 h while original columnar grains are still intact in the (Ag)-12In layer. IMC grains begin to show up in (Ag)-12In layer after 3 h. From Fig. 4.14b'and 4.14c', it seems that the grains randomly nucleate in the (Ag)-12In layer, which is the same as the situation when (Ag)-

12In is aging at 175 °C for 500 h. After 4.5 h, all of the original columnar grains vanish and the whole layer is transformed into IMCs. Meanwhile, it is worth mentioning that Al is still not fully consumed.

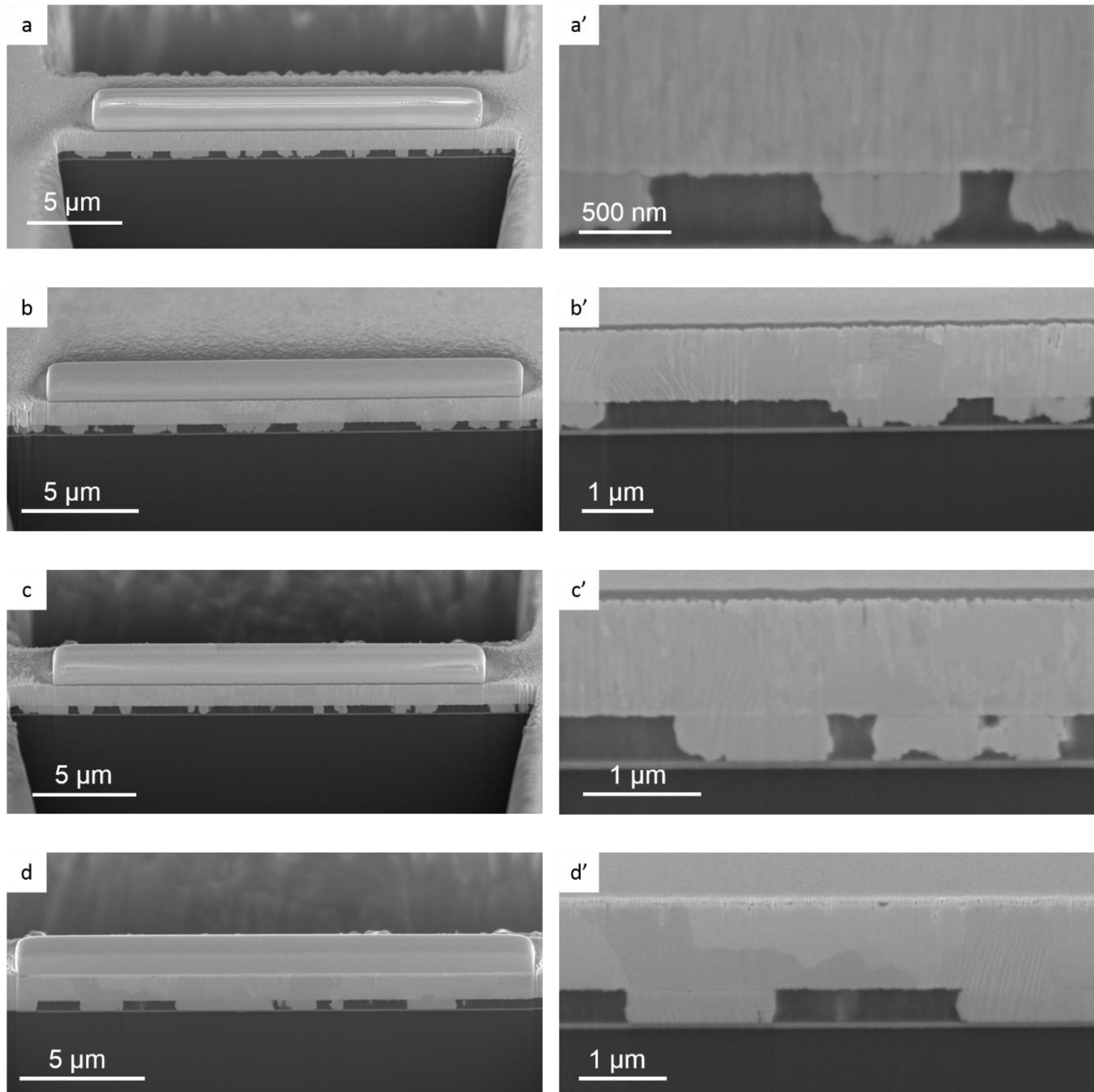

Fig. 4.14 Cross-sectional images of Al/(Ag)-12In sample aging at 250 °C for different duration: 2.5 h (a and a'); 3 h (b and b'); 3.5 h (c and c'); 4.5 h (d and d').

4.3.2 The sequence of intermetallic phase transformations

4.3.2.1 Al/(Ag)-5In samples

When the sample is aged at 175 °C, isolated IMC islands firstly occur in the Al layer. According to Fig 4.15b, these islands are composed of Ag and Al with quite limited indium concentration and only small amount of Al can be detected in (Ag)-5In solid solution layer. The SAED result (Fig. 4.15d) and the lattice image collected from region A-1 in Fig. 4.15a show that the Al-rich region is crystallized and diffraction pattern is consistent with the Ag_2Al (hexagonal closed packing (HCP)) [011] zone axis pattern (ZAP).

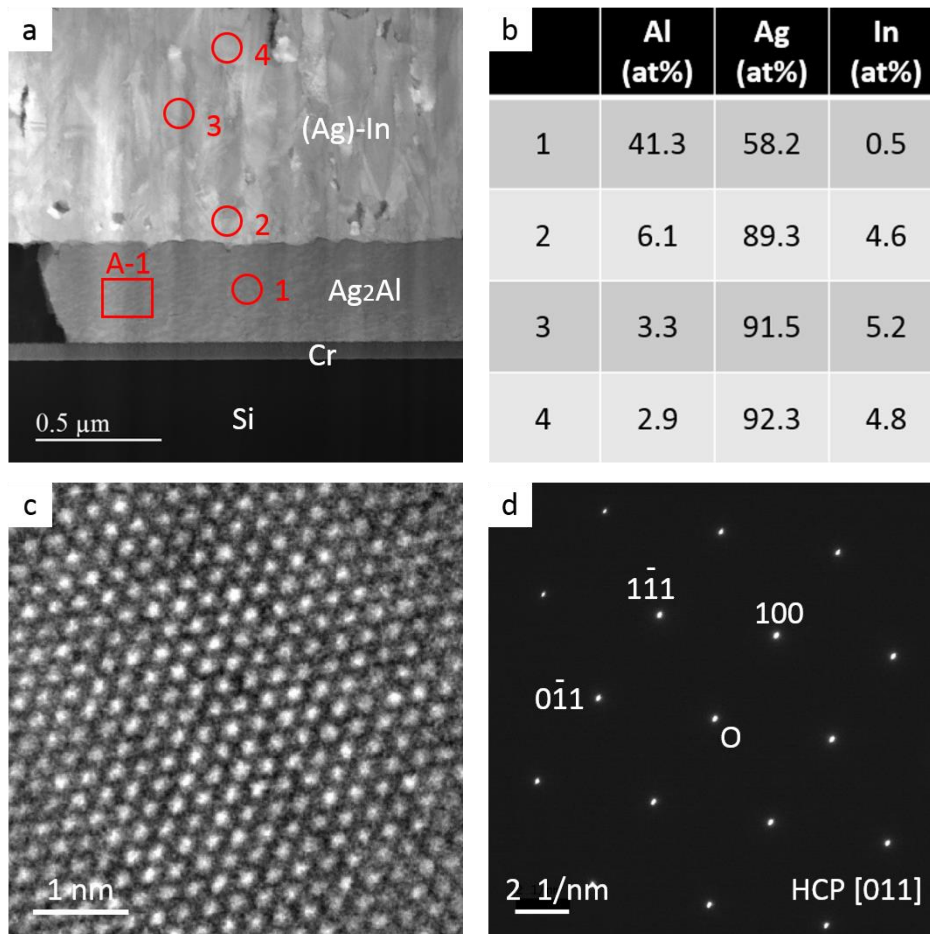

	Al (at%)	Ag (at%)	In (at%)
1	41.3	58.2	0.5
2	6.1	89.3	4.6
3	3.3	91.5	5.2
4	2.9	92.3	4.8

Fig. 4.15 (a) HAADF image of Al/(Ag)-5In interface after 72 h aging at 175 °C; (b) STEM-EDX results collected from circled region in (a); (c) and (d) are lattice imaging and SAED from region A-1 in (a), respectively.

An IMC layer forms within (Ag)-5In layer after 144 h aging at 175 °C (Fig. 4.16a) and it is found to be an Ag-rich phase with limited indium concentration based on EDX result. Lattice imaging (Fig. 4.16c) shows that the d-spacing of crystallographic plane is significantly larger than that of Ag_2Al. SAED is captured from region A-1 in Fig. 4.16a and it is identified as β-Mn structure [111] ZAP, which indicates that the IMC phase is Ag_3Al. A black line can be observed between Ag_3Al and Ag_2Al which is identified as native oxides and will be discussed later.

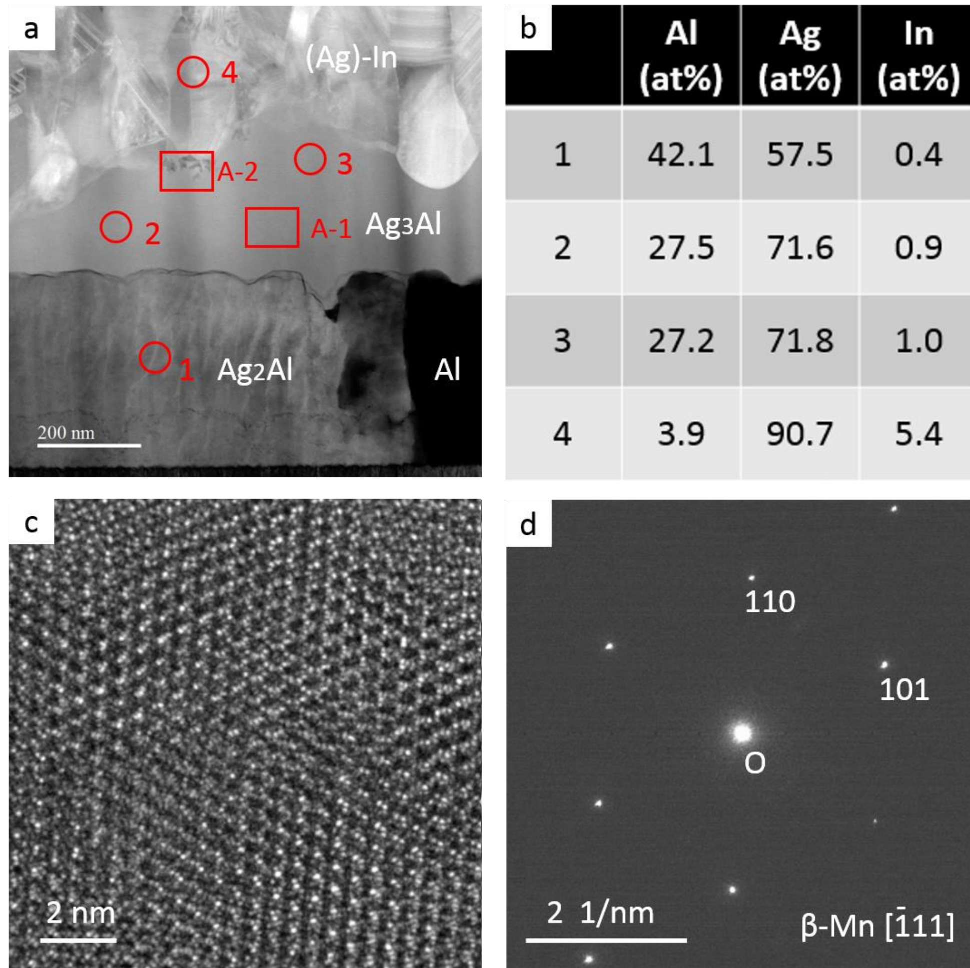

b	Al (at%)	Ag (at%)	In (at%)
1	42.1	57.5	0.4
2	27.5	71.6	0.9
3	27.2	71.8	1.0
4	3.9	90.7	5.4

Fig. 4.16 (a) HAADF image of Al/(Ag)-5In interface after 144 h aging at 175 °C; (b) STEM-EDX results collected from circled region in (a); (c) and (d) are lattice imaging and SAED from region A-1 in (a), respectively.

After 192 h at 175 °C, two types of IMC phases (regions 2 and 3 in Fig. 4.17a are from these two layers, respectively) can be observed in original (Ag)-5In layer and the residue (Ag)-5In grains still appear in columnar shape. EDX result shows that the Al concentration of region 2 is higher than that of region 3 and SAED collected from these two regions show that they crystallize in Ag_2Al and Ag_3Al phases, respectively. It is also worth mentioning that In can hardly be found at all in IMC region whereas the content of In in the unreacted (Ag)-xIn region is higher than the original value.

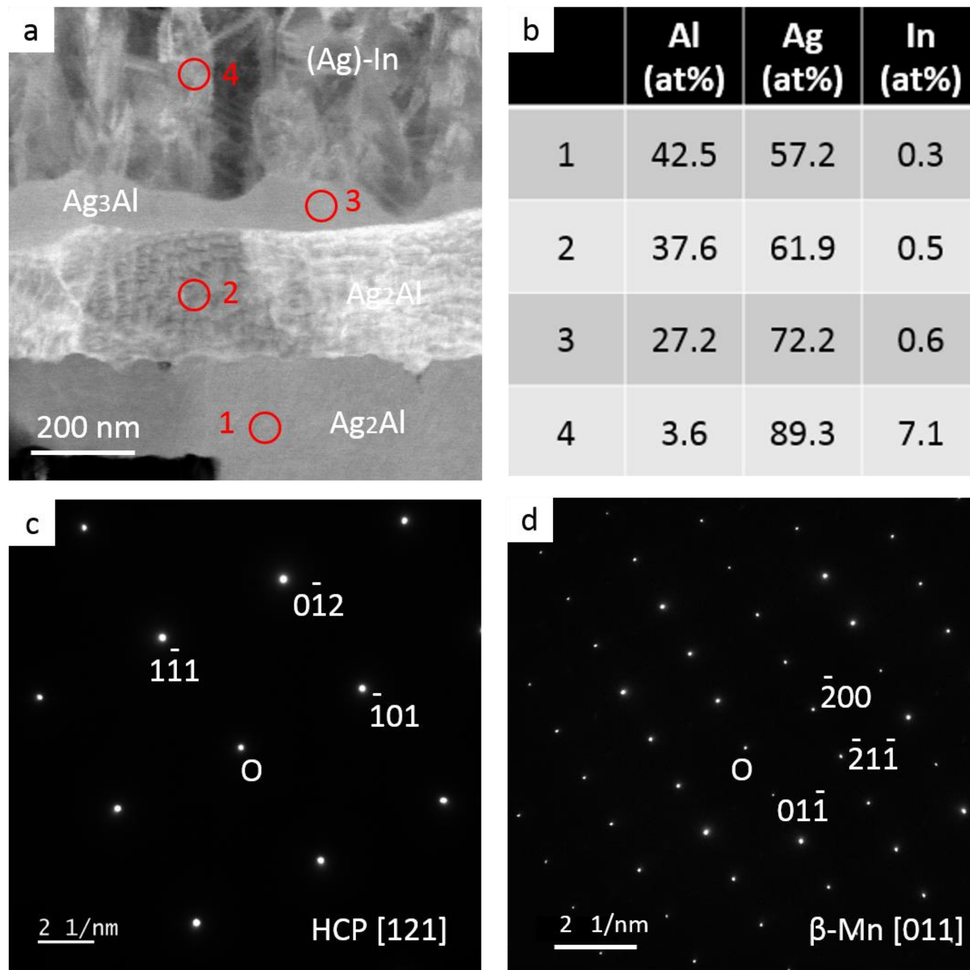

	Al (at%)	Ag (at%)	In (at%)
1	42.5	57.2	0.3
2	37.6	61.9	0.5
3	27.2	72.2	0.6
4	3.6	89.3	7.1

Fig. 4.17 (a) HAADF image of Al/(Ag)-5In interface after 192 h aging at 175 °C; (b) STEM-EDX results collected from circled region in (a); (c) and (d) are SAED collected from region 2 and 3 in (a), respectively.

After 264 h aging at 175 °C, the (Ag)-xIn columnar grains are almost consumed and replaced by two types of IMC grains. In the meantime, the Al layer is depleted and transformed into Ag_2Al phase. Based on EDX result, the grains near the original interface are Ag_2Al and the rest of grains are identified as Ag_3Al by the lattice image and FFT in Fig. 4.18c. In the top region of the sample, a few (Ag)-xIn grains can be detected (region A-1 in Fig. 4.18a). Fig. 4.18d shows the interface between the Ag_3Al and residue (Ag)-xIn phase. No crystallographic orientation relationships can be found between two phases, which may be due to the large difference in crystal structure.

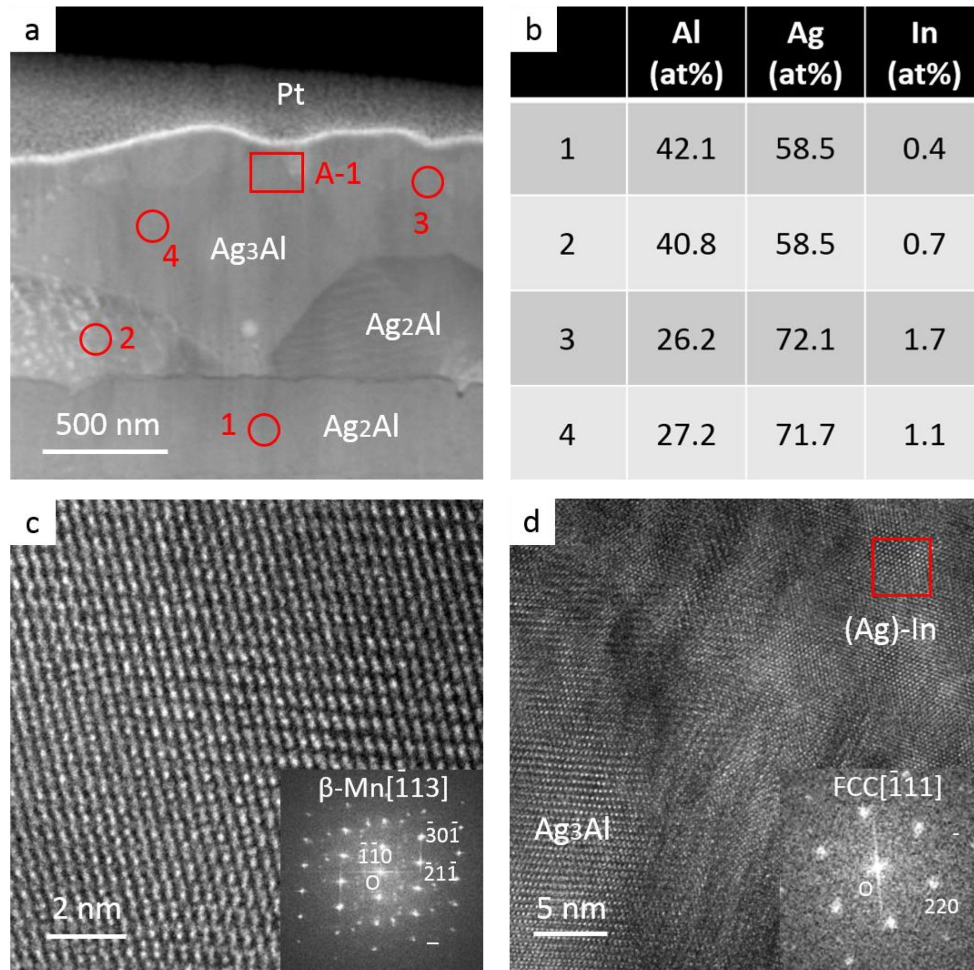

	Al (at%)	Ag (at%)	In (at%)
1	42.1	58.5	0.4
2	40.8	58.5	0.7
3	26.2	72.1	1.7
4	27.2	71.7	1.1

Fig. 4.18 (a) HAADF image of Al/(Ag)-5In interface after 264 h aging at 175 °C; (b) STEM-EDX results collected from circled region in (a); (c) lattice imaging and corresponding FFT

result from region 3 in a; (d) lattice imaging from region A-1, FFT are from marked region in d.

Higher aging temperature leads to higher IMC growth rate. Fig. 4.19a shows that two layers of IMC can be observed in the original (Ag)-5In layer and there are columnar grains left on the top region of the sample (region 3 and 4). Based on EDX result, these two IMCs are identified as Ag_2Al and Ag_3Al, respectively. It is also worth mentioning that the concentration of In in the IMC region is pretty low while the content of In on the remnant (Ag)-xIn layer is much higher than the original value, which is also observed in the sample aged at 175 °C. The uphill diffusion of In along with the growth of IMCs will be discussed later.

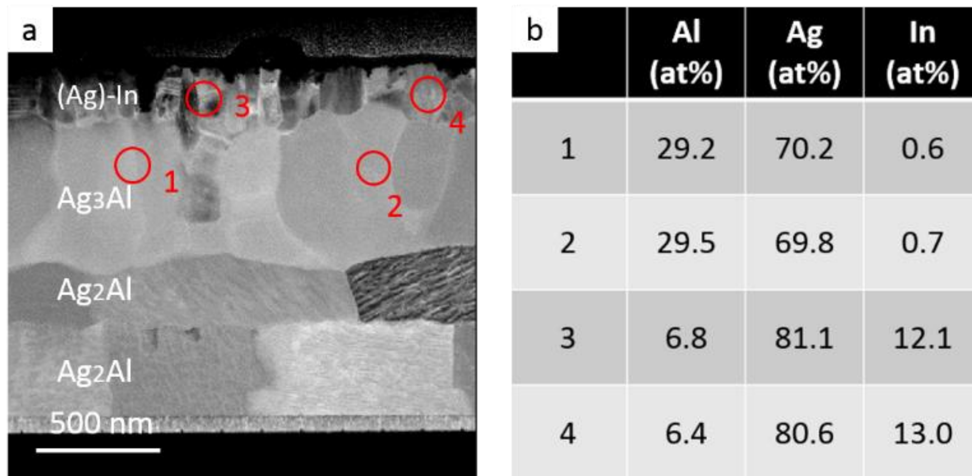

	Al (at%)	Ag (at%)	In (at%)
1	29.2	70.2	0.6
2	29.5	69.8	0.7
3	6.8	81.1	12.1
4	6.4	80.6	13.0

Fig. 4.19 (a) HAADF image of Al/(Ag)-5In interface after 2 h aging at 250 °C; (b) STEM-EDX results collected from circled region in (a).

4.3.2.2 Al/(Ag)-12In samples

Based on the result in section 4.3.1.3, the IMC growth rate in (Ag)-12In sample is low compared to that of (Ag)-5In. Fig. 20a shows that no IMC grains can be observed in (Ag)-xIn region after 2.5 h aging at 250 °C. However, according to the EDX result collected

from the (Ag)-xIn region (Fig. 20b), the concentration of Al is more than 10 at. % near the interface and 8 at.% in the top region, which indicates that the Al atoms diffuse into the solid solution layer during aging but do not segregate near the interface to form IMCs. Fig. 20c shows that the grain right along the interface is still face centered cubic (FCC) structure with same lattice constant of Ag. This is in contrast to the situation in (Ag)-5In where Ag_3Al nucleates after aging and grows in laminar form.

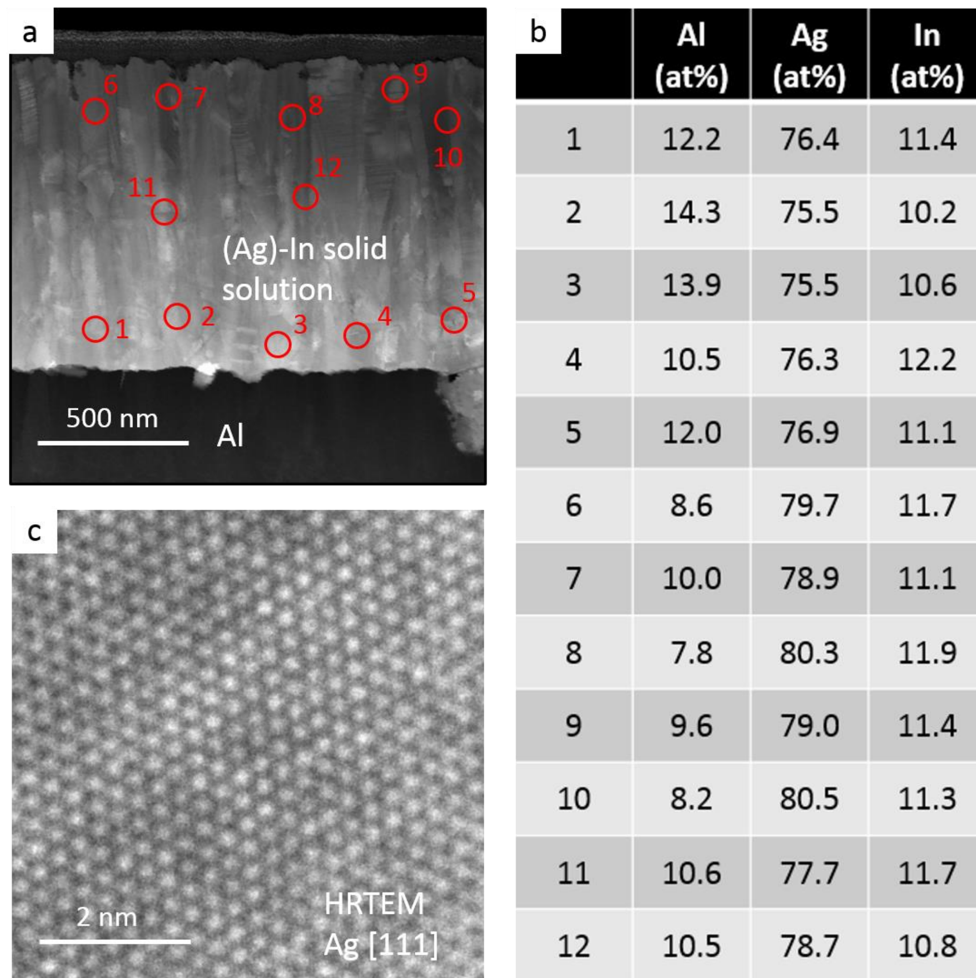

	Al (at%)	Ag (at%)	In (at%)
1	12.2	76.4	11.4
2	14.3	75.5	10.2
3	13.9	75.5	10.6
4	10.5	76.3	12.2
5	12.0	76.9	11.1
6	8.6	79.7	11.7
7	10.0	78.9	11.1
8	7.8	80.3	11.9
9	9.6	79.0	11.4
10	8.2	80.5	11.3
11	10.6	77.7	11.7
12	10.5	78.7	10.8

Fig. 4.20 (a) HAADF image of Al/(Ag)-12In interface after 2.5 h aging at 250 °C; (b) STEM-EDX results collected from circled region in (a); (c) lattice image captured in region 3 in (a).

IMCs start to show up in (Ag)-12In layer after 3 h at 250 °C based on previous SEM images. Fig. 4.21a and d show two typical morphologies in the sample. It can be seen that IMCs not only nucleate near the interface but also in the matrix of the (Ag)-12In solid solution layer. SAED of grains from these two regions show that the IMCs crystallize in HCP structure. Based on the EDX result, the chemical compositions of the solid solution grains and IMCs grains are almost same. The concentration of Al near the interface and in the top region are 15-17 at.% and 11-13 at.%, respectively. The distribution of In is uniform in the whole region which is different from (Ag)-5In sample where the In atoms are repelled out of the IMC grains.

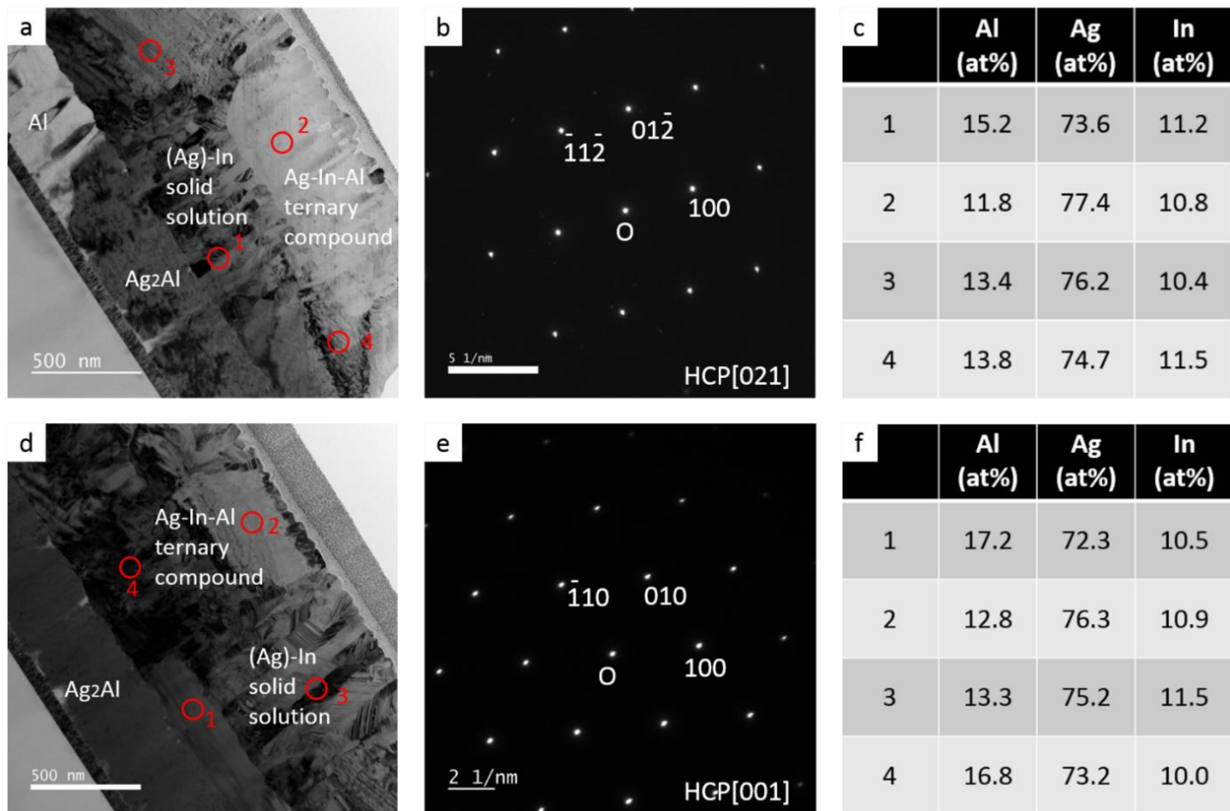

c	Al (at%)	Ag (at%)	In (at%)
1	15.2	73.6	11.2
2	11.8	77.4	10.8
3	13.4	76.2	10.4
4	13.8	74.7	11.5

f	Al (at%)	Ag (at%)	In (at%)
1	17.2	72.3	10.5
2	12.8	76.3	10.9
3	13.3	75.2	11.5
4	16.8	73.2	10.0

Fig. 4.21 (a) and (d) BF images of Al/(Ag)-12In interface after 3 h aging at 250 °C; (b) and (e) SAED captured from region 2 in (a) and region 1 in (d), respectively; (c) and (f) STEM-EDX results collected from circled regions in (a) and (d), respectively.

All the columnar grains vanish and are replaced by IMCs after 4.5 h at 250 °C. Moreover, as it can be seen from Fig. 4.22a that new IMC grains start to show up near the interface. Based on EDX result and SAED from region 1 in Fig. 4.22a, these grains are identified as Ag_2Al and most of the In atoms are repelled out of that region. For grains far from the interface, no further phase transformation occurs and they still crystallize in HCP structure.

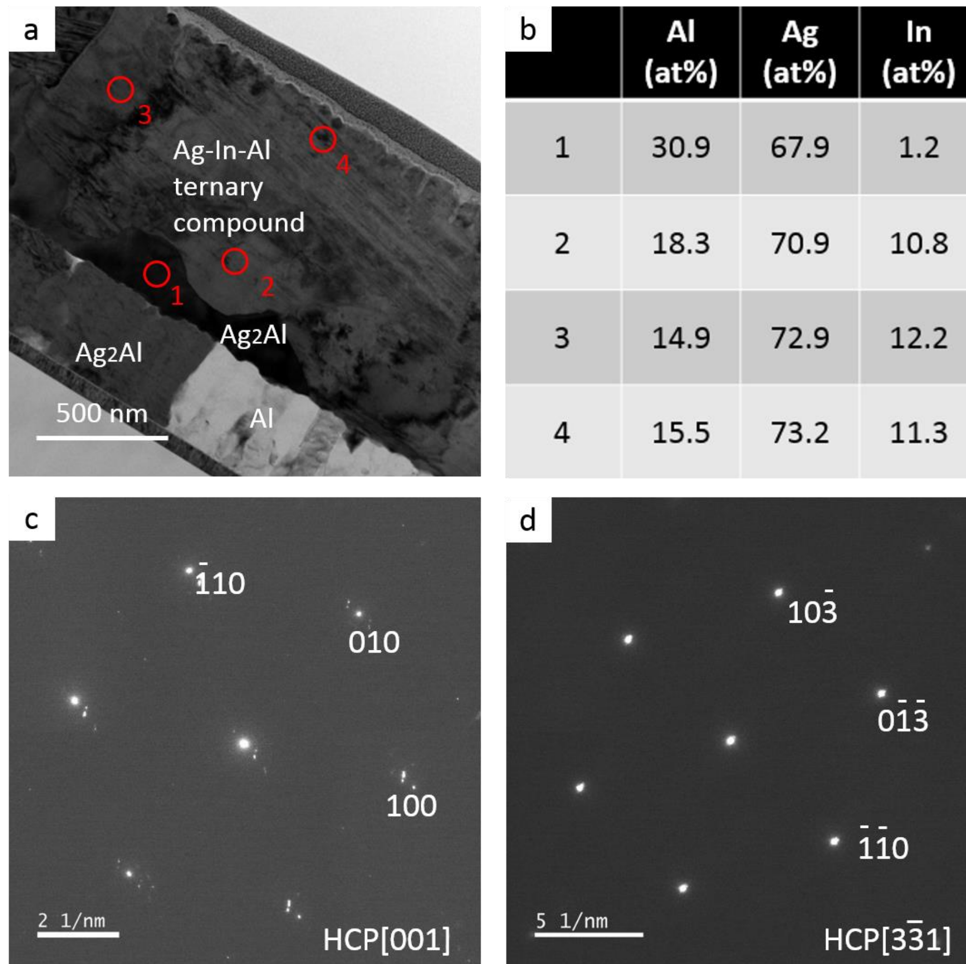

	Al (at%)	Ag (at%)	In (at%)
1	30.9	67.9	1.2
2	18.3	70.9	10.8
3	14.9	72.9	12.2
4	15.5	73.2	11.3

Fig. 4.22 (a) BF image of Al/(Ag)-12In after 4.5 h aging at 250 °C; (b) STEM-EDX results collected from circled region in (a); (c) and (d) are SAED collected from region 1 and 3 in (a), respectively.

4.3.3 Behavior of oxides and voids

4.3.3.1 Oxides and voids in Al/(Ag)-5In

In general, when Al or Al-containing systems is exposed to oxygen, the formation of alumina is inevitable. In our research, the E-beam evaporation is conducted under 10^{-8} torr vacuum to ensure intimate atomic contact between Al and (Ag)-xIn. However, very tiny amount of alumina forms on the top of Al surface and is thickened in the aging process. After 144 h aging at 175 °C, Fig. 4.23a shows that the no continuous oxide can be found and the thickness of alumina is within 1 nm. As the aging time increases, the oxide is thickened. According Fig. 4.23b, the largest thickness of oxides is around 1 nm.

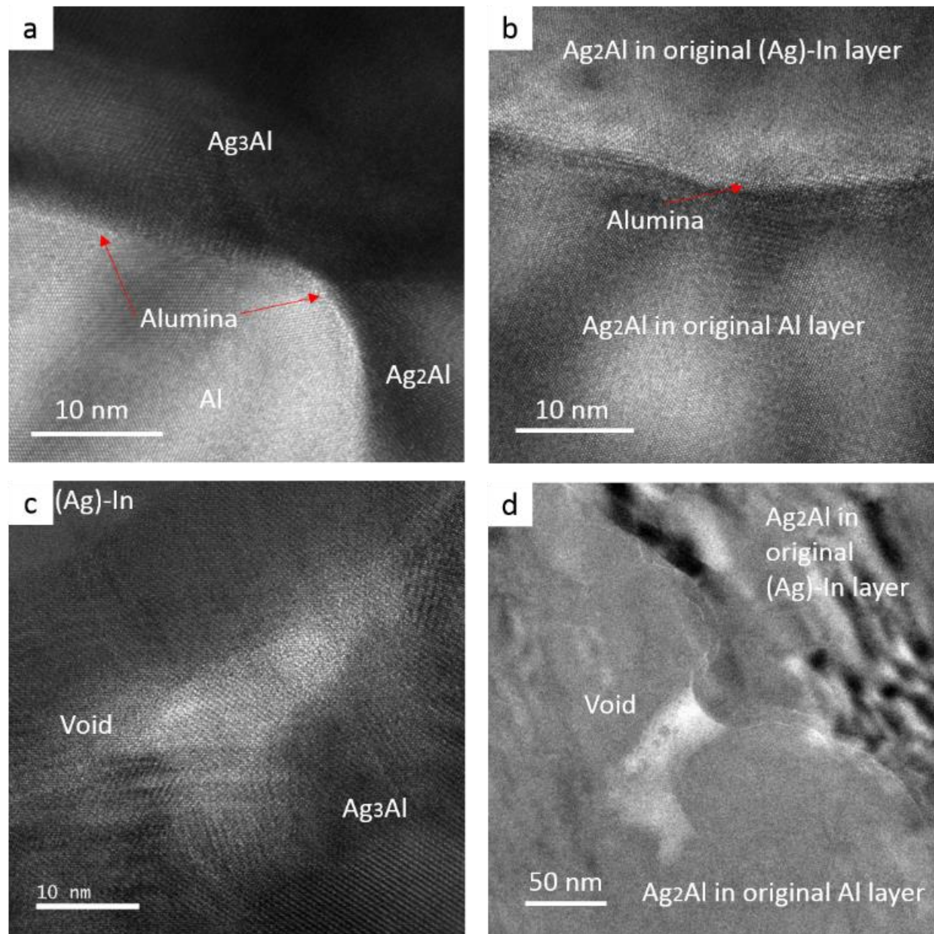

Fig. 4.23 HRTEM images of the original interface of Al/(Ag)-5In samples and void issue after aging at 175 °C: (a) and (c) 144h; (b) and (d) 264 h.

Another thing which accompanies the inter-diffusion and intermetallic reaction is the formation of voids. As it can be seen at region A-2 in Fig. 4.16a, a few voids formed near the boundary between Ag_3Al and unreacted (Ag)-xIn phase. A high resolution image of one of the voids is shown in Fig. 4.23c is and its size lies between 10 - 20 nm. However, as the aging time increases, the voids between Ag_3Al and remnant (Ag)-xIn vanish and voids begin to form near the alumina (Fig. 4.17a and 4.18a). Fig. 4.23d shows that this type void is adjacent to the alumina and its size is more than 50 nm after 264 h at 175 °C.

4.3.3.2 Oxides and voids in Al/(Ag)-12In

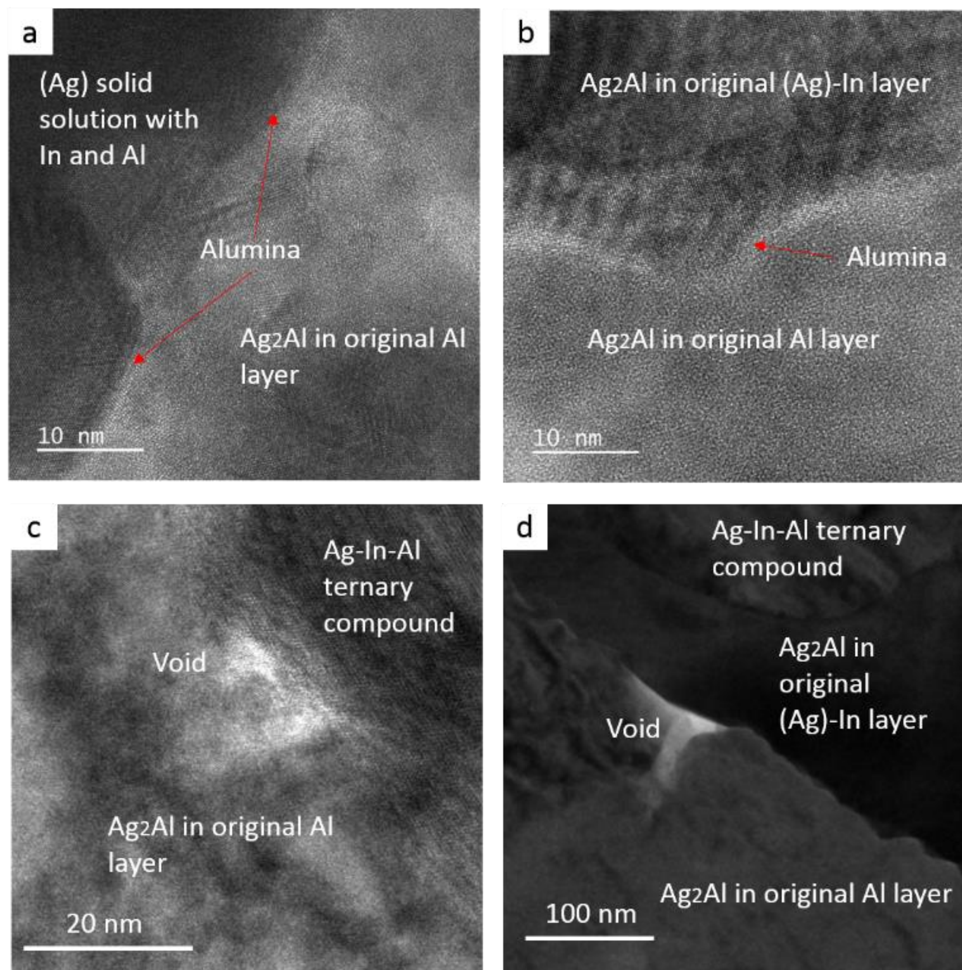

Fig. 4.24 HRTEM images of the interface of Al/(Ag)-12In samples and void issue after aging at 250 °C: (a) 2.5 h; and (c) 3 h; (b) and (d) 4.5 h.

For Al/(Ag)-12In sample, the oxide issue is the same as the situation in Al/(Ag)-5In samples (Fig. 4.24a and b), since the preparation process and aging process are carried out under virtually identical conditions. However, the void issue of (Ag)-12In is different from that of (Ag)-5In in which voids are firstly observed between Ag_3Al and remnant (Ag)-In. No voids can be observed in the original (Ag)-12In layer in the early stage of aging process. Voids start to show up after 3.5 h aging at 250 °C and are located near the alumina (Fig. 16c). After 4.5 h aging at 250 °C, the size of the voids lies between 50 - 100 nm.

4.4 Discussions

4.4.1 Microstructural evolution and phase transformations

The evolution of interfacial microstructures in Al/(Ag)-5In as a function of aging time is schematically presented in Fig. 4.25. Based on previous results, there is a discontinuous layer of alumina at the original interface, which cannot be fully eliminated even though the deposition is performed under high vacuum. During aging, isolated Ag_2Al islands form firstly in the Al region, whereas no IMCs can be observed in (Ag)-5In region. In addition, In can hardly be found at all in Al side, which indicates that In tends not to diffuse into Al. Then, a layer of Ag_3Al forms and thickens in the (Ag)-5In region and the In atoms are mostly repelled out of their original sites and move into the unreacted (Ag)-5In region. A few small voids of 10 nm can be observed near the Ag_3Al/unreacted (Ag)-5In boundary but only in the Ag_3Al side. With the increase in aging time, Ag_2Al which firstly formed in Al region crosses the alumina line and starts to grow and consume Ag_3Al. Voids in the Ag_3Al vanish and new voids start to grow in the original Al side near the alumina. Eventually, the Al is completely transformed into Ag_2Al and the (Ag)-5In is transformed into Ag_2Al and

Ag_3Al. In addition, voids of 50-100 nm can only be observed in the original Al side right near the alumina.

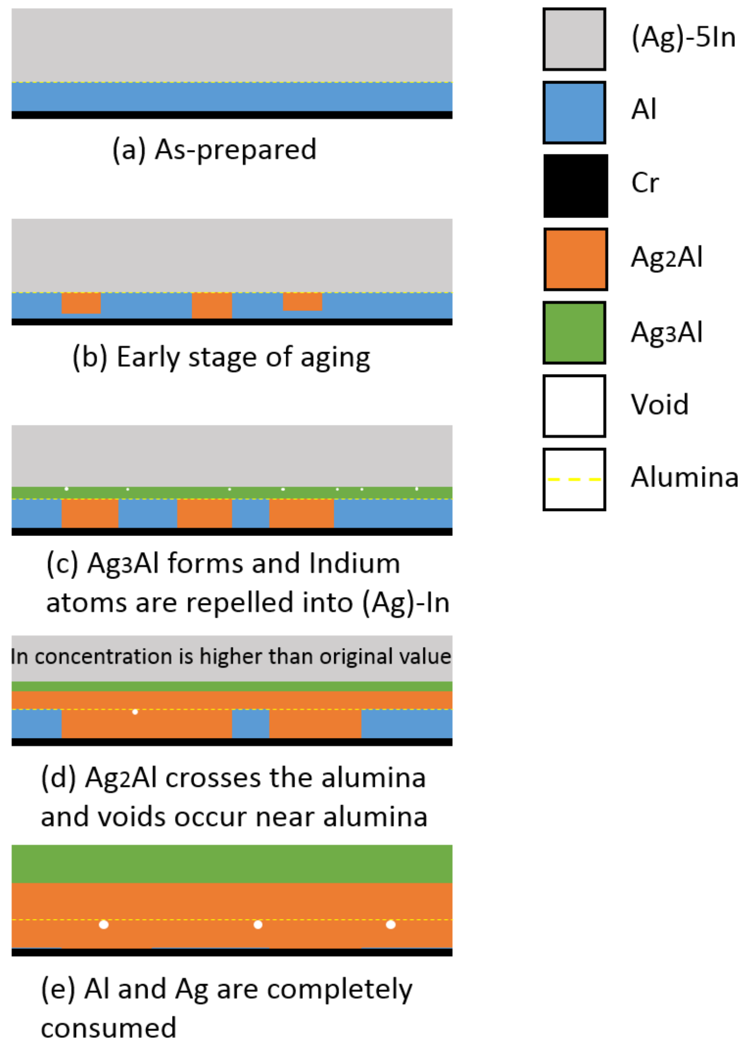

Fig. 4.25 Illustration of phase transformation in Al/(Ag)-5In during thermal aging.

All the crystallographic information of involved phases are listed in Table 4.3 [13, 14] and the Ag-Al phase diagram is shown in Fig. 4.26 [15]. During the early stage of aging, Ag_2Al forms firstly in the Al side since it is aluminum-rich IMC in Ag-Al binary system. The reason for the island growth mode is due to the activation energy of nucleation being much larger than that of further growth, which is also observed in the Cu-Al system [16]. As a

result, more Ag_2Al nucleation sites can be observed when the temperature is elevated from 175 °C to 250 °C. In addition, In atoms do not diffuse into Al layer due to the immiscibility between Al and In. The Ag rich IMC, Ag_3Al, does not occur in the early stage but later forms in the (Ag)-5In. In general, the prerequisite of IMC formation is that the solute concentration near the interface must exceed the solid solubility. According to Fig. 4.26, the solid solubility of Ag in Al is quite limited (1 at. %) while the solid solubility of Al in Ag is around 14 at. % at 175 °C, which can be used to explain the late formation of Ag_3Al. It is noticeable that In atoms are repelled from their original sites and concentrate in the unreacted region as the nucleation and growth of the Ag_3Al, which will be discussed together with the situation of Al/(Ag)-12In.

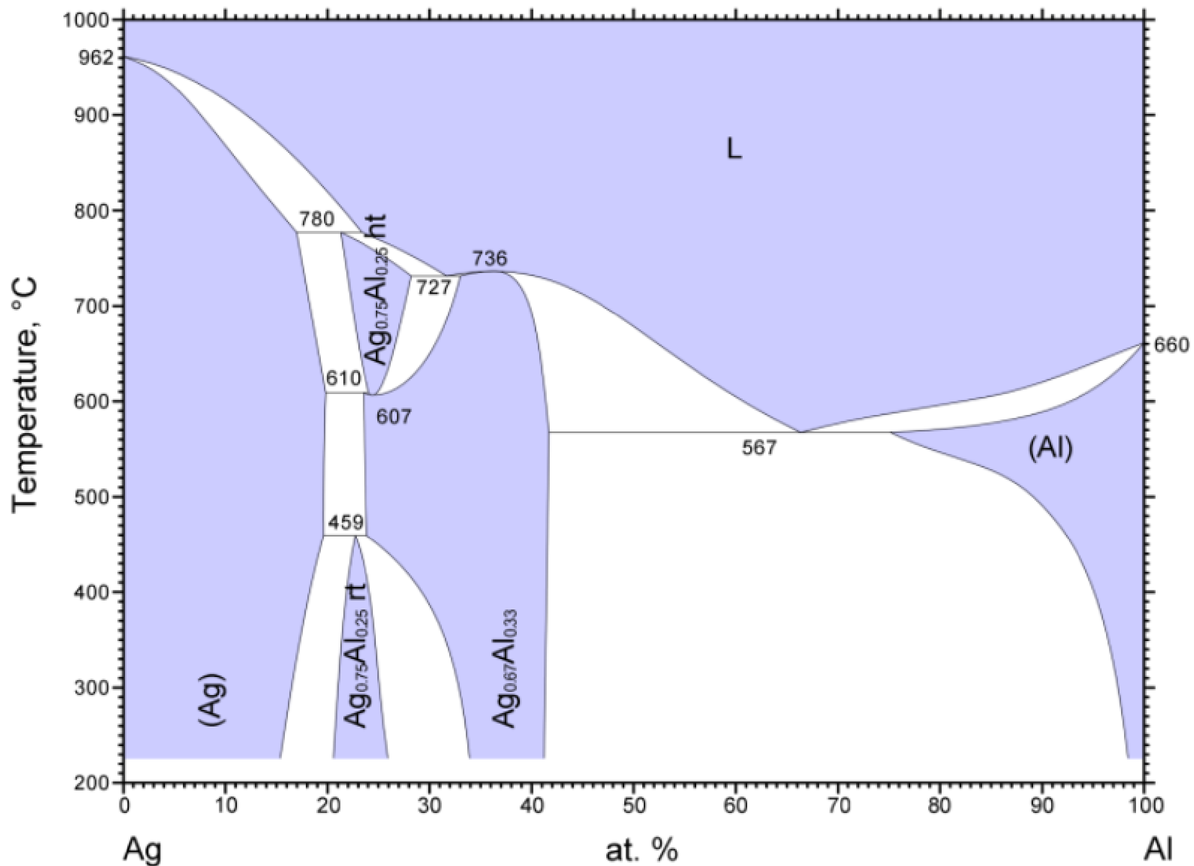

Fig. 4.26 Ag-Al binary phase diagram [18] (Recolored by ASM international).

Table 4.3 Crystallographic information molar volume of phases involved in this paper. The molar volume is calculated by V_C*N_A/Z where V_C is the volume of the unit cell, N_A is the Avogadro constant and Z is the number of formula weights per unit cell.

Phase name	Bravais lattice type	Space group	Atoms per unit cell	Unit cell volume(Å^3)	No. of formula weights per unit cell	Molar volume (10^{-6} m^3)
Ag	FCC	Fm-3m	4	68.217	4	10.27
Al	FCC	Fm-3m	4	66.423	4	10.00
Ag_2Al	HCP	$P6_3/mmc$	6	101.7	2	30.92
Ag_3Al	Cubic	$P4_132$	20	334.544	5	40.28
Ag-In-Al	HCP	$P6_3/mmc$	6		2	

The phase evolution of Al/(Ag)-12In during aging is exhibited in Fig. 4.27. Ag_2Al forms firstly in Al layer and In does not diffuse into Al, which is the same as the situation in Al/(Ag)-5In. However, Ag_3Al does not occur as the aging time increases. Instead, Al atoms continue to diffuse towards the far end and accumulate in the whole (Ag)-12In region without phase transformation. Later when the Al concentration reaches around 15 at. %, Ag-In-Al ternary phase nucleates at random sites and the grains coarsen during the following aging process. Later, Ag_2Al crosses the alumina and starts to grow in the origin

(Ag)-12In side while repelling In atoms into Ag-In-Al ternary phase. In addition, the voids are only visible in the Al side near the alumina during the whole aging process.

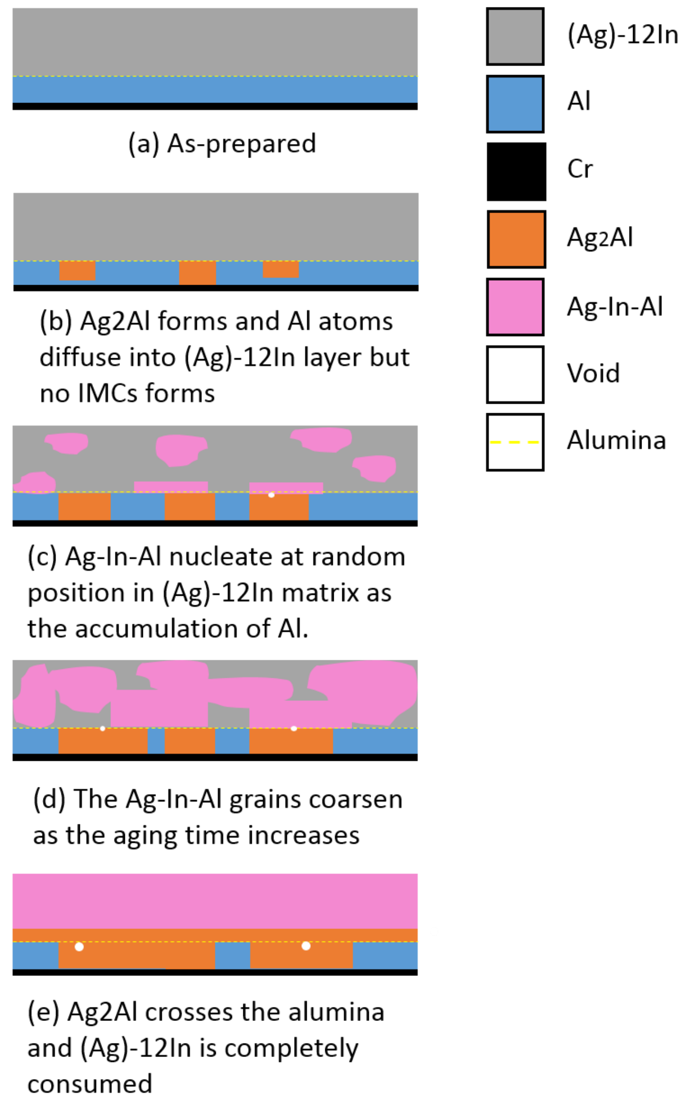

Fig. 4.27 Illustration of phase transformation in Al/(Ag)-12In during thermal aging.

4.4.2 The impacts of In on thermodynamics and kinetics

4.4.2.1 Thermodynamics of nucleation and growth of IMCs

In literatures, Au and Pd are also reported to be added into Ag wires and the intermetallic reactions have been studied [1, 3, 4]. Based on their results, both Pd and Au are still within Ag_2Al and Ag_3Al phases and they occupy the lattice points which are

occupied by either Ag or Al atoms in pure Ag_2Al and Ag_3Al. However, the In atoms behave differently and are repelled from their original sites to the unreacted solid solution phase. The above phenomenon can be described in another way in that Au and Pd can be dissolved in Ag_3Al and Ag_2Al while In atoms cannot be. Based on traditional solid solution theory, the solid solubility may be influenced by a few parameters including atomic size, electronegativity and electron concentration [17]. The atomic radius (metallic) and electronegativity of Al, Pd, Ag, In, Au are listed in Table 4.4 [18, 19].

Table 4.4 Atomic size and electronegativity of selected elements.

Element	Atomic radius (pm)	Electronegativity (Pauling scale)
Al	143	1.61
Pd	137	2.20
Ag	144	1.93
In	167	1.78
Au	144	2.54

Based on Table 4.4, it's surprising that the difference in atomic radius between Al, Ag, Pd and Au is small whereas the size difference between In and Ag is about 16%. In addition, the Ag_3Al crystallizes in β-Mn structure in which the atoms are further compressed compared to the situation in FCC and HCP. Therefore, the existence of In atoms in the lattice may hinder the formation of Ag_3Al and affect its stability, which results in the repelling of the In atoms during the nucleation and growth of Ag_3Al. However, no Ag_3Al

formed when the Indium concentration reaches 12% indicating that the driving force of the formation of Ag_3Al is not capable of repelling the In atoms.

It is therefore very interesting to investigate the thermodynamics during the formation of Ag_3Al in which the In atoms are repelled out. Based on thermodynamics, the Gibbs free energy change during solid-solid phase transformation can be expressed as:

$$\Delta G = \Delta G_V * \Delta V + A * \sigma + E_S * \Delta V \quad (1)$$

where ΔG is the overall Gibbs free energy change, ΔG_V is the difference of the Gibbs free energy (per volume) between the Ag_3Al and (Ag)-25Al, ΔV is the volume of the new phase, A is the area of the interface between new phase and mother phase, σ is the corresponding interfacial energy, and E_S is the strain energy (per volume) induced by the volumetric change during phase transformation. Specifically, E_S is a function of the volumetric change (δV) that can be calculated by,

$$\delta V = \frac{V_m^N - V_m^M}{V_m^M} \quad (2)$$

where V_m^N and V_m^M are the molar volume of the new phase and mother phase, respectively. According to Table 1, the calculated δV is only -1.3%, which indicates that $E_S*\Delta V$ can be ignored in this case.

The interfacial reactions between metals have been studied extensively and various models have been proposed to indicate the reaction products [20-23]. Recently, a new model has been proposed to predict the interfacial reaction products between metals with same lattice structure though thermodynamic modeling [24]. In this model, the authors proposed that an oversaturated solid solution will form near the interface between two metals with same lattice structure and the IMC is assumed to form preferentially from the

matrix of the same composition. The assumption is confirmed to be reasonable after examining a few binary systems such as Al/Cu, Al/Pt and Al/Au and can be used in Ag/Al system. More specifically, a solid solution phase where the ratio of Ag to Al is 3:1 must form firstly so that Ag_3Al can form after. In Al/(Ag)-xIn samples, Al atoms diffuse into Ag matrix and oversaturated (Ag)-Al-In solid solution forms. A model can be proposed, where the prerequisite of the formation of Ag_3Al is that the ratio of Ag to Al must reach 3: 1 and all the In atoms are repelled out. Since the Al concentration is low and the In concentration is relatively uniform in unreacted (Ag)-In region based on EDX results, it is reasonable to assume that the unreacted region is pure (Ag)-In binary solid solution and the repelled In atoms are uniformly distributed in the unreacted region. A term (ΔG_{out}^{In}) associated with the outgoing of In needs to be added into the equation (1). For Al/(Ag)-xIn, to form Ag_3Al of ΔV,

$$\Delta G_{out}^{Indium} = (G_{(Ag)-25Al} - t * G_{(Ag)-\frac{100-x}{3}Al-xIn}) * \Delta V + G_{(Ag)-\left(x+\frac{x*\Delta V}{V-\Delta V}\right)In} * (V - \Delta V) - G_{(Ag)-xIn} * (V - t * \Delta V) \quad (3)$$

Where V is total volume of the (Ag)-xIn, (V—ΔV) is the volume of unreacted (Ag)-In phase and (x+(x*ΔV)/(V-ΔV)) is the corresponding In concentration. $G_{(Ag)-25Al}$ and $G_{(Ag)-(100-x)/3Al-xIn}$ are free energy (per volume) of over saturated Ag solid solution with Al and ternary solid solution phase. t is equal to 1/(1-x/100), which ensures that the amount of Ag and Al atoms are conserved. In Ag solid solution phase, the Gibbs free energy is a differentiable function of In concentration and ΔV is much smaller than V, equation (3) can be further simplified as,

$$\Delta G_{out}^{Indium} = \left[G_{(Ag)-25Al} - t * G_{(Ag)-\frac{100-x}{3}Al-xIn} + \frac{dG_{(Ag)-x'In}}{dx'}\Big|_{x'=x} * x\right] * \Delta V \quad (4)$$

Then, Equation (1) can be rewritten as,

$$\Delta G = \left[G_{(Ag)-25Al} - t * G_{(Ag)-\frac{100-x}{3}Al-xIn} + \frac{dG_{(Ag)-x'In}}{dx'}|_{x'=x} * x + \Delta G_V \right] * \Delta V + A * \sigma \qquad (5)$$

Assume that the new phase is spherical with r in radius, and the critical radius (r^*) can be acquired when $d(\Delta G)/dr$ is zero and expressed as,

$$r^* = -\frac{2\sigma}{G_{(Ag)-25Al} - t * G_{(Ag)-\frac{100-x}{3}Al-xIn} + \frac{dG_{(Ag)-x'In}}{dx'}|_{x'=x} * x + \Delta G_V} \qquad (6)$$

In view of thermodynamics, the nucleation and growth can proceed spontaneously only when the denominator in equation (6) is a negative number. It is worth mentioning that the above Gibbs free energy is measured in volume and corresponding molar free energy can be acquired by dividing the G in (6) by the molar volume of corresponding phases. In this case, the difference of molar volume between (Ag)-xIn, (Ag)-xAl and Ag_3Al is quite small (less than 2%) [25]. Thus, equation (6) can be expressed in molar free energy as,

$$r^* = -\frac{2\sigma V_m^{Ag}}{G_m^{(Ag)-25Al} - t * G_m^{(Ag)-\frac{100-x}{3}Al-xIn} + \frac{dG_m^{(Ag)-x'In}}{dx'}|_{x'=x} * x + \Delta G_m} \qquad (7)$$

The molar free energy of solid solution phase and IMCs can be calculated based on Redlich-Kister model [26, 27], where the molar free energy of ternary system can be expressed as,

$$G_m = \sum_{i=1}^{3} x_i G_i + RT \sum_{i=1}^{3} x_i \ln(x_i) + \sum_{i=1}^{2} \sum_{j=i+1}^{3} x_i x_j \sum_{n=0}^{2} L_{ij}^n (x_1 - x_2)^n + L_{123} x_1 x_2 x_3 \qquad (8)$$

And it can be simplified in binary system, that is,

$$G_m = x_1G_1 + x_2G_2 + RT[x_1\ln(x_1) + x_2\ln(x_2)] + x_1x_2[L_0 + L_1(x_1 - x_2) + L_2(x_1 - x_2)^2] \quad (9)$$

Where x_i is molar free energy of each component, R is gas constant, and T is the temperature measured in Kelvin. G_i, L_i, L_{ij} and L_{123} are temperature-dependent parameters, which are previously measured or optimized and can be found in Ag/In, Ag/Al and In/Al thermodynamic databases [15, 28, 29]. Due to the absence of L_{123} in literature, the last term is ignored which is reasonable since the last term is very small compared to other terms. Some parameters in the denominator of equation (7) are calculated when x is 5 and 12 and listed in Table 4.5. The molar Gibbs free energy of Ag solid solution phase with In is calculated and the plot of (G_m vs. x) and (dG_m/dx vs. x) are shown in Fig. 4.28. 523 K is used as the temperature during the calculation.

Table 4.5 Calculated molar free energy values involved in equation (7).

Notations	Value, (kJ/mol)
$G_m^{(Ag)-25Al}$	-22.8
$G_m^{(Ag)-23.75Al-5In}$	-25.3
$G_m^{(Ag)-22Al-12In}$	-25.1
ΔG_m	-3.5

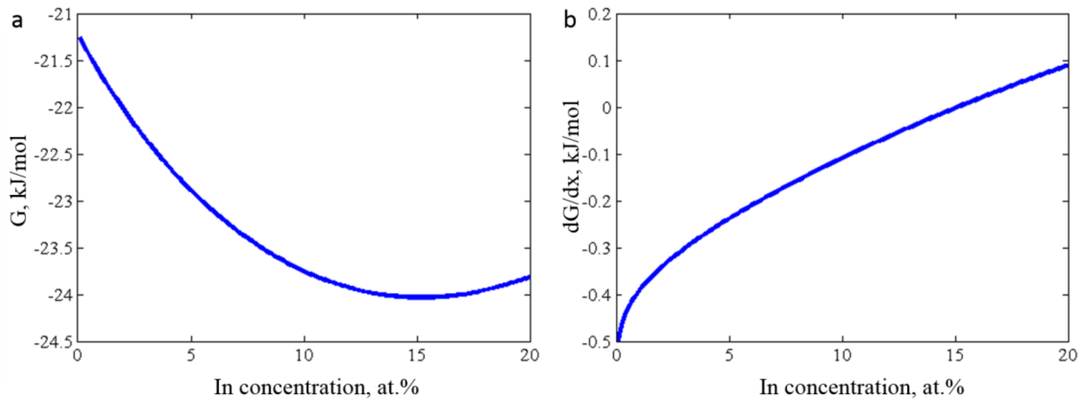

Fig. 4.28 Thermodynamic calculation result: (a) Molar Gibbs free energy (G_m) of (Ag)-xIn vs. In concentration; (b) dG_m/dx vs. In concentration.

Based on Table 4.5 and information in Fig. 4.28, the value of the denominator in equation (7) is calculated to be -0.86 kJ/mol for (Ag)-5In. Compared to pure Ag-Al reaction (-3.5 kJ/mol), although the formation of Ag_3Al in (Ag)-5In is still thermodynamically favorable, the critical radius is much larger. For (Ag)-12In, the denominator in equation (7) is 1.44 kJ/mol, which indicates that the formation of Ag_3Al will not proceed spontaneously in terms of thermodynamics. As a consequence, Al atoms do not segregate at the interfacial region and continue diffusing towards the far end and accumulate in the whole (Ag)-12In layer. Ag-In-Al ternary phase starts to show up when the Al concentration reaches around 15 at. %. Due to the lack of the thermodynamic data of ternary systems, an experimental approach is utilized and an ingot with the composition of Ag-12In-15Al is prepared. Raw materials sealed in quartz tube are melted and homogenized at 1000 °C, quenched with liquid nitrogen and annealed at 250 °C for 2 weeks. The XRD result (in Supplementary Materials) shows that only one phase can be detected in the ingot and the crystal structure is HCP with almost the same lattice constant as ternary phase observed during aging, which indicates that the Ag-In-Al is a thermodynamically stable phase rather than a transitional metastable phase.

Based on these thermodynamic calculations, we can conclude that the increase in the concentration of In in the Ag solid solution phase will affect the nucleation of Ag_3Al. The process becomes thermodynamically unfavorable when In concentration exceeds a critical value. As a result, Al atoms don’t segregate on the interface to form Ag_3Al and continue to accumulate in the whole (Ag)-xIn region. In (Ag)-12In, when the Al concentration reaches

around 13 at. %, the FCC-HCP transition occurs and is confirmed to be attributed to the higher stability of a ternary phase rather than to a solid solution phase.

4.4.2.2 Kinetics and local structure

From kinetic point of view, the process of repelling the In atoms relies on diffusion, and time is needed to finish the whole process. In (Ag)-5In, there are 5 In atoms per 100 atoms on average. As mentioned in the last section, the critical radius must be reached during phase transformation. Assuming that the critical volume of the formation of Ag_3Al in (Ag)-5In contains 10 Ag_3Al unit cells (which in turn contains 200 atoms in total), only around 10 In atoms are needed to diffuse out. As a comparison, even if the conclusion of last section overestimates the effect of In and the formation of Ag_3Al in (Ag)-12In is still thermodynamically favorable, the critical radius of Ag_3Al is much larger, which necessitates more time to repel all the In atoms.

Another thing that can be observed based on the STEM-EDX results is that the inter-diffusion rate between Ag and Al is reduced with the increase in In concentration. In general, the diffusion rate is influenced by a few parameters including temperature, crystal structure, grain size, type of solid solution (interstitial or substitution), external stress, and chemical composition [30]. Specifically, chemical composition is the only variable in this paper and no robust model has been reported to explain the influence of solute on the inter-diffusion between solvent and a third element. According to the experimental results, the addition of In only influences the diffusion rate rather than the diffusion direction, which indicates that kinetics factors play a much more important role in this issue.

To investigate this phenomenon, the mechanism of inter-diffusion between Al and Ag must be reviewed. Firstly, it has been recognized that the dominant inter-diffusion

mechanism between metallic materials with comparable atomic size is the vacancy mechanism. An atom is said to diffuse by this mechanism when it jumps into a neighboring vacancy. Therefore, the availability of neighboring vacancy and the atom/vacancy exchange rate are two major factors affecting the inter-diffusion rate.

In dilute substitution solid solution phase, vacancies can be found not only to be surrounded by solvent atoms but also formed on a neighboring site of the solute. The former case is same as the vacancy in pure metal and the latter is called solute-vacancy pair. The solute-vacancy interaction can be evaluated by comparing the Gibbs free energy of vacancy formation in the undisturbed solvent ($G_F^{Solvent}$) and next to a solute (G_F^{Solute}). When $G_F^{Solvent}$ is larger than G_F^{Solute}, the solute-vacancy interaction is attractive, and vice versa [31]. In addition, it has been reported that G_F^{Solute} is approximately 0.2 eV smaller than $G_F^{Solvent}$ when the solvent is a noble metal with the solute lying to its right in the periodic table [32]. Therefore, the solute-vacancy interaction is attractive in Ag solid solution phase with In. Another thing which is ignored in this model is the atomic size effect. As it is mentioned in last section, the radius of In is about 16% larger than that of Ag, which indicates that the stress state near the solute is in dilation and thus the vacancies are easily to be trapped by the In atoms.

The interface between Al and (Ag)-In solid solution phase at atomic scale is shown in Fig. 4.29. As it was previously mentioned, In can hardly diffuses into Al and remains in (Ag)-In before the formation of IMCs. On the Ag solid solution side, vacancies and vacancy-solute pairs can be found near the interface. Al atoms can diffuse into the right side though exchanging with vacancies along the boundary belonging to the undisturbed Ag matrix, just like diffusing into pure Ag while the exchanging between Al and vacancies in the vacancy-In

pairs is harder due to the attraction or trap effect described in last paragraph. Therefore, the availability of vacancies for Al diffusion into (Ag)-xIn side decreases as the In concentration increases. Similar phenomena have been observed in magnesium (Mg) solid solution phase with zinc (Zn), where the diffusion rate of Al into this matrix is decelerated since some vacancies are attracted by the Zn atoms [33]. However, this model cannot explain the reason why the diffusion rate of Ag into Al is lower when the concentration of In increases.

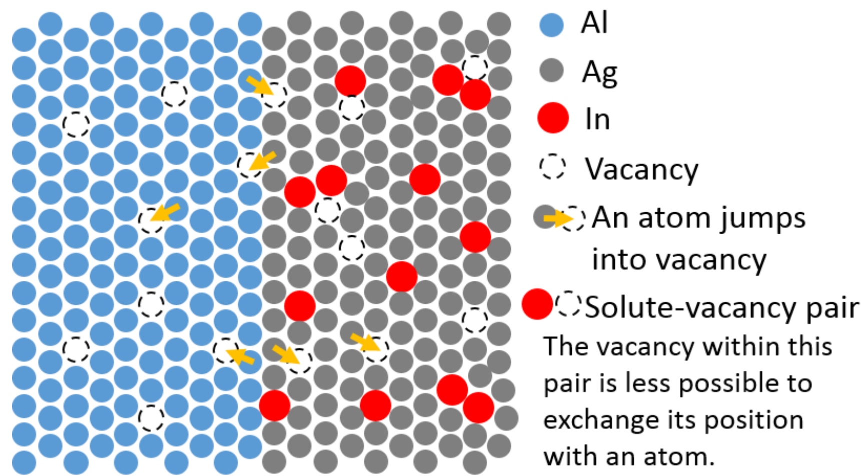

Fig. 4.29 Sketch of interfacial atoms and vacancies (the quantity of vacancies is exaggerated).

The inter-diffusion rate is influenced by many factors and only a qualitative model is proposed here. To fully uncover the underlying mechanism, the diffusivity, activation energy, formation energy of vacancies, and the vacancy-multi-solute atoms interaction must be quantified, which will be addressed in our future work.

4.4.3 Growth mechanism of voids and aluminum oxide

Voids are detrimental to joints, and the formation of voids during inter-diffusion and inter-metallic reaction have been reported in many systems. For example, in Au-Al bonds,

voids nucleate during the bonding process and grow rapidly during the aging process, with large cavities up to 10 μm appearing after prolonged aging [34]. So far, two possible mechanisms of void formation have been proposed. One of them is due to the inequity of inter-diffusion flux, and then vacancies segregate on the fast diffusion species side leading to the formation of voids (also called Kirkendall voids), which is commonly observed in solder reactions [35-38]. Another mechanism focuses on the volumetric change during the phase transformation [39], which has been observed and confirmed in the Au-Al and Cu-Al systems [16, 34].

Possible intermetallic reactions during aging process and corresponding volumetric changes have been listed in Table 4.6. The calculation of volumetric changes is based on the molar volume listed in Table 4.3 and equation (2) in last section. The volumetric change during phase transformation of ternary system is almost zero since both HCP and FCC are closest packing structure just with different stacking sequence and the molar volume is thus thought to be almost equal.

Table 4.6 Possible inter-metallic reactions and corresponding volumetric changes.

Reaction formula	**Volumetric change**
$2Ag+Al \rightarrow Ag_2Al$	+1.2%
$3Ag+Al \rightarrow Ag_3Al$	-1.3%
$2Ag_3Al+Al \rightarrow 3Ag_2Al$	-0.8%
(Ag)-12In-13Al(FCC)→ (Ag)-12In-13Al(HCP)	almost 0

Based on the above results, the volumetric changes during the formation of IMCs are very small compared to that of Cu-Al and Au-Al systems. For (Ag)-5In sample, during the early stage of aging, small voids of 10-20 nm in diameter can be found in Ag_3Al layers, which can mainly be attributed to the shrinkage in volume induced by the formation of Ag_3Al. No voids can be observed in the Al side since volumetric change is positive during the formation of Ag_2Al. Later, the nano-voids in the Ag_3Al layer vanish and large voids (50 nm) occur around the alumina because Al became the dominant diffusion species in the late stage of aging. As it can be seen from Fig. 4.25, the Ag_2Al/Ag_3Al interface moves upward, indicating that the diffusion flux of Al is higher than that of Ag. Therefore, more Al atoms diffuse upwards and fill the nano-voids, and Kirkendall voids appear in original Al side. The voids tend to form near alumina since the interfacial energy between IMC and alumina is high. For (Ag)-12In sample, no voids form during the early stage since no Ag_3Al forms. The voids are only formed around alumina in the late state of aging which is also due to the Kirkendall effect. In addition, the growth rate of voids is also reduced since the inter-diffusion between Al and Ag is decelerated. Compared to Au-Al and Cu-Al system, the size of voids is much smaller, which is a strong indication of high reliability of Ag-Al bonds.

The thickening of alumina line has also been reported in Au-Al and Cu-Al systems. The main reason is that voids form near original alumina line during inter-diffusion and the Al atoms in IMCs get oxidized. The voids are small in Ag-Al bonds and thus may not induce the overgrowth of alumina. Based on Figs. 4.23 and 4.24, the thickening of alumina is quite limited (within 2 nm). As a comparison, the alumina reaches 50 nm after aging at 250 °C for 10 h in Au-Al bonds [40].

4.4.4 Properties of ternary phase

To study the properties of the ternary phase, the ingot of the same composition is prepared. The phase identification is carried out by XRD and the composition is examined by EDX. The results are shown in Fig. 4.30 and 4.31. According to Fig. 4.30, the resulting ingot consists of only one phase which crystallizes in HCP. The result is consistence with the SAED result in the Al/(Ag)-12In joint. In addition, the EDX results show that the ingot is uniform and the composition is close to the STEM/EDX result of the ternary phase in the joint.

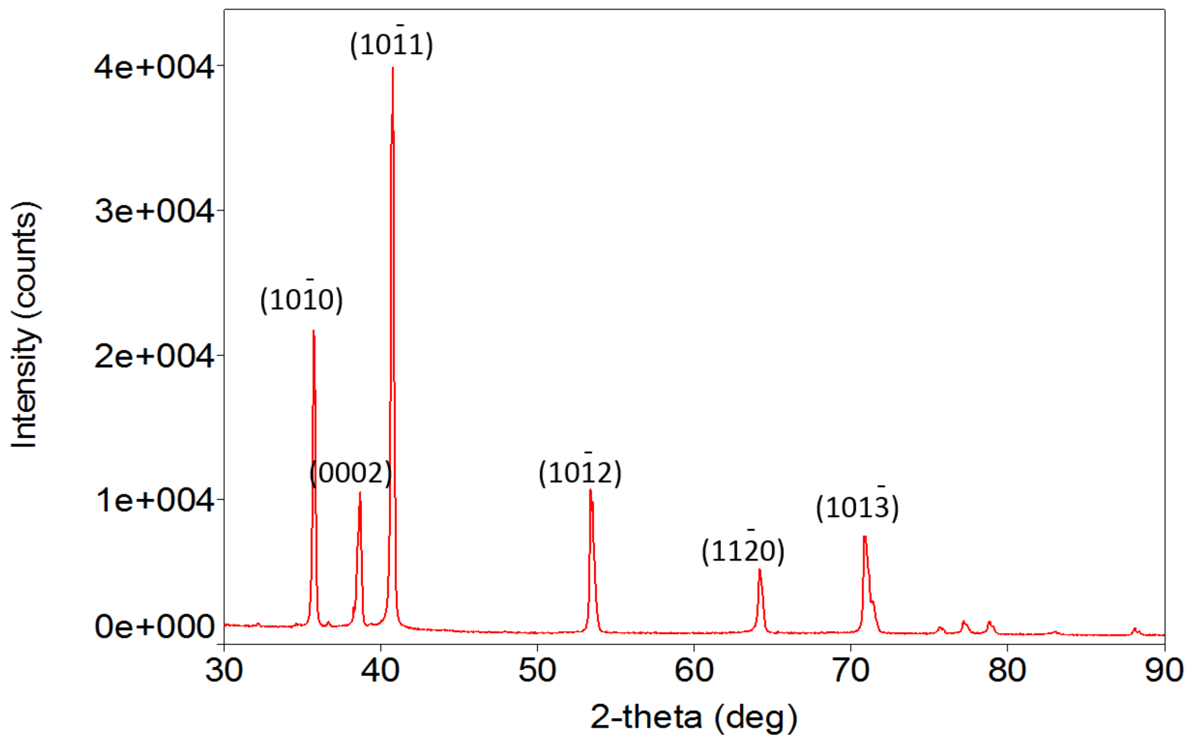

Fig. 4.30 XRD result of the ingot consisting of the ternary phase.

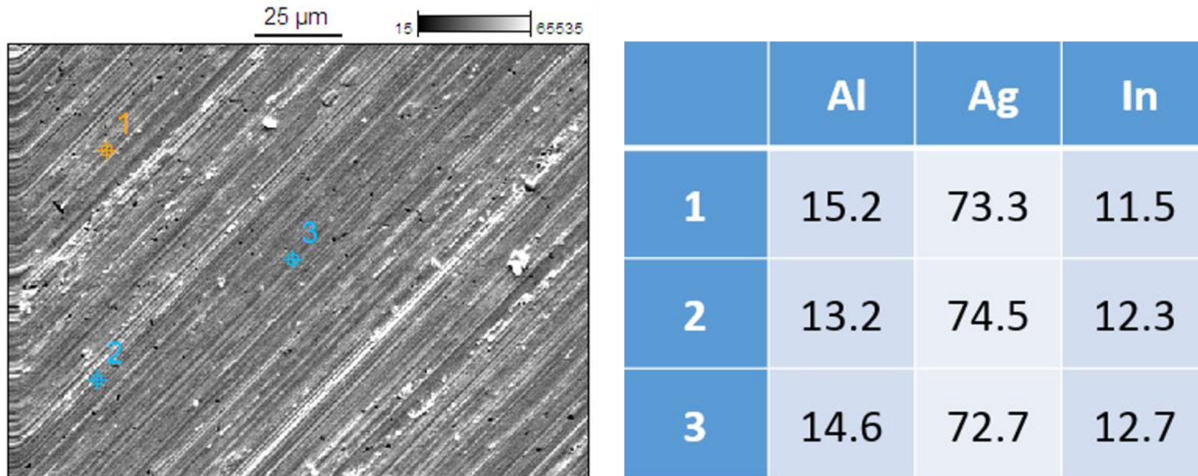

	Al	Ag	In
1	15.2	73.3	11.5
2	13.2	74.5	12.3
3	14.6	72.7	12.7

Fig. 4.31 EDX result of the ingot.

The hardness, modulus and fracture toughness are studied though Vickers hardness and Knoop hardness tests. The images of the Vickers indentations and Knoop indentation are shown in Fig. 4.32. The properties of Ag_2Al, Ag_3Al and ternary phase are listed in Table 4.7 for comparison. The results of Ag_2Al, Ag_3Al are measured using same instrument under same condition. Based on Table 4.7, the hardness (Vickers) of this ternary phase is 998 (±73) MPa and the Young's modulus is 88 (±6) GPa. The fracture toughness cannot be measured since no cracks can be observed even though the largest load (1000 g) is applied (expressed by '-' in the table). The mechanical properties of this ternary phase are pretty close to those of Ag_2Al. Compared to Ag_3Al, the ternary phase is softer and much tougher.

Table 4.7 Comparison of mechanical properties of Ag_2Al, Ag_3Al and ternary phase.

Phase name	Crystal structure	Vickers Hardness (MPa)	Young's modulus (GPa)	Fracture toughness ($MPa\sqrt{m}$)
Ag_3Al	β-Mn	2207±141	110±2.5	1.61±0.3
Ag_2Al	HCP	1222±94	106±2.1	-
Ag-In-Al	HCP	998 (±73)	88 (±6)	-

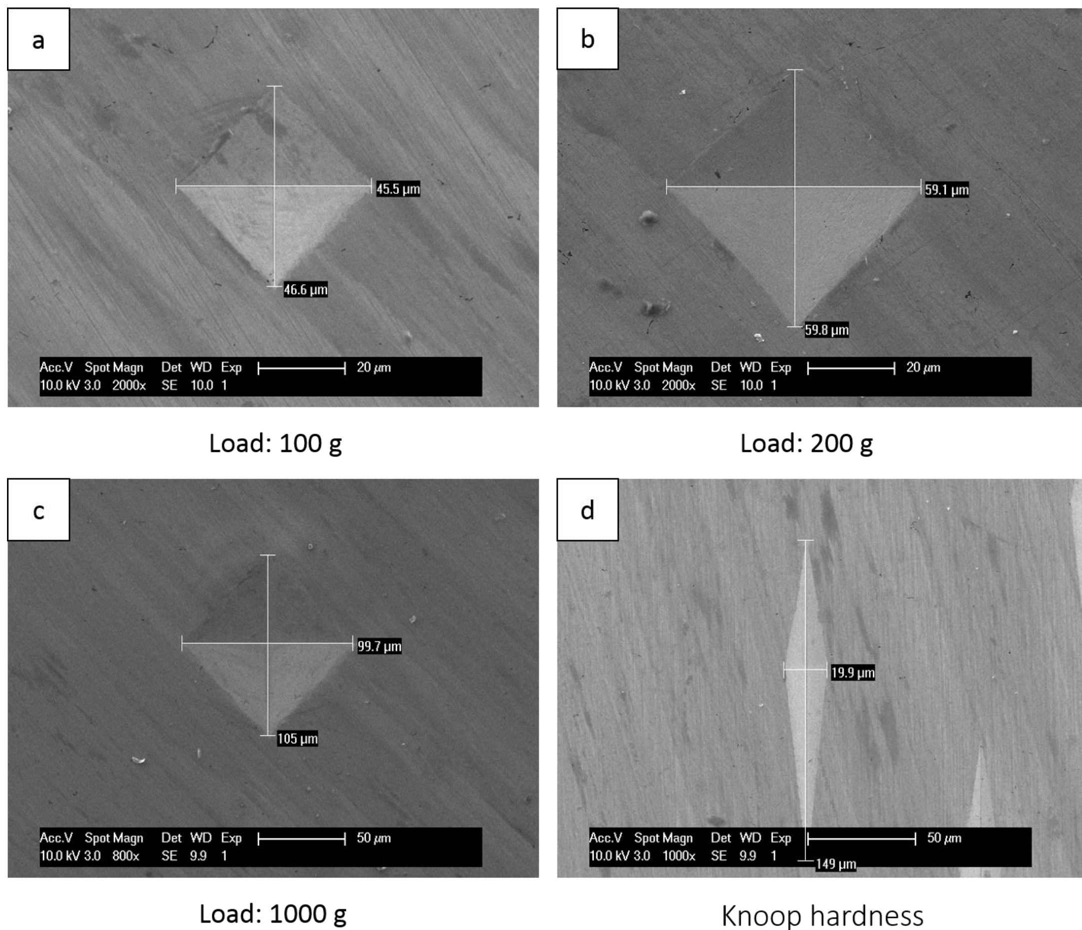

Fig. 4.32 Hardness test results: (a), (b) and (c) are Vickers indentation under different load; (d) is Knoop indentation.

The corrosion resistance of the ternary phase is evaluated through HAST test following the standard JEDEC JESD22-A110C. The experimental setup is shown in Fig. 4.33. The fine polished disk sample is mounted in epoxy resin and the chlorine content is 1000 ppm at the start of the experiment. The epoxy resin is placed in a closed chamber with constant temperature and relative humidity. The thickness of the corroded layer on the surface of the sample is measured after 50 h.

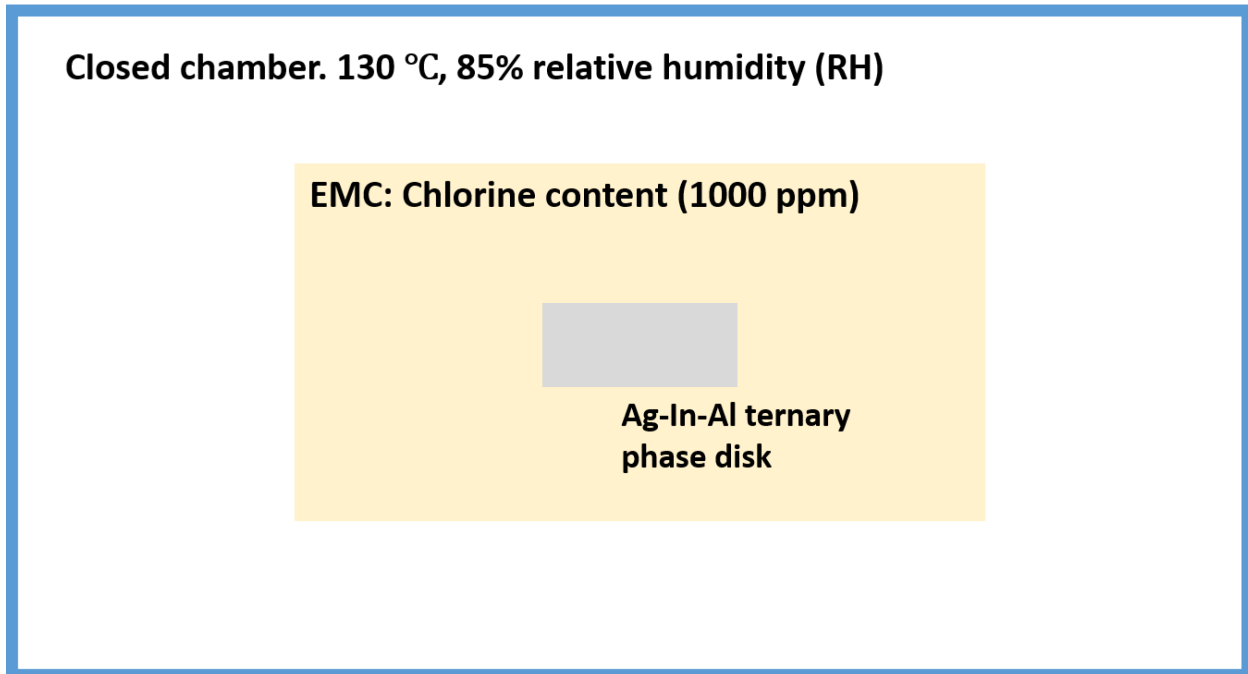

Fig. 4.33 HAST test setup, following JEDEC JESD22-A110C.

The image of the corroded layer is shown in Fig. 4.34. The corrosion rate of Ag-In-Al during HAST is 0.4 μm/h. The corrosion behavior of Ag_2Al, Ag_3Al are studied using same instrument under same condition. As comparisons, the corrosion rates of Ag_2Al and Ag_3Al are 0.6 μm/h and 1.5 μm/h, respectively. Therefore, by replacing Ag_3Al with Ag-In-Al ternary phase, the weakest part of the joint is replaced by a much stronger and more corrosion resistive phase.

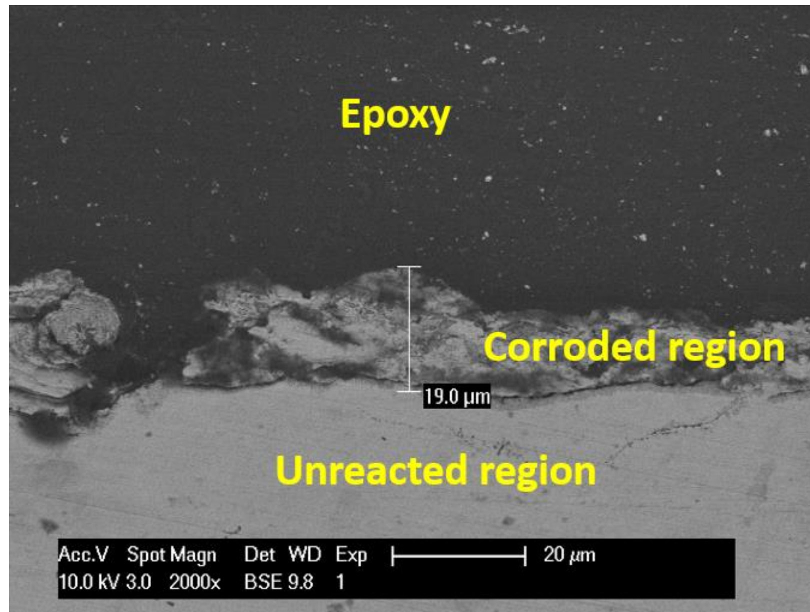

Fig. 4.34 The measurement of the corroded layer on the surface of ternary phase.

4.5 Conclusions

The effects of In alloying on Ag wire bonding onto Al pads have been investigated, particularly in terms of IMCs formation and defect evolution. We report the method of completely eliminating Ag3Al and it could be an effective solution to current Ag-Al wire bonding reliability issue. The mechanism is studied through SEM/TEM/HAADF and thermodynamic modelling. In principle, it could be further generalized to serve as a design guidance in the controlling of interfacial solid-state reactions and IMCs in other metallic systems.

In summary, In in Ag serves as inhibitor towards the formation of Ag_3Al due to its large atomic size. Ag_3Al cannot nucleate until all of the In atoms are repelled out. When the In concentration is low, the driving force of the formation of Ag_3Al is capable of repelling the In atoms. However, if the In content exceeds the critical value, the increase in Gibbs free energy induced by the uphill diffusion of In is larger than the decrease in free energy caused by the phase transformation. Thus, the formation of Ag_3Al is no longer

thermodynamically favorable. Kinetically, the inter-diffusion rate between Ag and Al can also be decelerated since some vacancies in the (Ag)-xIn side are attracted by In atoms/groups and the availability of vacancies for diffusion is reduced. Voids and alumina are less of issues in Ag-Al system, owing to the small volumetric changes during phase transformation, and voids formed around alumina have been categorized as Kirkendall voids. It has been demonstrated that the problematic Ag_3Al is completely eliminated and thus the weakest part in Ag-Al bonds vanish and replaced by a softer, tougher and more corrosion resistive phase, which is believed to greatly improve the reliability of the joint. Given that the machinability, tensile strength and tarnish resistance of (Ag)-xIn is much better than pure Ag, Ag-In alloy can be a valuable alternative to Ag-based alloy wires to the electronic packaging industry.

4.6 Reference

[1] W.-H. Huang, K.-L. Lin, Y.-W. Lin, Y.-K. Cheng, The Intermetallic Compound Formation for the Wire Bond Between an Al Pad and Ag-xPd Alloy Wire, J Electron Mater 45(12) (2016) 6130-6136.

[2] T.-H. Chuang, H.-C. Wang, C.-H. Tsai, C.-C. Chang, C.-H. Chuang, J.-D. Lee, H.-H. Tsai, Thermal stability of grain structure and material properties in an annealing-twinned Ag–8Au–3Pd alloy wire, Scripta Mater 67(6) (2012) 605-608.

[3] R. Guo, T. Hang, D. Mao, M. Li, K. Qian, Z. Lv, H. Chiu, Behavior of intermetallics formation and evolution in Ag–8Au–3Pd alloy wire bonds, J Alloy Compd 588 (2014) 622-627.

[4] Y.-W. Tseng, F.-Y. Hung, T.-S. Lui, M.-Y. Chen, H.-W. Hsueh, Effect of annealing on the microstructure and bonding interface properties of Ag–2Pd alloy wire, Microelectron Reliab 55(8) (2015) 1256-1261.

[5] M. Schneider-Ramelow, C. Ehhardt, The reliability of wire bonding using Ag and Al, Microelectron Reliab 63 (2016) 336-341.

[6] M.-R. Choi, H.-G. Kim, T.-W. Lee, Y.-J. Jeon, Y.-K. Ahn, K.-W. Koo, Y.-C. Jang, S.-Y. Park, J.-H. Yee, N.-K. Cho, I.-T. Kang, S. Kim, S.-Z. Han, S.-H. Lim, Microstructural evaluation and failure analysis of Ag wire bonded to Al pads, Microelectron Reliab 55(11) (2015) 2306-2315.

[7] S.W. Fu, C.C. Lee, Solid-State Reactions of Silver and Aluminum Associated with Silver Wire Bonds, 2016 IEEE 66th Electronic Components and Technology Conference (ECTC), 2016, pp. 648-653.

[8] S.-W. Fu, C.C. Lee, A corrosion study of Ag–Al intermetallic compounds in chlorine-containing epoxy molding compounds, J Mater Sci-Mater Electron 28(20) (2017) 15739-15747.

[9] S.-W. Fu, C.C. Lee, A study on intermetallic compound formation in Ag-Al system and evaluation of its mechanical properties by micro-indentation, J Mater Sci-Mater Electron 29(5) (2018) 3985-3991.

[10] Y. Huo, C.C. Lee, The growth and stress vs. strain characterization of the silver solid solution phase with indium, J Alloy Compd 661 (2016) 372-379.

[11] Y. Huo, J. Wu, C.C. Lee, Study of Anti-Tarnishing Mechanism in Ag-In Binary System by Using Semi-Quantum-Mechanical Approach, J Electrochem Soc 164(7) (2017) C418-C427.

[12] P.C.J. Gallagher, Stacking-Fault Energy of a Ag-In Alloy from Node Measurements, J Appl Phys 37(4) (1966) 1710-1717.

[13] N. Yuantao, Z. Xinming, Metastable extension of solid solubility of alloying elements in silver, J Alloy Compd 182(1) (1992) 131-144.

[14] M. Ellner, K. Kolatschek, B. Predel, On the partial atomic volume and the partial molar enthalpy of aluminium in some phases with Cu and Cu3Au structures, J Less Common Met 170(1) (1991) 171-184.

[15] S.S. Lim, P.L. Rossiter, J.E. Tibballs, Assessment of the Al-Ag binary phase diagram, Calphad 19(2) (1995) 131-141.

[16] H. Xu, C. Liu, V.V. Silberschmidt, S.S. Pramana, T.J. White, Z. Chen, V.L. Acoff, Behavior of aluminum oxide, intermetallics and voids in Cu–Al wire bonds, Acta Mater 59(14) (2011) 5661-5673.

[17] W.D. Callister, D.G. Rethwisch, Fundamentals of materials science and engineering: an integrated approach, Wiley, Singapore, 2016.

[18] W. Gordy, W.J.O. Thomas, Electronegativities of the Elements, J Chem Phys 24(2) (1956) 439-444.

[19] L. Pauling, Atomic Radii and Interatomic Distances in Metals, J Am Chem Soc 69(3) (1947) 542-553.

[20] T. Nishizawa, A. Chiba, Phenomenological Consideration on Inter-phase Equilibrium in Diffusion Couple, J. Jpn. Inst. Met. 34(6) (1970) 629-637.

[21] B.-J. Lee, N.M. Hwang, H.M. Lee, Prediction of interface reaction products between Cu and various solder alloys by thermodynamic calculation, Acta Mater 45(5) (1997) 1867-1874.

[22] W.K. Choi, H.M. Lee, Prediction of primary intermetallic compound formation during interfacial reaction between Sn-based solder and Ni substrate, Scripta Mater 46(11) (2002) 777-781.

[23] C.V. Thompson, On the role of diffusion in phase selection during reactions at interfaces, J Mater Res 7(2) (2011) 367-373.

[24] Y. Sun, H. Liu, Z. Xie, Z. Jin, Prediction of interfacial reaction products between metals with same lattice structure though thermodynamic modeling, Calphad 52 (2016) 180-185.

[25] W.B. Pearson, CHAPTER XI - AN ALPHABETICAL INDEX OF WORK ON METALS AND ALLOYS, A Handbook of Lattice Spacings and Structures of Metals and Alloys, Pergamon1958, pp. 254-894.

[26] O. Redlich, A.T. Kister, Algebraic Representation of Thermodynamic Properties and the Classification of Solutions, Ind Eng Chem 40(2) (1948) 345-348.

[27] Y. Muggianu, M. Gambino, L. Bross, Comparison Between Calculated and Measured Thermodynamic data of liquid (Ag, Au, Cu)-Sn-Zn alloys, J Chim Phys 72 (1975) 85-91.

[28] T.-M. Korhonen, J.K. Kivilahti, Thermodynamics of the Sn-In-Ag solder system, J Electron Mater 27(3) (1998) 149-158.

[29] R. C. Sharma, M. Srivastava, Phase equilibria calculations of Al-In and Al-In-Sb systems, Calphad 16(4) (1992) 409-426.

[30] H. Meher, Diffusion in solids: fundamentals, methods, materials, diffusion-controlled processes, Springer Science & Business Media2007.

[31] W.M. Lomer, Vacancies and other point defects in metals and alloys, Institute of Metals, 1958.

[32] H. Ullmaier (Vol. Ed.), Atomic Defects in Metals, Landolt-Börnstein, New Series, Group III: Crystal and Solid State Physics, Vol. 25, Springer-Verlag, Berlin and Heidelberg, 1991.

[33] C. Kammerer, The influence of alloying additions on diffusions and strengthening of magnesium. PHD Thesis. University of Central Florida; 2015.

[34] H. Xu, C. Liu, V.V. Silberschmidt, S.S. Pramana, T.J. White, Z. Chen, V.L. Acoff, Intermetallic phase transformations in Au–Al wire bonds, Intermetallics 19(12) (2011) 1808-1816.

[35] M. He, Z. Chen, G. Qi, Solid state interfacial reaction of Sn–37Pb and Sn–3.5Ag solders with Ni–P under bump metallization, Acta Mater 52(7) (2004) 2047-2056.

[36] J.Y. Kim, J. Yu, S.H. Kim, Effects of sulfide-forming element additions on the Kirkendall void formation and drop impact reliability of Cu/Sn–3.5Ag solder joints, Acta Mater 57(17) (2009) 5001-5012.

[37] Y. Yang, J.N. Balaraju, Y. Huang, H. Liu, Z. Chen, Interface reaction between an electroless Ni–Co–P metallization and Sn–3.5Ag lead-free solder with improved joint reliability, Acta Mater 71 (2014) 69-79.

[38] V.A. Baheti, S. Kashyap, P. Kumar, K. Chattopadhyay, A. Paul, Bifurcation of the Kirkendall marker plane and the role of Ni and other impurities on the growth of Kirkendall voids in the Cu–Sn system, Acta Mater 131 (2017) 260-270.

[39] G.B. Stephenson, Deformation during interdiffusion, Acta Metall 36(10) (1988) 2663-2683.

[40] H. Xu, C. Liu, V.V. Silberschmidt, S.S. Pramana, T.J. White, Z. Chen, M. Sivakumar, V.L. Acoff, A micromechanism study of thermosonic gold wire bonding on aluminum pad, J Appl Phys 108(11) (2010) 113517.

Chapter 5. Low pressure solid-state bonding technology using fine-grained silver foils for high temperature electronics

5.1 Reliability issues of joint produced by sintering Ag nanoparticles

Recently, sintering Ag nanoparticles has attracted lots of research and industrial interests. A recent report shows that as the size of Ag nanoparticle scales down to 2.4 nm, the surface pre-melting temperature can be as low as 350 °C due to increased proportion of atoms on the surfaces [1]. With further process improvements, the sintering temperature has been reduced to 275 °C [2]. Based on most experimental results, the joints produced by this process exhibit high strength at room temperature and long term reliability near room temperature. This type of joint is expected to be reliable at high temperature. However, when the operating temperature is elevated above 150 °C, serious reliability issues will be raised [2-5].

As shown in Fig. 5.1, it has been reported that the strength of the joints produced by sintering Ag process will be largely reduced when the joint is aged in air at a temperature above 150 °C [3]. It is worth mentioning that there is no degradation of strength if the joint is aged under vacuum. The cross-sectional study (Fig. 5.2) shows that copper oxides can be detected near the interfacial region. The root cause of the oxidation issue is studied and schematically shown in Fig. 5.3. The joints produced by sintering Ag process are porous, which is the nature of this process since the degassing paths cannot be filled during sintering. Many of the pores are not isolated but connected so that oxygen can penetrate inside the joint. When the temperature is elevated, the diffusion rate of oxygen in Ag is increased. As a result, the oxygen can reach the Ag-Cu interface and react with Cu. In Fig. 5.2(a), some isolated islands of copper oxides can be observed, which is due to the diffusion of Cu into Ag. The oxidation induced strength degradation can be confirmed by

aging the joint under vacuum. In Fig. 5.1, the strength of joints remain almost constant during the aging at 250 °C under vacuum. However, in practical application scenarios, electronic devices work in air or even more corrosive environment. Therefore, the oxidation issue must be mitigated.

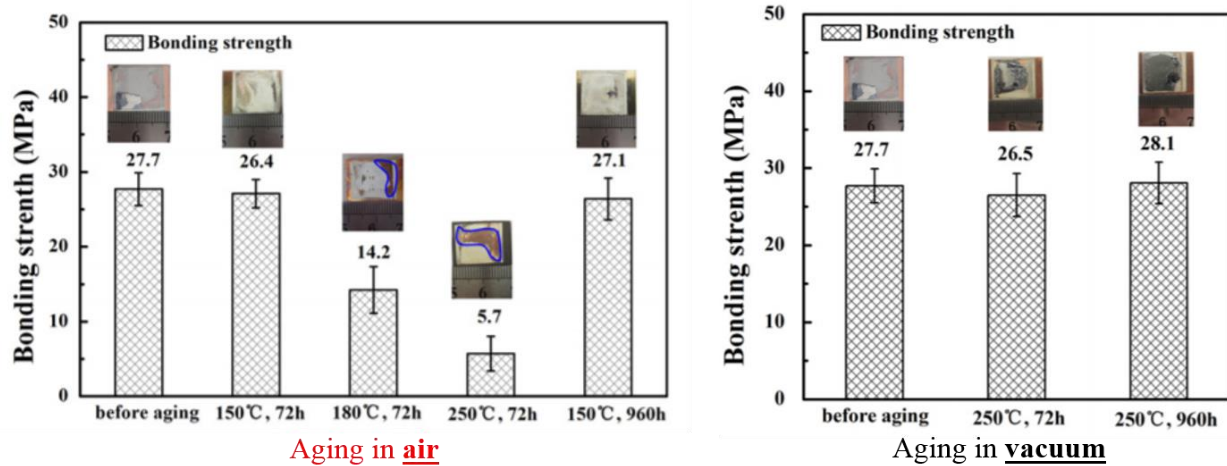

Fig. 5.1 Strength degradation of joints produced by sintering Ag on Cu substrate during HTS test in air [3].

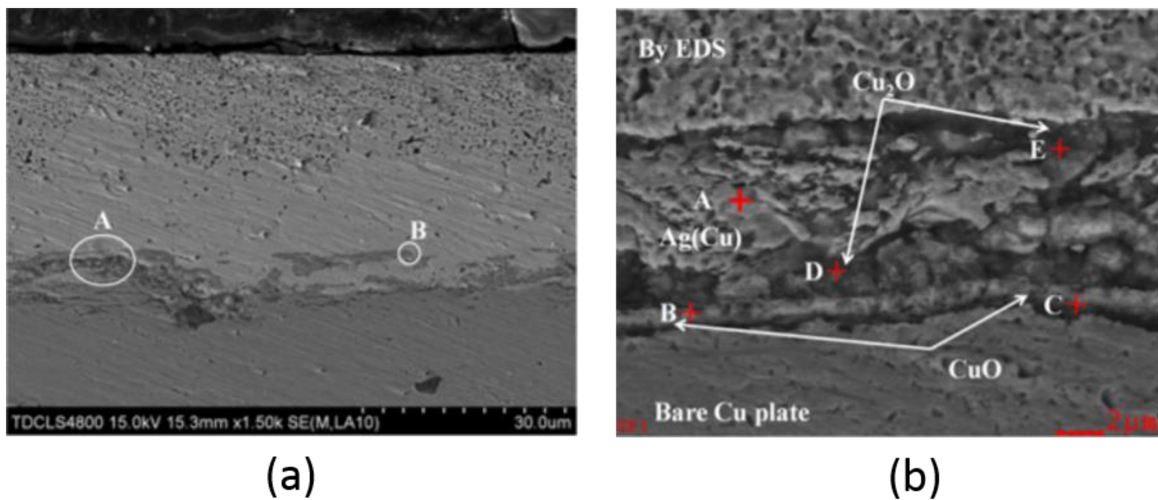

Fig. 5.2 Cross-sectional study of joints produced by sintering Ag process: (a) low magnification image; (b) high magnification image [3].

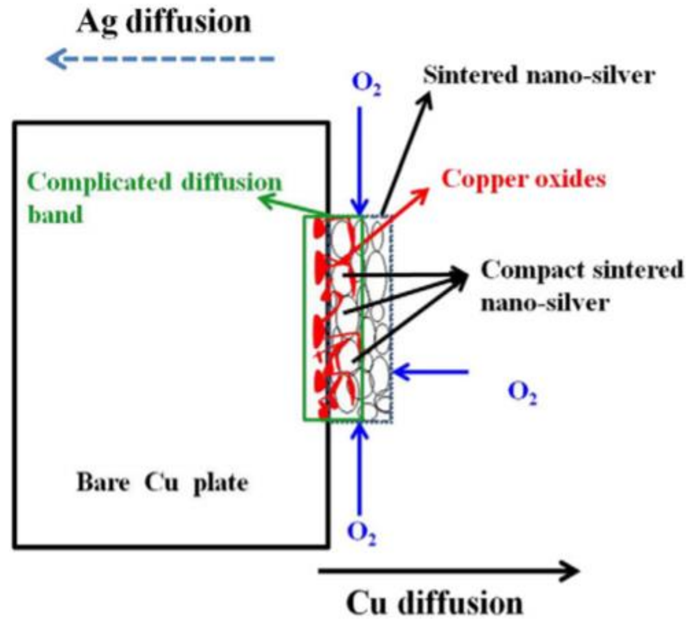

Fig. 5.3 Sketch of the penetration of oxygen and formation of copper oxides [3].

To alleviate the oxidation issue, a few approaches have been tried. Firstly, a layer of pure Ag is coated on Cu substrate prior to the sintering process to protect the Cu underneath [4]. However, as it can be seen in Fig. 5.4, the Cu oxides are continuous. Some Ag atoms diffuse into the oxide layer, which may increase the strength in a limited manner.

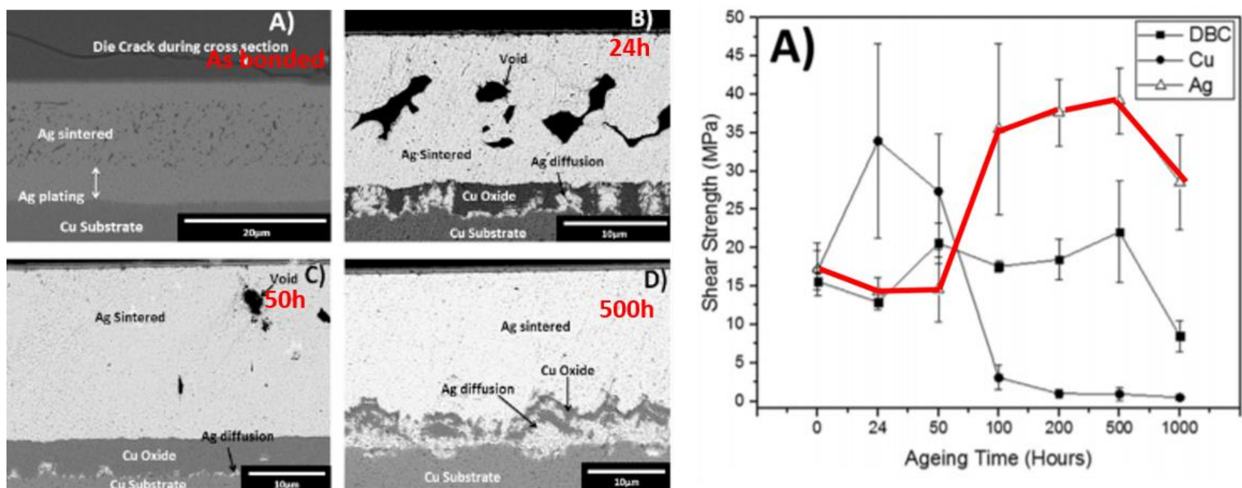

Fig. 5.4 Ag-coated Cu substrate still get oxidized during aging process [4].

Au is a more common protective layer on top of Cu. A study using Cu with ENIG (electroless nickel immersion gold) surface finish in sintering Ag process is conducted [5]. The cross-sectional study is shown in Fig. 5.5 and the strengths of these four joints are described in the caption. It can been seen that the pores near the Ag-Au interface grow as the aging time increases. The authors proposed that it's the interdiffusion between Ag and Au and subsequent coalescence of pores that induce the enlargement of the pores.

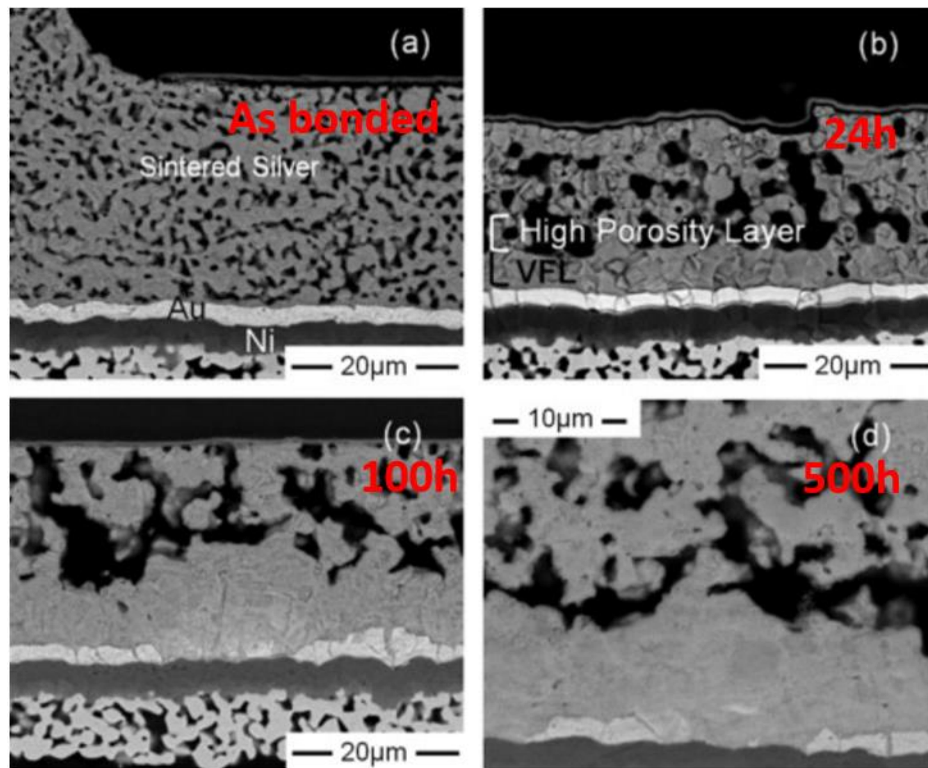

Fig. 5.5 Sintering Ag process using Cu substrate with ENIG surface finish. The strength corresponding to these four images: (a) 15MPa, (b) 17MPa, (c) 12 MPa, (d) 10 MPa [5].

Based on above results, the deposition of protective layer (i.e. Au or Ag) can somewhat mitigate the degradation of the joints' strength. However, the reliability issues such as the oxidation or enlargement of pores are not well addressed. The root cause of the

reliability issues is the porosity nature of the sintering technology. Therefore, reducing the porosity is the key to the solution.

5.2 Solid-state bonding technology

Nowadays, many materials joining technologies rely on solid-state bonding process due to its low process temperature and small heat affected zone. Different from traditional thermal compression bonding, the process time of solid-state bonding is short, ranging from several seconds to a few hundred seconds. The prerequisite of forming solid-stat bond is that the atoms from both surface must be brought within atomic distance. As a result, the atoms from one side fall into the potential well of the atoms from the other side and the bond is thus formed [6]. The behaviors of materials around the interface are illustrated in Fig. 5.6, which can further clarify the differences between solid-state bonding and traditional thermal compression bonding. Firstly, the surface of materials cannot be absolute smooth even if the surface is either fine polished or processed by chemical mechanical planarization (CMP). We can use asperities to describe the surface of materials in practical cases [7]. During the bonding process, the materials are heated to certain temperature and the bonding is assisted by pressure. At the initial stage, the real contact area is extremely small and the stress on the tips is much larger than the nominal applied pressure. As a result, these asperities deformed and the actual bonded area is increased. As the increase in bonding process time, the asperities deform further and most area are bonded with some small voids along the interface. So far, it’s still in the regime of solid-state bonding. If the process time is further increased or the process temperature is elevated, either recrystallization or massive inter-diffusion occurs, resulting in the formation of a region of recrystallized grains or alloys such as solid solution and IMCs. In

practical, the last stage corresponds to the traditional thermal compression bonding. Since it is associated with diffusion or recrystallization which is thermal activated process, the bonding temperature must be higher than the critical temperature and the bonding time should be long.

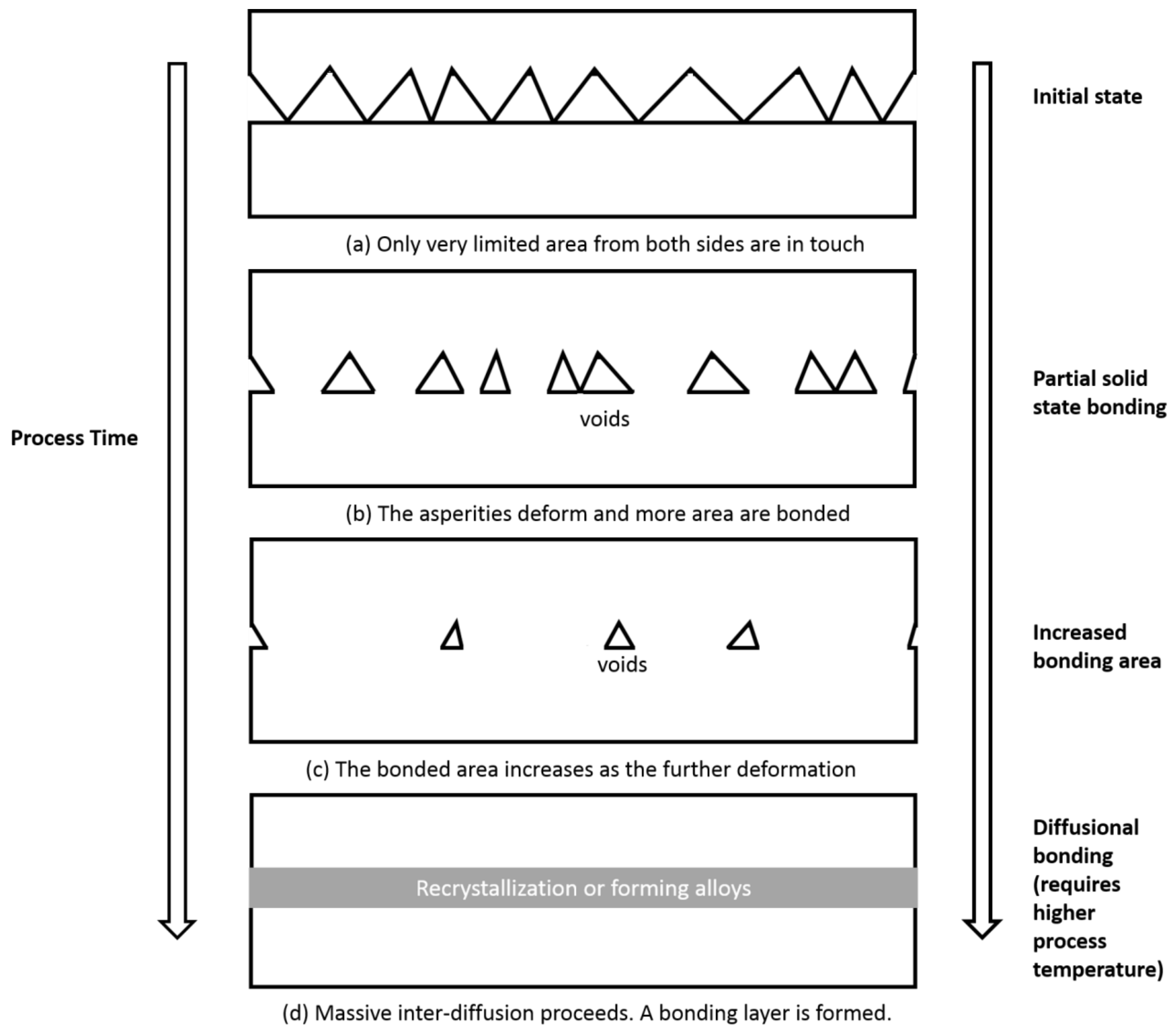

Fig. 5.6 Illustration of the behaviors of materials near the interface during bonding assisted by pressure and heat.

In the present work, Ag is still the bonding medium due to its superior physical properties: highest electrical conductivity (63×10^6S/m) and highest thermal conductivity

(429 W/m-K) among metals, high melting temperature, and high ductility. Since Cu is the most commonly used material for leadframes, electrodes, and bond pads in electronic packaging, high quality joints of semiconductor chips to Cu using Ag would be of significant contribution to electronics in general and to high temperature power electronics in particular. Based on Ag-Cu binary phase diagram [8], the Ag and Cu are almost immiscible at temperatures lower than 300 °C and no IMC phase forms. Thus, traditional thermal compression bonding may be redundant for the Ag-Cu bonding. Therefore, we turn to the idea of solid-state atomic bonding. The Ag foil of 75 μm in thickness is prepared and chosen as bonding medium between Si chips and bare Cu substrate. The bonding is conducted at 300 °C assisted by 1000 psi (6.9 MPa) pressure. It is worthwhile to indicate that this pressure is a few orders smaller than the pressure used in industrial thermo-compression bonding processes, which is considered to be safe to the Si chips.

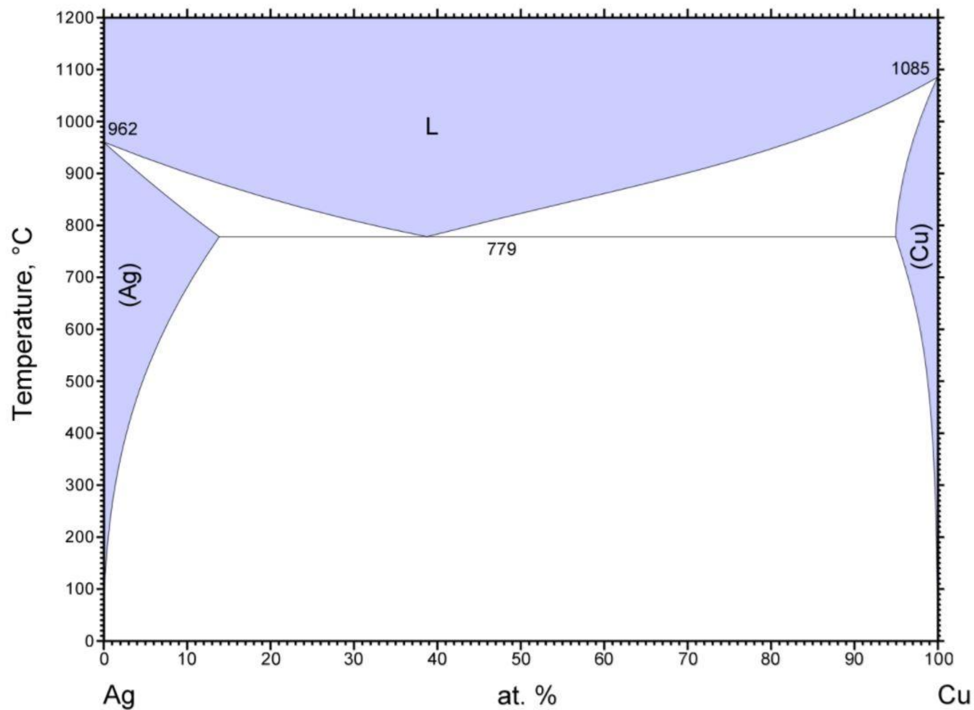

Fig. 5.7 Ag-Cu binary phase diagram [8] (Recolored by ASM international).

5.3 Experimental procedures

5.3.1 Preparation and characterization of Ag foils with recrystallized microstructure

To produce Ag foils, Ag ingots are first grown by melting Ag shots under vacuum, followed by natural cooling down to room temperature. Several runs of cold rolling and subsequent annealing are then performed to reduce the thickness of an ingot. As it was mentioned in previous section, Ag foil needs to be soft enough to be deformed easily during the bonding process. Therefore, grains with low dislocation density are preferred, which can be acquired after recrystallization [9]. On the other hand, the initial grain size of the ingot ranges from hundreds of microns to a few millimeters, refinement of grains is necessary since the thickness of the foil is within 100 μm. These rolling and annealing conditions are determined after many rounds of trials and adjustments. In each run, the thickness is reduced by 70%, and the annealing temperature is optimized at 300 °C, corresponding to a homologous temperature of 0.46 at which recrystallization is expected to complete and excessive grain growth doesn't occur within one hour [10]. The final foil thickness is approximately 75 μm, suitable for bonding experiments. Prior to each bonding experiment, the foil is slightly polished by 1 μm diamond suspension solution and rinsed with de-ionized water.

In general, metallic materials become harder and less ductile after cold work because the heavy increase in dislocation density makes dislocations harder to glide within crystal grains [11]. In addition, texture is formed within polycrystalline metals during cold rolling, making the materials exhibit certain anisotropy in mechanical properties. In this research, an isotropic and texture-free Ag foil microstructure is highly preferred since the Cu electrode and substrates used in electronics do not have a preferred orientation. To

confirm that residue stress and texture are removed by the annealing process, X-ray Diffraction (XRD) and Pole Figure (PF) measurement are conducted.

5.3.2 Solid-state bonding process

To produce the semiconductor chips for bonding experiments, 3-inch silicon (Si) wafers are deposited with 30 nm Cr and 100 nm Au thin films by E-beam evaporation in one high vacuum cycle. The Si wafers are then diced into 5 mm × 5 mm chips and ready for bonding. Cu substrates of 7 mm × 7 mm are cut from a Cu sheet purchased from a vendor. Right before bonding, they are slightly polished by 1 μm diamond powder suspended solution and rinsed with thin hydrochloric acid and DI water to remove the oxides and contaminants.

The bonding structure design is illustrated in Fig. 5.8. The metallized Si chip, Ag foil, and Cu substrates are held together by a fixture with a pressure of 1,000 psi (6.9 MPa) onto a graphite heater stage in a vacuum chamber. The chamber is pumped to 0.1 torr and the graphite stage is heated to 300 °C in 5 minutes, kept isothermally for 5 minutes, and cooled down naturally in vacuum to room temperature. The vacuum environment reduces Cu oxidation during the bonding process.

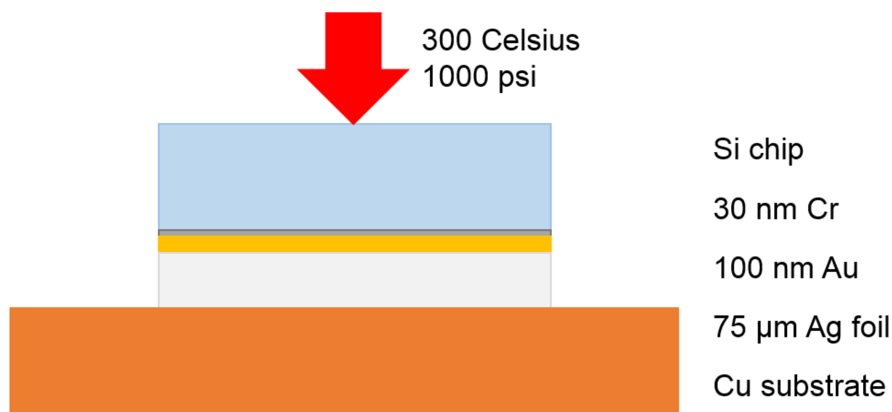

Fig. 5.8 Illustration of bonding structure (dimensions of small features are exaggerated).

In the following sections, the cross-sectional study is performed on OM, SEM. The strength is evaluated by shear test. High temperature storage (HTS) tests at 300 °C are performed, following the process specified in JESD22-A103E. The cross-sections and strength are also evaluated after HTS. To further study the structure evolution of Ag-Cu interface during aging, TEM sample is cut from sample after 200 hours aging by FIB. BF imaging and EDX are conducted for interfacial morphology examination and compositional analysis.

5.4 Results and discussions

5.4.1 XRD and PF measurement

XRD result of a typical as-annealed Ag foil is shown in Fig. 5.9. The data collected in the test are processed and analyzed by PDXL, an integrated polycrystalline XRD analysis software package. The peaks in Fig. 5.9 are indexed and the crystallographic information are sorted and listed in Table 5.1.

Table 5.1 XRD peaks and analysis results.

Peak #	2-Theta (deg)	d (Å)	(hkl)	a (Å)
1	38.10	2.359	(111)	4.088
2	44.23	2.045	(200)	4.090
3	64.39	1.445	(220)	4.087
4	77.32	1.233	(311)	4.088
5	81.48	1.180	(222)	4.087

From Fig. 5.9, it is clear that the crystal structure of the Ag foil is face centered cubic (FCC) in terms of the diffraction peaks' systematic absence. Several peaks associated with

Cu were also detected because the Ag foil was attached to a Cu sheet during the scan process. In Table 5.1, 'd' is the d-spacing of corresponding crystallographic planes, (hkl) is the Miller's indices with classical denotation, and 'a' is the calculated lattice constant. The deduced lattice constant of 4.088 Å fits with the data recorded in ICDD card (03-065-2871) perfectly with only 0.5% deviation, an indication of Ag material nearly free from macro-scale residue stresses.

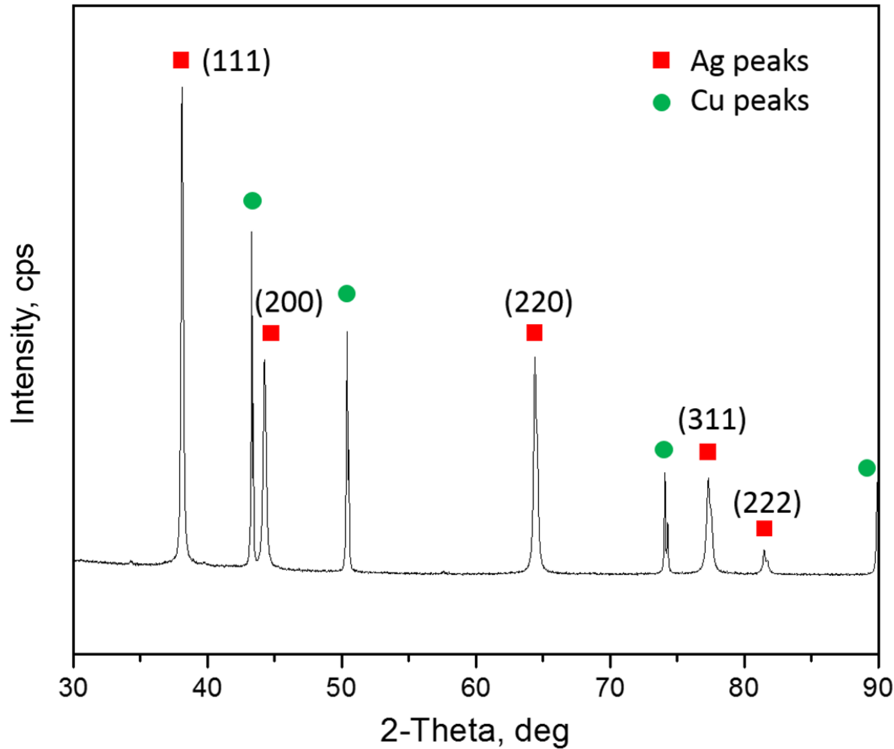

Fig. 5.9 XRD pattern of a typical annealed Ag foil, where the Cu peaks were caused by X-ray incident on the Cu sheet on which the Ag foil was adhered to.

The PF measurement results of as-rolled and as-annealed samples are exhibited in Fig. 5.10. Fig. 5.10(a) and 5.10(b) show that the (111) poles of an as-rolled sample are

concentrated near 45 degrees and the (220) poles are concentrated near 90 degrees, which are consistent with the theoretically calculated results based on mechanics and the operation of slip systems in FCC polycrystalline metals with low stacking fault energy [12]. From Fig. 5.10(c) and 5.10(d), it is seen that the concentration of (111) poles and (220) poles are greatly reduced after annealing, which indicates that the strain energy stored during cold work was released to trigger recrystallization resulting in a near texture-free microstructure.

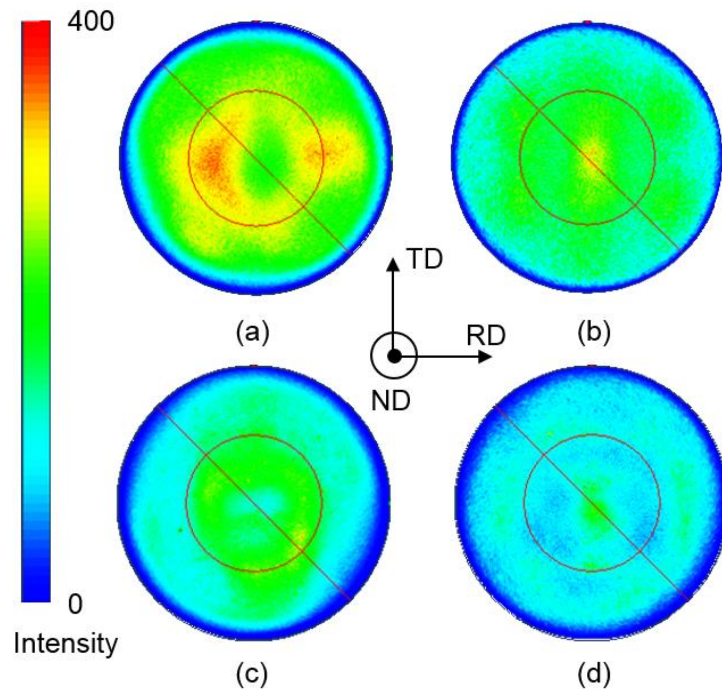

Fig. 5.10 PF measurement results: (a) (111) poles of as-rolled sample, (b) (220) poles of as-rolled sample, (c) (111) poles of annealed sample, (d) (220) poles of annealed sample.

The XRD and PF measurement results presented are representative and repeatable for silver foils from different batches. In conclusion, high quality, stress-free and near texture-free silver foils have been successfully prepared by cold rolling and subsequent annealing processes.

5.4.2 Cross-section examinations of as-bonded Si/Ag/Cu structures

According to Fig. 5.11, the Si/Ag and Ag/Cu bonding interfaces are clear and sharp without defects under optical microscope inspection. Given the large difference of coefficient of thermal expansion (CTE) between Cu (17×10^{-6}/°C) and Si (2.7×10^{-6}/°C), the crack-free silicon implies that the ductile Ag layer is capable of managing the strains induced by the CTE mismatch. It is worth reminding that the Si chips were coated with thin Cr and Au layers. It is the Au layer that bonds to the Ag foil. To study the Ag/Cu bonding interface, it is a challenge to produce a clear and sharp interface using mechanical polishing processes because of smearing effects of ductile Ag and Cu during polishing. We thus turned to FIB cutting to produce a clear and sharp interface. Fig. 5.12(a) displays the high magnification SEM image of the FIB-cut interface. The bonding interface is clear and sharp. No IMCs are observed near the interface, as suggested by the Ag-Cu phase diagram. There are a few voids less than 100 nm in size, probably caused by contaminations as the samples were prepared in a typical laboratory rather than in cleanroom environment. To quantify the fraction of voids along the interface, several images contain interface of 25 μm in total length have been captured and the number of the voids counted. The result is calculated to be 0.56/μm. Fig. 5.12(b) is an SEM view showing the Ag grains in the foil. The grain size is within 5 μm and the recrystallization was completed during the annealing process after cold rolling in consideration of the shape of these grains and the vanishing rolling textures as well.

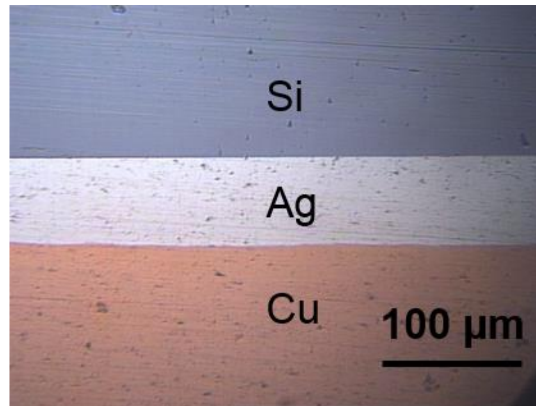

Fig. 5.11 Optical microscopy image of an as bonded Si/Ag/Cu structure.

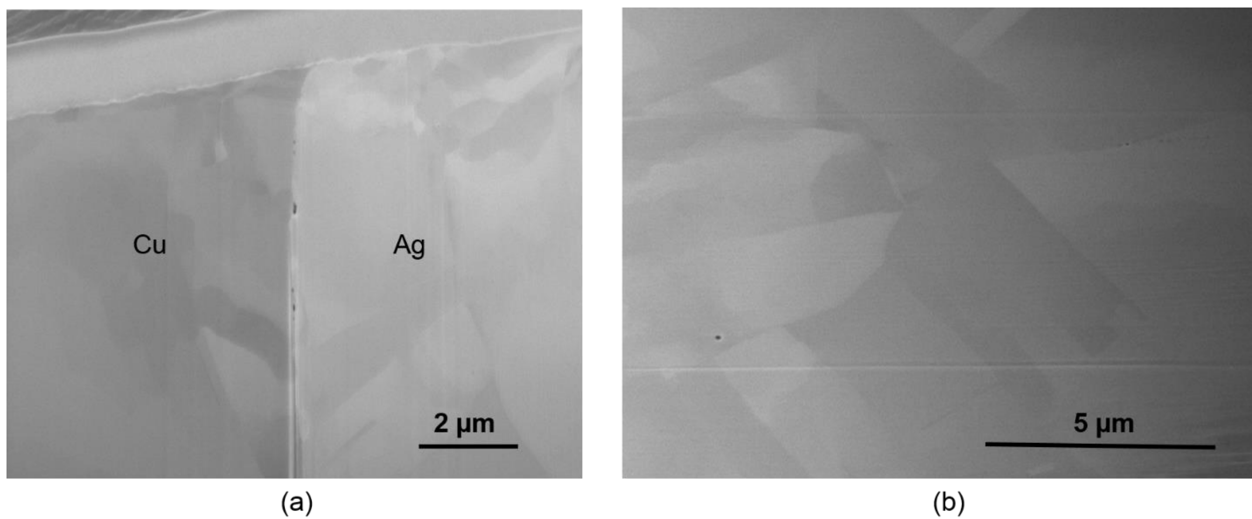

Fig. 5.12 SEM images of interface region of a sample prepared by FIB cutting: (a) Cu/Ag bonding interface, (b) orientation contrast image on Ag region.

5.4.3 HTS test results

The high temperature reliability of joints was evaluated through HTS tests. Samples were aged at 300°C for 72 hours and 200 hours in air, respectively. Afterwards, cross section studies were performed following the same procedures as for as-bonded samples. OM and SEM images were captured and shown in Fig. 5.13 and Fig. 5.14, respectively.

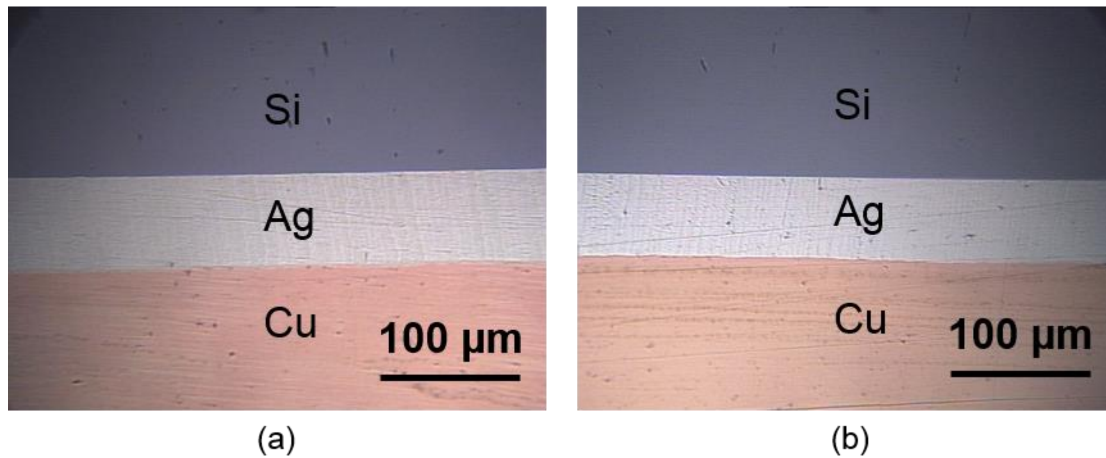

Fig. 5.13 Cross section OM images of samples after aging at 300°C in air: (a) sample after 72 hours, (b) sample after 200 hours.

According to Fig. 5.13(a) and (b), the joints remain at good conditions after long term aging. The Si/Ag/Cu structure is still very clear and no cracks are observed in Si chips. Fig. 5.14 displays high magnification SEM images after FIB cutting of aged samples. Figs. 5.14(a) and (c) exhibit the Ag/Cu bonding interfaces, respectively, after 72-hour and 200-hoour aging. After such a high temperature storage test, the bonding interfaces are still intact aside from a few voids of size less than 100 nm. The fraction of voids for these two conditions are measured to be 0.64/μm and 0.44/μm, respectively. No cuprous oxides or other compounds were found. This means that the bonding interface is so robust that no oxygen could penetrate through the Cu/Ag bond even at 300°C. That is, the Cu/Ag interface is air tight at 300°C. This feature is important in applications where hermetic seal is required. Fig. 5.14(b) is an orientation contrast SEM image on an Ag region after 72-hour aging. The Ag grains are about 5 μm, similar to those on as-bonded sample. Fig. 5.14(d) is an orientation contrast image after 200-hour aging. It is observed that the Ag grains have

grown to more than 10 μm with a preferred orientation. It is worth pointing out that the Ag foil thickness is 75 μm. Thus, further grain growth will be constrained by the foil thickness.

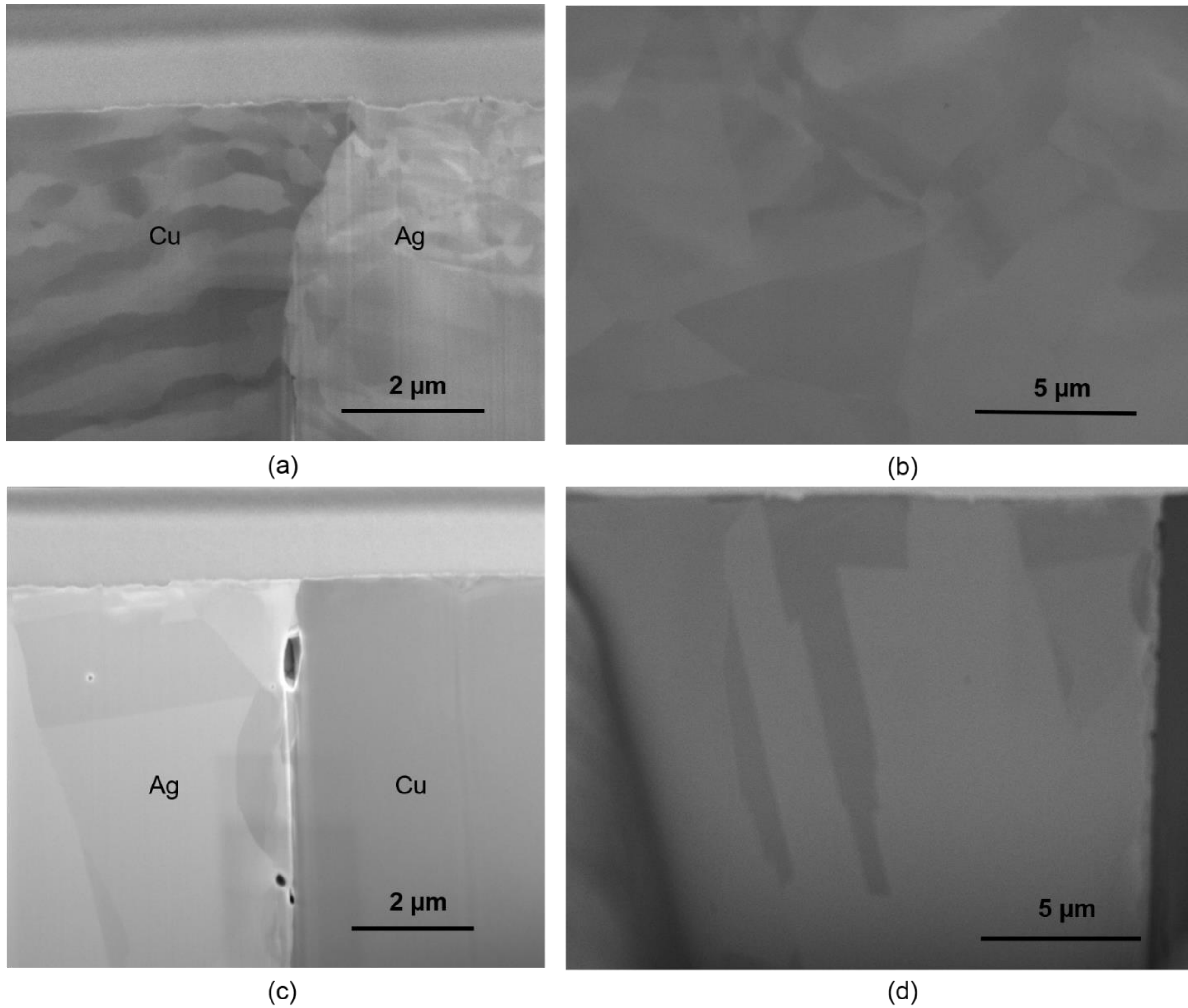

Fig. 5.14 SEM images of cross sections produced by FIB cutting on samples after aging at 300°C in air : (a) interfacial region after 72-hour aging), (b) orientation contrast image of Ag region after 72-hour aging, (c) interfacial region after 200-hour aging, (d) orientation contrast image on Ag region after 200-hour aging.

5.4.4 Shear test results, fractography and discussion

Regardless of how good the bonding interfaces look under optical microscope and SEM, the strength of samples is still unknown until it is measured. A commonly used method to determine the strength is the shear test, as illustrated in Fig. 5.15(a). To perform shear tests, instead of using Si/Ag/Cu structures, we turned to Cu/Ag/Cu structures. The reason is that Si of the Si/Ag/Cu structure will break first during the test and the true strength of the structure cannot be determined. From our experience, a 5mm x 5mm Si chip cannot endure a shear force of 15 kgf applied to an edge by the shearing tool. Accordingly, a 5mm x 5mm Cu instead of a Si chip was bonded to a 7 mm x 7mm Cu substrates using the same conditions to produce samples for the shear test. As-bonded samples, samples after 72-hour aging, and samples after 200-hour aging were tested. There were 12 samples total, 4 per type. The average breaking load, corresponding shear strengths, and standard deviations are presented in Table 5.2. The results show that the strength of 3 types samples far exceed the value (5 kgf) specified in American military standard (MIL-STD-883H method 2019.8) [31]. In addition, it is seen that the average breaking force actually increases a little after aging at 300 °C for 75 hours and it increases further after aging for 200 hours. That is, the strength is enhanced by the 300 °C aging process. This strengthening phenomenon further supports the idea that there is little oxygen penetration through the bonding interfaces to oxidize the Cu atoms on the interfaces. This is really a dream coming true: a structure that gets stronger during usage.

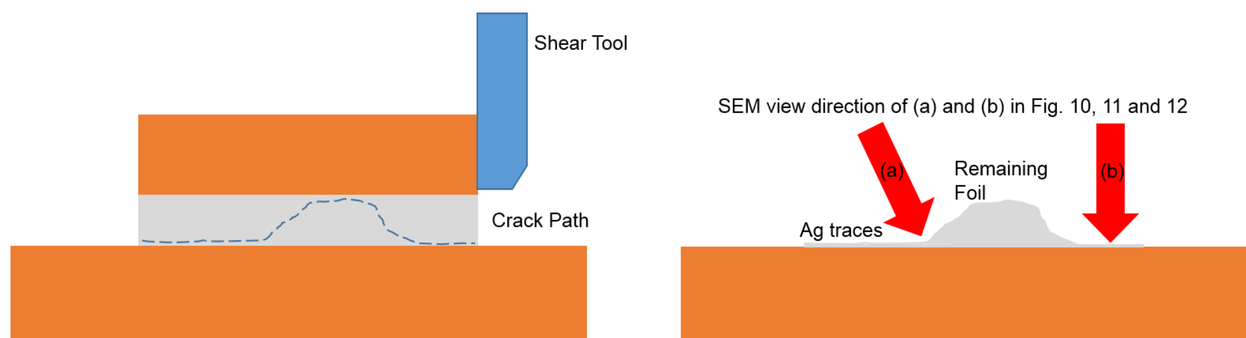

Fig. 5.15 Configuration of shear test and illustration of fracture surface examination.

Table 5.2 Shear test results.

Conditions	Average breaking load (kgf)	Average shear strength (MPa)	Standard deviation (MPa)
as-bonded	73.9	29.0	2.9
after 72-hour aging	81.5	32.0	3.9
after 200-hour aging	86.1	33.7	2.8

After preliminary inspection, the surface at which fracture incurred are similar for all samples, shown as the dash path on the cross-section sketch, Fig. 5.15(a). To study the fracture in more details, all fractured samples were examined by SEM with view directions depicted in Fig. 5.15. The results of samples with three conditions indicated in Table 5.2 are presented in Figs. 5.16, 5.17, and 5.18, respectively.

From Fig. 5.16a, the broken end of the Ag foil is smooth with certain plastic deformation features. On the Cu substrate side, there are Cu regions and Ag-trace regions. The Cu regions have only Cu, indicating weak or no bonding between Ag and Cu. There are two types of Ag-trace regions. Fig. 5.16b exhibits the region with Ag traces that have lots of

submicron and micron size dimples. Fig. 5.16c shows the region with Ag traces of cleavage nature. Fig. 5.16d is an enlarged portion of Fig. 5.16c, exhibiting torn-apart appearance. For as-bonded samples, fracture occurred either within the Ag foil or near the Ag-Cu bonding interface but inside the Ag.

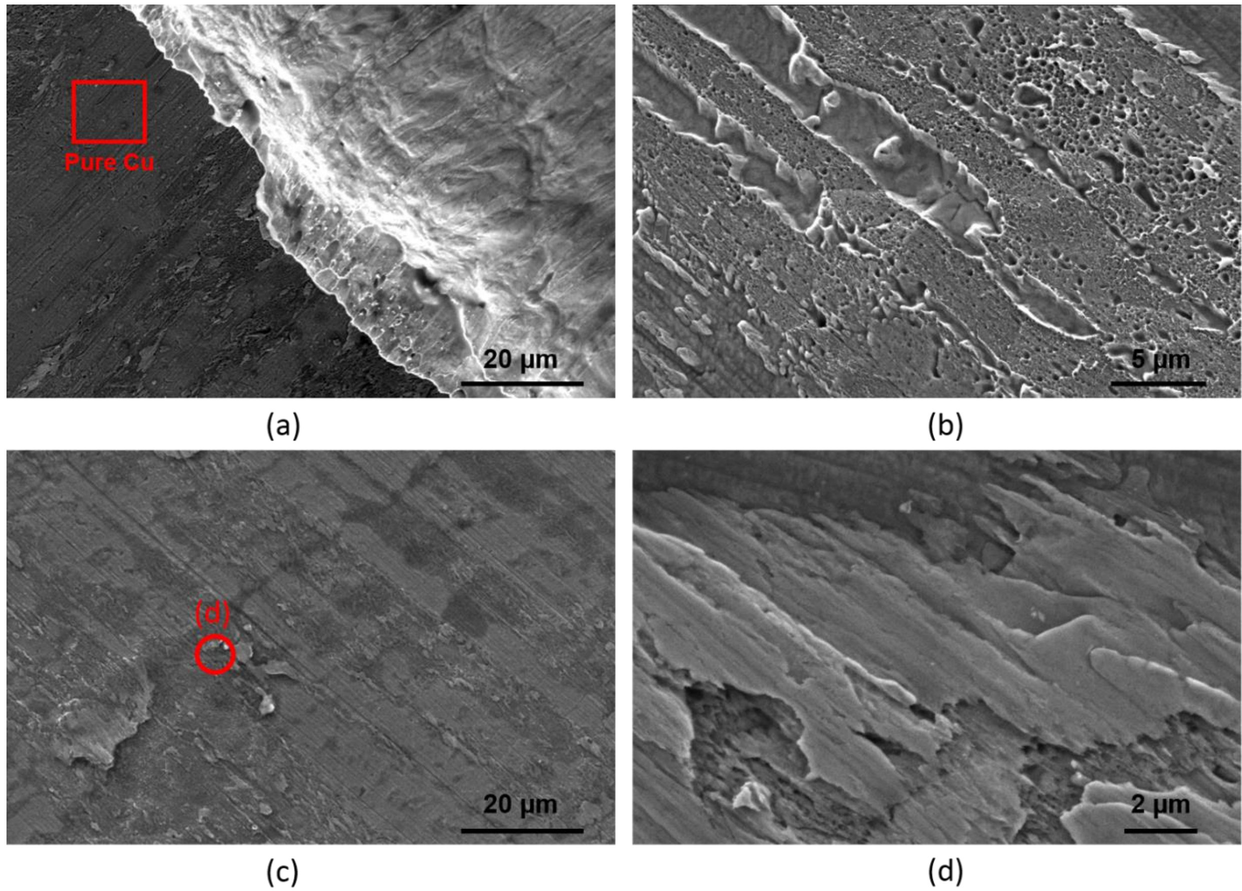

Fig. 5.16 Fracture surfaces of an as-bonded sample: (a) overview of broken end of Ag foil and Ag traces on Cu substrate, (b) one type of morphology of Ag traces on Cu substrate, (c) another type of Ag traces, (d) high magnification image of circled region in (c).

For a sample after 72-hour aging, Fig. 5.17a shows that the broken end of the Ag foil appears similar to that of the as-bonded sample, but with a little bit more plastic deformation features. On the Cu substrate side, in addition to Cu regions, two types of Ag-

traces are found and circled as "c" and "d" in Fig. 5.17b. Region "c" region is enlarged as Fig. 5.17c, displaying dimples with size ranging from submicron to 5 μm. Region "d" is enlarged as Fig. 5.17d that exhibits cleavage features with very small dimples on top of them.

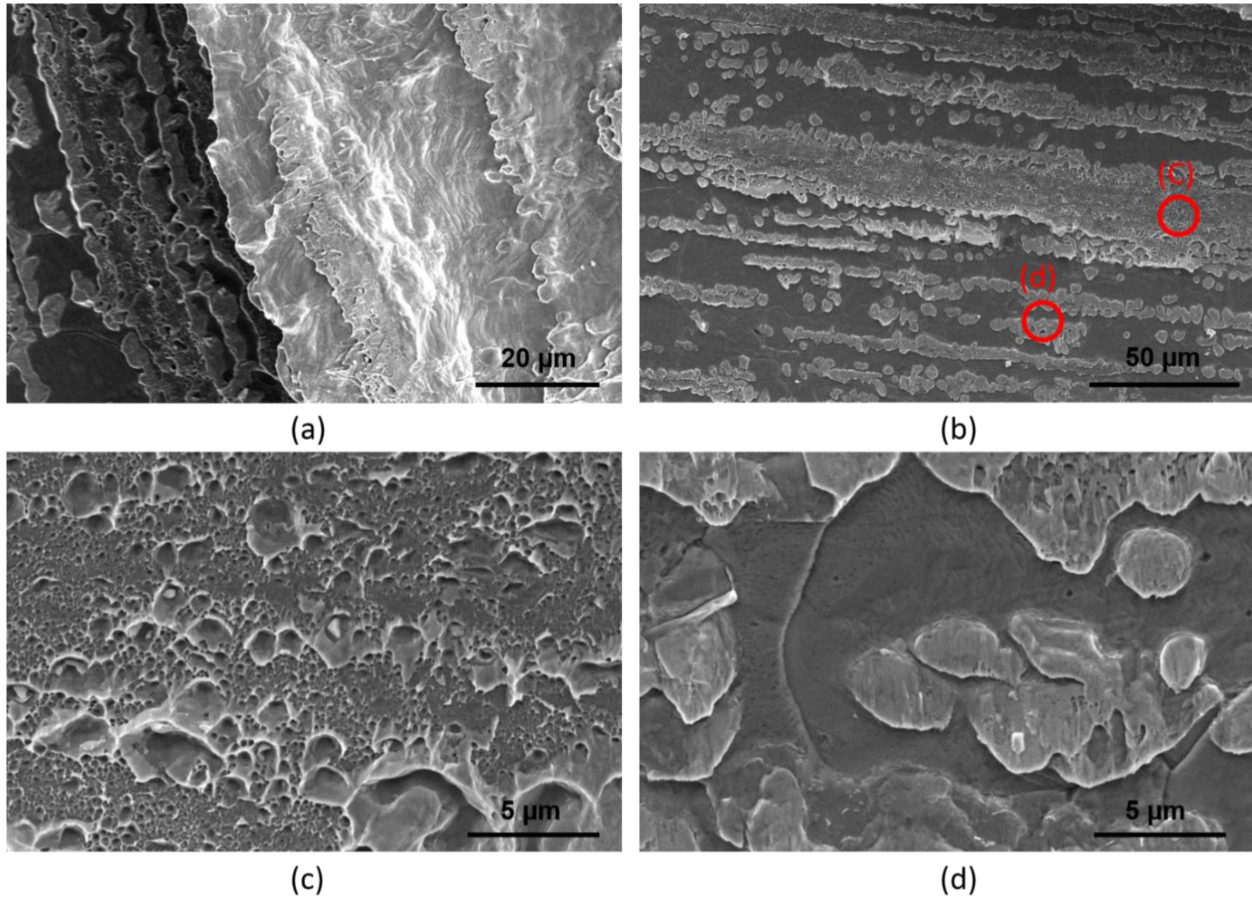

Fig. 5.17 Fracture surfaces of a sample after 72-hour aging at 300°C: (a) overview of broken end of Ag foil, (b) overview of Ag traces on Cu substrate, (c) and (d) are high magnification images of circled regions in (b).

Fig. 5.18a shows the broken end of the Ag foil of a sample after 200-hour aging, where numerous deep dimples are observed on the ridge. On the Cu substrate side, the area of Cu regions has significantly reduced, as exhibited in Fig. 5.18b. This means that the area of no bonding or weak bonding on the Ag-Cu interface has decreased. Accordingly, the

shear strength is expected to be higher, as indicated in Table 5.2. On the Ag-traces, the dimples are more consistent and more uniformly distributed. Figs. 5.18c and 5.18d are enlarged portions of Fig. 5.18b, where the dimple geometries indicate very ductile fracture.

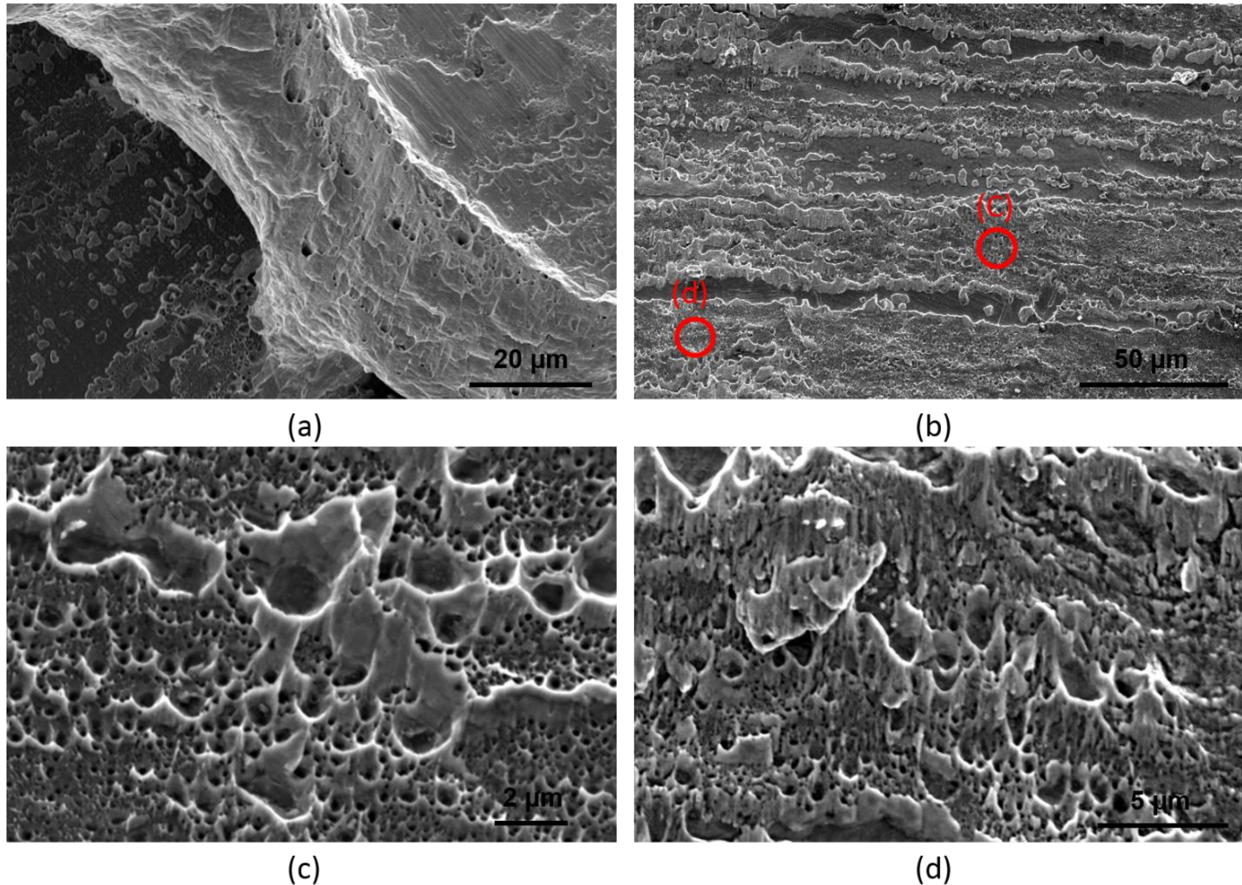

Fig. 5.18 Fracture surfaces of a sample after 200-hour aging: (a) overview of broken end of Ag foil, (b) overview of Ag traces on Cu substrate, (c) and (d) are high magnification images of circled regions in (b).

The fracture evaluations presented above show that the joints become stronger and more ductile after aging. This can be attributed by inter-diffusion and rearrangement of atoms within the interfacial region. Although inter-diffusion is quite limited between Ag and Cu because of limited miscibility, it has been discovered that the grain boundary

diffusion can proceed at elevated temperatures, as analyzed by ultraviolet photoelectron spectroscopy (UPS) depth profiling [13]. Fig. 5.19a also shows the TEM image of Ag-Cu interface after 300 hours aging. It is obvious that Ag and Cu mate each other very well without any oxides or compounds. EDX line scan is conducted along the red arrow and the result is shown in Fig. 5.19b. It can be seen that small amount of Ag can be detected tens of nanometers away from the bonding interface, indicating that slight diffusion proceeds during the long term aging. It is worth mentioning that Cu can also be detected on the Ag side, however, the intensity of signal cannot be directly related to concentration due to fluorescence since the TEM sample was welded on Cu grid. In conclusion, slight inter-diffusion can proceed within tens of nanometers near the interface during the aging process. The HRTEM image of the Ag-Cu bonding interface is shown in Fig. 5.20. It can be seen that the bonding is between Ag and Cu, no other impurities or IMCs can be found in between. Since the sample is under aging, certain orientation relationship can be found. The (111) of Cu is aligned with (200) of Ag. Given that the lattice constant of Cu and Ag are 3.615 Å and 4.088 Å, the d-spacing of (111) Cu and (200) Ag are 2.08 Å and 2.044 Å. This orientation relationship indicates that the atoms near the interface redistribute during the aging process. The redistribution of atoms is due to the large quantity of defects existing in the as-bonded joint. Due to large difference in lattice constants and random orientation of grains on both sides of the interface, large quantity of crystal defects and residue stress are expected within the interfacial region such as vacancies and misfit dislocations at the initial stage. Given that the lattice misfit of Ag-Cu system is 11%, coherent interface is not favorable in terms of strain energy penalty. Reducing the high distortion energy is the driving force of the redistribution of the atoms. During aging, the temperature is 300 °C

which is high enough to trigger the redistribution of atoms and recrystallization, the (111) Cu and (200) Ag align with each other. The difference in d-spacing is only 1.7% so that the distortion of the boundary is largely reduced.

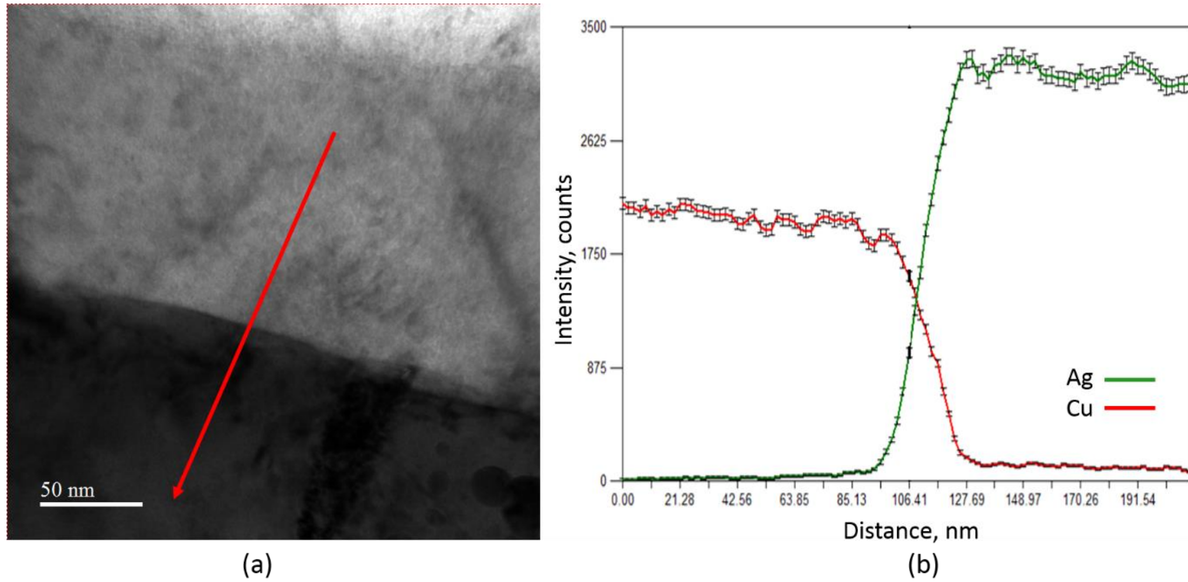

Fig. 5.19 TEM analysis of Ag-Cu bonding interfaces after 200 hours aging: (a) bright field imaging, (b) EDX line scan along the red arrow in (a).

The Au-Cu interface prepared by sputtering has been studied through high-angle annulus dark-field (HAADF) illumination which can provide atomic resolution Z-contrast imaging [14]. At the initial stage, both coherent phase boundary and incoherent region can be found. After annealing, the stress due to the lattice misfits is relaxed by the climb and glide of misfit dislocations. All these processes proceed within 20 nm near the interface. In total, although the initial state of our Ag-Cu interface is different from that of deposited Au-Cu, similar process may proceed to facilitate the stress relaxation and to strengthen the interface after long term aging. Another thing which is noticeable is that the fractured end of the Ag foil on the Cu substrate appears differently for samples after 200-hour aging. This may be caused by different localized stress state during shear test given that the grain

grows significantly after 200 hours aging. In addition, excessive grain growth may result in loss of foil's strength. On the other hand, the strengthening in interfacial region during aging increases the overall strength of the samples. Fortunately, given that the thickness of foil is 75 μm, the space of grain growth is quite limited after 200-hour aging. As a result, the Ag/Cu bonding interfaces are expected to be reliable for high temperature applications.

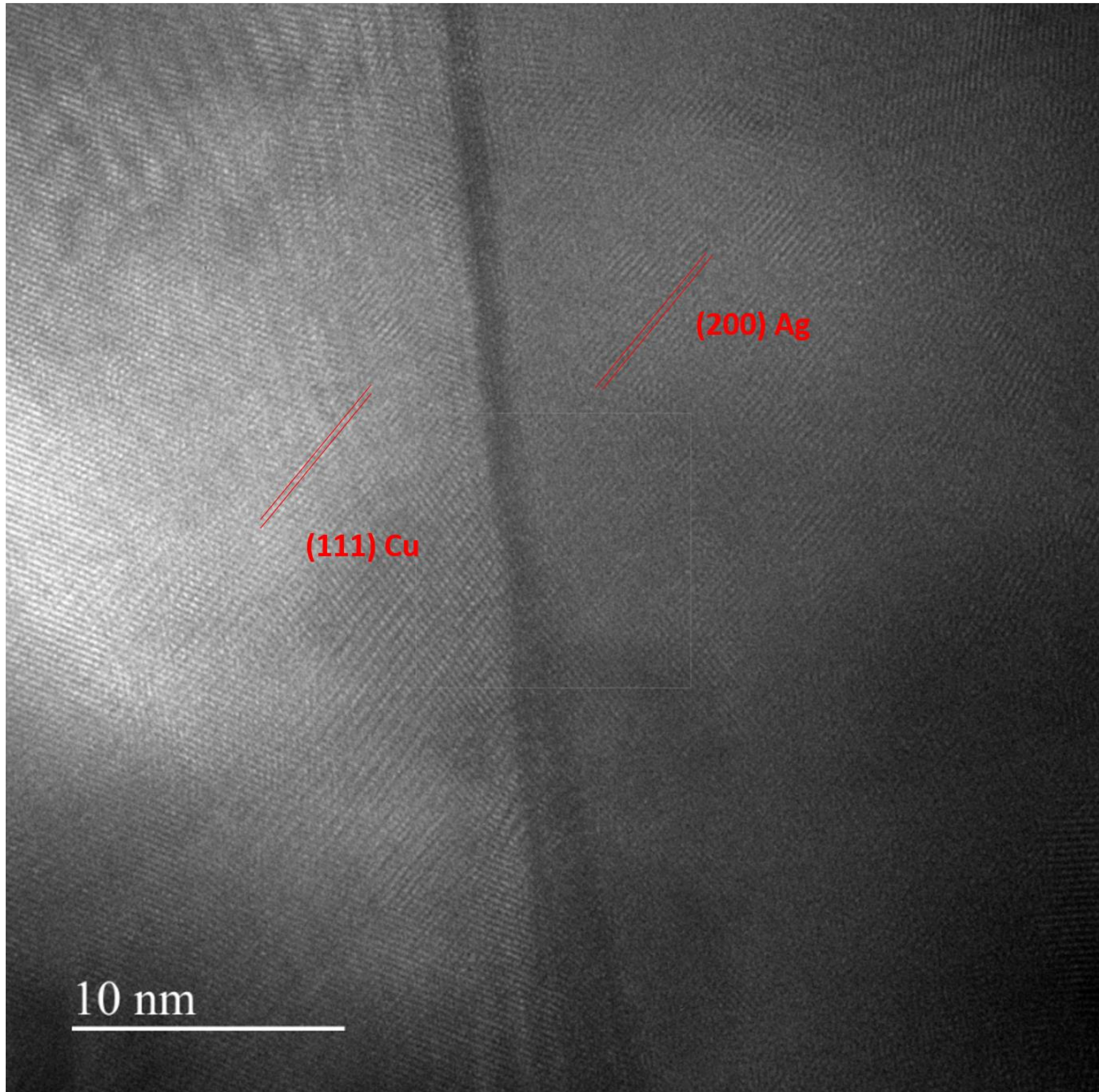

Fig. 5.20 HRTEM image of the Ag-Cu bonding interface after 200 h aging at 300 °C. (111) Cu and (200) Ag are aligned.

It is interesting to compare our results with that of Ag-Cu joints produced by sintered silver technology. Fig. 5.21 shows the comparison of our data and HTS results available in literature so far [3, 4]. It can be seen that the sintered silver can produce strong joints at the initial state. However, the strength drops drastically after aging at 250 °C due to the growth of cuprous oxide. Since de-gassing paths are needed for the escape of resultant binders and organic compounds during the sintering process, numerous pores are formed in the sintered Ag joints. These pores are connected rather than isolated, allowing oxidizing species to penetrate through the network of pores to reach the Cu substrates. In contrast, our Ag joints are pore-free. The Ag-Cu bonding interfaces are shown to be air-tight even at 300 °C. Accordingly, our Ag-Cu joints formed by solid state bonding technology exhibit superior reliability after aging at 300 °C for 200 hours.

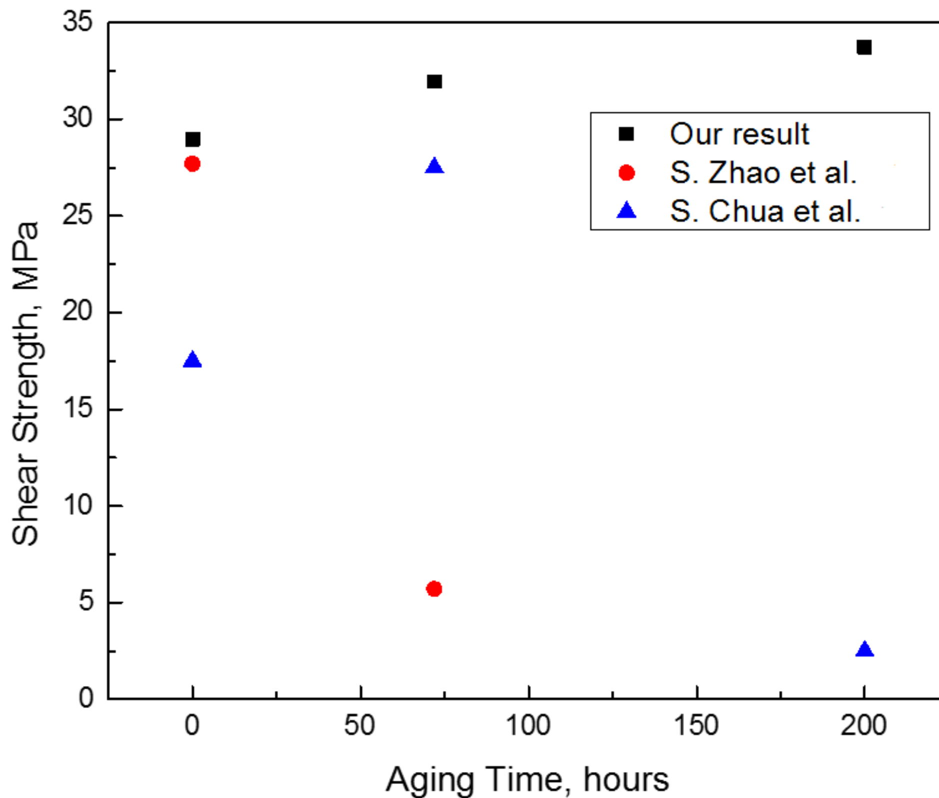

Fig. 5.21 Strength comparison after HTS tests between our result and reports of sintered Ag technology (S. Zhao et al. conducted the aging at 250 °C).

5.5 Conclusion

Solid state bonding technology using ductile Ag foil as the bonding medium has been developed. The fine-grained Ag foils were produced in house. Two structures, Si/Ag/Cu and Cu/Ag/Cu, were bonded at 300 °C with 1,000 psi static pressure in 0.1 torr vacuum. The Si chips were coated with thin Cr and Au layers prior to bonding. HTS tests at 300 °C were conducted to evaluate long term reliability. The Cu/Ag/Cu samples were used for shear test because the Si of the Si/Ag/Cu samples could not sustain much shear force. After shear test, fracture analyses were performed to evaluate the fracture surfaces and fracture modes. Major important results are summarized below:

a. Despite large CTE mismatch between Si and Cu, the Si/Ag/Cu structures did not break after cooling down to room temperature, indicating that the ductile Ag joint could manage the induced shear strains.

b. The breaking force of the joints is 74 kgf, far exceeding the 5 kgf requirement specified in Military Standard, MIL-STD-883H method 2019.8.

c. The corresponding average shear strength is 29 MPa. The shear strength increases for samples going through 300 °C storage tests, meaning that the structures are expected to get stronger during high temperature usage.

d. The HTS test results indicate that the Ag/Cu bonding interfaces and Ag joints are air-tight, meaning that oxygen cannot penetrate through them even at 300 °C.

f. Fracture analyses reveal that the Cu/Ag/Cu structures broke within the Ag foil rather than on the Cu/Ag bonding interfaces.

It is well known that silver Ag has the highest electrical and thermal conductivities among all metals. Its melting temperature is as high as 962 °C. Accordingly, the solid-state bonding design reported in this paper probably not only represents the best possible design for high temperature semiconductor device packaging applications but also can be applied in devices in which air-tight is required.

5.6 Reference

[1] M. Maruyama, R. Matsubayashi, H. Iwakuro, S. Isoda, T. Komatsu, Silver nanosintering: a lead-free alternative to soldering, Appl Phys A 93(2) (2008) 467-470.

[2] Q.Y. Xu, Y.H. Mei, X. Li, G.Q. Lu, Correlation between interfacial microstructure and bonding strength of sintered nanosilver on ENIG and electroplated Ni/Au direct-bond-copper (DBC) substrates, J Alloy Compd 675 (2016) 317-324.

[3] S.-Y. Zhao, X. Li, Y.-H. Mei, G.-Q. Lu, Study on high temperature bonding reliability of sintered nano-silver joint on bare copper plate, Microelectron Reliab 55(12, Part A) (2015) 2524-2531.

[4] S. Chua, K.S. Siow, Microstructural studies and bonding strength of pressureless sintered nano-silver joints on silver, direct bond copper (DBC) and copper substrates aged at 300° C, J Alloy Compd 687 (2016) 486-498.

[5] S.A. Paknejad, G. Dumas, G. West, G. Lewis, S.H. Mannan, Microstructure evolution during 300 °C storage of sintered Ag nanoparticles on Ag and Au substrates, J Alloy Compd 617 (2014) 994-1001.

[6] C.C. Lee, L. Cheng, The quantum theory of solid-state atomic bonding, Electronic Components and Technology Conference (ECTC), 2014 IEEE 64th, IEEE, 2014, pp. 1335-1341.

[7] G. Chen, Z. Feng, J. Chen, L. Liu, H. Li, Q. Liu, S. Zhang, X. Cao, G. Zhang, Q. Shi, Analytical approach for describing the collapse of surface asperities under compressive stress during rapid solid state bonding, Scripta Mater 128 (2017) 41-44.

[8] P. Subramanian, J. Perepezko, The Ag-Cu (silver-copper) system, J Phase Equilib 14(1) (1993) 62-75.

[9] F. Humphreys, A unified theory of recovery, recrystallization and grain growth, based on the stability and growth of cellular microstructures—I. The basic model, Acta Mater 45(10) (1997) 4231-4240.

[10] W.D. Callister, D.G. Rethwisch, Fundamentals of materials science and engineering: an integrated approach, John Wiley & Sons2012.

[11] G.E. Dieter, D.J. Bacon, Mechanical metallurgy, McGraw-hill New York1986.

[12] I.L. Dillamore, W.T. Roberts, Rolling textures in f.c.c. and b.c.c. metals, Acta Metal 12(3) (1964) 281-293.

[13] A. Bukaluk, AES depth profile studies of interdiffusion in the Ag-Cu bilayer and multilayer thin films, Phys Status Solidi A 118(1) (1990) 99-107.

[14] F. Hartung, G. Schmitz, Interdiffusion and reaction of metals: The influence and relaxation of mismatch-induced stress, Phys Rev B 64(24) (2001).

Chapter 6. Direct Ag-Ag bonding by in-situ reduction of pre-oxidized surface for high performance interconnects

6.1 Recent accomplishments in direct bonding technology

When it comes to the bonding that only involves solid state materials, Fig. 5.6 must be discussed again (Fig. 6.1). For Cu-Cu direct bonded joints for advanced interconnection, grains from two sides must be joined together to reduce the density of defects neat the interfacial region. Therefore, the redistribution of atoms or recrystallization is required during the bonding process. It is worth mentioning again that the driving force of the redistribution or recrystallization is the reduction of energy penalty which induced by that large amount of defects such as lattice distortions and misalignments within the joint for an early-age joint (Fig. 6.1c). To trigger the final step, elevated temperature is required since the diffusion and nucleation are thermal activated. Therefore, processes that facilitate either diffusion or nucleation can help reducing the bonding temperature. Based on this theory, a few approaches have been proposed to realize direct bonding at relatively low temperature. It has been reported that Cu-Cu bonding can be realized at room temperature under ultra-high vacuum (UHV) after surface activation which can increase the mobility and reactivity of the surface atoms [1]. However, the process is rather time consuming and the requirement of UHV limits the wide acceptance by industry. Recently, nanotwined Cu have attracted lots of research interests and it has been demonstrated that the Cu-Cu bonding could be achieved using (111) preferred orientated nanotwined Cu at temperatures ranging from 150 °C to 250 °C under 10^{-3} torr vacuum [2]. The reason of using (111) prefer-orientated structure is due to the highest surface diffusivity on (111) among all the crystallographic planes. Therefore, the redistribution of atoms can proceed at a lower temperature and the alignment of atoms are easier due to the same texture of both

sides. However, the issue of this technology is associated with the actual bonded area. The highest strength of the joints under tension is ranges from 1.3 MPa to 4.3 MPa. Given the strength of Cu, the actual bonded area is just a few percentage of the total area.

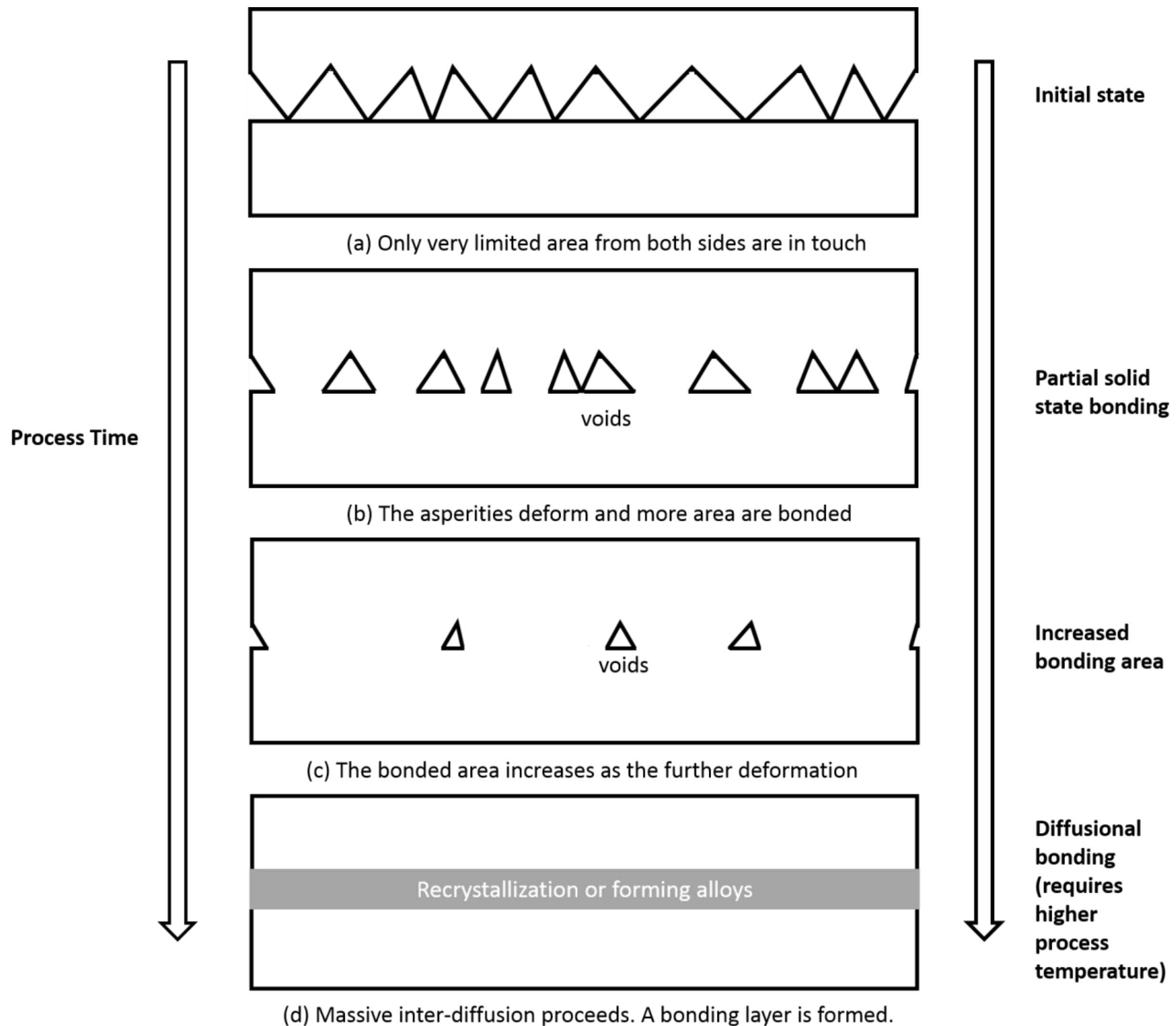

Fig. 6.1 Evolution of interfacial structure during bonding that only involving solid state materials.

Another method to facilitate the diffusion is stress-migration bonding. Through controlling the deposition process (i.e. magnetron sputtering), the internal stress of the film can be controlled. The stress can be measured through XRD diffraction. To reduce the

internal compressive stress, atoms tend to diffuse. If thermally activated, the diffusion could generate protrusions like hillocks and whiskers on the surface, or form internal voids as well. Since diffusion is driven by the internal compressive stress, the higher the internal stress, the more the number of hillocks formed. It has been reported that using pre-stressed Ag films, the stress migration bonding can be realized at 190 °C without the assistance from external pressure [3]. Another reason to use Ag films instead of Cu is due to the oxidation-free of Ag at elevated temperature.

To realize direct bonding between Cu, sintering Cu nanoparticles is also proposed. However, there are still lots of issues with the sintering Cu process. Firstly, Cu get oxidized easily. The situation is more serious when the diameter of the particle is smaller than 50 nm. The whole sintering process must be conducted under reducing atmosphere. Secondly, the sintering process would always result in porous joints due to the formation of degassing path during sintering. These pores and organic residues may affect the properties of the joints such as resistance and strength. Although a few anti-oxidation approaches have been proposed such as Ag@Cu core-shell [4] and polymer covered Cu [5], these can't solve the oxidation issue thoroughly. Also, the preparation and storage of Cu nanoparticles are costive since nanoparticles always tend to agglomerate into large particles which is poor in terms of capability of sintering. Recently, a new Cu sintering process is proposed, which address some issues mentioned above [6]. In this research, Cu particles of few microns in diameter are used instead of nanoparticles. To prevent the formation of natural oxides and agglomeration, these particles are intended to be oxidized. The sintering is conducted under reducing atmosphere and results are shown in Fig. 6.2. From Fig. 6.2b, it can be seen that sintering Cu particles cannot result in a compact

structure since the particle is large so that the tendency of agglomeration is not high. Fig. 6.2d shows that the porosity has been significantly reduced through reducing the surface oxides. The strength also confirm this effect. The authors found that the in-situ reduction of surface oxides will generate very tiny Cu atoms groups/particles of nanometers on the surface large particles. These tiny Cu particles have much higher surface diffusivity and thus facilitate the agglomerate of large particles.

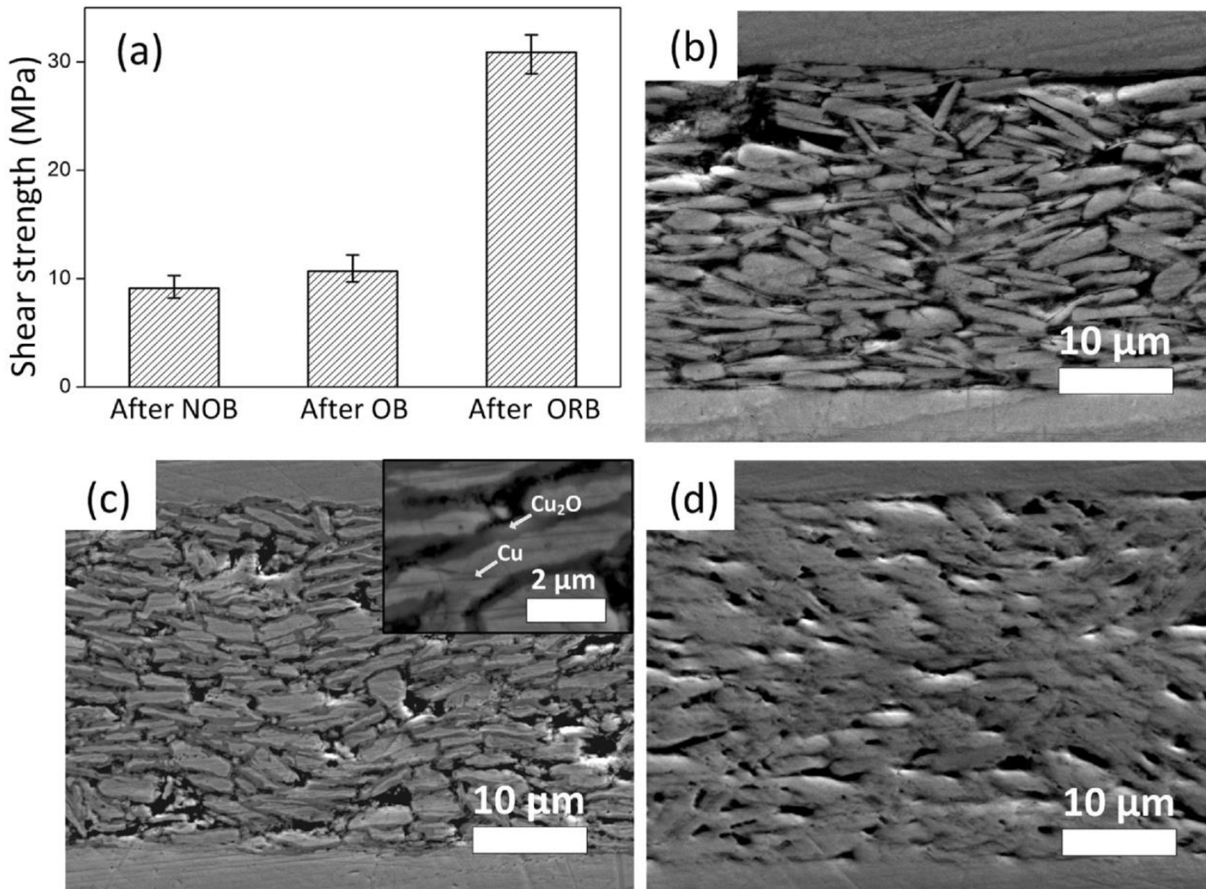

Fig. 6.2 Joints produced by sintering Cu particles: (a) shear strength; (b) sintering pure Cu particles under reducing atmosphere; (c) sintering pre-oxidized Cu particles without reducing atmosphere; (d) sintering pre-oxidized Cu particles under reducing atmosphere.

6.2 Materials selection and motivation

Based on last sections, to realize direct bonding at low temperature, the surface diffusivity is required to be enhanced. The surface diffusivity can be improved through controlling surface texture, surface activation (bombarded by ion), film internal stress and in-situ reducing surface oxides.

On the other hand, the Cu-Cu bonding process requires high vacuum since the Cu get oxidized easily. In industry, processes that can be done in ambient is preferred. After going over all the metals without oxidation issues, Ag looms large in my mind. As it was mentioned in Chapter 3, Ag^{+} is a soft base while O^{2-} is hard acid. Therefore, Ag tends not to react with oxygen and silver oxide is not stable. By employing Ag as bonding layer, oxidation is no longer an issue. Moreover, the instability of silver oxide can also be utilized. The Ag-O binary phase diagram is shown in Fig. 6.3 [7]. Based on the phase diagram, no silver oxide can exist above 186 °C. Therefore, if the surface of Ag can be pre-oxidized by either reacting with oxygen plasma or anodizing process, the thermal decomposition of silver oxide will generate tiny particles which facilitate the surface diffusion. The bonding temperature doesn't need to be very high, only 10 or 20 °C higher than the temperature (200-210 °C) of phase transformation should be enough. No reducing atmosphere is needed. Given that the thickness of the oxide layer is very thin, the porous issue should not be serious. The bonding structure is illustrated in Fig. 6.4.

Since solid-solid direct bonding requires the surface roughness to be as low as possible, e-beam evaporation is selected to deposit Ag films of 1 μm on Si substrate. Prior to the deposition of Ag, 30 nm Cr and 50 nm Au are deposited on Si. One piece of film with surface oxides is bonded to another piece without surface oxides at 210 °C. The bonding is

conducted under vacuum of 0.1 Torr which prevent the Ag from being corroded by other species in air in a lab environment. After pumping, the temperature is ramped up to 210 °C in 10 min, kept isothermal for 30 min and cooled down to room temperature naturally. Only 200 psi (1.38 MPa) pressure is applied to fix the whole structure.

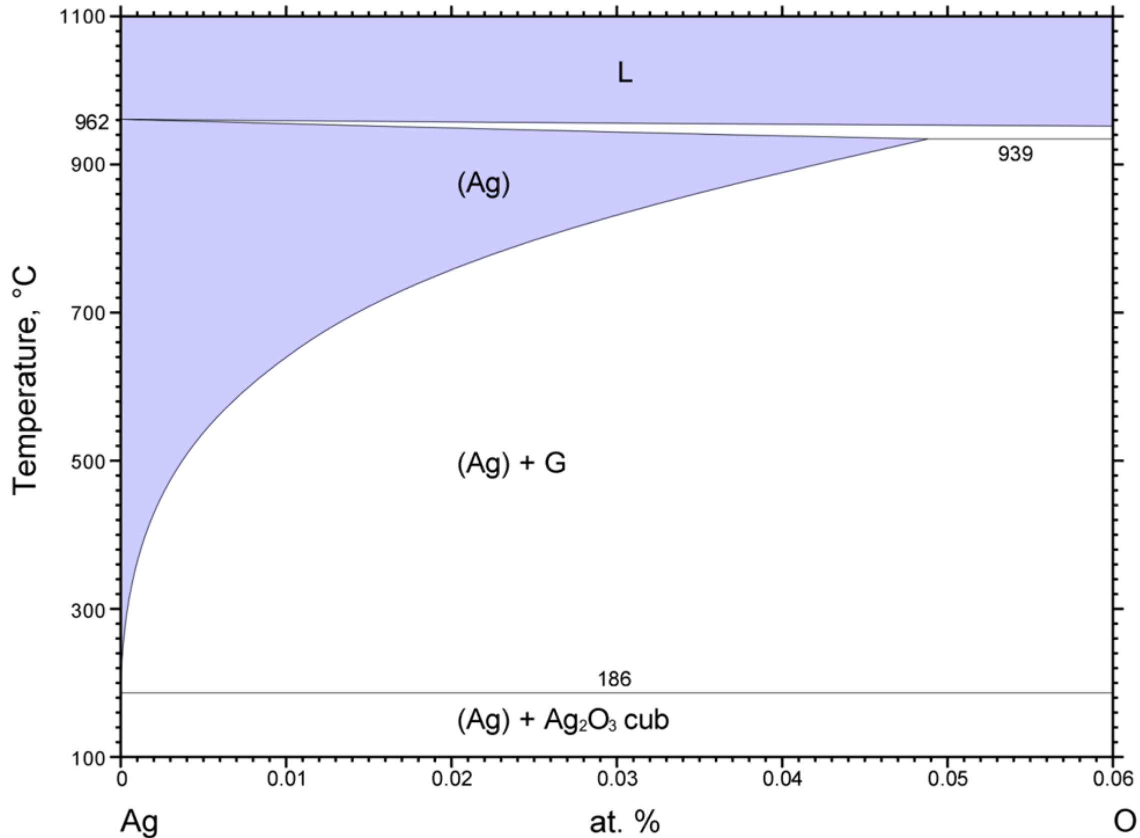

Fig. 6.3 Ag-O binary phase diagram [7] (Recolored by ASM International).

In the following sections, the microstructure and surface morphology of as-deposited Ag films will be firstly described. Then, the morphology of surface oxides as a function of plasma treating time will be illustrated. After reducing silver oxide, the surface morphology is also discussed. Then, quality of bonding is evaluated by SEM and the optimum condition is determined. The TEM sample is cut from the sample of best quality.

The interfacial structure and chemical composition analysis in nano-scale are conducted by HRTEM and STEM/EDX.

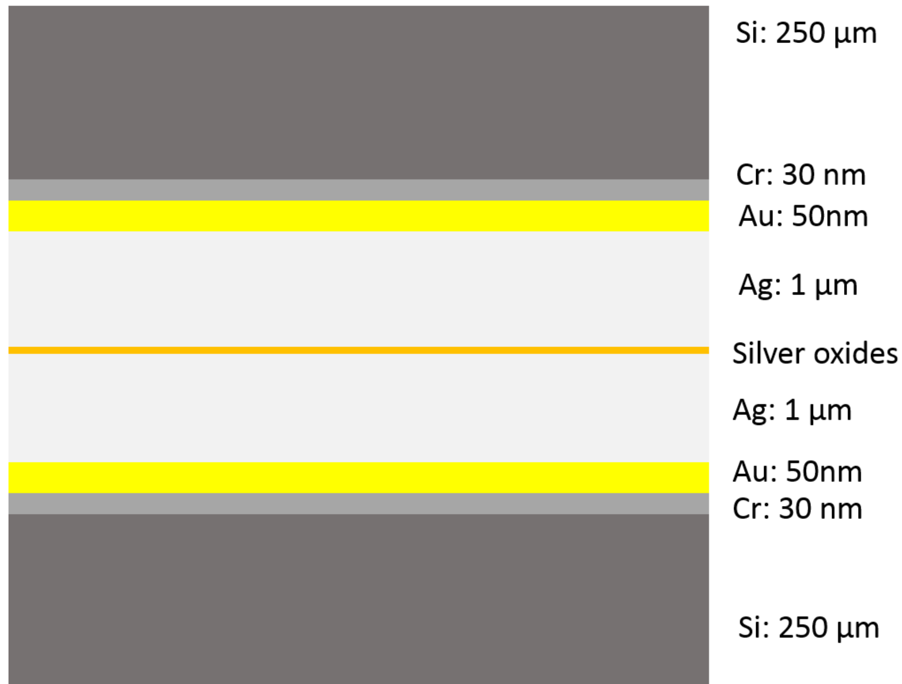

Fig. 6.4 Pre-bonding Structure of joint formed by in-site reducing silver oxides.

6.3 Results and discussion

6.3.1 Characterization of as-deposited Ag film

The top view and cross-sectional view of the as-deposited Ag film are shown in Fig. 6.5 and 6.6, respectively. From Fig. 6.5, it can be seen that the surface is compact without voids and cracks. Since e-beam deposited films usually exhibit island-growth, the surface would appear as if there were lots of particles on the surface. In this case, the particle size ranges from 50 nm to 200 nm. Fig. 6.6 shows that the film is dense without any visible voids inside. The geometries of the grains are quite random. The one dimension size ranges from a few tens of nanometers to a few hundred nanometers, which is consistence to the size of surface particles. The microstructure and surface morphology can be finely tuned during deposition in the future.

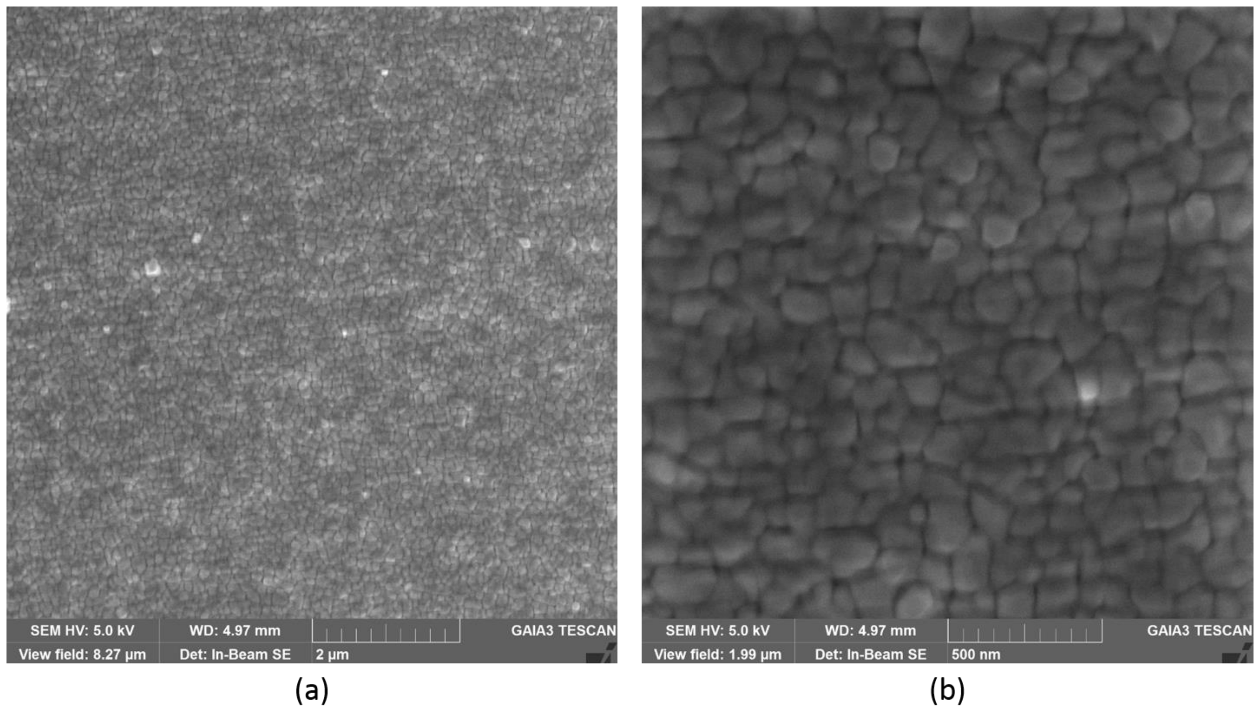

Fig. 6.5 Surface morphology of as-deposited film.

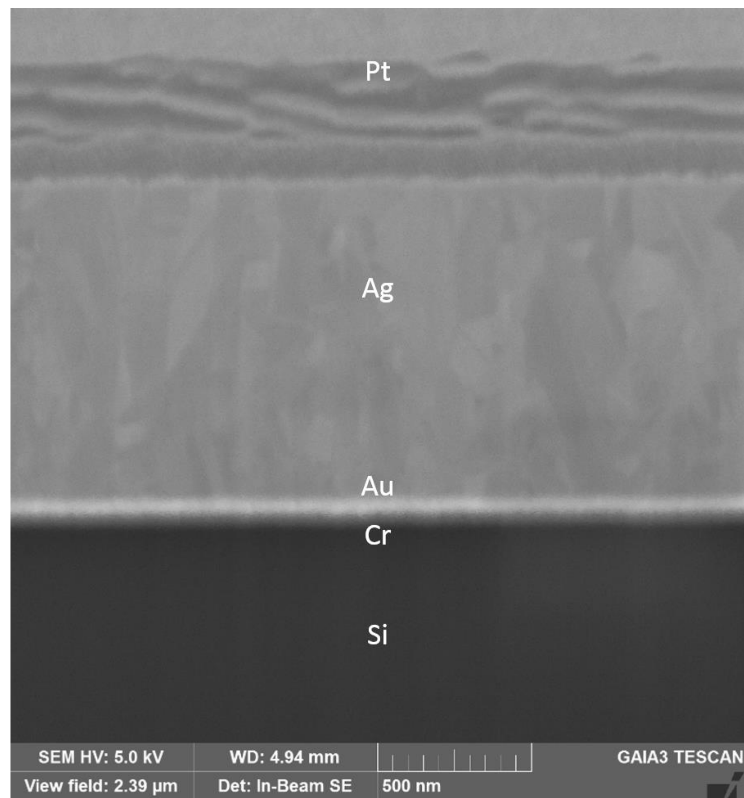

Fig. 6.6 Cross-sectional view of the as-deposited film.

6.3.2 Optimization of oxidation condition

In this research, the oxygen plasma is used to produce silver oxides on the surface of the Ag film. The oxidation process is performed on Gatan® SOLARUS™ Model 950 Advanced Plasma System. The specifications of the normal operation are listed in Table 6.1. After loading the samples into the chamber, the chamber is pumped down to 70 mTorr in 1 min. Then the oxygen (99.995%) flows into the chamber to reach the operating vacuum (400 mTorr). Then the RF is applied and the plasma is generated all over the chamber. After reaction of designated duration, the RF is turned off and the chamber is vented by argon. In this study, a few reaction durations including 3s, 5s and 10s are tried. The surface morphologies of as-reacted samples are examined by SEM and shown in Fig. 6.7 and 6.8. Then these samples are placed on graphite stage, heated up to 210 °C under 0.1 Torr vaccum, kept isothermal for 30 min and cooled down naturally. The low vacuum here is to protect the film from being corroded by other species in air of the lab storing chemicals. After reduction, the surface morphologies are examined by SEM and shown in Fig. 6.11.

Table 6.1 Specifications of Gatan® plasma system.

Parameter	Value
RF frequency	13.56 MHz
RF power	50 W
Vacuum target	70 mTorr
Operating Vacuum	400 mTorr
Oxygen flow rate	33.3 cubic cm per minute

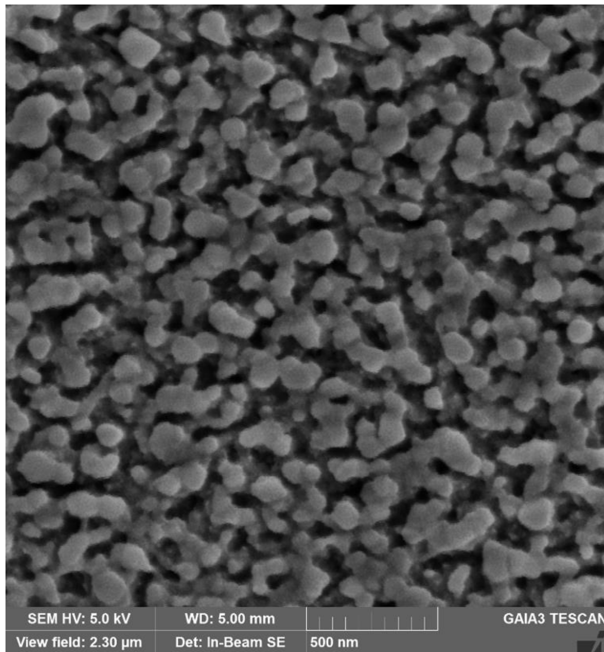

(a)

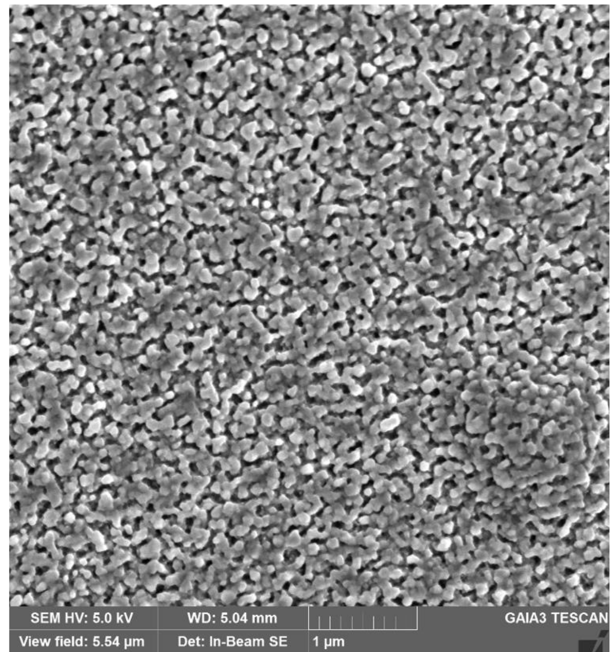

(b)

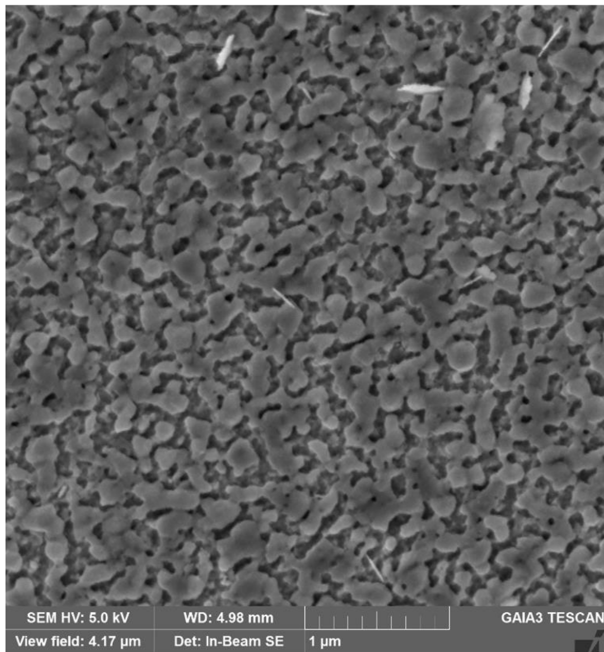

(c)

Fig. 6.7 Surface morphologies of samples with difference plasma treatment time: (a) 3s; (b) 5s; (c) 10s.

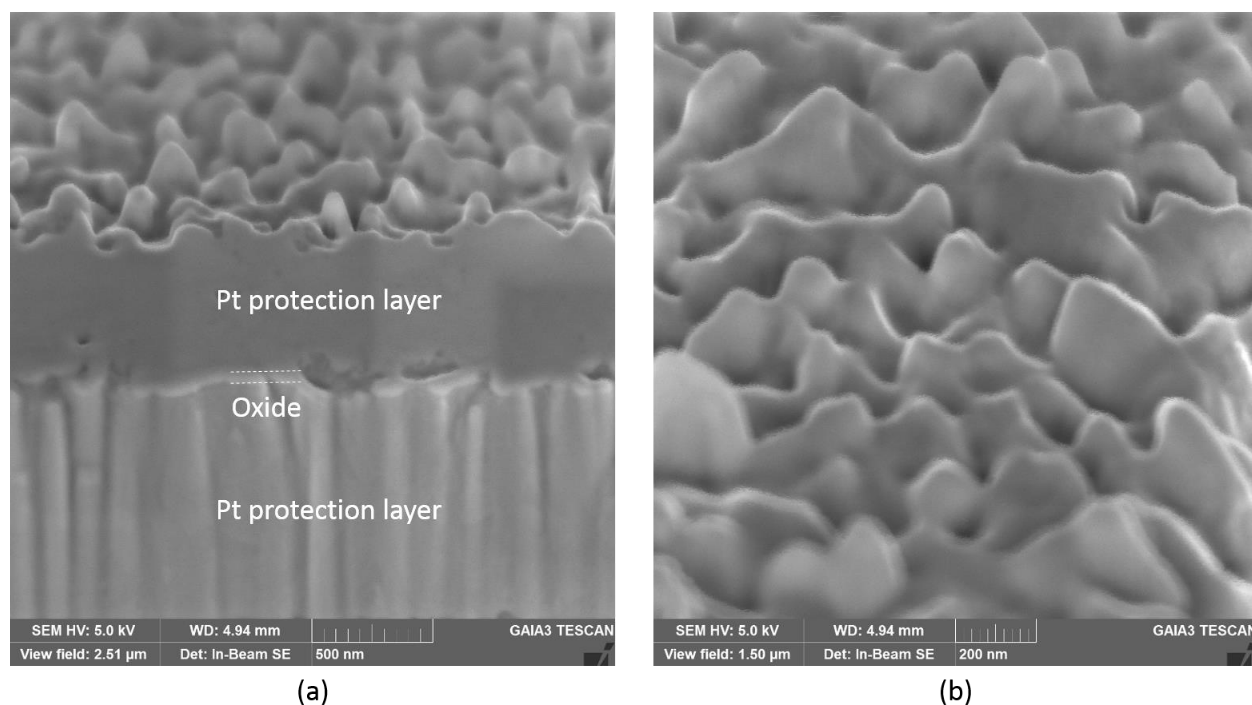

Fig. 6.8 Cross-sectional view of surface oxides after 3s plasma treatment.

From Fig. 6.7, it can be seen that the surface oxides grow in the form of islands. After 3s plasma treatment, the surface of pure Ag is not fully covered by the oxides. As the increase in reaction time, the islands grow and also the coverage is increased. However, the thickening of the oxide is not uniform. The oxide on lower right corner region of Fig. 6.7b is thicker than oxides of other regions. Eventually, the islands connect to each other and form large islands. As shown in Fig. 6.7c, the original Ag grains are invisible and the surface is covered by large islands of silver oxides.

The cross-section of the surface oxides is also examined and shown in Fig. 6.8. After 3s plasma treatment, the thickness of surface oxides is within 50 nm. However, it is worth pointing out that the oxide is not a uniform and flat layer. After reactions, there are lots of asperities on the surface. The height of these asperities ranges from tens of nanometers to two hundred nanometers.

The surface composition and chemical state of Ag are studied by XPS and the results are shown in Fig. 6.9 and 6.10. According to Fig. 6.9, only oxygen and silver can be detected from the surface. The quantification is conducted by using the intensity of Ag 3d and O 1s. The algorithm is pre-defined by in the software-CasaXPS. The surface composition determined by this method is Ag 63 at.% and O 37 at.%, which is pretty close the stoichiometry of Ag_2O. To further study the chemical state of the Ag and O, regional scans are conducted for Ag 3d and O 1s. For both scan, the resulting curve is smoothened by averaging the results of 20 scans. The results are shown in Fig. 6.10.

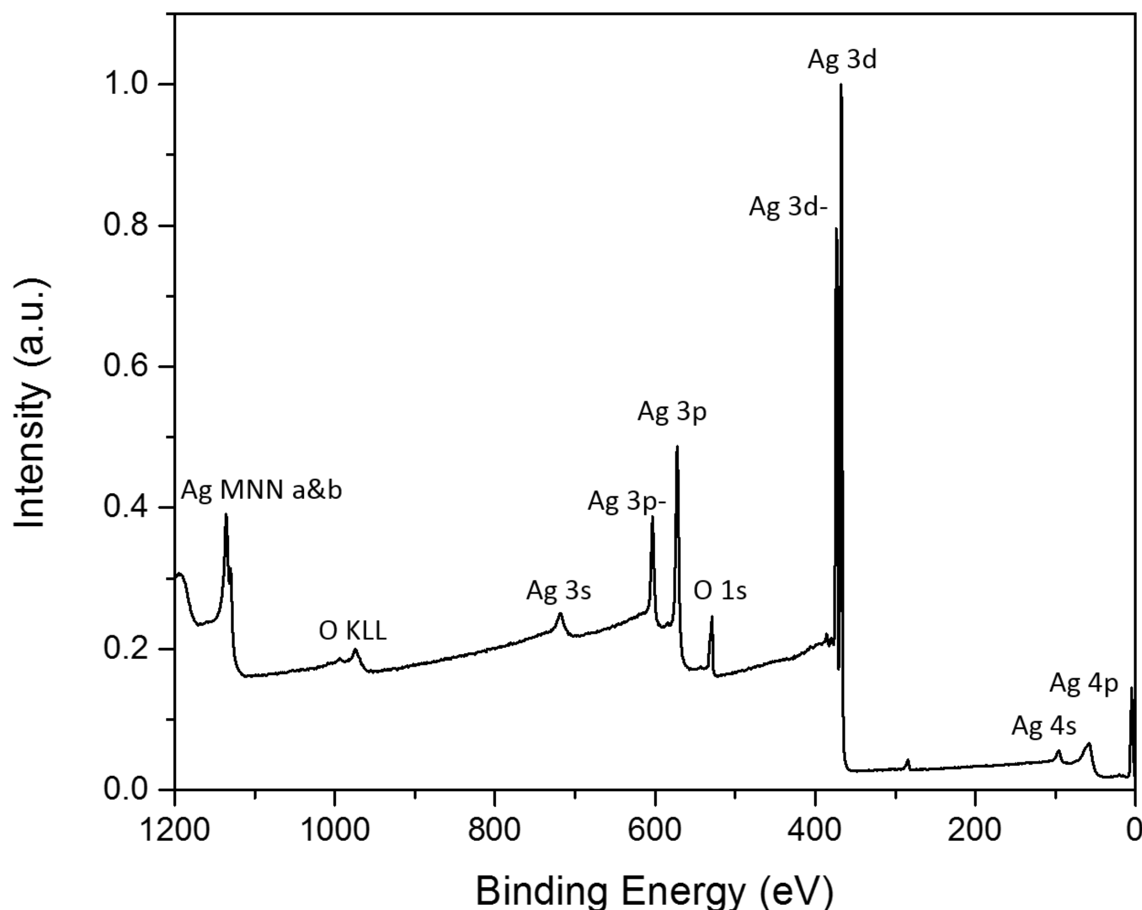

Fig. 6.9 XPS survey scan of the oxidized surface.

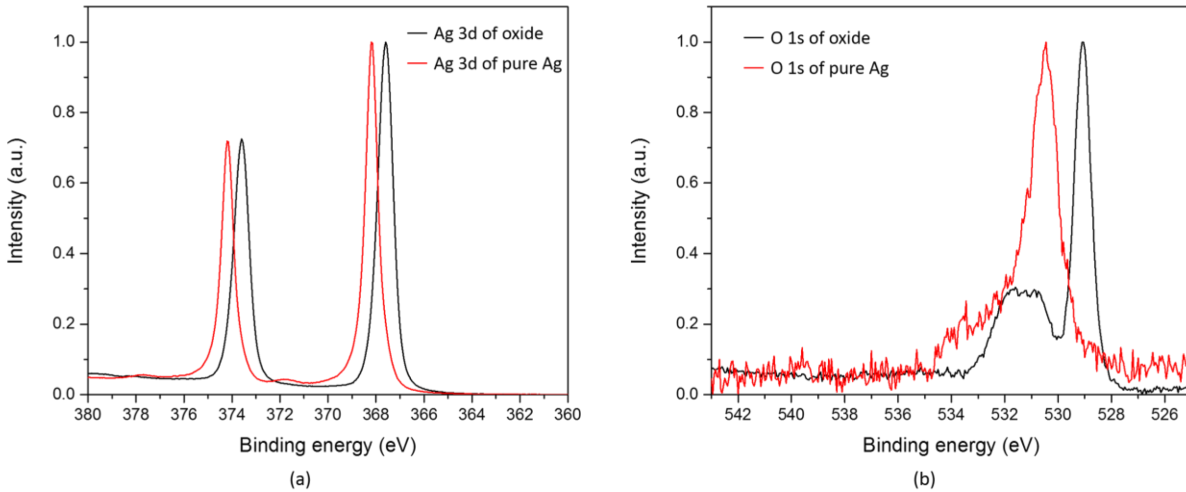

Fig. 6.10 XPS regional scan results: (a) Ag 3d; (b) O 1s.

From Fig. 6.10a, it can be seen that there is significant right-shift of binding energy of Ag 3d in silver oxide compared to that of Ag 3d in pure Ag. The binding energy of Ag $3d_{5/2}$ in oxide is measure to be 367.7 eV, which is consistent to the published result of Ag $3d_{5/2}$ in Ag_2O [8]. From Fig. 6.10b, for O 1s on oxide and Ag, there are broadened peaks centered approximately at 531 eV, which are considered to be originated from a mixture of atomic oxygen and hydroxyl groups [9]. However, for the spectra of O 1s of oxide, there is distinct peak with much higher intensity, symmetry and sharp line width, which is consistent to the published result of O 1s of Ag_2O [10]. The regional scan result also explains the deviation of surface composition from 2 to 1. Due to the exposure of sample to air, the oxygen and hydroxyl groups are absorbed on the surface. However, the quantity is small and they not considered to affect the in-situ reduction process.

In total, the Ag is covered by Ag_2O after reacting with oxygen plasma. The surface becomes rougher and the oxide is not a flat layer. In the following paragraph, the behavior of oxide during in-situ reduction will be examined.

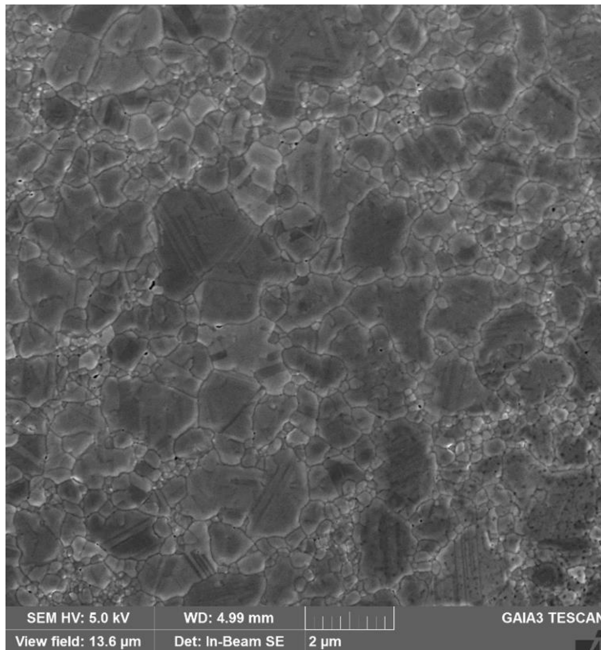

(a)

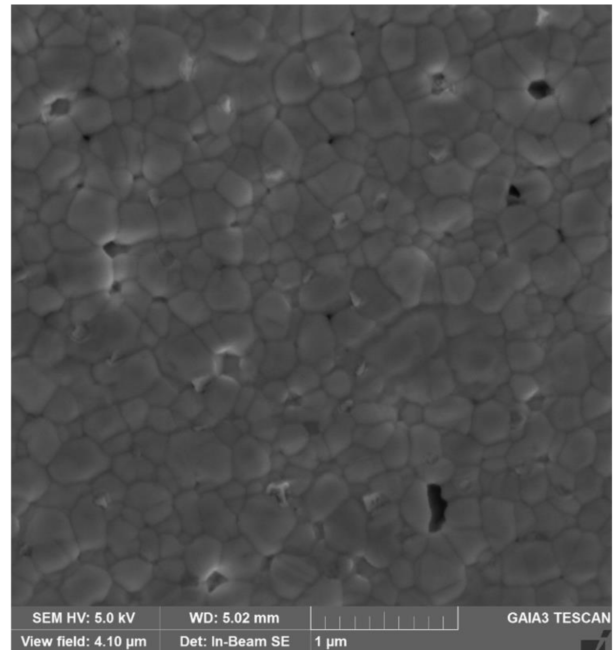

(b)

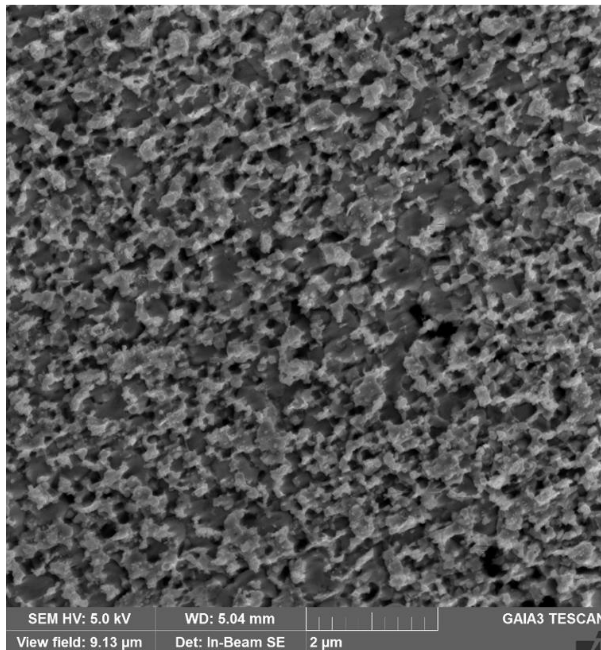

(c)

Fig. 6.11 Surface morphologies after decomposition of surface oxides at 210 °C: (a), (b) and (c) are corresponding to the conditions specified in (a), (b) and (c) of Fig. 6.7.

Theoretically, after decomposition of silver oxides, pure Ag should occur on the top surface. The only thing that remains unknown is the change of surface morphology as the

function of original thickness of silver oxides. Fig. 6.11 shows the surface morphologies of samples which are corresponding to the samples shown in Fig. 6.7. As it can be seen if Fig. 6.11a, the surface is smoother than that of as-reacted sample. Some grains grow significantly during the reduction. However, there are lots of sub-grains and twins in these large grains, which is due to the low stacking fault energy of Ag. In addition, there are sparse voids on the top of the surface. These voids are very small and most of them are in the range of a few tens of nanometers. Fig. 6.11b shows that the surface is not as smooth as the surface in Fig. 6.11a. Although only pure Ag grains can be observed, the size of voids is larger. Lots of voids in the range of a few hundred nanometers can be observed. The surface shown in Fig. 6.11c is much rougher. It can be seen that Ag grains are covered by lots of particles. A possible reason is that the Ag atoms generated by decomposing silver oxides don't merge with the original grains underneath but forming particles themselves, which may be due to the overgrowth of silver oxides during 10 s plasma treatment.

The surface roughness of the as-deposited film, as-oxidized (3s) sample and as-reduced sample are measured by atomic force microscopy (AFM). According to Fig. 6.12, the root-mean-square (RMS) value of the as-deposited film is around 5 nm. After oxidation, the surface became much rougher, which is consistent with the SEM result in Fig. 6.8b. However, the film becomes smother after reduction. The RMS value decreases from 49 nm to 19 nm. Same phenomenon is observed in SEM results. The smoothening process is due to the high surface diffusivity of the Ag decomposed from Ag2O, which facilitates the wetting process of the newly formed Ag on the Ag surface. In other words, the smoothening is a confirmation of the high surface diffusivity of the Ag. Therefore, during bonding, the Ag

decomposed from $Ag2O$ could wet surface of the other piece as well and the bonding could be easier to be formed.

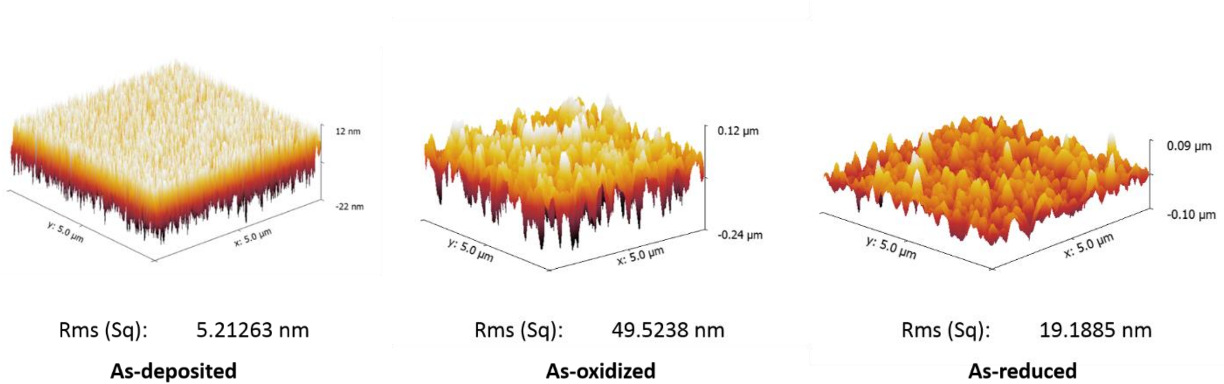

Fig. 6.12 AFM results of the film of different conditions.

Therefore, given that the surface roughness and size voids are major concerns during bonding, only samples treated by plasma for 3 s and 5 s are used for the following bonding process. After that, the cross-sections of these samples are examined by SEM.

6.3.3 Cross-sectional study (SEM/FIB)

The cross-sectional images of the bonding interface between the pure Ag film and Ag with surface oxides by 3 s plasma treatment are shown in Fig. 6.13. Fig. 6.13a is an image with low magnification showing a large area of the joint. The bond line is straight and no cracks can be observed in Si. The details of the joint is shown in Fig. 13b. It can be seen that the width of the joint is around 2.2 μm which is close to the designed value (2.16 μm). Since Ag is very soft, any defects can be buried after mechanical polishing. Therefore, the joint is further examined after FIB cutting.

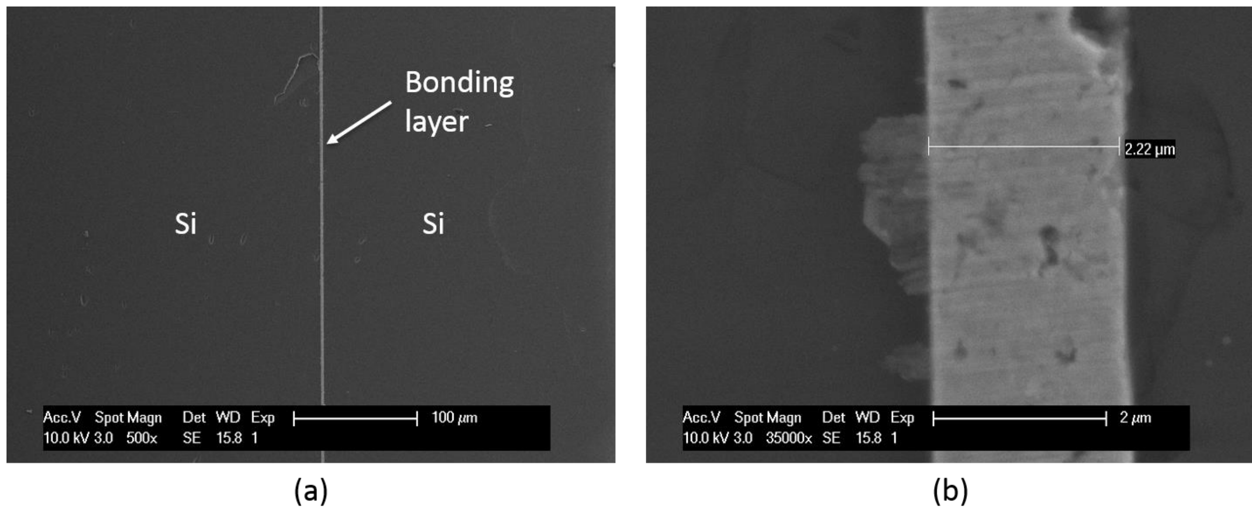

Fig. 6.13 Cross-sectional images of joint bonded by pure Ag film and Ag film with surface oxides produced by oxygen plasma treatment for 3 s.

Two sites are randomly chosen from the joints and clean cross-sections are acquired by FIB cutting and polishing. These two cross-sections are carefully examined by SEM and the results are shown in Fig. 6.14 and Fig. 6.15. Since the surface is cleaned by ion beam, contrast generated by channeling effect is revealed and the outline of grains inside the joint are visible. From Fig. 6.14a and 6.15a, it can be seen that Ag films from both sides are well bonded together in most regions. There are sparse voids along the bonding interface. Most voids are very small and the size is within 50 nm. The voids is generated by two reasons. Firstly, the volume of silver oxide is larger than the volume of pure Ag produced by in-situ reduction. Secondly, the surface is not absolute smooth. As indicated in Fig. 6.14, there will be some voids retained in the bonding interface. However, the voids are not always right along the interface. Some voids migrate towards the internal region of the Ag film, which is due to the redistribution of atoms near the interface. There are also some voids in the metallization layer, which is due to the dissolution of Au into Ag. Similar phenomenon has been reported and this could be suppressed by using Ti/Ni as metallization layer.

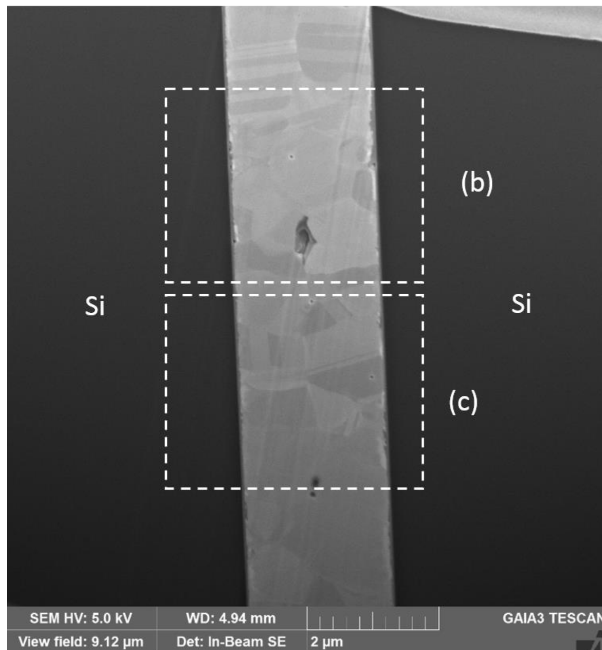

(a)

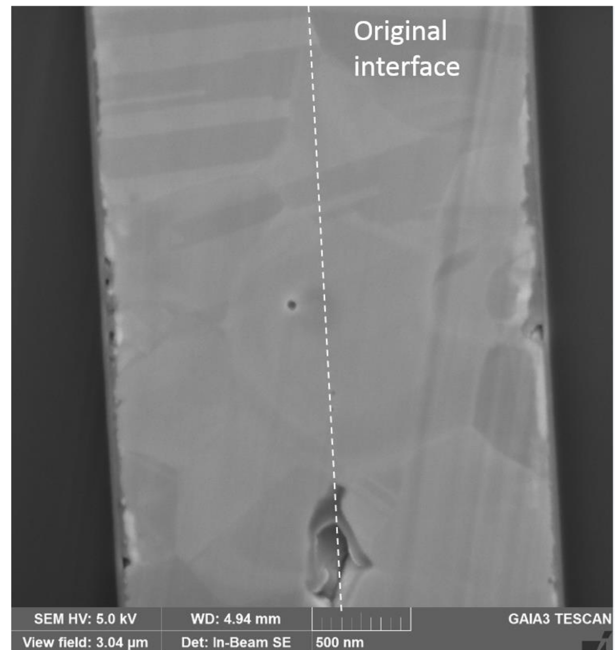

(b)

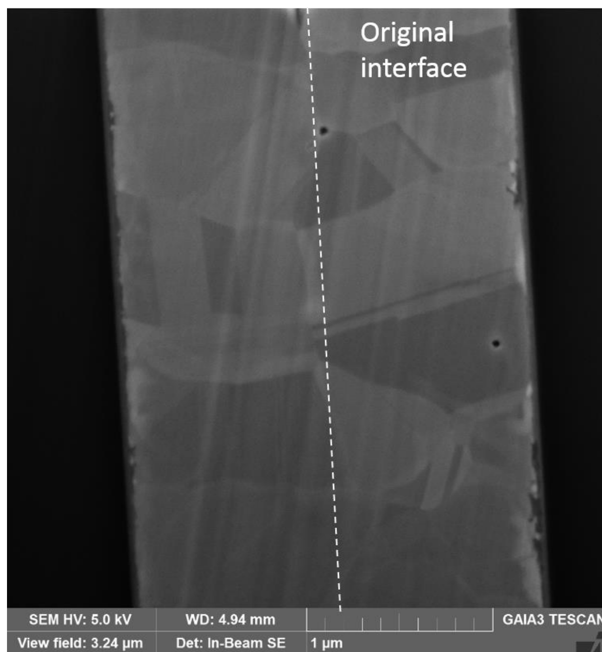

(c)

Fig. 6.14 Cross-sectional study after FIB cutting (Site 1): (a) Overview of the clean cross-section; (b) and (c): High magnification images of highlighted regions in (a).

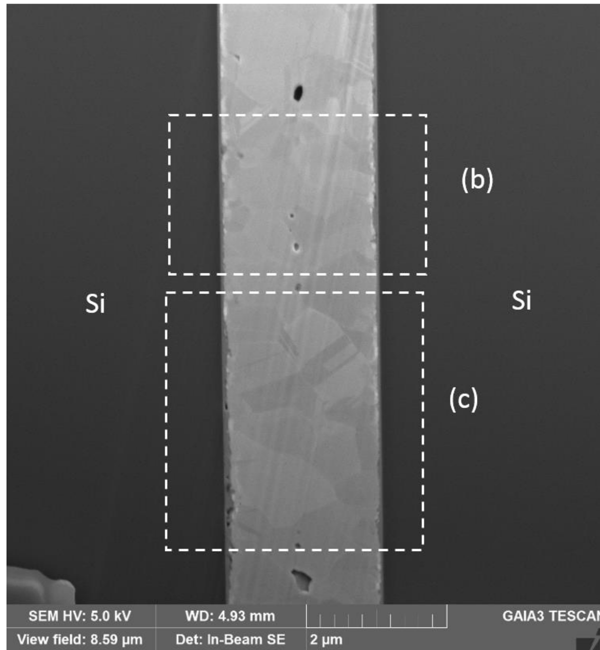

(a)

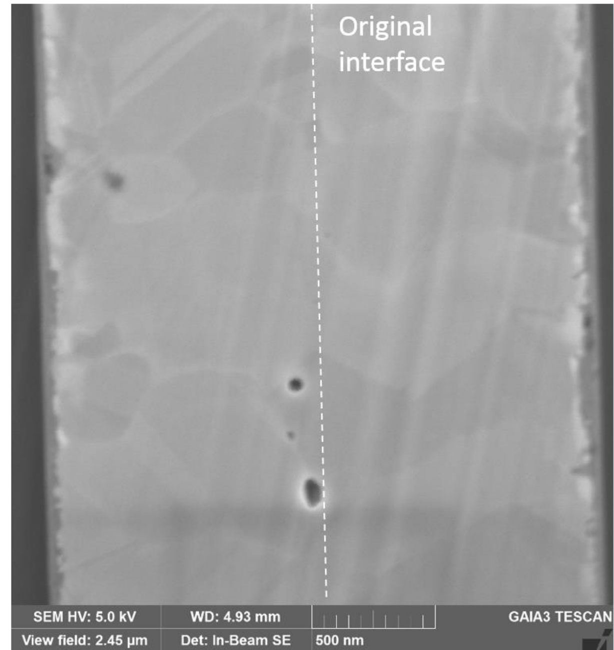

(b)

(c)

Fig. 6.15 Cross-sectional study after FIB cutting (Site 2): (a) Overview of the clean cross-section; (b) and (c): High magnification images of highlighted regions in (a).

Surprisingly, it can also be seen from Fig. 6.13 and 6.14 that lots of grains grow across the original boundary, which is same as the situation of traditional thermal

compression bonded joint. However, it is worth mentioning that our bonding is conducted at 210 °C and assisted by only 200 psi pressure. More specifically, three situations can be observed in the interfacial region. In the first case, the grains grow across the original boundary and the original interface vanishes. Secondly, new grains nucleate at the original boundary and the new grains join with grains from both sides. Thirdly, grains from both sides are joined directly. The first second situations are highly preferred since the original interface vanishes in both cases. The third situation is similar to the situation in solid-state bonding. To further study the grains within the joint, transmission kikuchi diffraction (TKD) is conducted on this sample and the result is shown in Fig. 6.16. The sample preparation for TKD analysis is same to the sample for TEM by using SEM/FIB. The TKD is conducted in SEM and the acceleration voltage is 30 kV. The orientation of the grains are mapped in three directions (X, Y and Z) and shown in the form of inverse pole figure (IPF). Based on TKD results, no preferred orientation or texture is formed during the bonding. The merging of grains can be observed clearly in the IPF result. In most regions, the grains grow across the original boundary. Some twins are also observed which is due to the low stacking fault energy of Ag. In the IPF, different types of grain boundaries are marked in different way. For low angle grain boundary (less than 10 degree), the boundary is not marked while the boundary the marked by black line for high angle grain boundary. However, there are some regions the boundary is still along the original boundary and it seems that it is large angle grain boundary. The structure of this type of boundary will be studied in HRTEM.

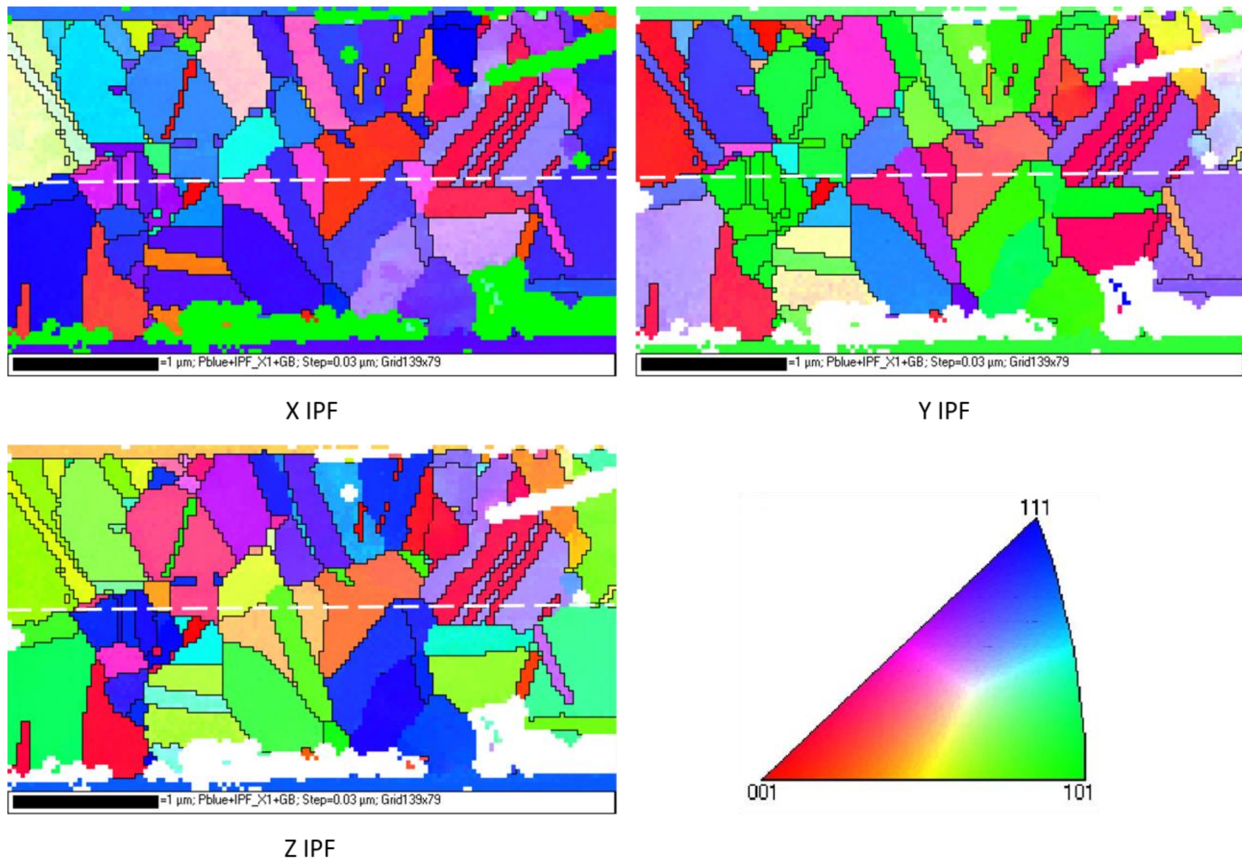

Fig. 6.16 TKD result of the bonded joint.

Ag film with surface oxides produced by 5 s plasma treatment is also used for direct bonding. The cross-sectional study is conducted after FIB cutting and the results are shown in Fig. 6.17. It can be seen that Ag films from two sides are well bonded. In most cases, the grains grow across the original bonding interface, which is the ideal result of the direct bonding. However, the issue of this joint is associated with the voids. As it can be seen that lots of huge voids (a few microns in one dimension) are inside the joint. Recall that the surface morphology of Ag film after thermal decomposition of Ag oxides is related to the thickness of the original thickness of oxides. There are lots of voids on the surface for the film treated by oxygen plasma for 5 s. In this case, the quantity of oxides is too much so that the volumetric retraction due to the decomposition of oxides is too much to be

compensated by surface plastic deformation during bonding. To reduce the size of voids, a higher bonding pressure should be used. However, the die is fragile and any process involving chip requires high pressure is not preferred.

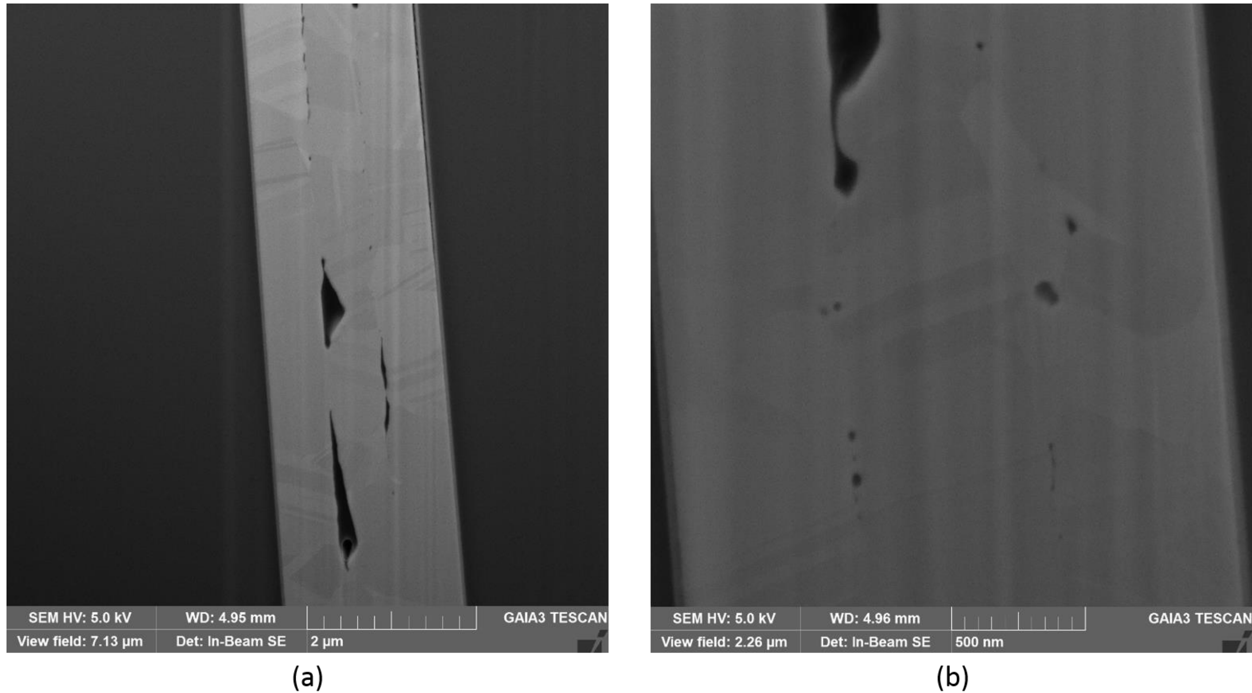

Fig. 6.17 Cross-sectional images of joint bonded by pure Ag film and Ag film with surface oxides produced by oxygen plasma treatment for 5 s.

6.3.4 TEM analysis of the joint

To further study the structure of the bonding interface, TEM analysis is performed. In this section, only the sample bonded by Ag films with 3 s plasma treatment is discussed due to the high quality. The sample is randomly cut from the joint and the result is shown in Fig. 6.18. It can be clearly seen that most grains near the interface grow across the original boundary. Also, only a few grains nucleate at the interface and join the grains from both sides (i.e. the one reside on the right of the red circle in Fig. 6.18). There are some grains directly bonded at the original bonding interface (i.e. those two grains inside the red

circle in Fig. 6.18). The images with high magnifications of this region is shown in Fig. 6.19. It shown that the [111] zone axis of one grain is aligned to the direction of incident beam while the [100] zone axis of the other grain is aligned to the direction of incident beam. This is an indication that the grain boundary is large angle grain boundary. On the other hand, this is no voids or oxides within the interface. The black region in Fig. 19b is due to overlapping of the grains within the boundary. This type of the boundary is same the large angle grain boundary which is commonly observed in polycrystalline materials.

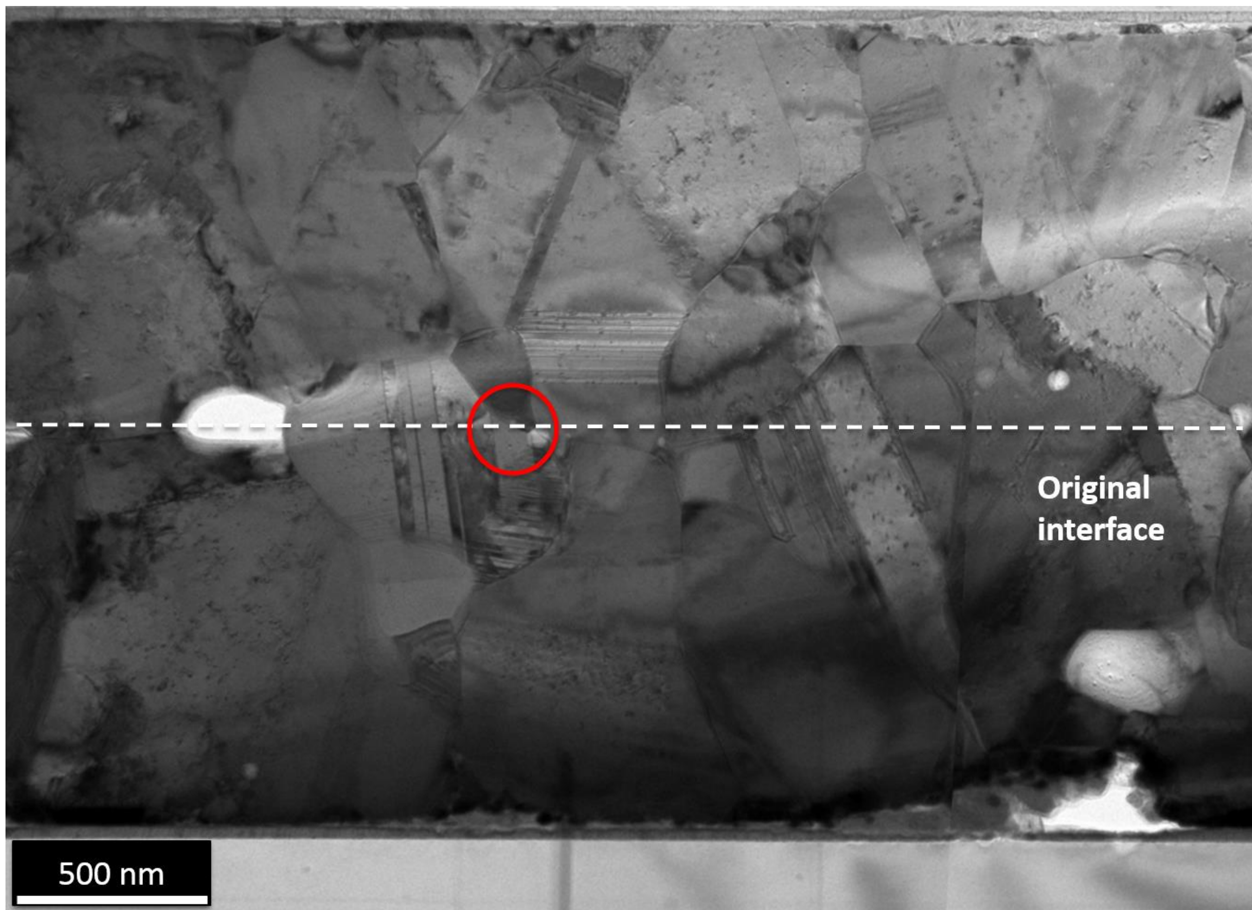

Fig. 6.18 BF image of the joint.

It is also worth mentioning that the Au in the metallization layer is almost consumed, leaving some voids between Ag and Cr. This has been reported in other

literatures. The effective remedy has been found by others, which is to employ Ti and Ni as metallization layer for Ag. Ti can provide good adhesion between Si and other metals. Ni provides good adhesion between Ag and Ti. The most important thing is that Ni doesn't get dissolved in Ag even at high temperature.

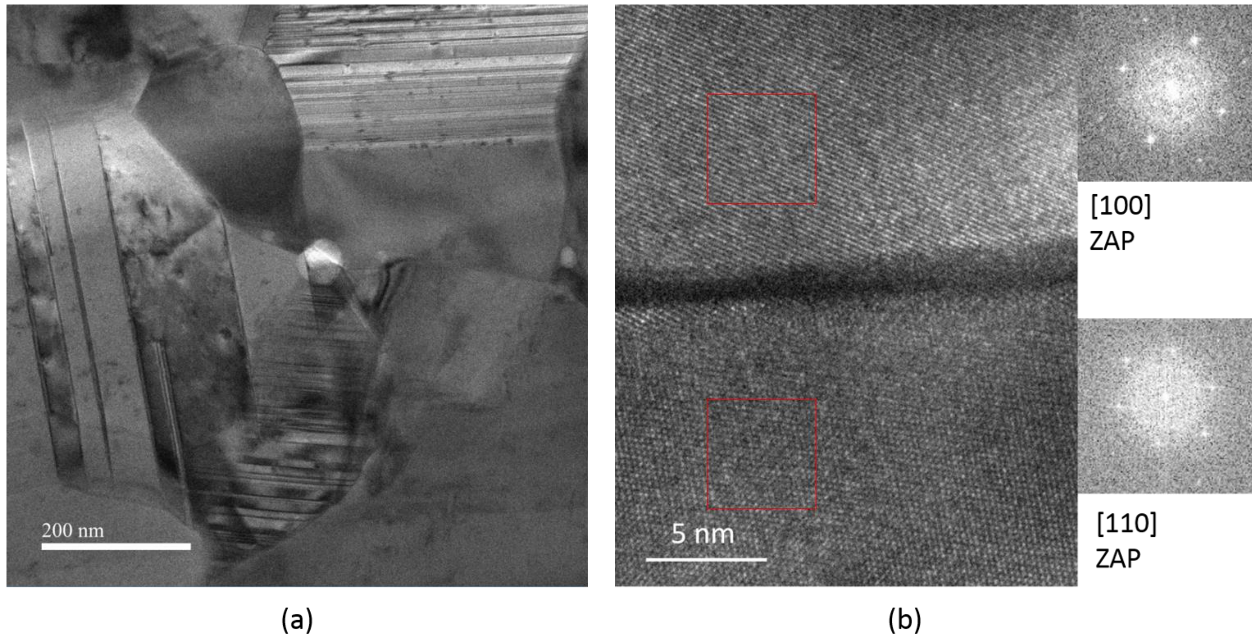

Fig. 6.19 Details of the bonding interface between two grains: (a) low magnification; (b) HRTEM with FFT results of the highlighted regions.

Another thing needs to be figured out is whether there is trapped oxygen or residue oxides in the joint. STEM/EDX analysis is conducted and the results are shown in Fig. 6.20. It can be seen that oxygen can only been detected in the Cr layer. Inside the joint there is no oxygen signal. The oxygen in Cr is quite common since Cr get oxidized easily during the e-beam deposition even though the deposition is conducted under high vacuum. However, the formation of Cr_xO_{1-x} is the reason why Cr can provide good adhesion between Si and other metals. To double check the content of oxygen near the original interface region, an EDX line scan is conducted and the result is shown in Fig. 6. 21. It shows that the signal of

oxygen is too weak to be identified. The signal of Ag is stronger in the upper part is because the upper part of the sample is a little thicker.

Fig. 6.20 STEM/EDX mapping of the joint.

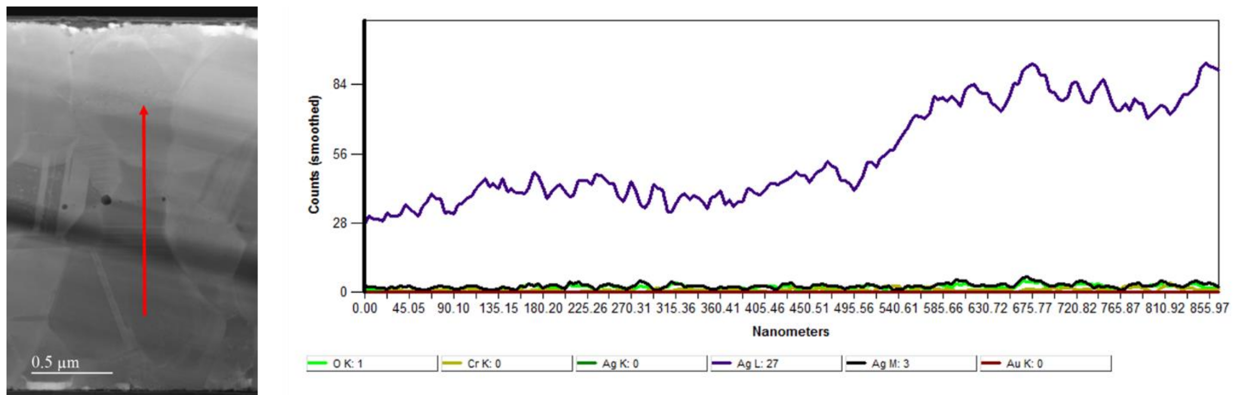

Fig. 6.21 EDX line scan result of the center region of the joint.

6.4 Conclusions

In this study, an Ag-Ag direct bonding technology is developed through in-site reduction of surface oxides. The surface oxides is prepared by the reaction between oxygen plasma and the surface of Ag film. To reduce the size and quantity of the interfacial voids, the thickness of surface oxides must be controlled. By using the plasma system mentioned in the context, 3 s is considered to be an optimized reaction time. The bonding temperature is 210 °C, which is much lower than the reflow temperature of lead free solders (240-250 °C). The bonding pressure is only 200 psi (1.38 MPa), which is several orders of magnitude lower than that in traditional thermal compression bonding.

The cross-sectional study shows that the Ag films are bonded with only sparse voids of tens of nanometers along the interface. In most regions, the grains grow across the interface and the original boundary vanishes. This is due to the high surface diffusivity of the Ag decomposed from Ag oxides. In some regions, new grain nucleate at the interface and joins the grains from both sides. It can be barely found that two grains from two sides are directly bonded. HRTEM shows the mismatch of orientation of those two grains are very small and the interfacial energy is too low to drive the merge of these two grains. EDX results show that there is no oxides residue within the joint and the content of trapped oxygen is too low to be detected by EDX.

The direct bonding technology reported here is a breakthrough in bonding technology since the pressure and temperature used is too low in the view of traditional thermal compression bonding to form joint where the grains grow across the original boundary. The resulting joint is pure Ag. Unlike soldering or sintering, no IMCs and large fractions of pores formed. Recall that pure Ag has the best thermal and electrical

conductivities among metals, high temperature stability and high ductility, this bonding technology exhibits great potentials in the packages high performance ICs and high temperature electronics and photonics.

6.5 Reference

[1] T. Kim, M. Howlader, T. Itoh, T. Suga, Room temperature Cu–Cu direct bonding using surface activated bonding method, J Vac Sci Technol A 21(2) (2003) 449-453.

[2] C.-M. Liu, H.-W. Lin, Y.-S. Huang, Y.-C. Chu, C. Chen, D.-R. Lyu, K.-N. Chen, K.-N. Tu, Low-temperature direct copper-to-copper bonding enabled by creep on (111) surfaces of nanotwinned Cu, Sci Rep-Uk 5 (2015) 9734.

[3] T. Kunimune, M. Kuramoto, S. Ogawa, T. Sugahara, S. Nagao, K. Suganuma, Ultra thermal stability of LED die-attach achieved by pressureless Ag stress-migration bonding at low temperature, Acta Mater 89 (2015) 133-140.

[4] H. Ji, J. Zhou, M. Liang, H. Lu, M. Li, Ultra-low temperature sintering of Cu@Ag core-shell nanoparticle paste by ultrasonic in air for high-temperature power device packaging, Ultrason Sonochem 41 (2018) 375-381.

[5] E.K. Athanassiou, R.N. Grass, W.J. Stark, Large-scale production of carbon-coated copper nanoparticles for sensor applications, Nanotechnology 17(6) (2006) 1668.

[6] X. Liu, H. Nishikawa, Low-pressure Cu-Cu bonding using in-situ surface-modified microscale Cu particles for power device packaging, Scripta Mater 120 (2016) 80-84.

[7] I. Karakaya, W. Thompson, The Ag-O (silver-oxygen) system, J Phase Equilib 13(2) (1992) 137-142.

[8] X.-Y. Gao, S.-Y. Wang, J. Li, Y.-X. Zheng, R.-J. Zhang, P. Zhou, Y.-M. Yang, L.-Y. Chen, Study of structure and optical properties of silver oxide films by ellipsometry, XRD and XPS methods, Thin Solid Films 455-456 (2004) 438-442.

[9] J.F. Weaver, G.B. Hoflund, Surface Characterization Study of the Thermal Decomposition of AgO, J Phys Chem 98(34) (1994) 8519-8524.

[10] A.I. Boronin, S.V. Koscheev, G.M. Zhidomirov, XPS and UPS study of oxygen states on silver, J Electron Spectrosc 96(1) (1998) 43-51.

Chapter 7. Summary

7.1 Main conclusions

In this dissertation, the growth and characterization of mechanical properties and tarnish resistance of the silver solid solution phase with zinc have been conducted. It has been found that the increase in zinc in concentration can effectively increase the tarnish resistance and improve the ductility compared to those of pure Ag. Secondly, the Ag3Al formed in Ag-Al wire bonds has been completely eliminated by alloying indium into Ag. The underlying mechanism and the accompanying evolution of voids and oxides have been studied. This dissertation also addressed the long term reliability issue encountered by the current sintering Ag technology through employing fine-grained silver foil as the bonding medium between Si and Cu substrate. A novel direct bonding technology is also proposed by in-situ reducing surface Ag oxides at low temperature and assisted by low pressure. The specific novelties and findings include:

1. Solid solution strengthening phenomenon is observed in (Ag)-5Zn while solid solution softening occurs in (Ag)-15Zn, which is due to the formation of short range order (SRO) when Zn concentration is high.
2. The enhanced ductility compared to pure Ag is due to the formation of deformation twining, which is easier to be observed when the stacking fault energy (SFE) is low.
3. The tarnish resistance is enhanced with the addition of Zn. With the increase in Zn concentration, the valence band shifts towards the higher binding energy, which increase the activation energy of the sulfurization reaction.
4. The IMCs in Ag-Al bonds are identified as Ag_2Al and Ag_3Al. The failure mechanism of Ag-Al bonds during HAST is concluded and a coupling effect of chemical reaction

and mechanical properties can be used to explain the failure in Ag_3Al, that is, the reaction between Ag_3Al and Cl^- and moisture will induce more defects (voids, micro-cracks) in Ag_3Al and the enlargement of these defects are easier due to the low toughness, which in turn facilitate the corrosive species invading deeper. As a result, the initiation and propagation of micro-cracks will be largely accelerated.

5. A method to eliminate the Ag_3Al through alloying indium (In) into Ag is demonstrated. The corresponding mechanism is studied through transmission electron microscopy (TEM) and thermodynamic modeling. We establish an analytical thermodynamic model for the nucleation process of Ag_3Al that considers the effects of In doping, and successfully explains the underlying reason for the elimination of Ag_3Al: it has to do with the necessity of repelling In into unreacted region.
6. The growth rate of voids is found to be low in Ag-Al bonds due to small volumetric change during phase transformation, which also reduces the growth rate of alumina. These are critical for long term reliability.
7. The root cause of the reliability issues in sintering Ag technology is associated with the porosity of the resulting joints. During aging at elevated temperature in air, the oxygen can penetrate into the joint and react with Cu, forming cuprous oxides along the interface between Ag and Cu. Although this issue can be somewhat mitigated by plating Au or Ag on Cu, other issues are raised due to in coating.
8. By using fine-grained Ag foil as the bonding medium between Si and Cu substrate, the resulting joint produced by solid-state bonding can sustain at 300 °C. After 200 h aging test, no degradation of the strength can be observed and the joint even

becomes stronger. Oxygen cannot penetrate dense Ag foil and the redistribution of atoms near the interface could effectively increase the strength of the bonding interface.

9. For traditional solid-solid direct bonding after which the original boundary vanishes, high bonding temperature, pressure and high process time are required. In this work, Ag-Ag direct bonding through in-situ reduction of surface oxides are proposed. The sample is bonded at 210 °C assisted by only 1.38 MPa pressure. Grains grow across the original boundary and the original boundary vanishes in most regions.
10. The reason why the grains can merge during such a low temperature process is associated with the Ag decomposed from the surface oxides. The in-situ reduction of surface oxides can produce Ag particles with very high diffusivity, which can effectively facilitate the redistribution of atoms near the interface or nucleation of new grains. The resulting joint only consists of pure Ag, which has the highest electrical and thermal conductivities among metals, high temperature stability and ductility. This technology should have great potential in electronic and photonic devices where high quality and high performance are required!

7.2 Recommendations to future work

The research in this dissertation also leads to a few recommendations for future work:

1. The quantitative model and direct observation of forming SRO in Ag solid solution phase zinc are of great interest to be investigated. A critical zinc concentration is expected to exist. When the concentration is lower than the critical value, the solid

solution hardening dominates while the formation of SRO plays more important role above the critical value.

2. The quantitative model of the formation and contribution of the deformation twinning with the change in zinc concentration is needed to be established.
3. It is more practical to fabricate Ag solid solution phase with Zn/In bonding wires and perform wire bonding on Al pads. The parameters during the bonding and the reliability test results can provides more information for the industry.
4. It is more interesting to try other metallic systems to generalize the mechanism of suppression of Ag_3Al in Ag-Al bonds by alloying In into Ag. This generalization could be critical and useful for the IMCs control.
5. Other physical properties such as electrical and thermal conductivities and reflectance of Ag solid solution phase with Zn and In should be studied quantitatively to evaluate the materials from a wider angle.
6. It is essential to perform solid-state bonding by using functional chip and evaluate the functionality of the chip after different reliability test, which can provides more information to the industry.
7. Applying Ag-Ag direct bonding process in real device packages (i.e. 3D integration or flip chip) and study the performance (i.e. electrical and thermal). Further optimization of the bonding condition such as surface roughness, temperature, pressure and thickness of oxides is highly recommended.